POLITECNICO DI MILANO
DEPARTMENT OF MECHANICAL ENGINEERING
DOCTORAL PROGRAMME IN MECHANICAL ENGINEERING

INNOVATION IN THE PRODUCTION PROCESS OF CUSTOM-MADE SCOLIOSIS BRACES WITH ADDITIVE MANUFACTURING

Doctoral Dissertation of:
Davide Felice Redaelli

Supervisor:
Prof. Giorgio Colombo

Co-supervisor:
Prof. Dr. Sakti Srivastava

Tutor:
Prof. Maurizio Vedani

Co-tutor:
Dr. Emilia Biffi

The Chair of the Doctoral Program:
Prof. Daniele Rocchi

2019 – XXXII Cycle

Abstract

THE work presents a new manufacturing process for the production of patient-specific scoliosis braces by using the 3D printing technology. The scoliosis is the most common spine disorder and the treatment consists on a combination of physical therapy and use of back braces, which are used to support and help realigning the spine. The current manufacturing processes are based on thermoforming a plastic plate, requiring the production of a positive mold to be wrapped, which is then discarded as a waste. Moreover, the production is still very dependent on the technicians manual operations reducing the repeatability of the process. This thesis proposes the use of 3D printing for manufacturing the brace, which could improve the repeatability of its characteristics. The production process should be changed also for the sculpting phase, which can be performed in a virtual environment by means of CAD tools. In order to reach a stable process, the work was organized in different steps: acquisition of patient's 3D skin, creation of brace and skeleton models, numerical simulations, analysis of additive manufacturing technologies and evaluation of materials.

First of all, to acquire the patient's 3D skin model, different 3D scanners were compared using both standard reference objects (*i.e.* flat plane and spheres) required by the common guidelines and also manikin parts, representative of the orthopedic application. The investigation included also the test of different motion approaches around the chest of a manikin for the handheld scanners. As a general result, the fixed scanners performed better in terms of reconstruction quality, but the model has to be acquired over a long time period. However, the orthopedic application requires to have a fast scan of about 30 seconds, making them impractical. The handheld scanners, on the other hand, can compute a fast reconstruction by moving around the patient in few seconds. Results showed that Artec Leo and Structure Sensor are the most appropriate for the orthopedic centers.The Artec Leo resulted in higher accuracy (about 0.2 mm), which could be required for very detailed parts, while the Structure Sensor can be stably used for the back brace design, with an accuracy of about 0.6 mm.

Next, analyzing the current CAD tools for sculpting the tessellated models, I identified issues in the different software packages, which would require a future integration. The most relevant gap is the absence of a 3D skeleton model that could be used as a

visual reference in the 3D virtual environment. The technicians are currently limited to using bi-planar X-ray images to assume how the brace would interact with the patient's body. For this reason, I developed a pseudo-parametric skeleton model that could be morphed according to these two projections to obtain an approximated patient-specific skeleton model, which can be used as a reference when sculpting the brace, in its low poly formulation.

Moreover, a NURBS-surface formulation of the model was imported in the numerical simulation tool to compute the interaction between the brace and the patient's body. A set of simplified simulations was performed to verify the usability of the developed model and the possibility to obtain a relatively fast numerical simulation to validate the sculpted brace before 3D printing it during the design phase. The simulations converged showing the possible interaction analysis, but they required more than an hour due to the non-linearity of the contact problem. Complementary simulations where performed on the simpler case of a wrist orthosis without considering the interaction with the patient's anatomy. The orthosis was constrained as a cantilever beam supported with a roller and loaded with a force in the hand palm. This simulation assessed the feasibility of using the Topology Optimization tool for reducing the weight of an orthotic device, obtaining an optimized material distribution in contrast to purely aesthetic patterns. The mass was reduced of about 25% in 6 minutes, which was more than 10 times the static structural simulation time. This means that applying the Topology Optimization to the more complex case of the chest brace with the contact interaction could be exponentially larger.

Regarding the Additive Manufacturing, the FFF technology was selected for the best compromise in terms of costs, speed and printing volume. Different materials were initially considered, but only PLA and PETG were deeply analyzed and compared to the thermoformed material (PP). The best results were obtained with the PETG, both for the mechanical properties and for the inter-layer adhesion, verified with a SEM analysis. This material was thus used for 3D printing a full brace that was successfully tested with a volunteering patient. The positive feedback regarded not only the patient but also the orthopedic physician and technicians involved in the experiment.

The overall conclusion of the thesis is that the process is currently feasible in all the different steps, even though these have to be performed separately by using different software packages. Thus, a further integration of the various tools is required in order to allow a simpler implementation of the process in the orthopedic centers.

Sommario

L A tesi presenta un nuovo processo manifatturiero per la produzione di corsetti personalizzati per il trattamento della scoliosi, utilizzando la tecnologia di stampa 3D. La scoliosi è la problematica più comune riguardo la colonna vertebrale ed il trattamento consiste in una combinazione di terapia fisica e utilizzo di corsetti ortopedici, i quali hanno lo scopo di supportare e aiutare il riallineamento della colonna.

La manifattura attuale si basa sulla termoformatura di una lastra polimerica, richiedendo la produzione di uno stampo in positivo che viene poi scartato tra i rifiuti. Inoltre, la produzione è ancora fortemente basata sulle operazioni manuali eseguite dai tecnici ortopedici, riducendo la ripetibilità del processo. Questa tesi propone l'utilizzo della stampa 3D per la produzione del corsetto, tecnica che può migliorare la ripetibilità delle caratteristiche del prodotto. Il processo complessivo andrebbe modificato anche nella fase di modellazione, che può essere completato nell'ambiente virtuale tramite l'utilizzo degli strumenti CAD. Al fine di ottenere un processo stabile, il lavoro è stato organizzato in differenti fasi: acquisizione della geometria esterna del paziente, creazione dei modelli di corsetto e di scheletro, simulazioni numeriche, analisi delle tecnologie di manifattura additiva e valutazione di materiali stampabili.

Innanzitutto, per acquisire il modello della pelle del paziente sono stati comparati diversi scanner 3D, utilizzando sia oggetti di riferimento standard (piano e sfere), richiesti dalle comuni linee guida, sia alcune parti di un manichino, considerate rappresentative delle possibili applicazioni ortopediche. L'analisi ha incluso anche il test di diversi approcci di movimento degli scanner manuali attorno al busto del manichino. Come risultato generale, gli scanner fissi da laboratorio hanno portato a risultati migliori in termini di qualità della ricostruzione, ma l'acquisizione ha richiesto un periodo di tempo molto lungo. Tuttavia, l'applicazione ortopedica richiede una scansione rapida di circa 30 secondi, il che li rende poco pratici. Gli scanner portatili, d'altra parte, possono compiere una ricostruzione più rapida, potendoli spostare attorno al paziente in pochi secondi. I risultati hanno mostrato che Artec Leo e Structure Sensor sono i più appropriati per i centri ortopedici. Artec Leo ha prodotto una maggiore precisione (circa 0.2 mm), che potrebbe essere richiesta per parti molto dettagliate, mentre

lo Structure Sensor può essere utilizzato stabilmente per la modellazione dei corsetti ortopedici, con una accuratezza di circa 0.6 mm.

Successivamente, analizzando gli attuali strumenti CAD per scolpire i modelli tassellati, sono stati identificati i problemi nei diversi pacchetti software, che richiederebbero una futura integrazione. La pecca più rilevante è l'assenza di un modello di scheletro 3D che potrebbe essere utilizzato come riferimento visivo nell'ambiente virtuale 3D. I tecnici sono attualmente limitati all'uso delle immagini radiografiche planari (frontale e laterale) per ipotizzare come il corsetto interagirebbe con il corpo del paziente. Per questo motivo, ho sviluppato un modello di scheletro pseudo-parametrico che può essere trasformato secondo queste due proiezioni ed ottenere così un modello approssimativo dello scheletro del singolo paziente, che può essere usato come riferimento quando si scolpisce il tutore, nella sua formulazione alleggerita con pochi poligoni.

Inoltre, è stata sviluppata una formulazione del modello con superfici NURBS che può essere importata nello strumento di simulazione numerica, permettendo di calcolare l'interazione tra il tutore e il corpo del paziente. è stata eseguita una serie di simulazioni semplificate per verificare l'usabilità del modello sviluppato e la possibilità di ottenere una simulazione numerica relativamente veloce per convalidare il modello di corsetto creato durante la fase di progettazione, prima di passare a stamparlo in 3D. Le simulazioni hanno raggiunto la convergenza, mostrando la possibile analisi delle interazioni, ma richiedendo più di un'ora a causa della non linearità del problema di contatto. Una serie di simulazioni complementari sono state eseguite sul caso più semplice di un'ortesi del polso per testare letecniche di Ottimizzazione Topologica, senza però considerare l'interazione con l'anatomia del paziente. L'ortesi di polso è stata vincolata come una trave a sbalzo sostenuta da un carrello e caricata con una forza posizionata all'estremità del palmo della mano. Questa simulazione ha valutato la fattibilità dell'utilizzo dello strumento di Ottimizzazione Topologica per ridurre il peso di un dispositivo ortesico, con una distribuzione del materiale ottimizzata in contrapposizione alle trame puramente estetiche. La massa è stata ridotta di circa il 25% in 6 minuti, tempo circa 10 volte superiore a quello richiesto dalla sola analisi statico-strutturale. Ciò significa che l'applicazione dell'Ottimizzazione Topologica al caso più complesso del corsetto ortopedico con l'interazione di contatto potrebbe portare ad un incremento esponenziale del tempo richiesto.

Per quanto riguarda la produzione additiva, è stata selezionata la tecnologia di stampa da filamento (FFF) per il miglior compromesso in termini di costi, velocità e volume di stampa. Inizialmente sono stati considerati diversi materiali, ma sono stati analizzati nel particolare solo PLA e PETG e confrontati con il materiale termoformato (PP). I risultati migliori sono stati ottenuti con il PETG, sia per le proprietà meccaniche che per l'adesione tra gli strati, verificata con un'analisi SEM. Questo materiale è stato quindi utilizzato per la stampa 3D di un corsetto completo che è stato testato poi con successo con un paziente volontario. Il feedback positivo ha riguardato non solo il paziente ma anche il medico ortopedico e i tecnici coinvolti nell'esperimento.

La conclusione generale della tesi è che il processo è attualmente fattibile in tutte le diverse fasi, anche se al momento devono essere eseguite separatamente utilizzando diversi pacchetti software. Pertanto, è necessaria un'ulteriore integrazione dei vari strumenti al fine di consentire una più semplice attuazione del processo completo nei centri ortopedici.

Contents

List of Figures

List of Tables

List of Abbreviations

2D	*Two Dimensional*
3D	*Three Dimensional*
ABS	*Acrylonitrile Butadiene Styrene*
AFO	*Ankle-Foot-Orthosis*
AIS	*Adolescent Idiopatic Scoliosis*
AM	*Additive Manufacturing*
CAD	*Computer Aided Design*
CAM	*Computer Aided Manufacturing*
CMM	*Coordinate-Measuring Machines*
CNC	*Computer Numberical Control*
CNR	*Consiglio Nazionale delle Ricerche* *National Research Council*
CT	*Computerized Tomography*
DICOM	*Digital Imaging and Communications in Medicine*
DIY	*Do It Yourself*
DOF	*Degree of Freedom*
DSC	*Differential Scanning Calorimetry*

FDM	*Fused Deposition Modeling*
FEA	*Finite Element Analysis*
FFF	*Fused Filament Fabrication*
FPS	*Frame Per Second*
HIPS	*High Impact Polystyrene*
HT	*High Temperature*
IPCB	*Institute of Polymers, Composites and Biomaterials*
IR	*InfraRed*
IRCCS	*Istituto di Ricovero e Cura a Carattere Scientifico*
JCGM	*Joint Committee for Guides in Metrology*
LEFM	*Linear Elastic Fracture Mechanics*
LT	*Low Temperature*
MPC	*Multi Point Constraint*
MRI	*Magnetic Resonance Imaging*
NIR	*Near InfraRed*
NURBS	*Non-Uniform Rational Basis Spline*
O&P	*Orthopedics and Prosthetics*
OBJ	*Object file format (.obj)*
OI	*Osteogenesis Imperfecta*
PC	*Polycarbonate*
PE	*Polyethylene*
PF	*Probing error in Form*
PETG	*Polyethylene Terephthalate Glycol*

PhD   *Philosophiae Doctor*

PLA   *Polylactide (or Polylactic Acid)*

PP   *Polypropylene*

PS   *Probing error in Size*

RGB   *Red, Green and Blue*

SD   *Spacing Distance*

SEM   *Scanning Electron Microscopy*

SLA   *StereoLithography Apparatus*

SLS   *Selective Laser Sintering*

STL   *StereoLithography File Format (.stl)*

TO   *Topology Optimization*

TOF   *Time of Flight*

TIJ   *Thermal InkJet*

TPU   *Thermoplastic-urethane*

Acknowledgements

CHAPTER *1*

Introduction

This chapter presents a brief explanation of the pathology called scoliosis and its treatment. This consists mainly of wearing an external orthopedic device, called scoliosis brace or orthosis, which is the focus of this PhD project. The text continues presenting the current manufacturing process and the proposed improvements that are discussed along in the following chapters. Finally, the chapter ends with the presentation of project structure.

The aim of this project is to analyze the current production process of the braces for scoliosis and to propose an alternative for the manufacturing method using 3D printing.

1.1 Scoliosis and back braces

Scoliosis is the medical definition for the musculo-skeletal disorder which consists in an abnormal curvature of the vertebral column on the lateral sides, with angles greater than a certain limit [55]. In particular, the physicians analyze the anterior-posterior radiography (front and back view) to measure the Cobb angle. This is defined as the maximum angle that can be measured considering the quasi-flat faces of the vertebral bodies (see Fig. 1.1). Some authors established that the threshold for this angle is equal to 10 degrees, in order to distinguish between a physiological and a pathological spine [61, 90]. There are different types of scoliosis: neuromuscular, congenital and degenerative. However, among adolescents and children, AIS is the most common [85].

In the frontal plane, the spine should be ideally straight along the vertical axis that passes through the center of the pelvis. In people with a marked scoliosis, the spine can be deformed on one side only or on both sides with respect to this axis (single, double or even triple curvature). In spite of the common use of 2-D radiography and the Cobb angle parameter, physicians are aware that the deformity is not simply represented by
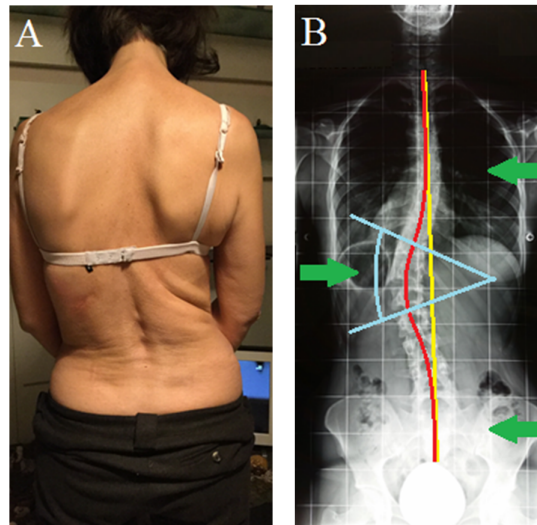
Figure 1.1: *Scoliotic patient, photograph (A) and relative radiograph on the coronal plane (B). On the radiograph there have been indicated: the ideal spine alignment (yellow line), the real scoliotic curve (red spline) the Cobb angle evaluation (in blue) and the theoretical three-point bending system (depicted by the green arrows).*

a curvature in the frontal plane in respect to the vertical axis. Indeed, the spine has a natural curvature also on the sagittal plane (lateral view), where the deviations from the standard curves are named kyphosis and lordosis (Figure 1.2). The combination of the curvatures on both planes often produces also a torsional rotation of the vertebrae around the vertical axis, which has to be considered when generating the orthosis.

This rotational effect appears when performing another typical screening test, which consists in analyzing the back of a person when bending the chest forward. Observing the patient from behind the back should theoretically show a symmetrical profile, while a scoliosis patient will have an evident hump (gibbosity) on a side. Moreover, the scoliosis is often accompanied by a decreased flexibility of the spine that is visible from the side when bent forward. Ideallly, the curvature should be continuous, but if the back has some flat parts, the person could have to undergo further investigation [97].

The possible causes of scoliosis can often be found in genetic alterations, which produce hyperelastic ligament and muscle weakness. The most common type of scoliosis affecting children is defined Adolescent Idiopathic Scoliosis (AIS) and shows a genetic inheritance in about 30% of the cases [96]. Probably the most critical situation is represented by Osteogenesis Imperfecta, a rare disease that affects also the bone growth, bringing to the most evident spine deformation since childhood due to ligament laxity and vertebral crushes. Moreover, also in patients with non-genetic causes, the curvatures can be increased by length difference of the lower limbs, bad posture and wrong repeated movements.

Since scoliosis is a disease that progresses with time, most of the patients who have a light scoliosis in the childhood, without a proper treatment will have a worsening of the spine deformation in the adulthood. Thus, it is important to intervene as early as possible for maintaining the deformation under control [95]. Previous studies established that the scoliosis affects about 2-3% of population in childhood [111] and about 4% in adolescence [18].

Normal spine **Kyphosis** **Hyperlordosis**
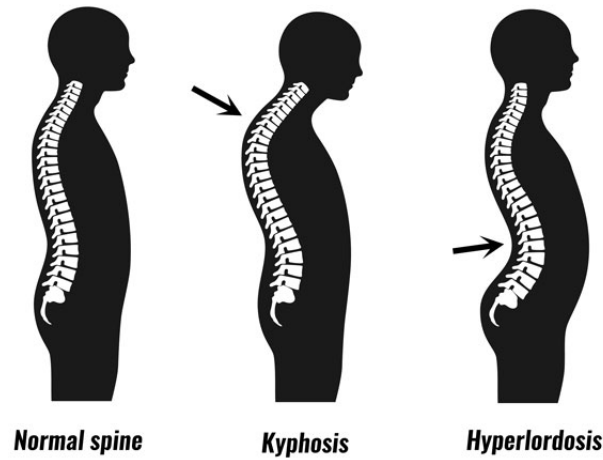
Figure 1.2: *Comparison of normal spine curvature (left) to deviations of type Kyphosis (center) and hyperlordosis (right) [98].*

When the back is aching but no clear deformation is evident, it could be mostly due to bad posture. In such cases, the doctors could refer to as scoliotic attitude which is not to be consider as a genuine scoliosis. The treatment in this case could be limited to performing physical exercises and paying more attention during daily activities and repeated movements.

Also the traditional treatment for scoliosis includes physical exercise to strengthen the muscles of the abdomen and of the back, but it is combined with the use of corrective braces. Only in critical cases, such as Cobb angle beyond 45 degrees or excessive vertebral deformations due to accidents, a surgery can be required to block the further progression of the deformation and the possible consequences on the internal organs. In these critical cases, the most known type of surgery is the spinal fusion, in which the vertebrae are fixed to metal rods in different possible arrangements [116].

The scoliosis brace is an auxiliary orthopedic apparatus used to support properly the back and commonly adopted also with the idea of correcting the spine curvature. This device is a special custom-made product, designed based on the shape of the patient's body and modified in order to apply a correction to the vertebral column, respecting also parameters of comfort and usability. For example, the technicians have to consider the freedom in performing daily movements, the comfort in sensitive areas and also the perspiration allowed by the materials.

The brace is commonly composed of a plastic thermoformed plate, that creates the main shell, and auxiliary components for closing the brace or for improving the comfort, as depicted in Figure 1.3. The shell can be opened in the front, on the backside or even on the side depending on the model. The typical closure system is composed of velcro straps fasteners riveted on a side of the opening and buckles riveted on the other side. The number of straps can vary depending on the dimensions of the brace, the width of the straps and their resistance, in relation also to the characteristics of the patient. In addition, it is common to find also soft foam covering the upper border in correspondence of the armpit and also of the breast for female patients, or in the lower border where there could be contact with the legs in the sitting position.
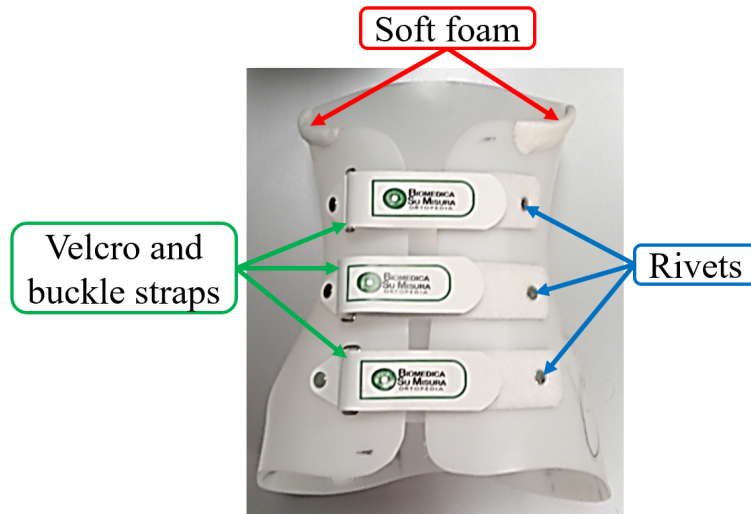
Figure 1.3: *Brace components.*

There exists a wide variety of orthopedic braces depending on the type of scoliosis (*e.g.*, single/double and lumbar/thoracic curvature), on the severity level of scoliosis (evaluated through the measurement of the Cobb angle and the back hump), on the flexibility of the spine and it variations along a time period, and on the available contact regions for the selected brace type (*e.g.* bony parts or only soft tissues on the navel level). Other differences regard the materials and the stiffness of the orthoses (rigid or semi-rigid, with or without metal bars), and the possibility of using the chest brace all day long (the full-time braces are commonly prescribed 23 hours per day) or only during the night (nighttime braces) [65].
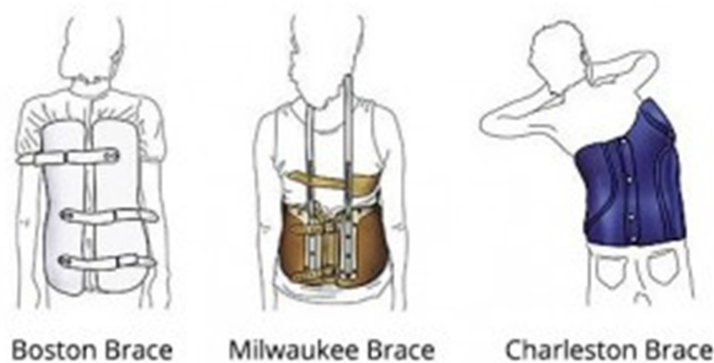
Figure 1.4: *Example of brace types [67].*

The orthoses should be designed not only to support the patient, increase the stability and protect the spine, but also to help the patient for daily life activities. Therefore, the braces should not be excessively big nor create new limits to patients' movements, but aid their motion abilities. Indeed, one of the basic tests performed when the brace is delivered is to try walking and repeating the sitting-standing movements.

In order to realign the spine, the orthosis is shaped in a way that produces forces in

precise regions, while unloading other zones. Depending on the type of brace chosen by the orthopedist, the corrections and the subsequent forces can have different levels of intensity. These forces are usually applied with respect to the spine deformation ideally miming the configuration of the three-point bend test, as outlined in Fig. 1.1B.
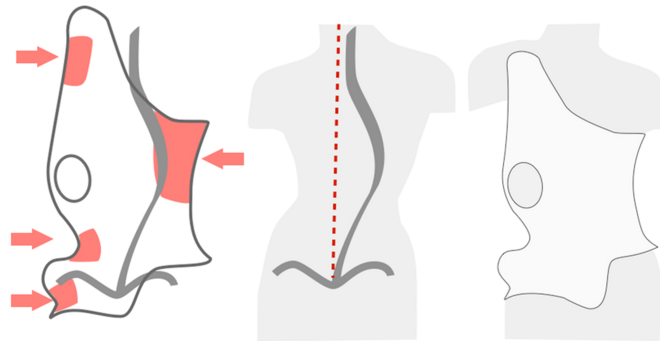
Figure 1.5: *Brace loading scheme.*

In addition, most of the braces [20, 82, 115] apply also a traction force to the spine, for example adding metal bars that ideally push the head far from the waist. In the Milwaukee brace model (Fig. 1.6), this is achieved by mean of neck collars and custom-made pads in order to distribute the forces on the pelvis. Similarly, also the other braces apply this traction load using the pelvis for the anchoring but there could be different solutions for the other end, *i.e.* it could be applied only to the ribcage or also using the armpit for stretching the spine.
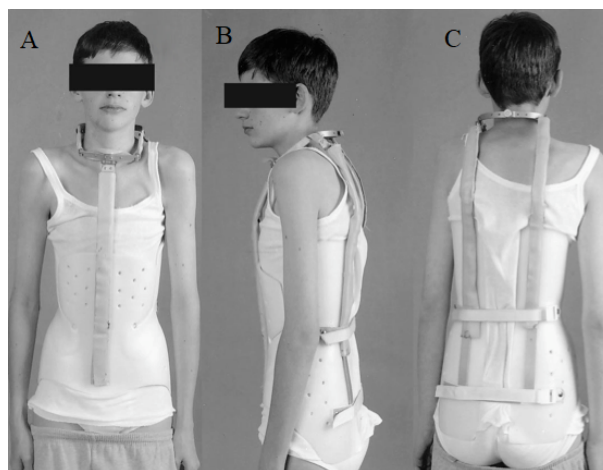
Figure 1.6: *Example of Milwaukee brace, photographs of the front [A], of the side [B] and of the rear [C] [60]*

The common applied forces can be considered normal for the correction in people without other critical diseases, which is not the case of patients with Osteogenesis Imperfecta. This particular disease creates mainly bone fragility and a strong ligament laxity. Hence, the application of highly corrective deformations could also lead to bone fractures. Moreover, since the scoliosis has to be corrected in the early childhood, a strong corrective shape of the braces could bring the bones to grow in a deformed way, resulting in more critical problems for internal organs, such as pulmonary deficiencies

caused by deformed chests. This possible issue has led to consider supporting braces instead of corrective ones and it is one of the reasons why there is still some discussion about the proper effectiveness of the chest orthoses [42]. Indeed, among the community of orthopedics, the braces are defined as "effective" when they do not harm the patient and decrease the progression of the deformity, which means that the curvature should be blocked without worsening or improvement. Even if studies about the effectiveness in realigning the spine curvature are available [17, 32, 112], also comparing different types of braces, it is important to stress that the device goal is mainly to support and limit the further increase of the curvature and that it has to be combined to physical exercises to improve the muscular situation.
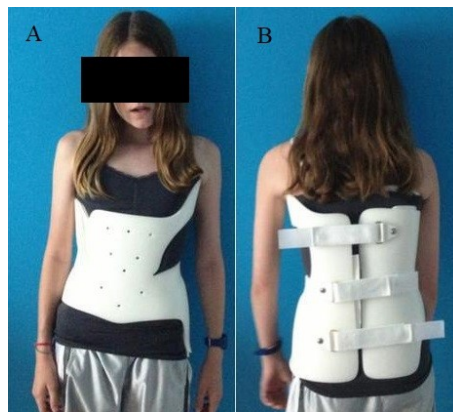
Figure 1.7: *Example of Boston brace, made of a plastic thermoformed layer with an opening on the backside to be closed with laces, [A] is the front view and [B] is the rear view [110].*

Figure 1.8: *Example of Cheneau brace, made of a plastic thermoformed layer with an opening on the front with laces, and holes for expansions in the opposite location to the applied corrective force [16].*

1.2 Manufacturing process as-is

Analyzing the current production process of semi-rigid plastic braces obtained by thermoforming (*e.g.* Charleston, Cheneau and Boston brace), both with literature review and visits to orthopedic workshops, it has been possible to classify the manufacturing

Figure 1.9: *Example of a night-time over-correcting Charleston brace, made of a plastic thermoformed layer with an opening on the front and a colorful texture applied on the outer skin [99].*

of the braces for scoliosis into traditional and modern processes (as presented in [85] summarized in Fig. 1.10).
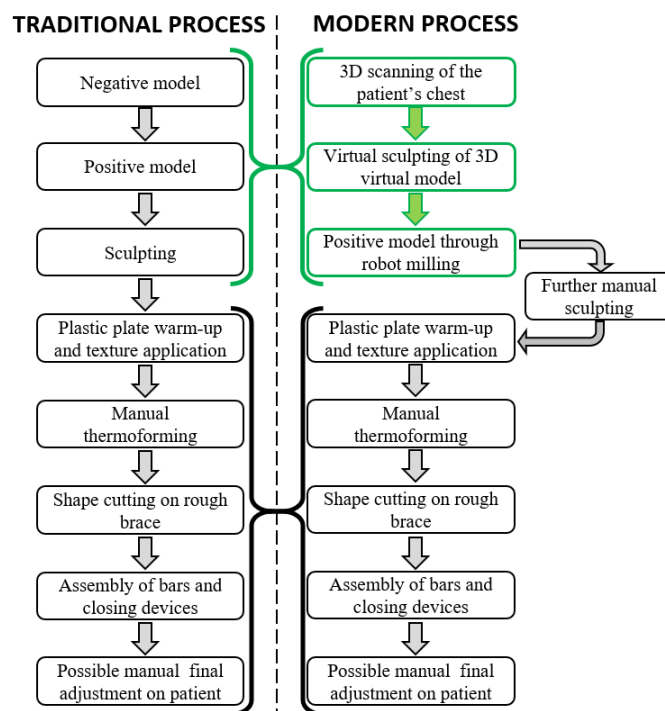
Figure 1.10: *Proposed summary scheme of the current brace production process: the green boxes represent the technologies introduced by the modern process in substitution to the black ones representing the phases of the traditional process.*

1.2.1 Traditional process

The traditional sequence of operations starts with the creation of a negative cast, wrapping the patient's chest with plaster of Paris bandages. The orthotist can already start having a first and light modeling phase, for example pressing the soft tissues around

the waist and the chest. The patient has to wait staying as still as possible until this first cast has solidified. Then the technician opens the cast and removes it from the patient. Subsequently he has to seal completely the vertical opening and the bottom, so that it is possible to create a solid positive model of the patient by filling the cast with liquid plaster of Paris (Fig. 1.11).

Once also this second model has solidified, the technician can start to manually sculpt it according to the desired deformations and corrections, as indicated by the orthopedist. When the positive model has reached the final shape, it is possible to thermoform a layer of Polyethylene or Polystyrene over the mold. The plastic plate has to be warmed-up in special ovens for a period of time that depends both on the material and on the thickness of the sheet, which then moved by two operators onto the positive mold. Here it is manually stretched to acquire the mold shape and then blocked for the cooling time in ambient temperature.

The rough orthosis has to be treated in order to trim the parts of the plastic plate that go over the limbs and smooth all the sharp borders. The final step in the laboratory involves the application of the closure laces, the addition of soft foamy layers in some sensitive areas and, if needed, metal bars for stronger support.

Eventually the orthosis can be worn by the patient to test it and apply small corrections to obtain a customized product.

A possible additional step performed by the technician before the manual thermoforming regards the application of a thin colorful plastic layer, such as the Charleston brace in Figure 1.9. This is attached to the plastic plate while it is warming up in the oven. The colorful texture is currently applied for kids in order to let them accept the brace as a funny thing to wear. In the past year, according to the personal experience of doctors and technicians, also the adolescents liked the colorful braces but the trend of the last years is to avoid the color in order to be able to wear the brace under any possible t-shirt, with the goal of hiding the brace to other teenagers.
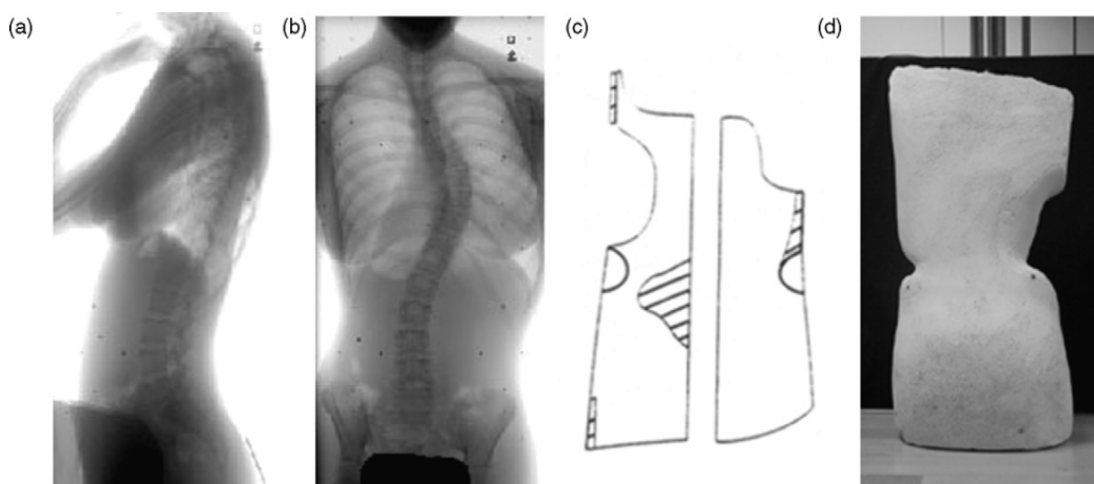
Figure 1.11: *Major steps of the traditional brace design process. After X-ray acquisition (a, b), the orthotist creates a blueprint or a plan of the Boston Brace System (c). In this case, the polystyrene plate is subsequently deformed on the positive plaster cast of the scoliotic patient (d) [35].*

1.2.2 Modern process

With the expression modern process, I consider the introduction of new technologies in the first steps of the procedure, which have already been adopted today in some orthopedic workshops. More precisely, a good step forward has been done with the use of 3D scanners and of software for modeling and sculpting the virtual 3D model of the skin. The main systems are provided by Rodin4D, Biosculptor and Vorum [13, 88, 108] and are composed of laser scanners or cheaper sensors and dedicated proprietary software, developed only for the orthopedic applications.
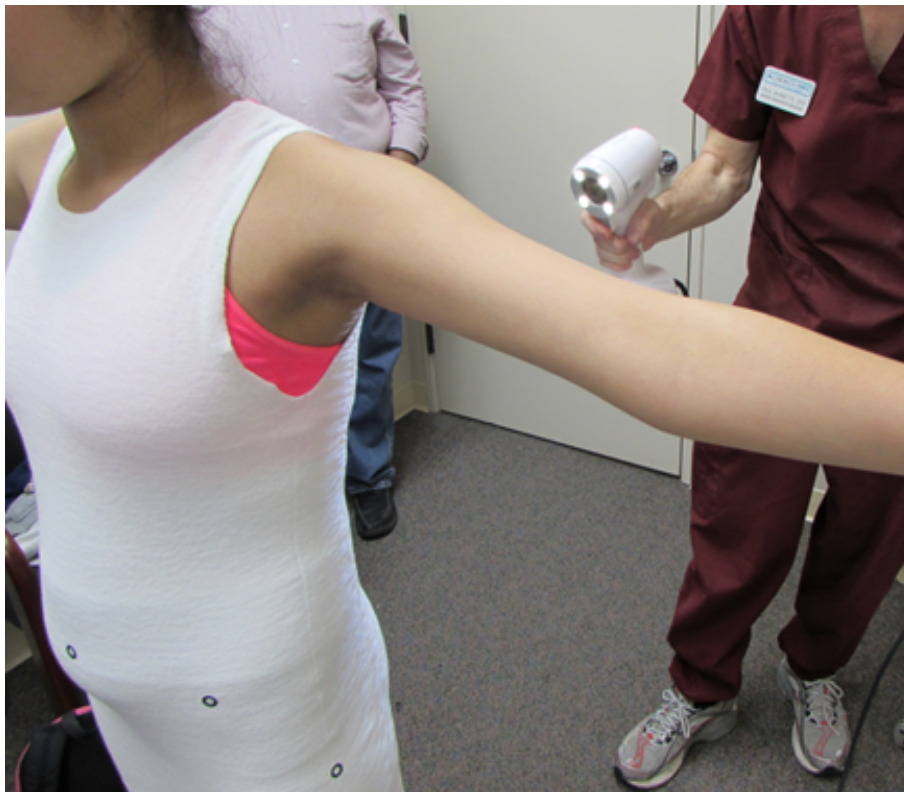
Figure 1.12: *Orthopedic 3D scanning phase using a hand-held device [4].*

These programs allow not only acquiring and modifying the models, but also sending them directly to the machine for the creation of a positive physical model passing through their built-in Computer Aided Manufacturing (CAM) modules. The production is commonly achieved using a lathe, a milling machine or an anthropomorphic robot with a drilling end-effector coupled with a rotating plate. The operator places a cylinder of polyurethane on the plate that is then worked by the robot while twisting at low speed. The created positive model is finally used to be wrapped with the plastic layer during the thermoforming step.

It has to be noted that the positive model obtained with the virtual sculpting is typically considered to be a first rough shape that has to undergo further manual sculpting before the thermoforming step.

The final steps remain the same described in Section 3.1 for the traditional process. An additional variation regards the possible use of a vacuum machine that sucks the air through the foam positive model, in order to assist during the thermoforming process,

instead of having only a manual stretching of the plastic plate.

Figure 1.13: *Initial polyurethane foam block (on the left) and lathing process in a CNC machine (on the right). In the lower part of the right picture it is possible to see the long drilling end-effector [7].*

1.3 Proposed manufacturing process

At present, both the traditional and the modern processes are adopted by different orthopedic workshops, depending on their size and on the available budget. On the one hand, with the traditional process, the overall cost for the tools is low and can be performed by one or two operators. On the other hand, it requires highly specialized orthopedic technicians to work on the various manual operations and the whole procedure takes long time to be completed, also because of the waiting time for the plaster to dry. Thus, it is appropriate for productions of limited numbers and for small centers.

Vice-versa, the modern process requires expensive tools for 3D scanning, virtual modeling, robotic scuplting the polyurathane foam and, when possible, for the vacuum assisted thermoforming machine. On the contrary, it is faster and it can bring to a higher number of braces produced per single orthopedic technician. In practice, I noticed that this process works well allocating the reverse engineering and virtual modeling to a single operator, specialized in computer operations, and leaving the following steps to different technicians with expertise on the manual operations. Thus, this approach is more suitable for medium and large centers.

In order to tackle the problems of each process, in terms of costs, time and expertise required, I analyzed the introduction of 3D printing in substitution of the thermoforming [85]. Even though an analysis of the innovations achieved in the first steps of the modern production process was required, the use of additive manufacturing for other products of the O&P field has been tested in terms of material choice and printing setups [25]. In the meanwhile, a similar approach to the use of 3D printing of back braces has been proposed by Weiss et al. [113]. In their work, they proposed to adapt some commands of the CAD/CAM software packages for the use of 3D printers, but a vali-

dation step of the designed brace would be required before the production. Moreover, the CAD software allow to import the X-ray images, which provide only a limited reference for the design of the brace. Instead, the use of a patient-specific 3D skeleton model would improve the modeling phase [87].

3D printing is an Additive Manufacturing (AM) process that, when based on Fused Filament Fabrication (FFF), produces the object by depositing the material, after having fused the filament through a hot nozzle, layer after layer. There exist other 3D printing technologies, such as StereoLithography Apparatus (SLA) and Selective Laser Sintering (SLS), that are described in Chapter 5 but were excluded for the present work due to their characteristics.

The 3DP technology has been already applied in other sectors of the medical field. Reference [69] presents physical models of patients' anatomical parts for planning a cardiac surgery and explaining both the problem and the surgery to the patient, with the aim of increasing his/her awareness and obtaining a real informed consensus. Other applications regard the production of customized implants and amputees' prostheses [19, 23, 46, 73, 106], foot and ankle orthoses [30] and orthosis for developmental dysplasia of the hip [72].

Despite some companies present their printers as able to produce perfect orthoses [2, 66], according to some orthopedic technicians there are still some issues related to the use of this technology. For example, the proper choice of the material and the 3D printing settings are still considered to be critical in a world (orthopedic workshops) that is still very artisan and based on handcrafting the orthoses, thus far from the use of additive manufacturing techniques.

In the late 2017, Weiss et al. [113] presented their approach of combined CAD/-CAM tools for producing back braces in Nylon with SLS technology. This was a good example but the use of the expensive machine in terms of cost and time did not prove to be effectively competitive in respect to the modern process. In the same period other researchers tried to improve the use of conventional brace by changing the closure straps or by adding inflatable 3D printed pads [5, 48].

In the beginning of 2019, a master thesis was published about the use of FDM technology for printing a brace in nylon [75]. Finally, a partner of the project EMPATIA@Lecco developed a master thesis regarding the economical evaluation, with cost analysis and business model, of the AM of back braces [41].

1.4 Objectives

The main goal of this PhD thesis was the substitution of the thermoforming of the plastic plate with 3D printing of polymers. In order to reach a reliable and feasible process to be adopted by the orthopedic workshops, all the steps have been evaluated.

- Analyze the accuracy of the 3D scanners and select the most appropriate for the application.

- Verify the current modeling tools and provide an improvement by using the 3D patient-specific skeleton model.

- Have a fast indication of the quality of the designed brace by using static structural analysis on the computer, before 3D printing.

- Evaluate available filament materials and select the one that best compares to the thermoformed PolyPropylene.

- Define the best printing setup and test a fully 3D printed brace both for post-processability with the orthopedic technicians and for comfort with a volunteer patient.

1.5   PhD project organization

Going with the order of the entire production process presented in Figure 1.14, I decided to focus the attention on the possible problems related to the input model deriving from the reverse engineering step, then to analyze the software available for virtually sculpting the braces, to test the braces with numerical simulation and finally to verify the printing abilities of a FFF 3D printer.

Regarding the Reverse Engineering, I noticed that the orthopedic technicians often start the process with faulty reconstructed models due to the improper settings of the scanners, both for lack of clear guidelines about the functioning mode of the device. This type of error on the input model, brings to successive difficulties in elaborating properly the patient's body shape when sculpting the brace. Chapter 2 presents a deep comparative analysis of different 3D scanners, both high level and low-cost devices, with the aim of defining the proper way to choose the correct device for this orthopedic application (scoliosis braces). Beyond the common tests performed on standard objects, such as flat planes, cubes and spheres, in this analysis I decided to consider also manikin parts that present the typical organic shapes of the human body. Moreover, a further analysis has been computed on a single device comparing different approaches to the 3D scanning (*i.e.* comparing how the operator should move around the patient), in order to provide better guidelines to orthopedic technicians that would like to adopt the proposed production process.

Chapter 3 regards the virtual modeling software comparison and the development of a pseudo-parametric 3D skeleton model that should be embedded in the available orthopedic software. This skeleton model should be used both as a visual reference in addition to the current bi-planar X-ray images and possibly also to perform a virtual test of the sculpted brace.

In this direction, the Chapter 4 describes the first attempts to use simplified numerical simulations for obtaining a fast feedback while sculpting the brace. This step is very important when considering that with the 3D printing of the brace, the orthopedic technicians has to abandon the production of a physical 3D positive model of the patient. Thus, he loses the common judgment ability based on the personal experience in the physical world, and has to define properly the virtual brace so that the 3D printed object will not have to be excessively modified.

Chapter 5 focuses on the additive manufacturing steps with an initial analysis of the current uses of 3D printing in the medical field. The core of the chapter is the analysis of the available materials to be used with the FFF 3D printer that has been identified and selected for the application. Different hemi-cylindrical samples were printed and tested for comparing both the mechanical properties and for defining the best printing setup. The chapter ends with the description of a preliminary test performed with a real patient.

Finally, Chapter 6 resumes the main contributions and presents a general discussion of the project, while drawing appropriate conclusions. Thanks to the positive preliminary test, a clinical protocol has been successfully submitted to the ethical committee of the Istituto di Ricovero e Cura a Carattere Scientifico Medea (IRCCS Medea). This was approved on June 13th 2019 and the chapter describes also how the experimentation of the proposed process will be performed beyond this PhD project. Moreover, there is a wide description of the possible sensors that were initially considered for the use in such application and the discussion about the selected ones for the final experimental protocol. In addition, further improvements and possible future works are presented based on the personal experience in the development of the project.
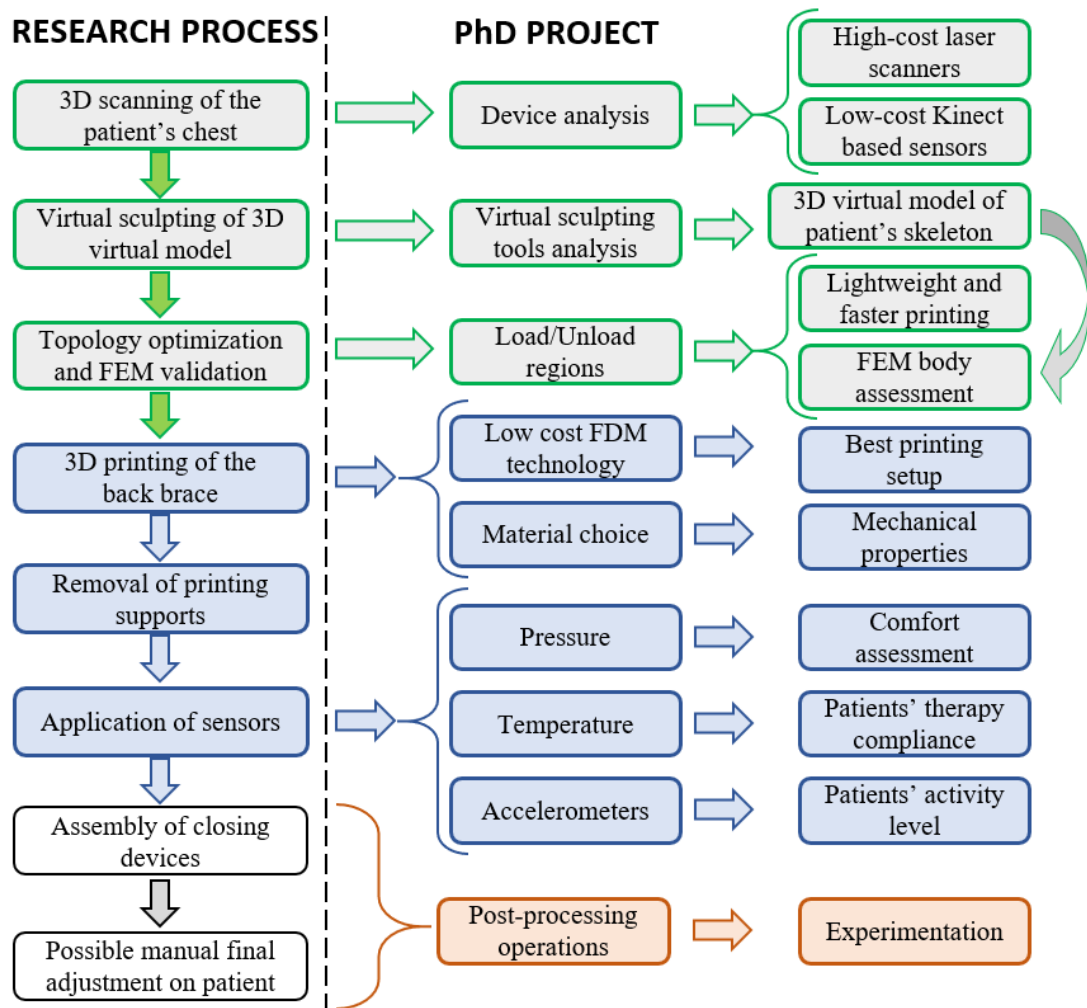
Figure 1.14: *Subdivision of PhD work into activities related to the multiple steps of the research process.*

Reverse Engineering: 3D scanning

In this chapter, the terms Reverse Engineering refer to the process that produces a 3D reconstruction of an object. The external surfaces are sampled and approximated with point clouds, either with contact coordinate-measuring machines (CMM) or by using non-contact 3D scanners (*e.g.* laser scanners). This technique is widely used in the engineering field for quality control, part inspection or reverse modeling.

The chapter presents a comparative analysis of different devices with the final goal of identifying which are the characteristics that should be considered in the field of orthopedic braces. The text is partly based on a paper that was published in June 2018 [86], with an improvement based on the wider set of available scanners.

2.1 Related Works

In the beginning, the standard technique was the laser triangulation; however, because of the high costs of the devices, the 3D acquisition was not considered attractive to orthopedic workshops [91]. Recently, new devices, more affordable thanks to cheaper technologies, have been introduced. The most famous device that signed the turning point is the Microsoft Kinect, which appeared on the market in 2010. It was originally designed for creating an interactive gaming experience, but its technology paved the way to different applications, among which the reverse engineering field. After the Microsoft launch, other triangulation-based low-cost devices were produced, such as Asus Xition, PrimeSense and Structure Sensor. In 2013, Microsoft presented a new version of the Kinect 2 (Kinect for Xbox One) implemented with a Time of Flight technology.

Among these low-cost devices (budget under 400 €) and the high-level laser or pattern triangulation scanners (budget over 20K €), other triangulation devices based

Figure 2.1: *Low-cost devices used also for reverse engineering. Microsoft Kinect V1 and V2 in the top row, Structure Sensor, Prime Sense and Asus Xition, in the lower row.*

on white or blue light have been presented. The most representative are Artec Eva, Creaform Go!SCAN 3D and the latest released Artec Leo. The interest of the medical community in such devices derives from the possibility of acquiring the shape of the patient easily and quickly, with low-cost systems that can be transferred from highly-specialized institutes to small satellite clinical centers spread over the territory.

The two Microsoft Kinect V1 and V2 were created as steady units for motion capture, considering the DOF of the objects in front of them. Until now, almost all the research in 3D modeling with low-cost devices regarded only the Kinect, both version 1 and 2. The first Kinect was released in 2010 starting from the Project Natal purposes. From proprietary device, the Kinect was soon opened to different aims, especially the use of the device as a moving unit for the acquisition of a steady environment and the collection of its geometric information as 3D data. The KinectFusion was the first project analysing the possibility to calculate the 6 DOF of a rigid object with a hand-held Kinect, allowing also aligning the single acquisitions for the creation of a 3D model [74]. Several publications dealt with the possibility of using this device as a 3D acquisition instrument considering also its calibration to evaluate its potential as a low-cost 3D instrument [50, 52, 53, 78]. The Kinect sensors, both version 1 and 2, have been used for several 3D applications in cultural heritage [114], for robotics [77] and for human body scanning [102].

In medical applications, the 3D scanning of a human body involved mainly highly-rated laser scanners for acquiring the parts of interest, in order to improve diagnosis or to facilitate the creation of 3D printed orthosis or prosthesis [10, 101]. On the other hand, low-cost systems, such as the Kinect V1, were used as a tracking system [109], for rehabilitation [54], for foot orthoses [30] and for improving the design of leg prosthesis [22] with the aim to find a proper way to acquire 3D data using low-cost sensors. On the other hand, recently the Structure Sensor was developed as an evolution of Kinect V1 for acquiring 3D data of the environment simply connecting it to an iOS device, but available researches were found regarding the use of the Structure Sensor in orthopedic applications. Problems related to motion and deformation of the acquired data have been analyzed by [107], proposing and testing a deformable alignment algo-

rithm both on static and real time acquisition with structured light devices.

In the past few years, the producers of orthopedic CAD-CAM solutions became interested in all these kinds of devices; therefore, they started adapting them to the biomedical applications, creating both software and new proprietary hardware devices. Examples are the Rodin4D app to use directly the Structure Sensor with iOS devices and communicate with their computer software Rodin Neo, or the Biosculptor and the Vorum systems, composed of laser scanners or pulsed white light devices and dedicated proprietary software.

These systems allow not only saving and modifying the models, but also sending them directly to a CNC (Computer Numerical Control) machine for the creation of a physical cast model for orthoses or prostheses production, passing through their built-in CAM modules. Vorum offers also the option of preparing an open surface that can be thickened and sent to a proprietary 3D printer for the particular case of an AFO (ankle-foot-orthosis).

In order to satisfy other fields interested in full-body 3D scanning, for example the animation movies and fitness-related apps, new devices have been developed. The simplest ones work either moving a common 3D scanner all around the person or adopting a combined used of multiple devices that acquire the body from different points of view. Examples are the Artec Shapify Booth or Vitronic VITUS 3D body Scanner. Other proposed systems are composed of a set of fixed cameras that work with the photogrammetric technique, such as in the case of 3D INSTAGRAPH Staramba. The advantage in O&P applications would be the higher speed of acquisition and low time (under 15 seconds and down to 1 second in some cases), but the limits of these systems for orthopedic workshops are both the high costs, starting from about 10k€, and the dimensions that require a dedicated room [62]. Moreover, if the focus of the orthotic product is limited to a single limb or even a foot, it would be probably necessary to have a different device dedicated to small parts.

For these reasons, the present work does not consider the full-body systems, even if they could be good for scoliosis braces, and focuses only on the general-purpose devices. In particular, the aim of this chapter is to evaluate the metrological accuracy of a set of devices currently used for medical purposes in an orthopedic workshop (*i.e.* the Structure Sensor by Occipital and the O&P Scan by Rodin4D), of other low-cost sensors that may be used for human body surface scan (*i.e.* Microsoft Kinect 1 and 2) and compare the results with professional triangulation based scanners and a manual CMM (coordinate measuring machine) device.

One of the novel aspects of the work is related to the new handheld scanner Artec Leo, that offers the best results for being a completely stand-alone device. Moreover, no research has been yet presented in the scientific community.

The starting point of the research was to evaluate the systematic error of each device with the use of a calibrated plane and a test-field composed of calibrated spheres. This type of measurements is defined to be the standard for comparison, as stated in the VDI/VDE guidelines and as shown in the literature [14, 24, 40, 49, 105]. In our case, it was also the best way to highlight which could be the best scanner to be used as a reference.

Indeed, the second part consisted in surveying three different test objects, representative of the biomedical application, and comparing the results with the selected

reference device. The idea is to fill the gap in the research, testing the devices described below in acquiring organic shapes of mannequin parts, representative of the human body parts that can be acquires in the orthotics and prosthetics (O&P) application. In particular, a polystyrene hand, a chest and a thigh from a mannequin were chosen to replicate different parts of the body of a patient, that are commonly the focus of orthopedic applications and that also allow to consider the different level of detail and possible scale effect due to the dimensions. This should provide better indications about the characteristics of the devices when used in a real context, as opposed to the standard laboratory tests only.

2.2 Requirements

With the idea of comparing the devices for the application in orthopedic workshops and producing the back braces, we have to consider a set of constraints for the choice of the appropriate device.

- *Low-cost*: the devices should be used also for those small orthopedic workshops that cannot afford the expensive tools of the modern process, *i.e.* below 1000 €.

- *Accuracy within 2 mm*: the orthopedic technicians defined that the maximum device error should be comparable with the error related to the traditional use of plaster of Paris.

- *Mesh resolution about 5 mm*: the spatial resolution on the skin model has to be fine enough to identify shape variations without detecting particular details, such as scars or veins.

- *Time to scan within 30 seconds*: this limit is related to the fact that the patient has to stand and stay as still as possible while the technician goes around him/her to acquire the shape of the region of interest (in our case, the chest).

- *Scan area limited to 2x2 m^2*: typically the 3D scanning has to be performed in the visiting room that are below 3x3 m^2 and contain other equipment, such as desk, chairs, wardrobe and examination table.

2.3 Methods and Tools

This section first introduces the devices that were used for the comparisons. Then a description of the types of error that are considered is proposed. Next, the test objects are presented. Finally, the acquisition procedures and the analyses are described.

2.3.1 Devices

Three low-cost general-purpose devices were evaluated in this work, the Kinect 1 and 2 by Microsoft, the Structure Sensor by Occipital. In addition, the O&P Scan by Rodin4D, specifically created for medical purposes, was also tested. Medium and high level scanners, a Vivid Minolta 9i, an GOM ATOS II and a NextEngine 3D scanner, were used for selecting which to take as a reference for comparing the mannequin parts, on the basis of the results on the standard objects. Moreover, for the comparison of the plane and the spheres, also the manual CMM device Microscribe G2LX was tested.

The Microsoft Kinect 1 was released for XBOX360 and is based on the structured light technology. The device uses a low number of patterns to obtain a depth estimation of the scenery at 30 FPS (Frame Per Second). It is composed of two cameras, a color RGB (Red, Green and Blue) one and a monochrome NIR (Near InfraRed) camera, plus a NIR projector with a laser diode of 850 nm wavelength. The baseline between the projector and the NIR camera is equal to 75 mm, comparable to the human eyes distance. The device uses triangulation technique to compute the depth information, thanks to the known and fixed dot pattern of the NIR projector to illuminate the scene.

The Microsoft Kinect 2 is based on a system originally patented by Canesta [81]. It involves the modulation of an IR light source with a square wave and a flash camera to determine the distance to the object, by measuring the round trip travel time at each pixel of an amplitude-modulated light going from the source to the target and back. The time needed by the light for reaching each pixel of the flash camera is evaluated by detecting the phase shift between the square wave and the signal received by each pixel. The device has a 512×424 depth image sensor where each $10~\mu\text{m} \times 10~\mu\text{m}$ pixel incorporates a TOF (Time Of Flight) detector that operates using the Quantum Efficiency Modulation (QEM). As shown in [8, 93] this technique uses two different modulating frequencies (80 MHz and 100 MHz) for solving possible range ambiguities.

The Occipital Structure Sensor was created to be coupled with an iOS device in order to have cheap and user-friendly hand device to capture 3D environments. It can also be used on a computer through its specific software Skanect. The device is based on the Kinect 1 technology, it projects a speckle pattern of near-IR light on the scene captured by the infrared camera and correlated to a reference pattern of a plane placed at a known distance from the sensor. For medical purposes, the Structure Sensor can be coupled with Rodin4D Captevia, an application for iOS devices, available for free in the Apple Store that can be used for generating and saving 3D scan files on the Apple devices and communicated directly with the computer software Rodin4D Neo for creating the patients database. An alternative is the use of the free app Scanner, developed by Occipital, for generating the 3D model and send it to anyone by e-mail, thus requiring an internet connection for saving the file. The system is composed of an IR projector and a 640x480 CMOS IR camera dedicated to range sensing. For acquiring the color texture of the object, the apps use the RGB camera of the iOS device after a proper calibration of the position in respect to the sensor.

The O&P Scan by Rodin is an handheld laser 3D digitizer to be used in the medical field for acquiring the parts of the body of the patient to be analyzed. The O&P Scan uses a magnetic field to position itself in the space and align the scans of the 3D surface. The acquisition is based on the triangulation of a fixed laser line with respect to the camera, with a declared accuracy up to ± 0.05 mm on the surface. The device is coupled with the Rodin4D CADCAM software and the real time display on the PC allows to control all the operations. It is certified to be able in acquiring data at a distance of maximum 400 mm and it is equipped with a tiny magnetic sensor to be attached to the patient's body in order to correct his relative movements.

The NextEngine is a 3D laser scanner of medium level, based on laser line triangulation. Its compact dimensions are good for a desktop application, typically for small objects, with a field size ranging from 5.1" x 3.8" (about 1300 mm x 970 mm) in macro mode to 13.5" x 10.1" (about 3430 mm x 2570 mm) in wide mode. The source is com-

posed of a twin array of four laser lines that tilt in respect to the camera, which has a twin 5.0 Megapixel CMOS RGB image sensor. Moreover it has a white-light LED illuminator for acquiring the texture. The system is finally composed of a small turntable, useful for automatic multiple acquisitions. The declared dimensional accuracy is of ± 0.1 mm for macro mode and ± 0.3 mm for wide mode.

The Konica Minolta Vivid 9i is also based on the principle of laser triangulation. In this case, the device is usually fixed on a tripod and the single laser line tilts in respect to the camera in order to measure 640 x 480 points with one scan, simultaneously acquiring surface shape data and color image data. It is stated to have an accuracy of ± 0.05 mm and a precision of 0.008 mm, using the "TELE" lens. The three interchangeable lenses (wide, middle and tele) and the possibility to finely control the laser intensity testify the higher quality of the system.

The GOM ATOS II 400 works with structured white light projection. It is composed of a central pattern projector and 2 side cameras, aligned on a straight line and located on the opposite sides of the projector, but inclined with the same angle to converge on the projector's output. The system projects a set of black and white fringes which are perpendicular to the line connecting the cameras in order to work with the triangulation method. The pattern is then shifted multiple times in order to obtain a denser point cloud. The maximum declared spatial resolution is 0.02 mm, but it also depends on the distance of the object from the scanner, while the declared accuracy is 0.03 mm.

The Microscribe G2LX is a manual CMM, which works as a passive robot arm that registers the position of the point we touch with the small spherical probe (3 mm of diameter) mounted on the end-effector. Its declared accuracy, based on 100 point ANSI sphere test, is equal to 0.3 mm.

Finally, the newest device on the market is the handheld scanner Artec Leo. This works with the white structured light projection and it is the evolution of the Artec Eva, both in terms of acquisition results and for its stand-alone capability. It is completely independent from a computer when acquiring and it allows to analyze also a preview of the 3D model on its small screen. It offer a 3D spatial resolution up to 0.5 mm and has a declared accuracy of 0.1 mm. In particular, it is important to highlight the working distance ranging from 0.35 to 1.2 m and the capability of acquiring about 22 frames per second which, combined with the sensor resolution, means that it is able to acquire up to 3 milions of points per second.

2.3.2   Test objects

Five test objects were used to evaluate the different devices: a calibrated flat plane, used to calculate the systematic and the flatness error [40], an artefact with 8 spheres to test the parameters recommended by the guidelines VDI/VDE and three anatomical parts of a mannequin to simulate the parts of a human body, chosen to investigate different dimensions and detail levels: a hand, a thigh and a chest. The characteristics of the different test objects are summarized in Table 2.2.

The reference plane was made with float glass, which dimensions was 700 mm $\times$ 528 mm and a thickness of 11 mm. The glass allowed to have a plane with a peak deviation from the theoretical plane in the order of few micrometers, suitable for testing the devices chosen for this research, characterized by measurement uncertainties in the range of millimeters. Due to the transparency of the material, not compliant with an

Table 2.1: *Specifications of the tested devices.*

Device	Technology	Range [m]	Declared accuracy [mm]	Cost [€]
GOM ATOS II 400	B/W fringe pattern triangulation	N/A	N/A	∼50k
Konica Minolta Vivid 9i (WIDE Lens)	Laser triangulation	0.5 − 2.5	0.1 − 0.2	∼80k
NextEngine 3D scanner HD	Laser triangulation	0.19 -0.71	0.13	∼3k
Microscribe G2LX	Manual CMM	N/A	0.05 − 0.13	∼8k
Artec Leo	White structured light	0.35 − 1.2	0.1	∼26k
Kinect 1	IR pattern triangulation	0.5 − 6	N/A	∼100
Structure Sensor	IR pattern triangulation	0.3 − 5	∼4	∼400
Kinect 2	IR TOF	0.4 − 5	N/A	∼200
Rodin4D O&P Scan	Handheld laser triangulation	0.05 − 0.3	0.5	∼10k

active range sensing device, the surface was painted matte white, with the process used in the car industry. In this way, the painting was uniformly distributed without distorting the geometry of the plane.

The sphere test object, reported in Figure 2.2, had a base of 300 mm × 400 mm onto which 8 spheres have been assembled with custom 3D printed supports of different heights. These were chosen to test the acquisition volume with just one scan, in opposition to the use of multiple shots of a two-ball bar located in different configurations [14]. The chrome-steel (AISI 5210) spheres had diameters ranging from 19.05 mm to 44.45 mm. Due to their mirror finish, the spheres were sprayed with a matte white powder.

Figure 2.2: *Sphere test object containing 8 spheres of different dimensions at different heights.*

The organic shapes of mannequin parts and their dimensions (Table 2.2) were chosen because representative of the human body segments that are usually acquired in the orthotics and prosthetics (O&P) applications. Despite the mannequin of the laboratory has also the arms with hands (Figure 2.3 – skin–toned one in the middle), the white polystyrene one was preferred because the geometrical detail level on the backside and on the nails was more realistic, and considered more challenging when testing the scanners on small details. Compared to a real hand (Figure 2.3 – left side), the mannequin hands have a more uniform color and are smoother. The mannequin chest and thigh are also a little bit more reflective, as visible on the hand in the middle of Figure 2.3, which has their same properties.

Table 2.2: *Objects used in this project with material, dimension and color specifications.*

Test Objects	Material	Dimensions (mm)	Color
Calibrated Plane	Glass (opaque)	700x528	White
Spheres	Metal (sprayed with matte powder)	19.05 : 44.45	White
Hand	Polystyrene	200x95 approx.	White
Thigh	Polyethylene	420x130 approx.	Skin tone
Chest	Polyethylene	700x230 approx.	Skin tone

Figure 2.3: *Tested white hand model on the right, compared to a real hand on the left and to the one of the mannequin in the middle.*

2.3.3   Types of error

The International Vocabulary of Metrology (Joint Committee For Guides In Metrology (JCGM), 2008) stated that the measurement uncertainty of each equipment or device is affected by the systematic errors – associated to the concept of accuracy – and unavoidable random errors – associated with the concept of precision –, dependent by unpredictable causes like the electronic noise, that can be only statistically characterized for making the end-user aware of the measurement system intrinsic limitations [40].

The global error can be evaluated by acquiring a certified test object and measuring the deviation of the model from the ideal one, theoretically the original CAD model.

The error can also be divided in spatial or temporal that is observable across multiple consecutive frames [63].

In this work, the attention is focused on the spatial error, neglecting the temporal error. This choice derives from what was stated by Guidi et al. [40]: in the practical application, a spatial characterization allows to obtain more statistically-significant results. Moreover, we noticed that the temporal error should be mitigated by the time averaging that software like Skanect and Artec Studio perform during the fusion of the different frames. In addition, we could neglect the effects of temperature in time, that have been proved to influence the performances of this range of devices over a time-span of several tens of minutes [29], because of our short time acquisition of the devices (from 10 seconds up to a maximum of 3 minutes were required by the low-cost devices).

In order to analyze the results of the different devices, a first comparison has been performed with the following parameters.

The flatness error was analyzed considering the standard deviation of the acquired point clouds in respect to the ideal CAD plane, which means that the point cloud is fitted with an ideal plane and the distance of the points from this plane is computed.

Regarding the use of the spheres, the VDI/VDE 2634 guidelines define different measurement indicators.

- The probing error in form (PF) evaluates the difference between the acquired points and a fitted sphere of variable diameter; in other words, it defines how much distorted the acquired shape is.

- The probing error in size (PS) measures the difference between the declared sphere diameter and the one of the fitted sphere, which evaluates the dimensional accuracy of the reconstructed spheres.

- The sphere spacing distance (SD) highlights the error in measuring the relative distances between the best-fit spheres and the reference dimensions.

Similarly to the sphere probing errors, when analyzing organic parts, we can measure the difference of the reconstructed point cloud in respect to the reference model. In particular, it is possible to fit the distribution with a gaussian distribution, the mean of which gives an idea of the scaling error while the standard deviation represents the accuracy of the reconstruction.

2.3.4 Acquisition

Each test object was surveyed with all the instruments placed on a tripod at a fixed distance. The only exceptions were the O&P Scan, because it is a handy scan with fixed angle between laser and detector, thus it was used only in free hand movement, and the CMM Microscribe, that had to be placed in the reach zone for the probe to touch all the plane and the spheres. Additionally, the acquisitions with the Structure Sensor and Artec Leo used both settings of fixed on a tripod and handheld mode, only when acquiring the mannequin parts and the spheres.

All the acquisitions were performed with the proprietary software of the devices. The Minolta laser, the GOM ATOS, the NextEngine, the CMM Microscribe and the

Rodin4D O&P Scan hand laser scanner performed the acquisition with their commercial software. The Structure Sensor and the Kinect 1 were connected to the pc by USB cable and used the Skanect software. The Kinect 2 was connected to the pc by USB cable too, but used the Kinect Fusion Explorer available in the SDK Browser v2.0.

A particular case is represented by the hand-held mode of the Structure Sensor, when mounted on the iOS device, and of the Artec Leo which are completely independent from computer. The first uses an app that can be freely downloaded on iOs devices and that creates directly the final model with a lower resolution in respect to the Skanect software on computer, due to the limited computational power. The second has been developed to be completely stand-alone and the frames are directly roughly aligned on the device itself, but a further fine registration and more processing for the fusion of the point clouds can be performed on the computer with the proprietary software Artec Studio.

The objects were all acquired emulating the application environment, that is the orthopedic workshop room with artificial lights (neon) and trying to avoid the use of markers, with the exception of the GOM ATOS. The reason of this choice is both because patients have usually difficulties staying still in respect to external references and because applying markers to the target objects could be trivial for the complete acquisition of their geometry.

Software tests for best settings

In order to better select the proper settings for each software, some preliminary tests were performed.

The software Skanect always subsamples the large amount of points deriving either from the Structure Sensor or from the Kinect V1, with fixed spatial resolutions independent from the sensors resolution, but depending on the size of the bounding box and on the *Fusion Fidelity* level. The points are sampled so that there are about 125, 250 or 500 levels for each side of the bounding box, respectively for the Fidelity set to Low, Medium and High. For example, with a bounding box equal to 0.4 x 0.4 x 0.4 m^3, the maximum resolution becomes about 3.2, 1.6 and 0.8 mm, respectively. Moreover, we have to consider that the bounding box is always centered at a distance equal to half its side dimension plus the minimum acquisition distance, that is 0.3 m for the Structure Sensor and 0.45 m for the Kinect V1. This means that the bounding box has to be as small as possible to contain the object to be reconstructed in order to obtain the maximum spatial resolution, and that we have to take care in centering the object for the starting relative position. For the previous example of a box dimension equal to 0.4 m, the center would be placed at 0.5 m from the Structure Sensor and 0.65 m from the Kinect V1.

Also the Fusion settings for the Kinect V2 SDK works in a similar manner but the commands are more explicit. The *Volume Voxels Per Meter* defines exactly the sampling levels (same available values 128, 256 and 512). This means that if a meter is divided in 128 levels the maximum spatial resolution becomes about 8 mm, while with 512 level we obtain a mesh edge of about 2 mm. The count is more complicated when we want to change the bounding box dimensions. We have to set the *Volume Voxel Resolution* parameter with a different value from the *Volume Voxels Per Meter*. Indeed, the tests reported in Table 2.3, demonstrated that the ratio of the two parameters defines

Table 2.3: *Setting combination for Kinect v2 SDK fusion.*

Volume Voxels Per Meter	128	256	512	256	128
Volume Voxels Resolution (X=Y=Z)	128	256	512	512	512
Bounding Box Size [m*m*m]	1*1*1	1*1*1	1*1*1	2*2*2	4*4*4
Squared Mesh Dimension [mm]	8	4	2	4	8

the bounding box dimensions.

For the *Artec Studio 14 Professional* software, I used the recommended sequence of operation for cleaning and aligning the frames. The only differences for the plane and the spheres were the removal of the extra frames (only 220 frames were preserved) and the use of the geometry only (without the texture) for the registrations. Moreover, the Key Frame Ratio was set equal to 1, which means that the 100% of frames is considered for the alignment, only for plane and spheres and set back to the default 0.1 value for the mannequin parts due to computational limits when processing the larger number of frames. Finally, the outlier removal and the sharp/smooth fusion parameters were set with the default values for the Leo scanner.

Flat plane

The first test object surveyed was the reference plane to evaluate the systematic error for each device and to start choosing the reference for the following comparisons on the mannequin parts. The calibrated flat plane was placed on a table and all the devices were put on a tripod slightly oblique in front of it, to limit possible reflections, choosing the distance for the acquisition and all the setting parameters considering the specifications for each instrument (*e.g* the field of view).

The survey started with the Minolta Vivid 9i, mounted with a *middle* lens at a distance of 1310 mm from the object. The choice of the lens depended on the dimension of the plane and the decision of limiting the maximum distance from the object, considering always the conditions of the final application environment, thus discarding the *tele* lens. Given the fact that the surface of the plane is opaque white, the parameter of the intensity for the scan was set equal to 12. The acquisition of the scan was performed using the proprietary software Polygon Editing Tool (PET) that exported the file in *.cdk format. The scan was then imported in Innovmetric Polyworks and directly exported in the standard format *.obj.

Similarly to the Minolta scanner, also the GOM ATOS was placed at a distance from the plane equal to 1100 mm. For acquiring an object, this device requires the use of at least three markers visible from both the cameras. In order to avoid placing the markers on the plane, they were attached to a support right under the plane. Due to the configuration of the instrument, the volume that can be acquired is limited and it was also hard to avoid the reflected light of the projector, but it was decided to have a single scan avoiding the possible errors related to the alignment of different scans.

The NextEngine works with the ScanStudio proprietary software. The relative distance from the plane was of 720 mm, which is the maximum limit for the WIDE mode. The resolution was set to HD and the target color to neutral, which is similar to set the laser intensity on the Minolta. The scan was a single one, but the device used all the four laser lines the device has, and required about 5 minutes to be completed. Unfor-

tunately, due to the limited field of view of the device, which has a fixed lens, only a portion of the plane could be acquired. The model was finally exported in binary *.stl format to reduce the size (which resulted to be anyway 114 MB for the single scan, with 1.2 mln points), removing the texture available in *.obj format and reducing the dimension in respect to the ASCII format.

The Artec Leo was located at a distance of 1270 mm in front of the plane. The preserved acquisition frames were limited to 220, because the idea was to limit to exactly 10 seconds the acquisition, to be comparable to the time necessary for scanning with the Minolta. The frames were then processed in Artec Studio and exported in 3 different ways, after a fine registration. The first considered all the single frames as individual point clouds in *.stl format, to be assembled together with a Matlab script. The second corresponded to the processing recommended for organic shapes, using an *outlier removal* filter and performing a *smooth fusion* for obtaining the final model. The third version is similar to the second but adopting the *sharp fusion* algorithm that, according to the producer, does not apply smoothing and allows to reconstruct fine features.

For the Structure Sensor and the Microsoft Kinect 1, it was used the Skanect software, imposing a bounding box of 1x1x1 m^3 and placing the device at a distance of 1 m. Given the fact that these devices acquire at a frame rate of about 30 FPS, it was decided, after several tests, to stop the acquisition after 10 seconds, as for the Artec Leo. This setting gave the possibility to average the measurements of the single frames, thanks to the fact that the devices were placed in a fixed position. The obtained 3D models were then exported in *.obj at high resolution.

The same setup was used for the Microsoft Kinect 2, using in this case the SDK software specifically implemented for this device. After the preliminary tests presented before, I concluded that the best setting was to fix the Voxels per meter at 768 and, the Volume Voxel Resolution at 512. Also in this case, the acquisition was stopped after 10 seconds, while the distance between the device and the object was set at 900 mm.

The Microscribe had to be placed on the table, next to the plane for its limited reach zone. It was used in manual mode, meaning that the points were acquired one by one while moving manually the probe over the plane and by pressing on the pedal for each point. The total number of points kept for the analysis is equal to 133. Since the acquisition is performed manually while writing directly the coordinates in a *.txt file, there is no visual feedback for the points distribution. For this reason the points are not as equally distributed on the surface as with the other devices.

For the O&P Scan, the RODIN4D software was used. This device is a handy scan, and the acquisition of the plane was performed generating several strips to cover the entire surface of the plane, manually moving the scanner in front of the plane. All the strips were automatically aligned by the software thanks to the magnetic field marker. To obtain the final 3D model in *.obj format, the software RODIN4D NEO was used, with the lowest value of smoothing to limit possible deformations.

Spheres

The general settings for the different devices was similar to the acquisition of the flat plane, locating the scanners perpendicular to the planar base of the test-field. The main differences were the relative position in respect to the test object. The following list reports the distances between the planar base and the center of the sensors.

- Minolta Vivid 9i: 850 mm and *wide* lens

- GOM ATOS II: 900 mm

- NextEngine Scanner HD: 780 mm

- Artec Leo: 780 mm

- Structure Sensor: 550 mm

- Microsoft Kinect 1: 720 mm

- Microsoft Kinect 2: 800 mm

In the Skanect software, used for acquiring with the Structure Sensor and the Kinect 1, the bounding box dimension was set equal to 0.4 m per side. This allowed improving the spatial resolution of the sampled points, with respect to the plane settings.

Moreover, both the Structure Sensor and the Artec Leo were used both in fixed mode on the tripod and in handheld mode going around the testfield, in order to evaluate also their usual acquisition approach for the final application.

Due to the fact that this additional analysis was performed after the work published in June 2018 [86], the Rodin O&P scan was neglected, both for the low quality results and for the possible issues related to the metallic spheres in terms of alignment with the magnetic field.

Hand

The Microscribe was neglected from the analysis on the mannequin parts, due to the fact that CMM devices are good for sampling only a limited number of points and measure few distances, but not to perform a 3D reconstruction. Moreover, the results of the tests with the flat plane and with the spheres established that it was not the device to be used as reference for the comparisons.

For the acquisition of the hand, the Minolta Vivid 9i was coupled with a middle lens and place at a distance of about 800 mm for the back part of the hand, 870 mm for the front and of 940 mm on average while tilting the object. The parameter regarding the light intensity was set equal to 13, and 28 scans were acquired moving the object in front of the laser scanner, and were then aligned and merged using Innovmetric Polyworks.

The GOM ATOS was set similarly to the acquisitions performed for the flat plane and the spheres. Indeed, due to the fixed inclination of the cameras in respect to the projector, it was not possible to vary the distance of the bounding box. For this reason 45 scans were acquired for the hand, trying to cover any region. The hardest part is always in between the fingers due to occlusions.

The hand was then placed on the turn table of the NextEngine, which performed 12 acquisitions in a full rotation. The center of the turntable was placed at about 635 mm (25 in) in order to respect the ideal configuration for the WIDE mode. Then, other 10 additional scans were complete by manually defining the orientation of the hand on the support in order to cover as much as possible the scanned surface.

For the Artec Leo, the Structure Sensor and the 2 Kinect versions, the hand was placed on a stool that was rotated in front of the devices at a fixed distance with two rounds, varying their relative height.

The Artec Leo was placed at a distance of 540 mm from the hand. The Structure Sensor and the Microsoft Kinect 1 were placed at a distance from the object of 450 mm and 600 mm respectively and the bounding box was set to be equal to 0.3x0.3x0.3 m^3, following the steps defined during the survey of the flat plane. For the Kinect 2, the distance was equal to 750 mm and the best setting for the SDK was to fix the Voxels per meter at 512 and, the Volume Voxel Resolution at 256, with a consequent bounding box of 0.5 m per side.

Thigh and chest

All the acquisitions were performed with a setting similar to the hand ones, with some differences related to the dimensions and the detail level of the objects. The Minolta Vivid 9i was in this case coupled with a wide lens and placed at a distance of 1100 mm for the acquisition of the thigh and at a distance of 1350 mm for the chest. The intensity was set at 18 because the colour of the object was not so light and the object was rotated in front of the scanner. At the end of the acquisition, the 19 scans of the thigh and the 25 scans of the chest were imported, aligned and merged in Innovmetric Polyworks to obtain the two final 3D models.

For the GOM ATOS the setup was the same as for the hand, but the number of scans that were performed become 43 for the thigh and 37 for the chest. The large number of scans is related to the limited bonding box per scan, the required overlap for multiple markers to be visible in the following scans and the sharp edges of the models where the mannequin had the connection with other parts (*e.g.* the rest of the leg or the arms for the chest).

Also for the NextEngine, the setup did not change. The thigh was placed on the turntable and two full rotations with 12 scan each were performed for acquiring the lower and the upper regions, but additional 6 scans were performed for the top and bottom surfaces by manually placing the object in front of the scanner. Instead, for the chest 27 scans were acquired separately by manually placing the object, due to its larger dimensions that did not allow to perform the automatic rotation.

Also in this case, for the other scanners, the objects were placed on a rotating stool. Two complete round were performed for the thigh and three for the chest at different heights.

The Artec Leo was placed at a distance of about 670 for the thigh and 650 for the chest. The Structure Sensor and the Kinect 1 were placed, respectively, at 450 mm and 750 mm distance with the bounding box set at 0.6x0.6x0.6 m^3 for the acquisition of the thigh and at 750 and 850 mm respectively with the bounding box set at 0.8x0.8x0.8 m^3 for the chest. The Kinect 2 was placed at 800 mm from both the objects. The best setting was to fix the Voxels per meter at 512 and, the Volume Voxel Resolution at 384, with a consequent bounding box of 0.75 m per side.

Handheld approach

In addition to the models acquired in fixed position, the handheld scanners Artec Leo and Structure Sensor were used with free hand movement. The Artec Leo was moved by the user moving around the objects, creating almost a loop at variable distances. In general, the motion took place staying far enough to acquire the whole model but in some moments getting closer and focusing on the details (*e.g.* the fingers for the hand)

or tilting the scanner to acquire from a different point of view. A similar approach was used also for the Structure Sensor, which was mounted on an iPad. The acquisition was computed using Captevia, the app developed by Rodin4D and setting the bounding box manually on the screen.

Finally, the O&P Scan was used by an orthopedic technician for all the objects, being moved in strips (mainly vertical) all around the objects at a distance of about 15 cm from the object and placing the magnetic marker right under the objects.

Different handheld motions

In order to evaluate the best approach to be used in the orthopedic workshops in a fast but reliable way, the mannequin chest was acquired multiple times with the Structure Sensor.

The tests were performed with the following movements of the operator walking around the mannequin, holding the iPad onto which the Structure Sensor was mounted.

1. One lap with the scanner at a fixed distance and without other motions, to mime the ideal circle that was obtained by rotating the objects in front of the fixed devices.

2. Two laps with the scanner at a fixed distance and without other motions, to mime the ideal circle that was obtained by rotating the objects in front of the fixed devices.

3. One lap with the scanner at a fixed distance and moved up and down, with a sinusoidal movement.

4. One lap with the scanner at a fixed distance and pitched up and down, rotating around its horizontal axis.

5. Operator allowed to move the scanner freely, changing distances and rotations in order to acquire the whole surface.

All the previous approaches were limited to about 20 seconds to perform the full rotation around the mannequin, except for the second case that took about 40 seconds for the two laps. Each approach was also repeated three times, to provide statistical confidence.

2.3.5 Analyses and processing

The first analysis regarded the estimation of the global error and the systematic error for the different devices analyzed in this project, following the basic steps presented by [40]. The second analysis regarded the performance evaluation on the spheres reconstructions. The three parameters PF, PS and SD described in Section 2.3.3 were evaluated. Finally, considering the results of both analyses, the reference scanner was set for the subsequent comparisons on the mannequin parts.

In all the analyses, the models acquired with the Kinect 2 were scaled with a factor of 1000 in order to change the measurement units from meters to millimeters, so that all the models where coherent with the Engineering measurement units.

For the analysis of the distance errors with the flat plane, a Taubin smooth filter was used according to the work by Guidi et al. [40]. The filter is basically a low-pass filter

that does not apply any subdivision to the mesh, *i.e.* the noise, which is commonly known for having high-frequencies, should be removed without altering further the point positions.

The analyses have been performed using CloudCompare, the Open Source Project 3D point cloud and mesh processing software. The version used is the latest stable release 2.9.1, installed on a Windows 10 notebook with i7-6700HQ CPU, 16GB of RAM memory and NVIDIA GeForce GTX 960M (2GB GDDR5 video memory). In addition, Autodesk Meshmixer (version 3.5.474) was used for the manual rough cleaning and MeshLab (version 2016.12) was used for applying the Taubin smooth filter.

In all the comparisons, the point clouds were extracted from each model in the same way using CloudCompare. The point clouds were analyzed in respect to the reference mesh models and the cloud-to-mesh comparison was thus chosen. The cloud-to-cloud option was not considered appropriate because the output values were only positive distances point-point and thus the scaling effects was not visible. The cloud-to-mesh instead solves both issues, giving the correct distance of the points from the reference mesh (that represents the ideal or the best one), with both positive values (outwards) and negative values (inwards), thus highlighting also the possible scaling effects.

Flat plane

First, the acquired models of the plane were cleaned roughly from the elements that were clearly part of the surrounding environment. Then in Cloud Compare an ideal plane was created using the "Primitive factory" and its dimensions were set equal to the real plane ones, 700 mm by 528 mm.

After having imported all the models, they were roughly aligned manually and then registered using a partial overlap of 80%. This step allowed using only the points related to the flat plane discarding the border. Afterwards, the models have been cropped using a bounding box of 680 mm by 500 mm by 40 mm, aligned with the plane in order to effectively remove the surroundings and the borders, thus keeping only the points of the plane. A final fine registration has been performed setting the final overlap to 100%, using up to 5.000.000 points (over the maximum number of points of any scanner) and fixing the translations on the plane, while allowing the perpendicular shift and the rotations.

This solution allowed aligning the scanned plane to the ideal plane without having the models shifted all around the plane. This is clear for the orthogonal translation and the rotations, but the lateral shifts (in horizontal and vertical directions) have been avoided because the 100% of the remaining model is aligned with the ideal plane that has the same external dimensions. This means that all the points should be as close as possible to the plane 680 mm by 500 mm and thus not be able to shift on an infinite plane.

At this point, the resulting cropped and aligned models were exported, and a Taubin smoothing filter (Taubin, 1995) has been applied onto them before being imported back to the comparison software. This step was performed using MeshLab (version 2016.12), setting λ=0.95, μ= –0. 98 and 50 iterations. These values have been set in compliance with the limits presented in (Taubin, 1995), λ>0, μ< $-\lambda$ and the threshold k_{pb}(=0.0315) > 0 (preferable between 0.01 and 0.1).

A particular case is represented by the Microscribe that provided only a point cloud

and thus it was not possible to apply the Taubin filter. In order to analyze the possible effect of a filter, the SOR (statistical outlier removal) option available in CloudCompare was used.

Finally, all the comparisons were performed using the vertices of the model with respect to the ideal plane created with the primitive factory, with the cloud-to-mesh option.

Spheres

The acquired models were cleaned manually in order to extract and divide the points belonging each sphere. The point clouds from the Microscribe were cleaned in order to preserve a constant number of 30 point for each sphere, number that satisfies the requirement of at least 25 surface points of the VDI/VDE guidelines.

All the point clouds where then analyzed with a Matlab script which performed a least squared fitting of a sphere with freely variable radius and center coordinates. Once each point cloud is fitted with a sphere, the script computes the error in the size approximation in respect to the calibrated dimensions of the spheres obtaining the Probing Error in Size (PS). Moreover, each point is evaluated in respect to the approximated sphere and the Probing Error in Form (PF) is evaluated as difference of the maximum measured error and the minimum one, which correspond to the difference of maximum and minimum measured radii. Finally, the distances between the approximated spheres were computed to esteem also the Sphere Distance (SD) error. In this case, the reference distances where taken from the scanner that best performed in the other parameters.

Hand

The models have been roughly cleaned removing most of the surrounding environment, each model separately. This step has been also a requirement in order to import all the models in a single comparison file. Since no smoothing filter had to be applied, the point clouds were immediately extracted and the following steps were computed without the mesh models. Similarly, to the analysis on the flat plane, the models were roughly aligned manually and then finely registered automatically, with the constraint of 90% final overlap. Subsequently all the models, aligned in respect to the reference one, were cropped in the region of the forearm at the same location. Finally, a fine automatic registration was performed using the 100% of the final models and the cloud to mesh distance was evaluated.

Thigh

The analysis is very similar to the previous one (Hand), with the exception of a double cropping of the models, both in the distal and proximal regions of the thigh, after the first 80% registration, and a change in the settings of the final 100% of overlap. The vertical translation (along the axis of the leg) was locked, so that no further shift could happen when aligning the cropped point clouds due to possible scale effects on this pseudo-conical shape.

Chest

For this object, the steps are exactly the same of the ones used for the hand, but having a multiple cropping to all the connections of the mannequin: on the neck, on the lower part of the abdomen (for the pelvis) and on the shoulders for the arms. In this case, the fine registration 100% final overlap was performed with all the degrees of freedom unlocked.

Different handheld motions

After removing the surroundings and the flying parts due to noise in the acquisitions, the models were aligned and compared in CloudCompare. For each approach, the 3 models were compared one each other and the standard deviations were averaged. Finally, the difference of the approaches could be compared and the statistical significance was evaluated.

Moreover, the right hip side was selected as region of interest, which is commonly bony for the iliac crests. Due to the fact that the brace has an anchorage on the pelvis for applying the corrective forces on the thorax, the acquisition of this region should be as precise as possible for modeling the brace. So, a further comparison was computed also for the portion of models extracted and, similarly, the statistical significance of the difference between the approaches was evaluated.

2.4 Results and Discussion

In order to understand better the following results, it is important to remember that the global error, obtained analysing the models without any filter, is composed of a systematic component, that can be highlighted applying the Taubin filter [40] because related to low frequency, and a random error, that has high frequency and that could be obtained by subtracting the systematic error from the global one. Moreover, the lower the standard deviation values are, the lower the error is and the better the device performances are.

2.4.1 Flat plane

The distance cloud-to-mesh has been computed between the ideal plane created in CloudCompare and each of the acquired models, both with and without the application of the Taubin filter. The results have been fitted using Gaussian distributions and the values of mesh average dimension and standard deviation are reported below in Table 2.4. Graphical results also depicted in Figures 2.4 and **??**.

As it was expected, the GOM ATOS had the lowest values of standard deviation among the scanners, both with and without the application of the Taubin filter. The Microscribe was expected to have better results than 3D scanners, but it has to be noticed that the limited number of acquired points could have reduced the averaging effect, thus increasing the standard deviation.

The Minolta laser scanner showed a behavior in line with the previous results presented in [86]. Figure 2.4, shows that an improvement could be obtained with a proper calibration in order to remove the vertical stripes effect and the horizontal bowing.

Table 2.4: *Values of mesh size and standard deviation of the cloud to mesh distance for the flat plane models before and after the application of the Taubin filter.*

Device	Mesh average dimension [mm]	Std Dev [mm]	
		Without any filter	With Taubin filter
GOM ATOS II 400	3.5	0.073	0.064
NextEngine Ultra HD	0.3	0.082	0.073
Microscribe MLX	-	0.078	0.074
Konica Minolta Vivid 9i	1.3	0.331	0.284
Artec Leo - Sharp Fusion	1.0	0.596	0.576
Artec Leo - Smooth Fusion	1.0	0.577	0.563
Artec Leo - 220 Frames	-	0.747	0.689
Occipital StructureSensor	1.9	1.767	1.660
Microsoft Kinect V1	1.9	3.187	3.142
Microsoft Kinect V2	1.56	1.025	1.014
Rodin4D O&P Scan	2	4.492	4.435

For the Artec Leo, we can notice how the smooth fusion performs better than the sharp fusion. As expected, both the algorithms behave much better than the raw point cloud of all the frames, thanks to their averaging effect in the sub-sampling step. It is also clear that the smoothing filter has a stronger effect on the sharp fusion model than on the smooth one.

The results regarding the global error of the Structure Sensor and the Kinect 2 are coherent with the ones found by Guidi et al. [40], considering that in the present tests, the acquisition lasted for 10 seconds and many frames were captured, so that the software applied a time averaging, while in that work [40] just one frame was used avoiding the time averaging. This could explain the reason why the random error on the acquisition of the plane, at more or less the same distance between the device and the object, was about half of the global error.

The first version of the Kinect presented the worst results in the reconstruction of the flat plane, with values over 3 mm that are almost double the ones of its evolution, Structure Sensor.

The O&P Scan instead was expected to have better results than the 2 low-cost devices, but, as visible from Figure A.1 in Appendix A, it showed its two main disadvantages: the bad behavior of the magnetic field for determining the relative position of the scanner with respect to the sensor, producing the spherical warping, and the small width of the laser blade and of the field of view, that determined the need of multiple strips, comparable to the ones left by a paint brush. Moreover, the survey had to follow specific rules: the strips have to be contiguous with a small overlap and following a straightforward path.

For all the devices, the standard deviation after the application of the Taubin filter still gave high values, meaning that the systematic error is the one affecting more the 3D acquisition. The analysis of the values before and after filtering the models has stronger effects on the ones acquired without any smoothing option or any averaging effect. For example, Minolta and GOM present the best improvements, together with the point cloud of all frames for the Artec Leo. Less effect is visible from results of the fusion of the frames that was performed with Artec Studio or that is automatically performed for creating the model by Skanect and Kinect SDK.
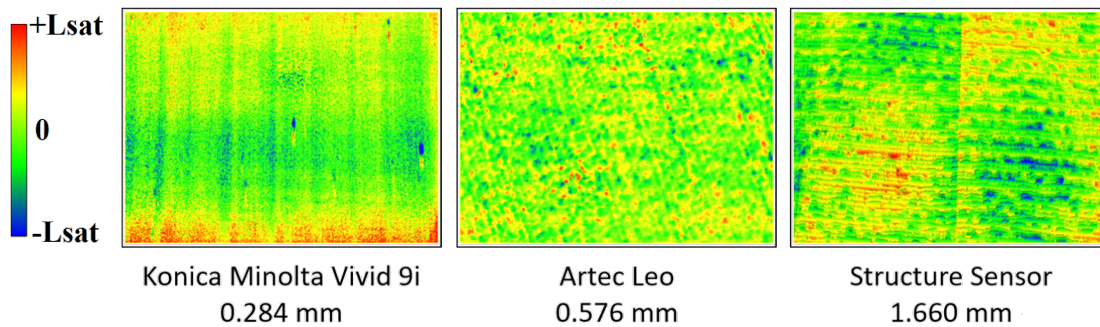
Figure 2.4: *Example of the flat plane comparison for Minolta, Artec Leo and Structure Sensor.*

Finally, analyzing only the values of table 2.4 is not sufficient to establish if the scanner is performing at its top level. We should instead evaluate also the error distribution over the model, as reported in Figure 2.4 and in Appendix A, because a better calibration could be needed. For example, the Minolta scanner shows a problem of stripes and bowing and also the Structure Sensor presents a clear deformation due to the sensor. On the other hand, the Artec Leo presents a random distribution of the error, which means that the calibration was correctly computed despite the overall deviation is higher than Minolta.

2.4.2 Spheres

Also for the spheres the best results were obtained with the GOM ATOS. The other scanners performed similarly for the order of results when considering the fixed configuration, with the exception of the Kinect 2 that became the worst.

The use of both the Artec Leo and the Structure Sensor in free hand mode provided better results, despite the same time limit. The improvements could be related to the best alignment of the frames when a larger portion of the object is acquired. For example, such improvement is clearly visible when acquiring an object in a 360 rotation around it, minimizing the overall alignment error, as opposed to the propagating of the error when the rotation around the object is not complete.

In the graph, the plots for Kinect 2 are cropped for visibility purposes. The large errors in the approximation of the sphere can be clarified analyzing the model that was reconstructed. The spheres did not maintain the shape but became more similar to cones, for a difficult processing of the shape with the SDK fusion.

The NextEngine, that is a medium cost device presents a very high level of results. The main problem of this device, though, is the amount of time required per scan (about 5 minutes in high resolution mode).

The sphere distances show clearly the error related to the sphere reconstruction of the Kinect 2 that was then cropped for the same issue of visibility. Also the Minolta results having a variation that is larger than expected, but we could relate the issue with the calibration pattern shown in Figure 2.4.

2.4.3 Hand, thigh and chest

Due to the results obtained both with the analysis of the flat plane and of the spheres, the GOM ATOS was selected as reference device. For this reason, the distance cloud/mesh

Table 2.5: *Numerical results of the sphere approximation evaluated in Matlab, in particular, probing error in form and in size as required by the VDI/VDE guidelines.*

Scanner	Probing error in form (PF)			Probing error in size (PS)		
	Average	Min	Max	Average	Min	Max
GOM ATOS II 400	0.074	0.056	0.094	0.035	-0.005	0.115
Microscribe MLX	0.240	0.086	0.592	-0.058	-0.181	0.027
Konica Minolta Vivid 9i	0.642	0.544	0.723	0.092	-0.150	0.259
Artec Leo - Fixed - Smooth Fusion	0.743	0.287	1.059	-0.690	-1.202	-0.165
Artec Leo - Fixed - Sharp Fusion	0.744	0.260	0.980	-0.141	-0.324	0.298
Artec Leo - Fixed - 220 Frames	3.675	3.025	4.716	1.506	1.053	2.378
Artec Leo - Handheld - Smooth Fusion	0.691	0.377	0.880	-0.064	-1.093	0.559
Artec Leo - Handheld - Sharp Fusion	0.535	0.299	0.710	0.151	-0.285	0.498
Artec Leo - Handheld - 220 Frames	4.181	3.766	4.759	1.572	1.023	2.022
Occipital StructureSensor - Fixed	11.472	7.833	15.877	3.461	-1.308	6.575
Occipital StructureSensor - Handheld	12.372	3.939	20.930	1.475	-0.741	3.193
Microsoft Kinect V1 - Fixed	14.140	7.947	23.071	4.457	-0.579	7.742
Microsoft Kinect V1 - Handheld	17.359	9.814	24.940	3.464	0.057	10.625
Microsoft Kinect V2	12.324	0.028	23.995	-9.709	-31.714	-1.247
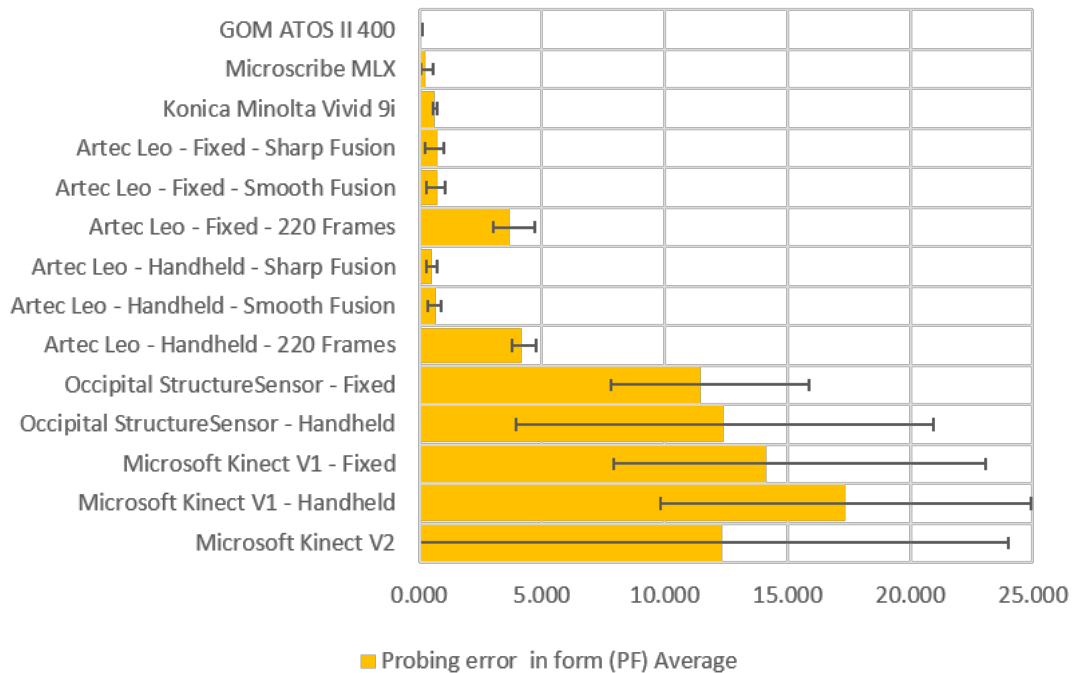
Figure 2.5: *Graphical representation of the probing error in form with error bars.*

has been computed between each of the acquired point clouds and the model obtained with the GOM ATOS.

The results have been fitted using Gaussian distributions and the values of standard deviation are reported below with the value of average mesh size, Tables 2.6, 2.7 and 2.8. For the comparison of these models, no filter was applied. All the comparisons are represented in Figures 2.9, 2.10 and 2.11.

The NextEngine scanner was the one that best performed among all the devices, in
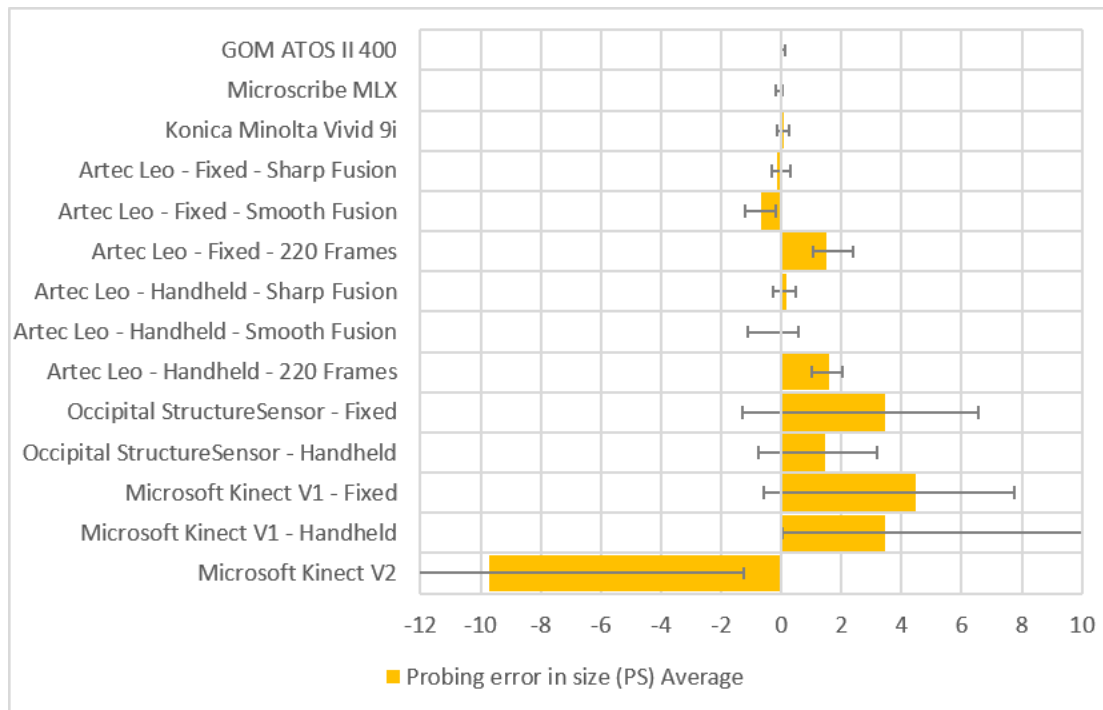
Figure 2.6: *Graphical representation of the probing error in size with error bars.*

Table 2.6: *Values of mesh size and standard deviation of the cloud to mesh distance for the hand models in respect to the model acquired with GOM ATOS.*

Device	Mesh average dimension [mm]	Std Dev [mm]
GOM ATOS II 400	0.8	-
NextEngine Ultra HD	0.25	0.142033
Konica Minolta Vivid 9i	1.4	0.242071
Artec Leo - Fixed - Sharp Fusion	1	0.2535155
Artec Leo - Fixed - Smooth Fusion	1	0.320135
Artec Leo - Handheld - Sharp Fusion	1	0.225523
Artec Leo - Handheld - Smooth Fusion	1	0.281245
Occipital StructureSensor - Fixed	0.6	0.623877
Occipital StructureSensor - Handheld	3	0.494728
Microsoft Kinect V1	0.6	0.873124
Microsoft Kinect V2	2	2.11744
Rodin4D O&P Scan	1	1.064505

all the acquisitions. Both the laser scanner, NextEngine and Minolta Vivid 9i, presented a similar trend for the standard deviation in respect to the analyzed object. The minimum was obtained for the thigh, thanks to the simpler shape in respect to the hand, which showed more difficulties for reconstructing the fingers. The worst results instead appeared on the biggest object, the chest model.

Surprisingly, the Artec Leo performed better than the Minolta in most cases. In particular, the use of the *sharp fusion* produced always lower deviation than the *smooth fusion* both in the case of sharp edges. This effect appeared both for sharp edges that had to be preserved (*i.e.* finger tips) and on completely smooth objects, such as the
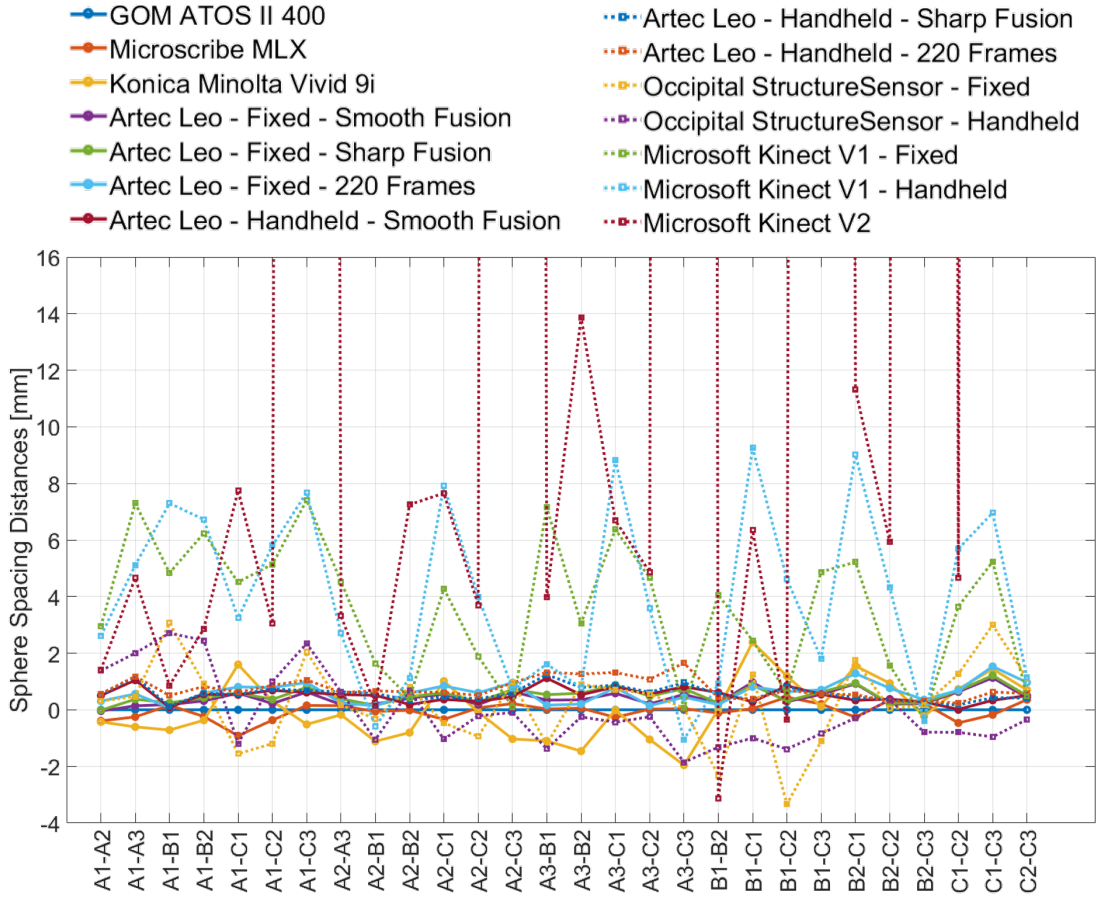
Figure 2.7: *Sphere spacing distances for each analyzed scanner.*

Table 2.7: *Values of mesh size and standard deviation of the cloud to mesh distance for the thigh models in respect to the model acquired with GOM ATOS.*

Device	Mesh average dimension [mm]	Std Dev [mm]
GOM ATOS II 400	2	-
NextEngine Ultra HD	0.6	0.083118
Konica Minolta Vivid 9i	1.5	0.227114
Artec Leo - Fixed - Sharp Fusion	1	0.120235
Artec Leo - Fixed - Smooth Fusion	1	0.147987
Artec Leo - Handheld - Sharp Fusion	1	0.101561
Artec Leo - Handheld - Smooth Fusion	1	0.121331
Occipital StructureSensor - Fixed	1.2	0.379739
Occipital StructureSensor - Handheld	3.5	0.392779
Microsoft Kinect V1	1.2	1.418603
Microsoft Kinect V2	2	1.431114
Rodin4D O&P Scan	2	1.375516

thigh and the chest, for a scaling effect applied by the smoothing filter.

The Kinect 1 obtained good results in terms of standard deviation with the objects, better than the one obtained with the flat plane. Comparing the objects, the value of deviation on the hand seems to be better than the ones with the thigh and the chest.
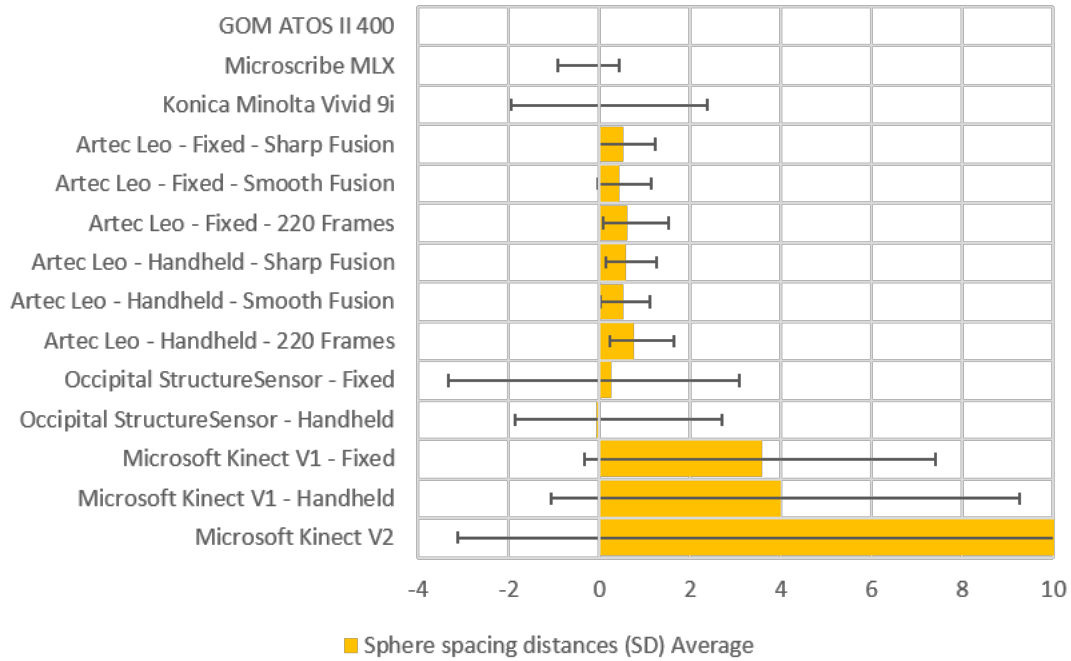
Figure 2.8: *Graphical representation of the sphere spacing distances with error bars.*
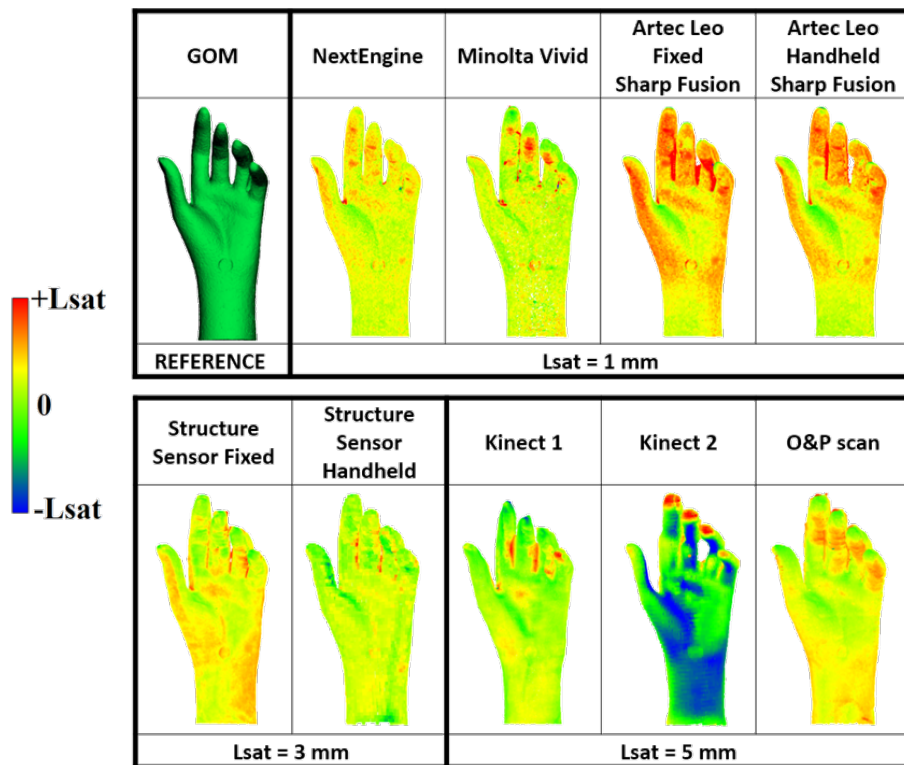
Figure 2.9: *Results obtained by the different devices, organized by column, acquiring the hand of the mannequin.*
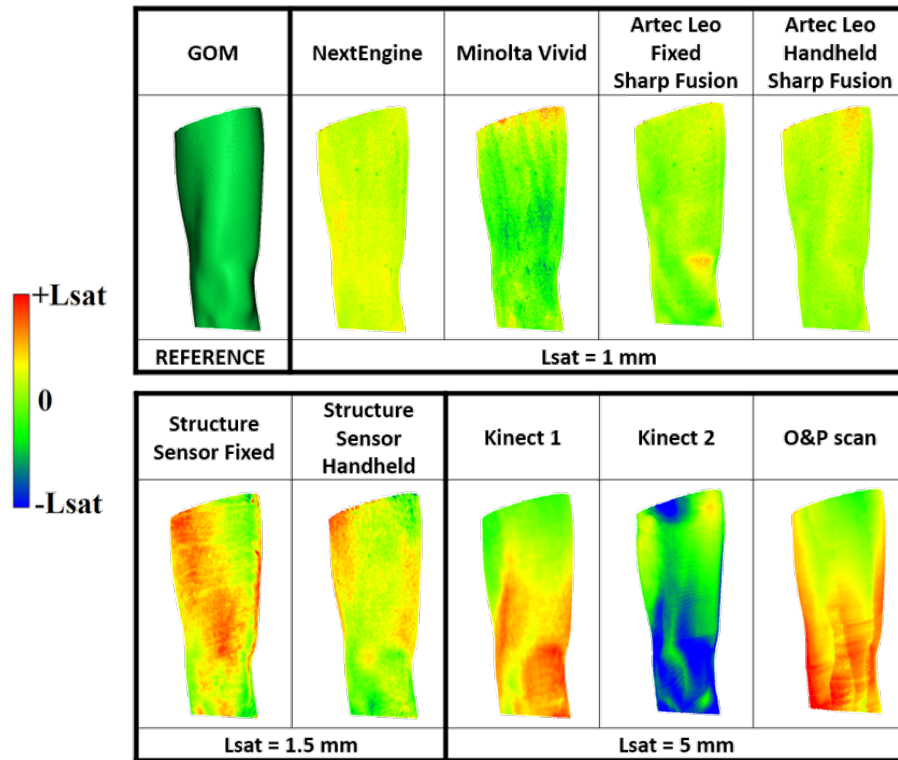
Figure 2.10: *Results obtained by the different devices, organized by column, acquiring the thigh of the mannequin.*

Table 2.8: *Values of mesh size and standard deviation of the cloud to mesh distance for the chest models in respect to the model acquired with GOM ATOS.*

Device	Mesh average dimension [mm]	Std Dev [mm]
GOM ATOS II 400	0.5	-
NextEngine Ultra HD	0.9	0.201
Konica Minolta Vivid 9i	3	0.358
Artec Leo - Fixed - Sharp Fusion	1	0.199
Artec Leo - Fixed - Smooth Fusion	1	0.260
Artec Leo - Handheld - Sharp Fusion	1	0.214
Artec Leo - Handheld - Smooth Fusion	1	0.287
Occipital StructureSensor - Fixed	1.6	0.586
Occipital StructureSensor - Handheld	4.5	0.657
Microsoft Kinect V1	1.6	2.016
Microsoft Kinect V2	1.6	2.587
Rodin4D O&P Scan	3	3.783

However, analyzing the models in Figure 3, we can notice that the hand is particularly good only on the wrist, palm and back, but the reconstruction on the fingers is poor.

The Structure Sensor mounted on a tripod demonstrated to have a stable deviation in all the models with respect to the references.When used as a hand-held device by the orthotist, mounted on an iPad with the Rodin4D app, the device performed again quite well, also with respect to the Rodin4D O&P scan, which was a higher budget one. The
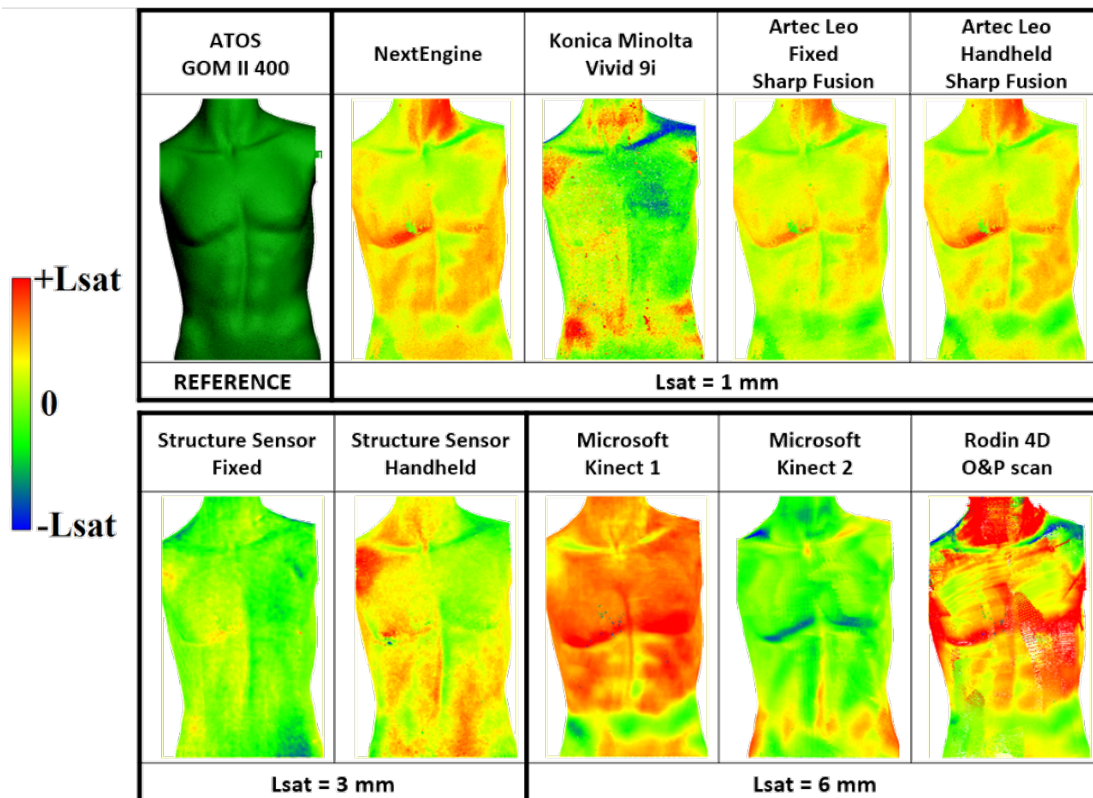
Figure 2.11: *Results obtained by the different devices, organized by column, acquiring the chest of the mannequin.*

lower spatial resolution is clearly a setting of the app, due to the computational power limits of the tablet in respect to a normal computer. Overall, this is still compatible with the goal of virtualizing human parts in order to design and produce patient-specific products, such as an orthosis or a prosthesis.

For both the Kinect 1 and the Structure Sensor, the values of the standard deviation showed that the averaging, due to the high number of frames acquired during the scans, and the paths followed around the objects, produced better results.

The Kinect 2 showed sensibly higher values of standard deviation with all the 3D objects, in respect to the ones obtained with the flat plane. The main reason was already clear during the real-time view of the acquisition and depended on the very poor alignment achieved by the software. The models are visibly deformed, for example the hand had connected fingers and the thigh was warped, and the acquisitions themselves required slow and smooth movements not to lose the tracking. Moreover, trying to use the maximal resolution, it presented issues in the capturing frequency that decreased from the normal 30FPS down to 2 FPS, making impossible to track the object with the same rotation speed of the other devices.

The O&P Scan demonstrated, similarly to the Structure Sensor, that the alignment of the strips on 3D objects performs better than on the flat plane. However, the device showed an increase in the error with the increase of the dimensions of the objects. This can be related again to alignment problems of the magnetic field technology. Probably the working environment, a room with some metal frames needed to keep the patient

in certain postures, could have biased the position tracking of the device around bigger objects.

From the numerical results we can understand that there is a clear distinction with 2 levels of devices: high quality with small errors and low level with large errors. This separation reflects the trend of the price at purchase of the devices.

2.4.4 Application-related choice of the device

The laboratory high-level scanners (GOM, Minolta and NextEngine) provided the best results in terms of spatial resolution and accuracy of the measurements. The problem of these devices is the type of technology that requires multiple scans from fixed view points. Each of them takes a long time (from 10 seconds up to 5 minutes) to be completed.

Moreover, it is not easy to move the scanners around the patients body. Thus, they would have to move in front of the scanner, probably changing also the geometry of the parts to be acquired, due to both joints and soft tissues movements (*e.g.* arms position or rib-cage breathing movement).

The best device, among the others tested in this project, resulted to be the Artec Leo, not only for the low deviation from the reference models but also for the possibility to move around the objects without any wire and without the need of an additional tracking system.

Similarly, also the Structure Sensor can be easily used in hand-held mode, when mounted on a tablet. The accuracy is worse than the previous devices, but not so bad when considering the application requirements. Indeed, the scoliosis braces are usually worn over a light cotton layer and, according to the technicians, the softness of the skin layers of the patients can mitigate errors of about 1 mm.

For the Kinect 1, we can state that it could be still a very cheap and acceptable device for acquiring medium to large body parts, depending on the final goal. For example, if we have to develop a new wrist orthosis, the shape could be still similar to the real one but the error would not be acceptable due to the thinner skin layers around the bones. On the other hand, the Kinect 1 would still be a valid device for creating a socket for the prosthesis of an above knee amputee, because the thicker layers of soft tissues around the bone and the use of silicon liners could mitigate the deviation.

Even though the Kinect 2 showed good performance on the flat plane, the poor alignment highlighted with the spheres and the mannequin parts, determined the inability in a realistic acquisition of patients for O&P purposes.

The Rodin4D O&P scan has a nominal high accuracy, but the problems due to the magnetic tracking system must have pushed towards the use of other technologies. The orthopedic solution companies, indeed, are offering today scanners based on white or blue light, with software that performs automatically the alignment of the frames.

2.4.5 Handheld motions results

Figure 2.12 illustrates the average standard deviation obtained comparing the different acquisitions using the 5 motions listed in Section 2.3.4, both for the whole chest and for the selected region of the hip side.

Even if the second method corresponded to doubling the rotation at a similar speed (thus doubling the acquisition time), the results did not show a significant improvement.

It appears that the motions 1, 2 and 4 can be overall comparable. The two full rotations(2) provide more stability in the results but the time required could be too large for some patients, for example scanning the children.

The best results on the hip region were obtained with the motion 3, probably thanks to the vertical movement up and down that allowed acquiring better the lower regions. Unfortunately, this motion did not perform so well on the whole chest, giving also a large variability of results. This could be explained thinking that the sinusoidal motion was performed manually, thus varying each time. Moreover, the limit of 20 seconds for completing the full rotation, combined with the vertical movement, meant that the device was moved in a faster way. The stability during the acquisition of each frame and the alignment of all the frames could have been then influenced negatively.

Also pitching the device up and down (motion 4) provided an improvement for acquiring the hip region because the wider acquisition of the lower regions could have helped the alignment. The whole chest did not show the same variation of motion 3, because of the more stable position in the fixed height.

The last approach corresponds to the free movement for the operator. This resulted to be the worst for the measured differences and the variability in the measurements, represented by the black error bar (that was cropped for visibility purposes and it is equal to $\pm\,0.36\ mm$).

We can thus conclude that it is better for the operator to move quietly, acquiring the whole surface with few movements, instead of continuously and rapidly changing the point of view. Indeed, slowly varying the device position could have more influence on the quality of the acquisition than the attempt to zoom some regions.
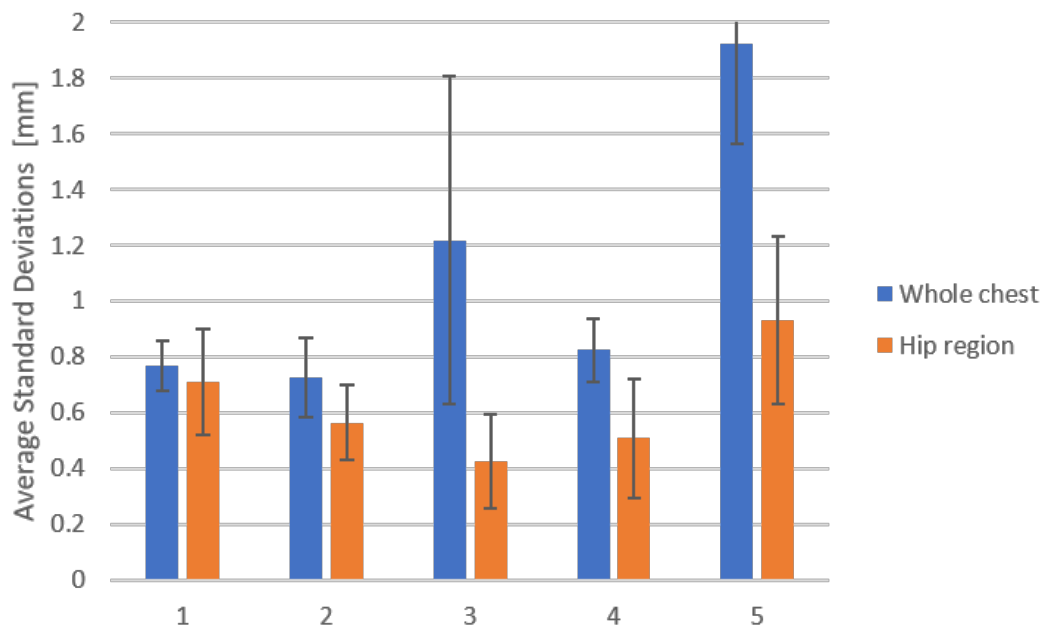
Figure 2.12: *Average standard deviation of the comparisons with five different scanning approaches. 1: one lap at fixed distance and no motion. 2: two laps at fixed distance and no motion. 3: one lap at fixed distance moving up and down. 4: one lap at fixed distance tilting up and down. 5: one lap and free movement.*

2.4.6 Final remarks

The analyses showed that a simple test of the devices on a standard object, like the flat plane or the spheres, is only a preliminary indication of the performances of the sensors, that will change in real application. At the same time, it remains an important step for the definition of the systematic error that could be removed using a proper calibration, thanks to standard testfields.

Therefore, a second test in conditions similar to the final application (*i.e.* scanning the human body in the case of this project) is always needed. Furthermore, depending on the field of use of the devices, a standardized object that could be used as a specific reference should be created, having also the original CAD model. In this way, the results could be compared without the bias due to the error of the device selected as reference.

Finally, regarding the use of hand-held scanners, the operator should take care when moving the device around the patient, preferring smooth movements to quick ones. The analyses showed also that having a stable path improves the repeatability of the acquisitions.

CHAPTER *3*

Virtual modeling

The chapter starts with a description of the current state of the art techniques for modeling the brace on computer, by analyzing some of the software available for dealing with the models acquired with the 3D scanners, considering both free, open-source and licensed tools. In particular the goal is to define the options already available for sculpting the brace and highlight eventual gaps to be filled.

For this reason, the chapter presents the development of a pseudo-parametric 3D skeleton model that should be embedded in the modeling software for different purposes. Indeed, the model can be used in the brace production process with the proposed approach as a reference for sculpting the brace, as an integrated model for simulations, and even for statistical analysis of the spine deformation of the same patient along time or as a comparison among different patients. This part of the project was developed during the exchange period in the Clinical Anatomy Division at Stanford University.

3.1 Current CAD tools

In the field of Mechanical Engineering, we refer to Computer Aided Design (CAD) thinking mostly to the solid modeling software (*e.g.* SolidWorks, SolidEdge, Inventor, etc.). To be precise and strict with the name CAD, we should also include the surface modeling software (*e.g.* Autodesk Alias and Rhinoceros) and the mesh sculpting and processing tools (*e.g.* Autodesk Meshmixer and Meshlab). This last type of software is indeed the one that is currently adopted for modeling the orthoses.

If the first two types of software use mathematical smooth formulations based on splines, B-splines and Non-Uniform Rational Basis Spline (NURBS) to represent the ideal surfaces and the volume which they included, the last type works with meshed/-faceted surfaces. These are always mathematical surfaces but they are constituted by

flat triangles (or quadrilaterals), of which the edges connect a set of points.

As presented in the previous chapter, the acquired data using the 3D scanners are point clouds. The software provided with the scanners usually processes and interpolates such point clouds in order to create the faceted surfaces, typically with the following standard formats: StereoLithoGraphy (STL) and Object (OBJ). Figure 3.1 depicts an example of the initial point cloud, the connection with the wireframe view and the final surface model.

| Point Cloud | Wireframe Connection | Surface Model |
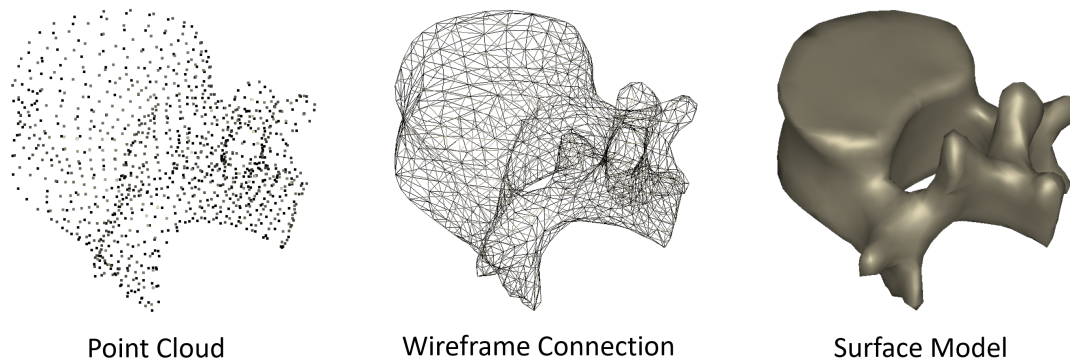
Figure 3.1: *Example of a 3D reconstructed vertebra: point cloud acquisition from the scanner (left), interpolation of the software (center) and final tessellated model (right).*

Each software uses different algorithms for interpolating the point clouds and creating the surfaces. Meshlab is one of the most powerful open-source tools that provide a large choice of algorithms to be used depending on the final object we want to reconstruct. Indeed, the software contains different algorithms (in the section *Filters*): some approximate the point cloud with open surfaces only where there are enough points and others create a closed surface (*e.g.* watertight models or convex hull), some apply a strong smoothing and others just simplify the point clouds.

After an excursus on the sculpting commands available in the different software packages, the following paragraphs present the current brace modeling process on the computer, which is based on the personal experience of the orthotists, and the additional step that can embedded with the aim of considering also the internal geometry of the patient's body.

3.1.1 Sculpting commands in modeling software

The sequence of operations that the orthopedic technicians currently perform for the rough creation of the positive mold starts by importing the model acquired by 3D scanning, already pre-processed as described above. This model is a tessellated surface mesh (STL/OBJ); hence, the best type of modeling software is the one that uses the dynamic mesh techniques, such as the free Autodesk Meshmixer and open-source Blender.

Moreover, other software commercialized for orthopedic applications were developed in this direction, *e.g.* Rodin4D Neo and Vorum Canfit. All these programs enable the direct deformation of the tessellated surface with commands similar to the manual sculpting operations that the orthotist would perform on the physical positive model.

We can distinguish between common commands that are available in the different software packages and specialized commands that were implemented in the orthopedic-oriented software.

Common commands

- *Smoothing*: it can be usually performed locally by using a brush or applied to the whole model. It reduces the detail level, but it is also adopted to remove the noise and some artifacts derived from the 3D scanning. Figure 3.2 exemplifies this command.

| Noisy surface | Light smoothing | Strong smoothing |
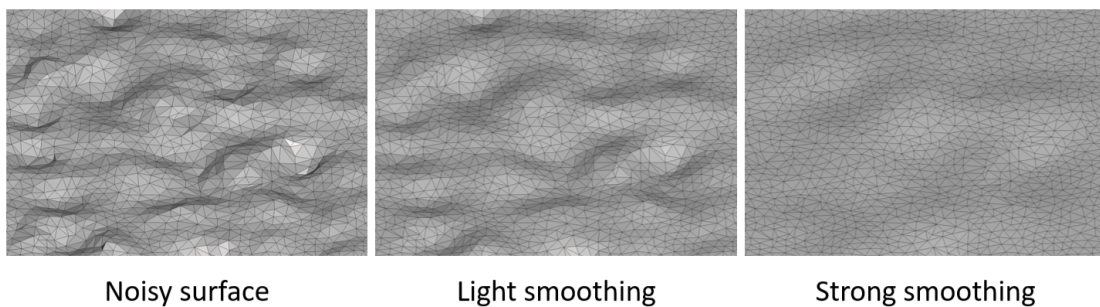
Figure 3.2: *Example of smoothing command in a noisy surface (left) using light (center) and strong (right) smoothing using Autodesk Meshmixer.*

- *Inflating and deflating*: it is the core of virtual modeling tools and it is frequently called sculpting because it allows to add or remove volume to the surface, to drag outward or inward specific regions and create particular surface textures. This type of command is typically applied locally and can be used with brushes or by selecting particular regions to be modified. Figure 3.3 exemplifies this command.

| Original sphere | Inflating | Deflating |
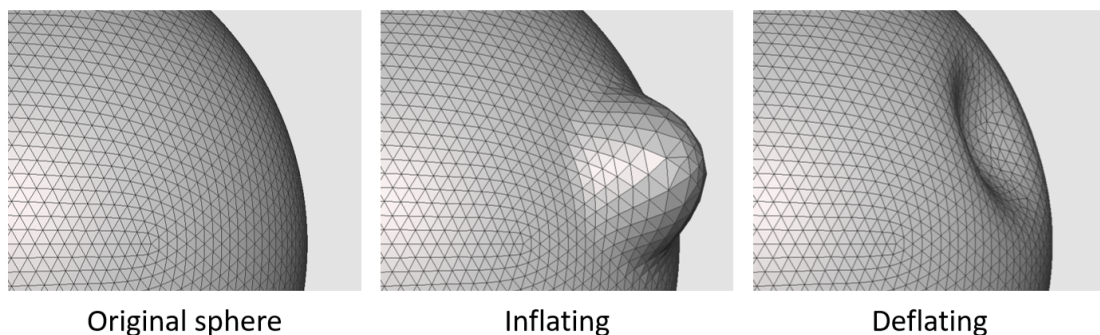
Figure 3.3: *Example of inflating (center) and deflating (right) command over a sphere (left) using Autodesk Meshmixer.*

- *Remeshing*: this command enables to reduce or increase the amount of faces that approximate the surface with a consequent effect on the dimensions of the mesh. Figure 3.4 exemplifies this command.

- *Crop border*: in its basic formulation it is simply the selection of a set of triangles to be removed, but it can also be implemented in order to draw a contour on the 3D

|| Uneven mesh || Fine uniform remeshing || Large uniform remeshing ||
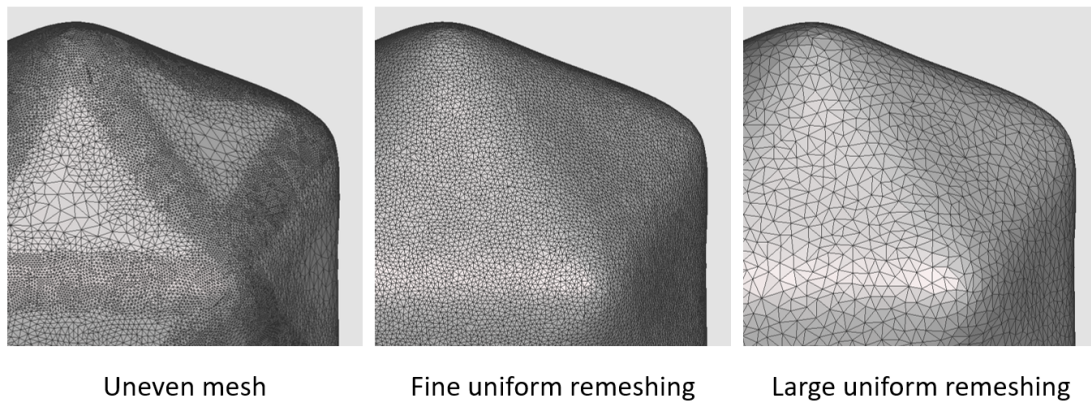
Figure 3.4: *Example of remeshing command over a surface with uneven mesh (left) using fine (center) and large (right) uniform remeshing using Autodesk Meshmixer.*

model and cut also across the triangles. Sometimes it is associated to a "smoothing border" option. Figure 3.5 exemplifies this command.

Original shape   Manual trimming   Border smoothing   Plane cropping
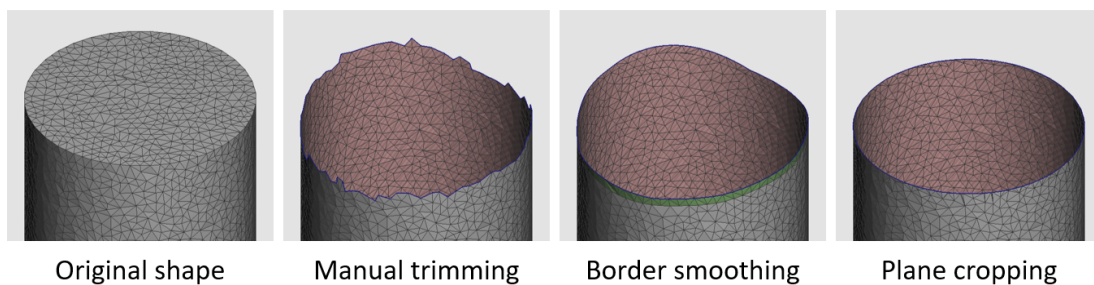
Figure 3.5: *Examples of border cropping command over a certain shape using Autodesk Meshmixer.*

Special commands

- *Bending according to an axis*: this command enables to use an axis inside the model that idealizes the spine and to bend the entire surface model according to flexion-extension, lateral and axial rotations distributed around segments of the axis.

- *Numerical comparison with input model*: the software allows to compare the sculpted shape with the original input file and receive not only a qualitative information, but also specific numerical data about regions, sections and volume changes. Similar to cloud compare used in Chapter 2.

3.1.2 Experience based modeling

The following description of the steps is based on what was directly observed in an orthopedic center for the creation of the rough positive mold surface on the computer, which is then milled by a robotic arm out of a cylinder of polyurethane foam according to the modern process presented in Chapter 1. The technician was already well trained both for the traditional process and for the modern use of scanners and modeling software. In particular, the description refers to the software Rodin4D Neo, but we
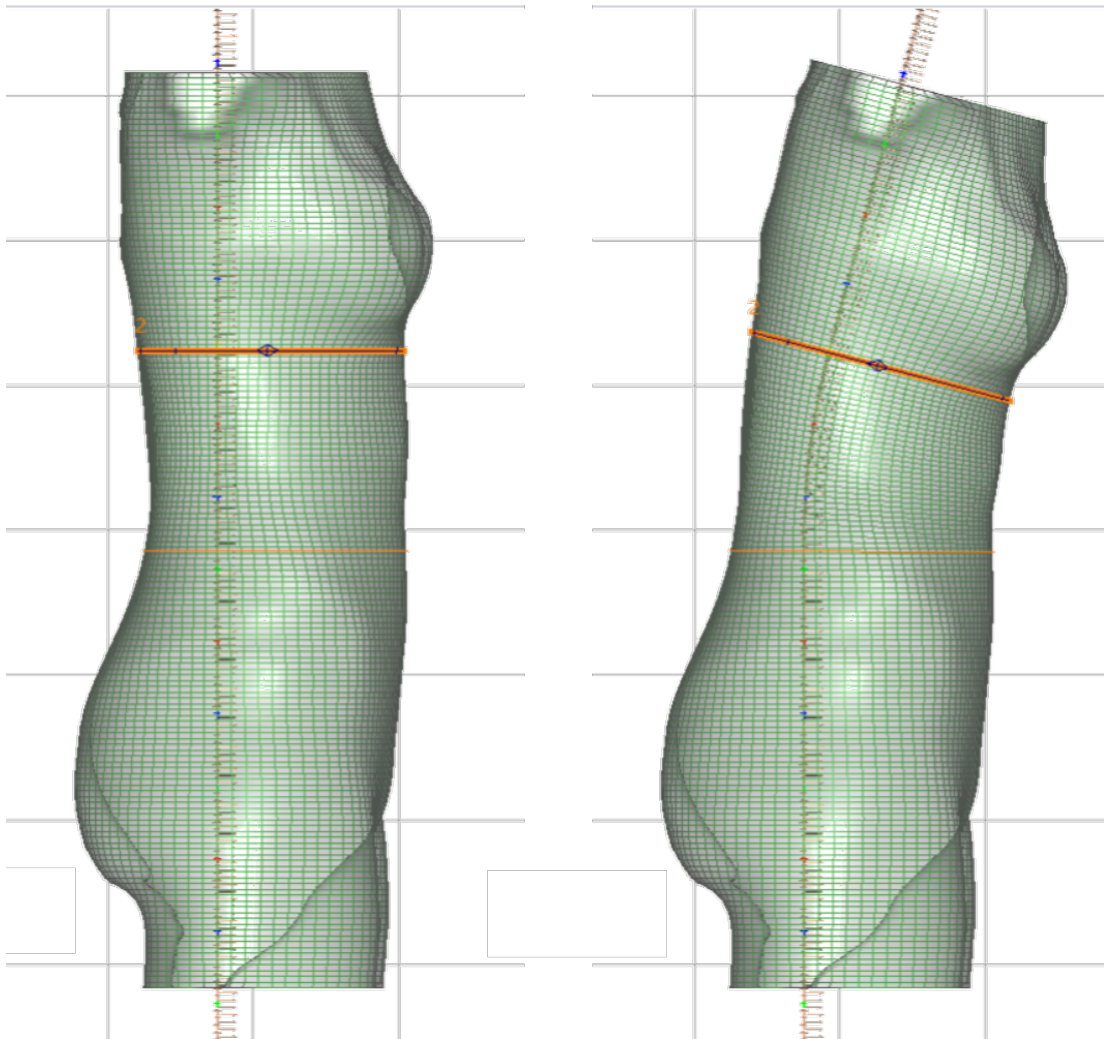
Figure 3.6: *Example of model flexion in respect to the ideal vertical axis using Rodin 4D Neo, right view.*

can assume that similar operations can be performed with the use of other commercial software developed for orthopedic applications, such as Vorum Canfit and BioSculptor BioShape.

Once the scanned model is imported, the technician has to align it to the base planes (frontal, sagittal and transverse, see Figure 3.7 and Figure 3.8), and crop the parts that are unnecessary for modeling the brace. In particular, the technician deletes those parts that are not related to the patient (*e.g.* room parts) and crops the head and limbs for the portion that is misleading the software in reconstructing a closed model. This last operation is driven by the vertical axis identified by the intersection between the frontal and the sagittal planes.

The software performs the reconstruction by re-sampling the scanned model with the intersection of a set of horizontal radial lines starting from the vertical axis. The output is a cylinder-like shape that is warped around the patient's body, which becomes the starting point for modeling the brace. For this reason, it is important to have the best input file possible and align it properly with the planes, otherwise the reconstruction

49

can fail (in case the axis is out of the model) or produce a very deformed shape (in case particular holes or flying parts).
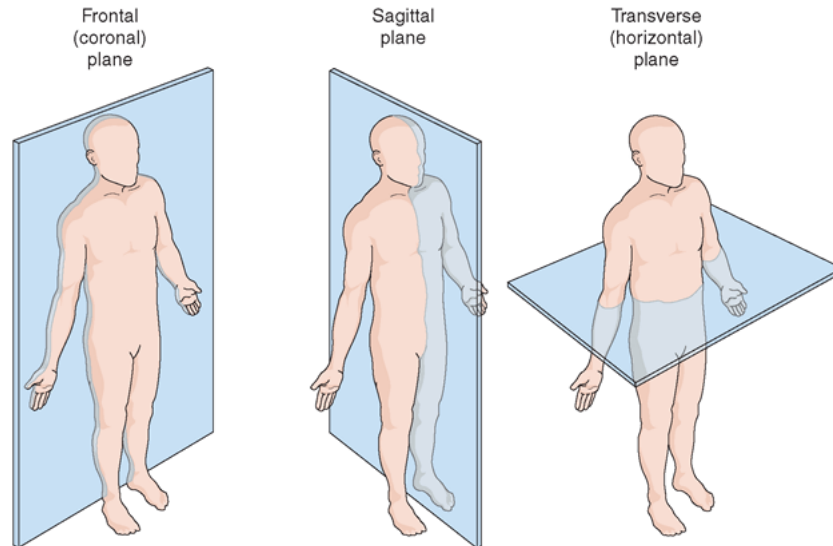
Figure 3.7: *Frontal (left), sagittal (center) and transverse (right) anatomical planes.*
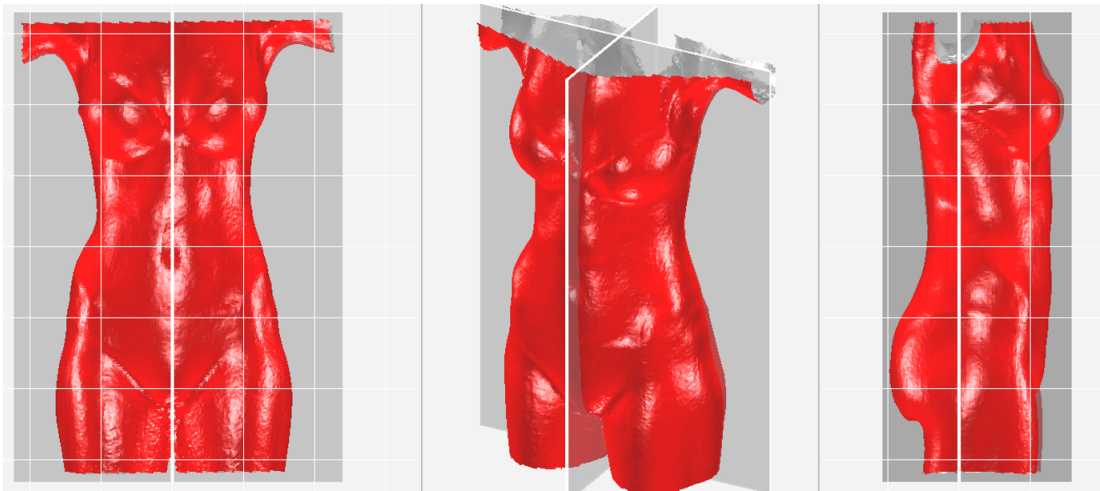
Figure 3.8: *Initial alignment of the scan model in respect to the frontal and sagittal planes. Frontal, isometric and right views.*

The previous steps can be considered as a quick pre-processing of the file received from the 3D scanning phase. Indeed, it is possible to activate the sculpting tools available in the software, only after the orientation, the cropping and the remeshing steps. It has to be noticed that the cropped and cleaned model, derived from scanning the skin of the patient, is then sculpted to define the internal surface of the brace, in the case of thermoforming or 3D printing with a thickness applied outwards. For this reason, the control of the volume amount is an important indication of the applied changes. In particular, we usually want to press the patient's body inside the brace shape for applying the corrections, but at the same time we need to maintain a balanced volume

(by expanding in the height) for allowing the normal functions to the inner organs (*e.g.* stomach and lungs).

The core of modeling starts always by smoothing the surface in order to reduce at most the noise and obtain a very smooth surface. The braces indeed should be in contact with the patient body, with the only interposition of a thin layer of cotton (*i.e.* tight t-shirt or tubular cotton undershirt).

The second step regards the symmetrization of the shape. This can be done with a percentage value that goes from 0% for the initial model to 100% for a completely symmetrical shape. The operation works averaging the position of the corresponding points on the two sides of the sagittal plane. We have to understand that the correction we can apply is strictly related to the initial condition of the patient. The fully symmetrical shape could be the ideal goal of the posture correction, but in some cases we cannot reach it with the first scoliosis brace (and we would need some intermediate steps) or, depending on the chosen brace type, we do want an asymmetrical shape for applying an over-correction (*e.g.* Charleston nighttime brace).

The procedure continues by bending the model forward and/or backward to correct the spine in the regions of lordosis and kyphosis. Moreover, additional changes could be necessary if the shape of the patient was acquired with the aid of a traction system, and if the patient was standing and leaning against a support. This system is used in some cases for producing an initial light correction, comparable to the one achievable with the deformation of the plaster of Paris during the first step of the traditional process.

If the traction system is not used during the 3D acquisition, the orthopedic technician has to stretch the model in the vertical direction on the computer. This deformation is typically applied in the lumbar region, between the rib cage and the pelvis because, without considering the cervical region, the lumbar region is generally the most flexible zone of the spine.

For correcting the thoracic curves, the technician usually bends the model on the sides, acting in the frontal plane. The rotations are usually small in the braces that we analyzed (*i.e.* Cheneau and Bolognese), but could be very large when observing the night-time braces (*e.g.* Charleston bending brace).

As described in the Chapter 1, the combination of scoliosis, kyphosis and lordosis often produces also an axial rotation of the spine. In order to correct this deformation, the software enables derotating the model around the axis that was originally identified by the intersection of the frontal and the sagittal planes (see Figure 3.8).

Once all the main changes were performed on the shape, one of the last important adjustments regards the reduction of the circumference in the waist for creating the so-called *anchorage* that allows to fix the brace in respect to the pelvis, as depicted in the left and center images from Figure 3.9. Other changes refer to the addition of material on the back, in the region of the spine, with the goal of creating a flatter support compared to the initial shape that could create discomfort when sitting or laying on the back. A similar adjustment is made also for the iliac crests in order to create a bit of clearance or at least to distribute better the pressure on the pelvis. The full sequence of operations performed to obtain the back brace model is reported in Appendix A with the Figure A.3.
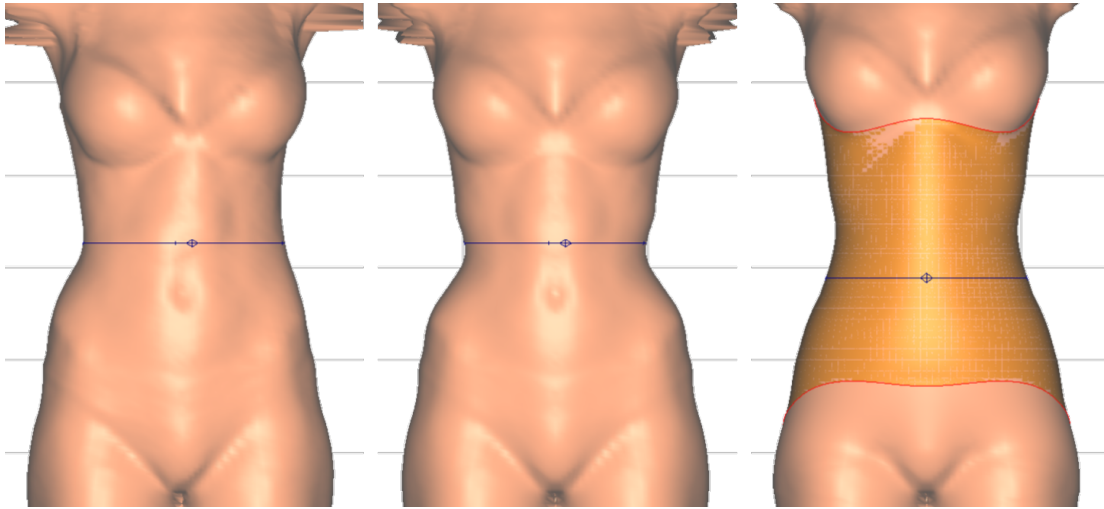
Figure 3.9: *Short sequence of steps to model the brace starting from the scan.*

3.1.3 Additional modeling steps

With the previous steps, we can obtain a good model of the brace (with a simple shape similar to the Cheneau and Boston brace types). For more complex shapes, additional steps require the use of inflating/deflating tools in regions where the forces should be applied or released, creating stronger loading areas and larger expansions on the opposite side.

In the modern process, the sculpting ends at this point and the model created is passed to the CAM module and then to the machine that carves the physical positive mold. For 3D printing the brace, instead, we need to add other steps: edge cropping and thickening.

All the programs enable selecting and cropping the edge of the orthosis, some easily and others with a series of operations. The right image of Figure 3.9 shows the brace model, in orange, cropped from the sculpted skin model. The problem encountered with the orthopedic-oriented software is the absence of the command to apply the thickness, necessary to pass from the ideal inner surface of the brace to the solid model that defines where the material is. This step is necessary for passing the model to the software that realize the slicing required for creating the commands of the 3D printer, because it cannot process an open surface but only a closed one surrounding the volume we want to print. Figure 3.10 shows the open surface model obtained from the orthopedic oriented software (on the left side), where the pink-striped color represents the back side of the faces, which is then thickened with the outward direction. So, in the right side of the figure the original green surface has flipped normals and the blue surface is the new offset surface, connected to the previous on the whole border.

The thickening does not always perform well in all the software. In the example of Figure 3.11, we can see that a spike appears once the thickness is applied in certain cases when using Meshmixer. This happens because of the difficulty of the software in evaluating the normals of the triangles along the border of the open surface. At the same time, it is not possible to smooth the surface in this region because constrained by the border itself.
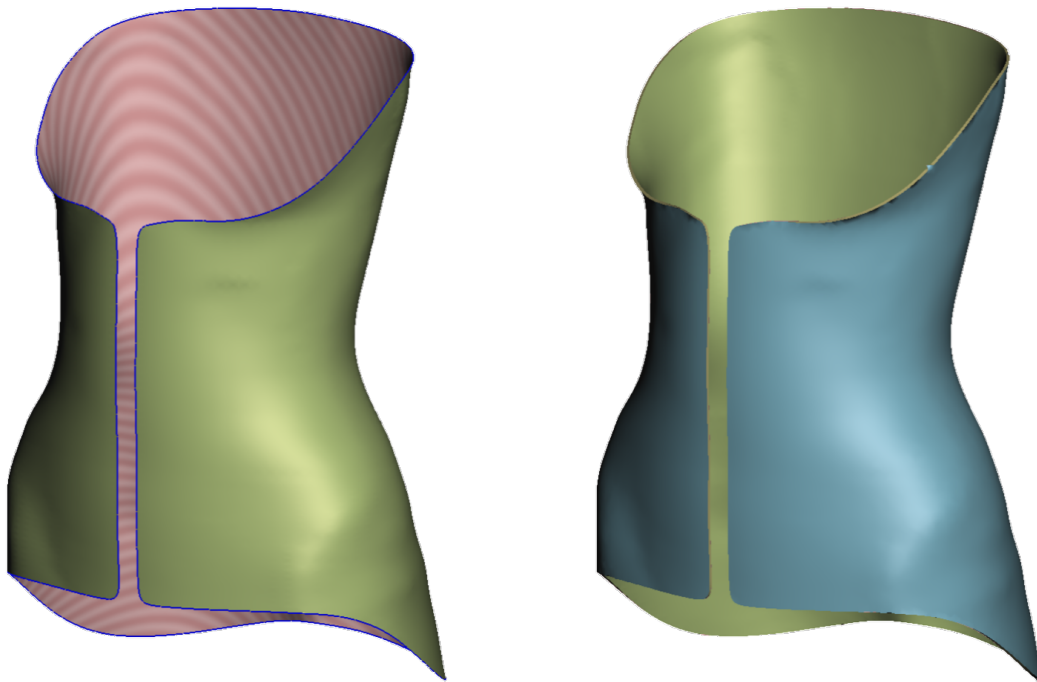
Figure 3.10: *Open surface model of the brace (on the left) and thickened solid version (on the right).*
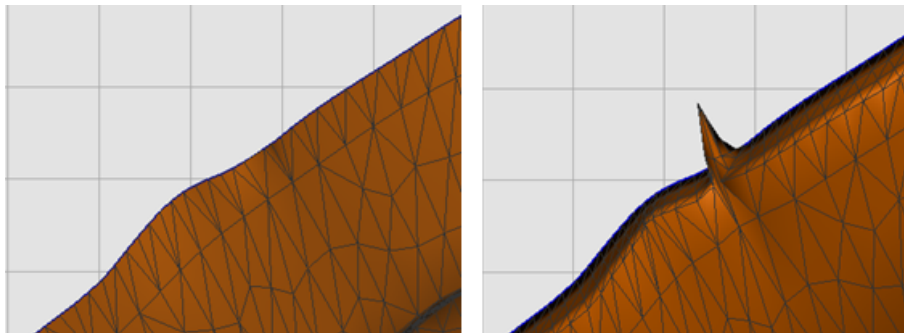
Figure 3.11: *Example of spike appearing on the border of the open surface (left) when the thickness is applied in Autodesk Meshmixer (right).*

3.1.4 Extra features of orthopedic-oriented software

Typically, the orthopedic-oriented software (Rodin4D Neo, Vorum CanFit and BioSculptor BioShape) enable a finer control of the operations, varying the sculpting tools settings with precise numerical values and custom profiles. They also provide a better visualization with a direct comparison between the initial model and the final one, showing also numerical values about the applied changes. Alternatively, the technician can import another brace model, ideally the previous or a similar one from a library (or also another patient), and have a direct comparison This part is missing in the general purpose software (*e.g.* Meshmixer), but can be performed by passing to other software

specialized in model comparison, such as the open-source CloudCompare.

Moreover, Rodin4D Neo maintains the history and the sequence of the performed operations on the model, as we are used to see in solid parametric CAD systems. We can also re-open and modify the different operations, suppress them or change the order, while in software like Meshmixer we can use only the undo step by step for a limited number of operations. This would mean that for a mistake we could have to restart every time from scratch.

Finally, the orthopedic-oriented software allow also to import a digital version of the bi-planar X-ray images of the frontal and the sagittal planes. The technician has to align the images manually in order to use them as a visual reference for modeling the brace. In particular, they are important to understand which regions are to be properly shaped for the anchorage on the pelvis and for applying the correcting loads.

In the industrial fields, it is common to reconstruct the 3D model of a product starting from the 2D projected views of the technical drawings. This might be a complex task even when clear and sharp edges are evident, but becomes harder when dealing with the organic shapes, typical of the human body. In particular, the abstraction effort becomes very challenging when it is required to identify the 3D geometry of the skeleton, using just one or two projections.

For this reason, I propose the use of a 3D skeleton model that can be quickly morphed for each patient and used as a 3D reference for better modeling the brace.

3.2 Related works

With the goal of using the internal models of the skeleton for the brace interaction with the patient's body, we could think of reconstructing the geometry from Computerized Tomography (CT) scans or Magnetic Resonance Imaginings (MRIs). This approach was performed in other fields where this medical examination is already available, for example in case of amputation [22] or for particular surgical planning [39, 100, 103]. The problems of such approach regard the invasive radiations, the costs and the position of the patient during the medical examination.

In the recent years, some attempts to reconstruct a parametric human model were presented. In particular, if we focus on the chest models, we find spine models that were prepared with different levels of detail and with various goals. We can distinguish the works depending on which type of parametrization was achieved: geometrical, on the bone 3D models, or kinematic, for the joint connections.

For example, Ceran [15] focused his attention to the geometrical modeling phase, using a simplified version of the vertebrae created with typical solid CAD simple features (*e.g.* extruded and lofted cylinders).

Devedzic et al. [28] presented a human spine model that is geometrically nice to see, but it has only parametric constraints in terms of connection between the vertebrae, which is appropriate only for the teaching and learning purpose of their application about the scoliosis deformity, without any change to the geometrical shapes.

In 2012 the Parametric Human Project [64] was started with the aim of creating a co-operative group of researchers managing solutions for human health, but unfortunately it seems that the project was interrupted in 2017.

Different researchers focused their evaluation only on portions of the spine, the most

interested regions are the lumbar and the cervical ones, because they are the most vulnerable to problems in common people, due to their higher flexibility. It is well known that the lumbar region is the most interesting for ergonomic evaluations, in particular the connection L4-L5 is considered so critical to be embedded in the ergonomic analysis software (*e.g.* Siemens Jack [94]) for the Lower Back Analysis (LBA). While the cervical region is famous to be subjected to the risk of whiplash injury, particularly considering the car accidents [47].

Other works related to the full spine are usually connected to the study of the deformity of the curvatures (scoliosis, lordosis and kyphosis). An example comes from the group of Toronto University [56] that developed different tools for reconstructing an approximated spine model and analyze the curvature.

The most recent improvement of such type of study is represented by the product EOS system, from the homonymous company. The machine produces good quality biplanar X-ray images (antero-posterior and latero-lateral) with a lower dosage of X-rays in respect to standard machines. The system comprises also a software that allows to reconstruct a 3D model of the spine of the single patient by selecting some reference points directly on the 2 planar images. The advantage for the medical staff is to have a 3D visualization of the patient's anatomy instead of abstracting the 3D information from the 2D projections.

All these works represent partial solutions for problems focused only on the spine (without considering the pelvis or the ribcage) or precise districts (*e.g.* the lumbar region of the spine). For this reason the result of the present work can be considered as a multipurpose solution, with models that can cover multiple fields: visualization, spine curvature analysis and numerical simulation (Finite Element Method - FEM). Since the project focuses on the design modeling and interaction analysis of scoliosis back braces, I tried to fill the missing gap regarding the absence of the ribcage in the 3D reconstruction of the EOS system while limiting the area of interest from the humeri to the femuri, without reaching the complexity of the models developed by the University of British Columbia, in their toolkit ArtiSynth for the case of *Coupled Jaw-Tongue-Hyoid Model* [59] [76].

3.3 Requirements

The 3D skeleton model should consider the following requirements with goal of the different applications.

- *Easiness of use*: the model should be easily morphed also by non-experts of CAD modeling tools, such as technicians and doctors.

- *Visual reference for sculpting*: the model should be a good indication for the modeling of the brace, for example to consider the shape variation in respect to soft and hard tissues.

- *Capability to export statistics*: the values of the model deformations should be saved for possible comparisons over time, for example to evaluate the correction progress.

- *Simulation-ready*: the geometry should be appropriate for running numerical simulations, without having topological errors or creating new limitations in processing.

3.4   3D skeleton model development

The model of the skin, acquired with the 3D scanners analyzed in the previous chapter, enables the technicians to model already the brace model on the computer. The skin model gives only an indication of the deformation applied to the patient's external shape, for this reason I propose the use of a patient specific 3D model of the skeleton with the goal of improving the virtual modeling phase of the scoliosis braces, by considering also the interaction with the patient's skeleton. Such model should consider not only the spine, but also the pelvis for the anchorage and the rib-cage for the transmission of the corrective forces.

At present, in order to obtain such model, a particular type of medical examination is required, the CT scan or, alternatively, the MRI. These exams produce a series of slices of the patient that can be stacked together to recreate the 3D volume. In order to obtain a 3D model from such medical images, known as Digital Imaging and Communications in Medicine (DICOM) files, we need to perform a segmentation. This process consists in setting a threshold for the gray scale (Hounsfield unit scale) values of the images to define the portion of the images that are part of the desired volume.

In terms of quality of the reconstruction of the bones, the CT scan is considered to be the most appropriate. The main the issue of reconstructing the skeleton model from CT scans is related to the amount of radiation. Indeed, it is usually hard to have this kind of medical examination for each patient, mainly if the patient is a child. Indeed, the scoliotic patients usually undergo only periodical bi-planar X-ray imaging examination, except for particular cases, *i.e.* accidents, extreme pathologies or before a surgery. On the other hand, the MRI is considered to be a non-invasive procedure, but it has other disadvantages related to time, costs and posture of the patient, who has to lie on the back for about half an hour.

We can state that the ideal situation would be to acquire simultaneously both the internal organs and the skin model with the patient standing straight. This posture reflects better the condition of use of common daily braces and is thus considered to be the best input for modeling a brace. Such approach is not feasible with the CT scans and the MRI for the above-mentioned time constraints.

Nevertheless, the EOS system [31] is already capable to acquire bi-planar X-ray images in the standing position, also with a low-dosage technology that best suits repeated examinations for the common scoliosis follow-up. The integrated software let the technician to visualize a 3D model of the spine (only the vertebrae) for qualitative analysis. The idea was thus to develop a parametric skeleton model that could be easily morphed on the information of the x-ray images to obtain an approximated patient-specific model. Moreover, a 3D scanner should be integrated in such system for obtaining simultaneously also the 3D external model of the skin.

In order to develop the pseudo-parametric skeleton model described in the following paragraphs, the starting point was a finely segmented 3D model, reconstructed from medical images by the group of Clinical Anatomy at Stanford University, for another

project in 2013. The purpose of that project was of teaching to their students the real human anatomy in the class, before passing to the analysis of cadavers in the dissection lab. However, I could adjust that patient-specific reconstructed model to create an ideally symmetric parametric skeleton model to be quickly morphed on the basis of the biplanar X-ray images.

3.4.1 Organ models from medical images

As an example to explain the process that was executed, let us first consider a simplified case performed in the open-source software 3D Slicer [33]. Here, we can apply a threshold filter to all the 2D images and connect the different segmented areas to create the final volume. Ideally, we can imagine that each pixel of the single 2D images that satisfies the threshold constraint is extruded till the following slice. The basic shape is then a volume composed of small rectangular prisms, but it can be then smoothly remeshed to obtain a more realistic surface.
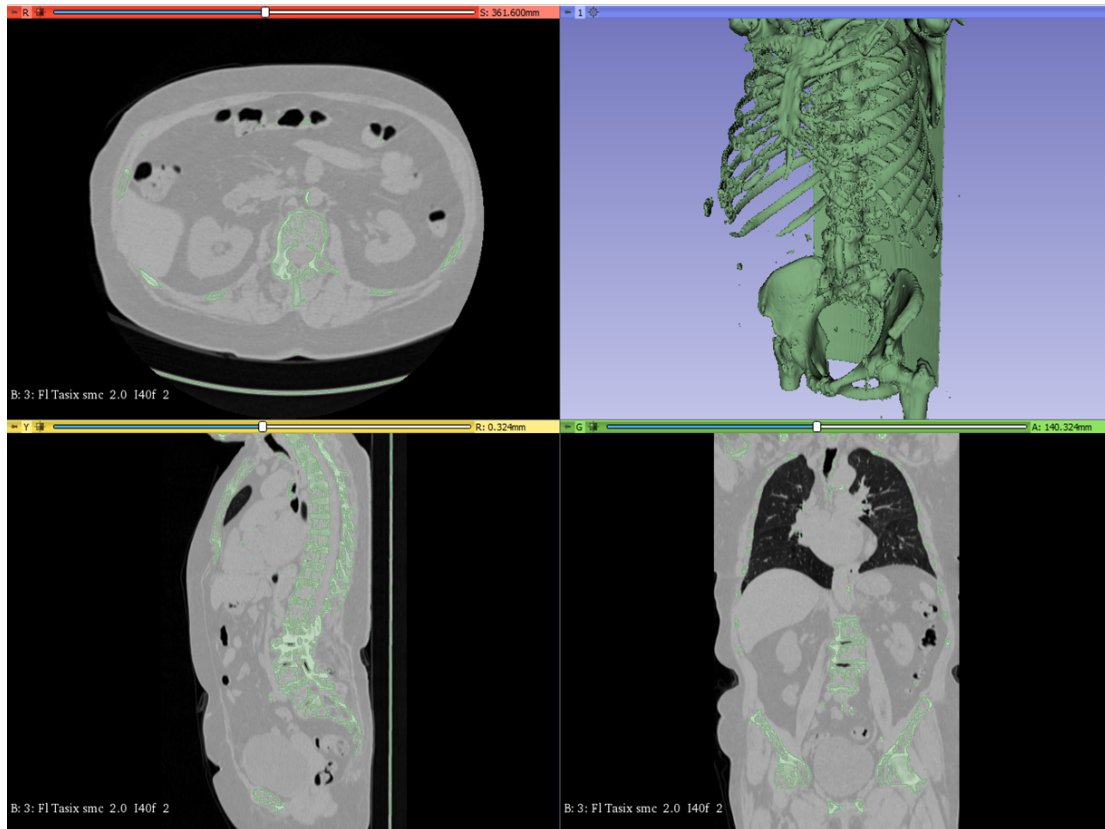
Figure 3.12: *Reconstruction of the internal organs 3D model (top right view) from a CT scan (other views) applying a threshold filter (green selection in the views).*

Figure **[3.12]** illustrates the first result of a segmentation example of bones obtained by applying a threshold value equal to 100 for the Hounsfield Units. Depending on the type of CT scan (machine brand and model, presence of contrast, etc.) we could obtain different results changing this threshold level [83]. In this case, the CT scan was segmented with the intensity threshold approach in its basic form, *i.e.* visual selection of the value by the operator. Moreover, we can notice that, with such approach, the

hard tissues are segmented all together, without distinction for the component of the sliding bed in respect to the bones. Moreover, we can notice that all the vertebrae are connected one each other and also the ribs seems to be fused.

There exist also other techniques that are semi-automatic. For example, the *grow from seeds* approach that lets the operator paint only a set of seeds for the different tissues on the 2D images and then performs the evaluation of how the regions of the highlighted tissues are distributed in the 3D volume.

After cleaning the model, it is possible to isolate the skeleton that can be then imported in the other modeling software. Figure **3.13** depicts the example of the previous model once it was cleaned and it is ready for being used in a software like Meshmixer. In a similar way, we extracted also the skin model from the medical images that, thanks to the same original data, is already aligned with the skeleton. From the gray scale images in Figure **[3.12]**, we can understand that the back part will result flat because of the patient laying on the bed. Moreover, we have to take care about the dimensions of the patient and the setting of the volume of the machine not to miss any portion of the acquisition.
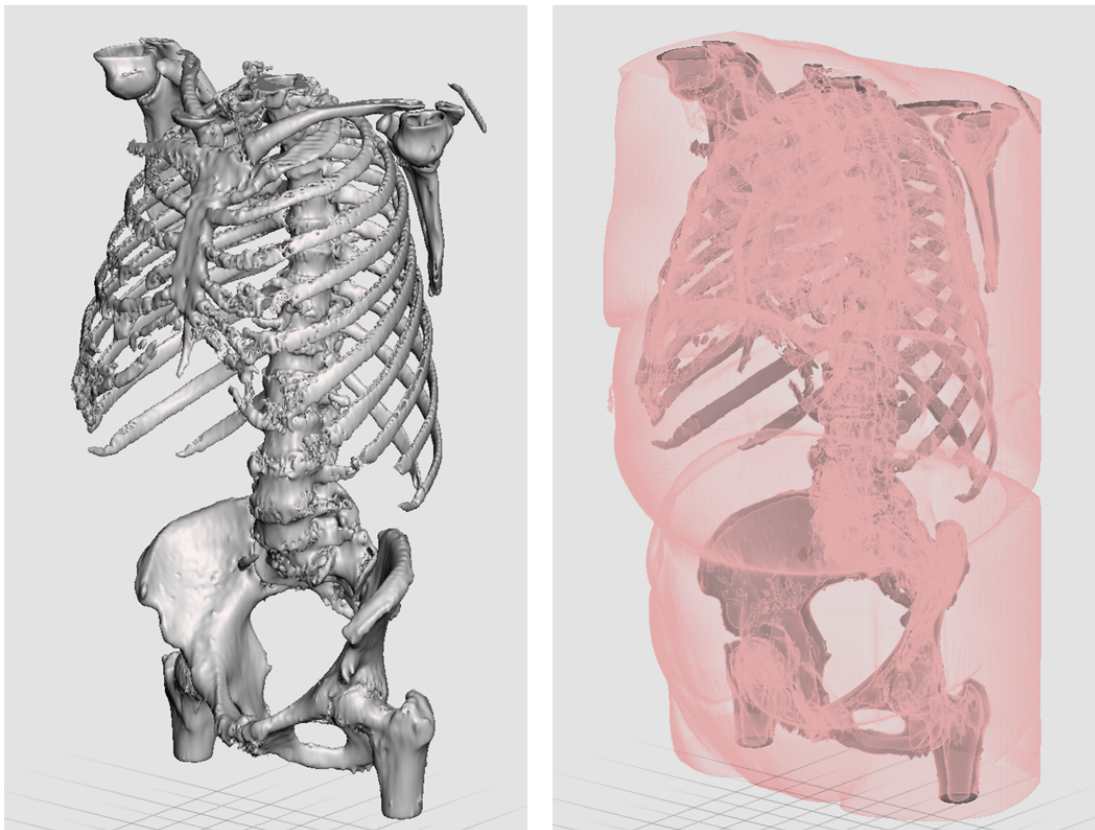
Figure 3.13: *Segmented skeleton model (left) and aligned skin model segmented from the same medical examination over the skeleton (right).*

In case we had the CT scan of our scoliotic patient and we wanted to follow the segmentation approach for obtaining the 3D skeleton model and use it as a reference for modeling, we would have to align the skin model acquired by 3D scanning. This operation can be accomplished by partially aligning the skin models (3D scan and seg-

mented) considering only the front part. As mentioned, the CT scan model of the skin is flat on the back because of the bed and it cannot be considered for shaping the brace. An alternative approach could contemplate the use of markers placed in anatomical reference points, for example iliac spines and xiphoid process, as it is done in other biomedical fields (*i.e.* for bio-mechanical analyses), in order to perform the relative alignment.

The problem of aligning the organ models of the medical images with the 3D scanned model could be simpler than considering only the 2 planar X-ray images, because we could also segment the skin from the same CT scan or MRI and keep it as a partial reference. Furthermore, the CT scan and the MRI are usually performed over a long period (20-40 minutes) and the patient has to lay on the mobile rigid table of the machine. As a result, not only is the reconstructed skin model always flattened on the back, but the spine is also stretched and has a different configuration in respect to the standing posture.

On the contrary, the 3D scan of the skin is always performed with the patient standing straight in order to evaluate the proper anatomical shape. This difference in the patient's posture can also lead to a reconstruction of the skeleton that does not match with the skin model acquired with the 3D scanner.

3.4.2 Parametric skeleton model

In order to create a generic reference model, I started modifying the anatomical 3D models reconstructed by segmenting a CT scan, obtained from a previous work of the Clinical Anatomy division at Stanford University. This model was already finely segmented bone by bone, but further modifications were needed due to the fact that the 3D parts had been created based on a real patient. Thus, the spine was not straight vertical in the frontal plane and in general the entire model was not symmetrical. As we can notice in the left side of Figure 3.15, the original spine was flattened in the lumbar region, while it presented a pronounced kyphosis in the top thoracic region, with a consequent lordosis of the cervical vertebrae. Moreover, it had to be re-adapted also in the lateral view in order to follow the ideal physiological curve depicted in Figure 3.14, which presents the normal sequence lumbar lordosis, thoracic kyphosis and cervical lordosis.

The programs that were used for applying the shape and position changes to the body model are: Autodesk Maya (version 2018) and Autodesk Meshmixer (version 3.5.474). The first is commonly known for creating animations and rendering for video-games. The second is a good mesh modeler (sculpting tool for tessellated models in format STL/OBJ) which can be used for creating organic shapes, mesh cleaning and repairing, and also for preparing the models for the 3D printers.

Alignment

To perform the required changes, a first approximate positioning phase was computed in Autodesk Maya. The single models of the vertebrae, pelvic girdle (sacrum, coccyx and hips), rib cage (ribs, sternum and rib cartilages), shoulder girdle (scapulae, clavicles and humeri), and femurs were moved in the front view according to the symmetric plane (sagittal plane). At the same time, the models were translated in the lateral view following the hypothetical physiological curve, depicted in Figure 3.14. Figure 3.15 shows the initial model on the left side and the final configuration on the right.
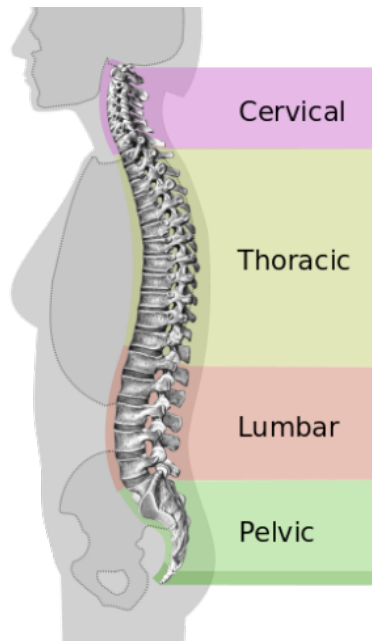
Figure 3.14: *Ideal physiological curve with identification of the regions of interest.*
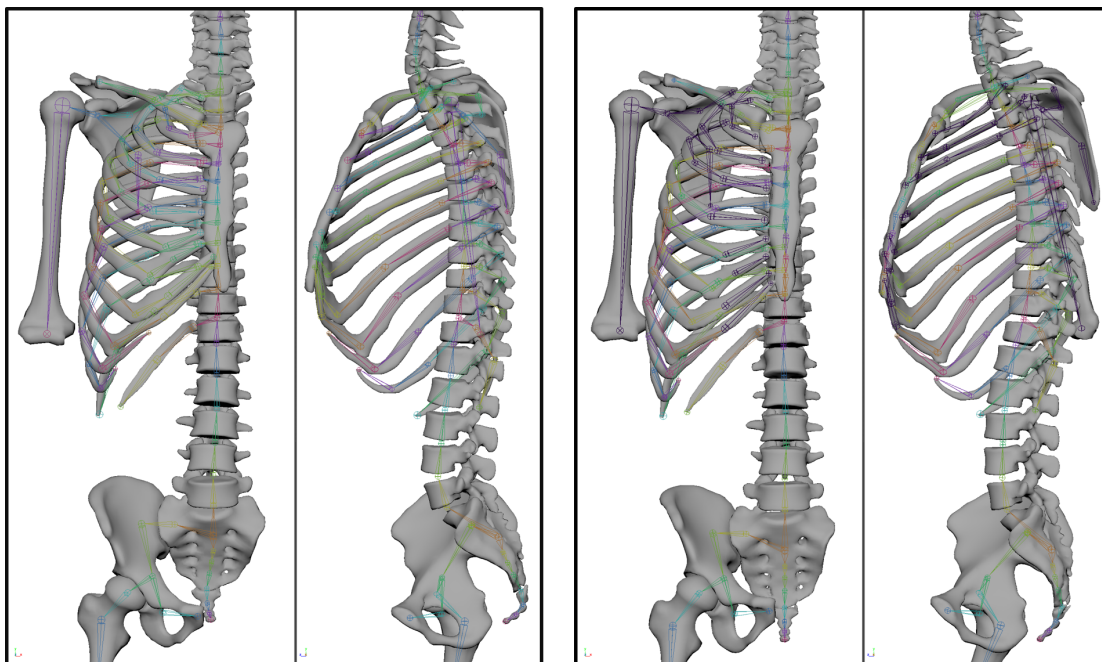
Figure 3.15: *Initial model (left) and the final aligned model (right). Front and left views.*

Symmetrization

Once the single models were put in the desired position (right side of Figure 3.15), they were symmetrized in respect to the sagittal plane using the mirror command. For this reason, the left side bones (femurs, hip, ribs and rib cartilages, and shoulder girdle) were removed completely, and they were replaced by the symmetrical copy of the right side. On the other hand, all the vertebrae, the sternum, the sacrum and the coccyx were

mirrored in respect to the sagittal plane. This operation was computed in Maya for ease of remaining with the same software but an equivalent command exists also for Meshmixer.
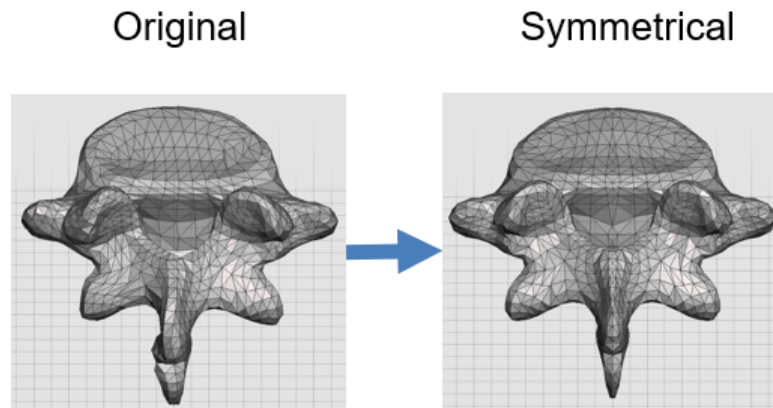
Figure 3.16: *Original model (left) and the resulting symmetrical model (right) in respect to the sagittal plane.*

Cleaning and remeshing

All the mirrored models were then exported from Maya and imported in Meshmixer to be manually cleaned in the midplane region. Both the remeshing and the smoothing operations were performed to remove the singularities created by the mirroring command. For example, the tiny and distorted triangles in Figure 3.17 that appeared were then merged in larger and more consistent triangles.
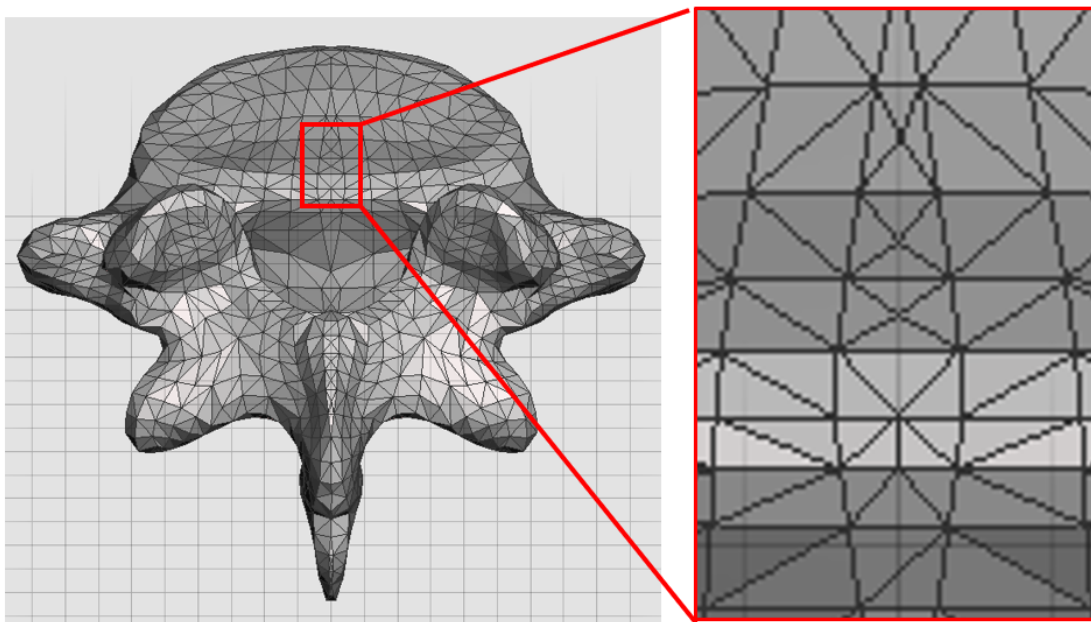
Figure 3.17: *Detail (right) of the fine and distorted triangles of a vertebra model (left) to be remeshed and cleaned.*

3.4.3   First version of the skeleton model

At this point, the first version of the chest model was ready for the creation of the kinematic chain. All the single parts were re-imported in Maya and a set of joints were created. The initial solution presented a joint for each part. Figure 3.18 shows the kinematic chain of the skeleton model (3D geometry in blue), with different colors for each joint and the connecting links. To be coherent with the idea of having a symmetrical model, in this phase the left side joints were created as a mirrored version of the right side.
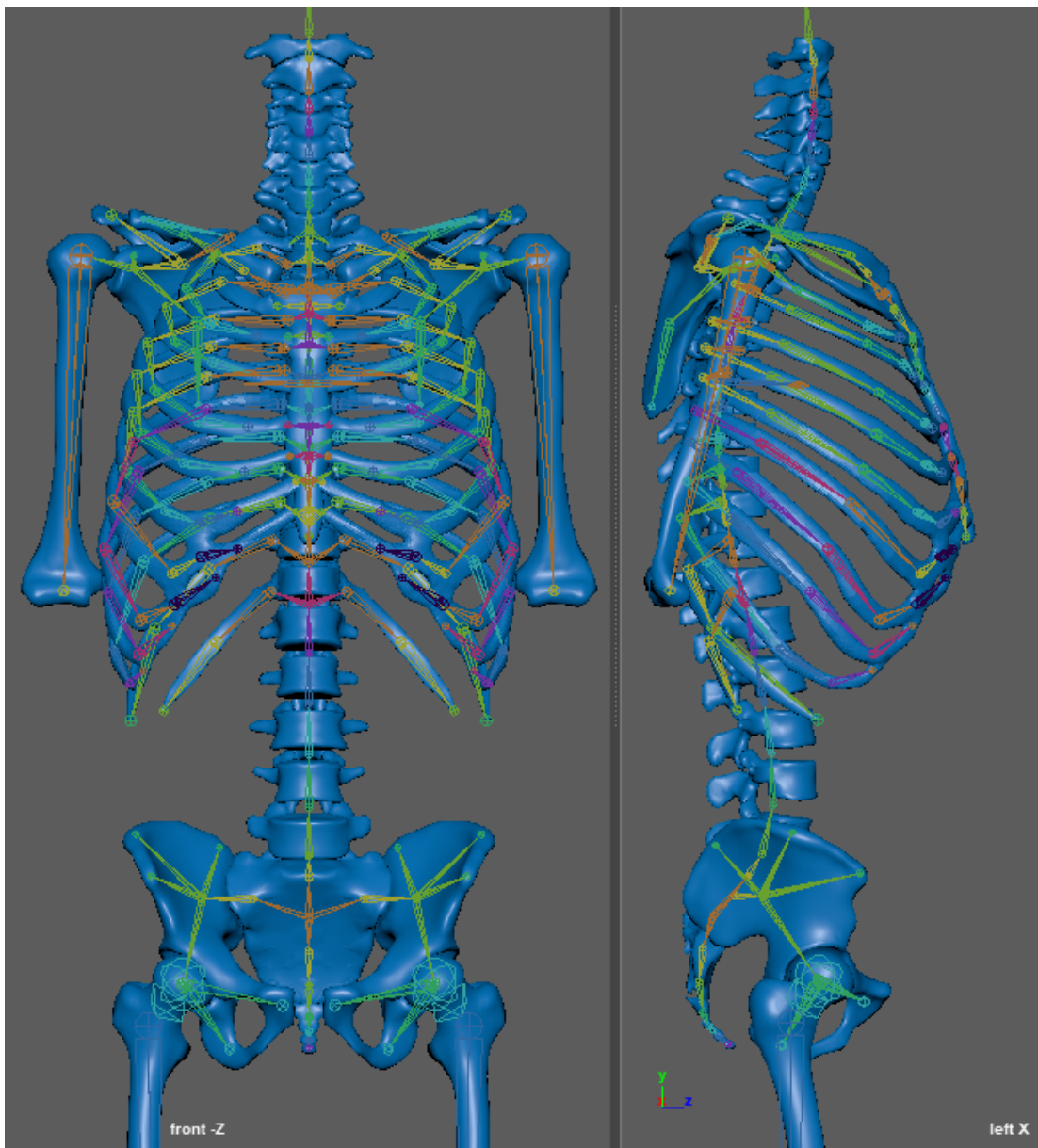
Figure 3.18: *Frontal (left) and lateral (right) of the initial configuration for the standard skeleton model with its kinematic chain.*

Skin Weight

Every single bone was then assigned to the respective joint with an initial flat skin weight. The *skin weight* indicates the influence that the joint has on the deformation of the 3D model. In Maya, it is represented by a color map from black (no influence) to white (100% of influence) and it can be assigned automatically or "painted" manually on the models using a virtual brush. The flat skin weight means that each bone is bound only to the relative joint and for this reason they are white only for the single respective joint. The center column of Figure 3.19 illustrates the flat skin weight for a rib, which deforms only according to the first joint that is connected to the spine.

On the contrary, as presented later for a different model version, if the part is assigned to multiple joints, the skin weight can be smoothly painted with a gray gradient. Consequently, the part will deform in the different regions according to the movements of the bound joints. The right images of Figure 3.19 show the effect of a smooth skin weight deforming the rig also according to other joints.
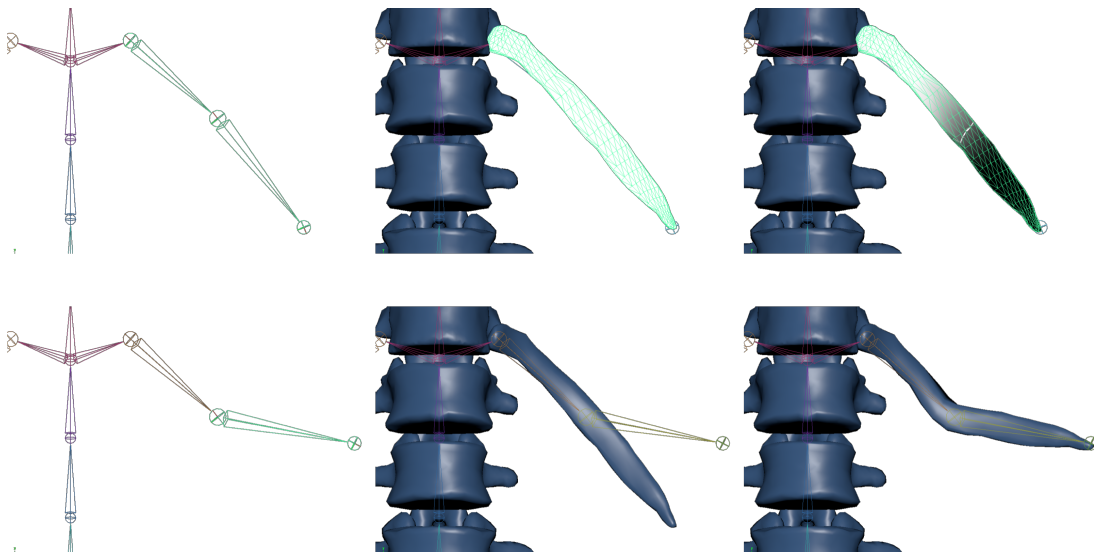
Figure 3.19: *Comparative example of flat and smooth skin weights for a rib. The left column contains the kinematic chain, the central column depicts the rib with flat skin weight and the right one shows the smooth skin example. In the first row the rib is undeformed, while in the second row the kinematic chain is modified in the second joint of the rib, affecting only the model with the smooth skin weight.*

It has to be noticed the particular type of connection created for the ribs in respect to the spine. This version of the model replicates the anatomical chain, where the base joint of the ribs is attached to the corresponding vertebra, while the end of the connection is ideally located in the sternum. This is visible in Figure 3.18 thanks to the direction of the pyramid shapes of the links connecting the joints, where the base is the parent joint and the peak is the apex represents the child joint.

In the software Maya, unfortunately, it is possible to create only open kinematic chains, but the ribs should be considered as closed chains that connect the vertebrae to the sternum through the relative cartilages. For this reason, other configurations of the kinematic chains were tested.

3.4.4 Second version of the rigged model

This section first presents some changes applied to the geometry and then the new assembled version in Maya.

Pelvis and ribs simplification

The model of the pelvic girdle (sacrum, coccyx and hip bones) was simplified and the different parts were fused together. The reason of such choice is double: on a hand, we can use the smoothed variable skin weights to deform the single bone in the different regions and, on the other hand, I wanted to avoid the interference effects that easily appear, for example when moving the hip bones.

The first factor is important when we want to better adapt the models to the patient's particular anatomy, considering the possible asymmetries and deformations that appear in the medical images, mainly visible on the ribcage. The second consideration instead regards the limited accuracy of the final model with unreal interference. This could create a misunderstandings for the software when the models are imported in a virtual reality environment, because of the overlaps and it could become even critical if considering the setup of numerical simulations.

Moreover, as depicted in Figure 3.20, the sacral foramina were closed, for sake of simplicity, and the mesh was refined, mainly in the detailed region of the coccyx to better follow the possible deformations of the subjective shape.
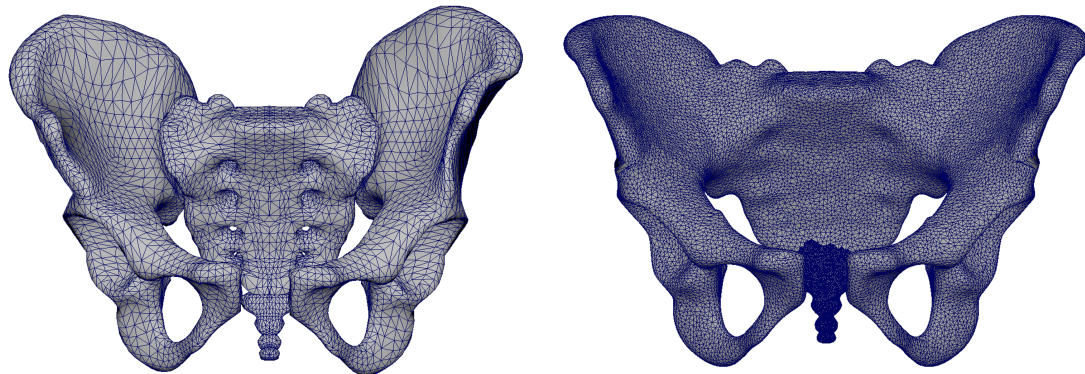
Figure 3.20: *Simplification of original model presented on the left image by closing the sacral foramina and refining the meshes.*

Also, the ribs have undergone a simplification step. The costal cartilage that connects the ribs to the sternum was already fused together with the relative ribs. But a further approximation consists in the connection of all ribs from 6 to 10. This was performed for the small proximity that would have caused other possible overlaps of geometries.

NURBS reconstruction

The tessellated models (STL/OBJ) are the standard for Virtual and Augmented Reality applications, where the main purpose is to visualize the geometry. Thanks to particular rendering settings, the flat triangles (comparable to a first order formulation for triangular mesh in the FEM) can be also visualized as smoothed surfaces to improve the 3D

visualization without acting on the real geometry, as depicted in Figure 3.21. This type of model is currently the standard not only in research but also in the video-gaming industry and in the animation movies.
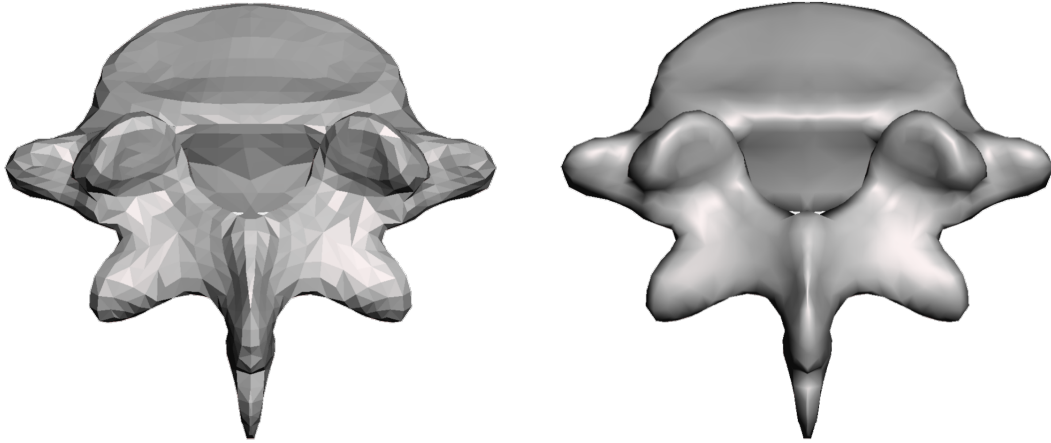
Figure 3.21: *Same tessellated model of the lumbar vertebra number 5, without and with the smooth rendering filter.*

Another type of surface model is instead available in the design and engineering fields, which is the NURBS. This is a mathematical model that is typically used in solid and surface CAD (computer aided design) modeling software for generating finely controlled geometries. The NURBS are like a matrix of splines that, connected together, create the 3D surface, which is controlled with a set number of points, depending on the order of the curves we set. Figure 3.22 exemplifies a 2-D spline and the respective 3-D extrusion in NURBS surface. By moving these control points, the curvature and the shape of the surface patch can be modified. The formulation allows smooth connections resulting in a very organic geometry, typical of the human body parts.
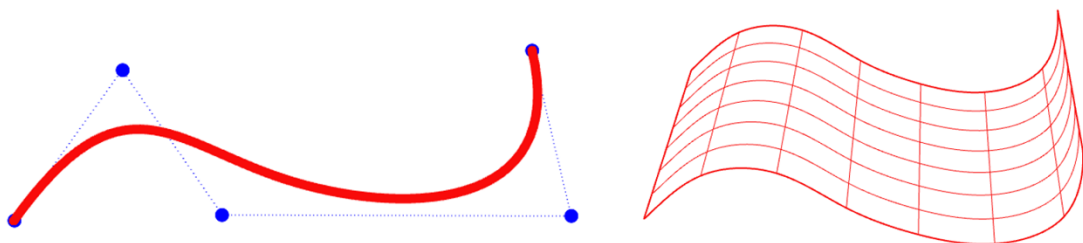
Figure 3.22: *Example of a spline curve with the relative control point and a NURBS surface, as generated by the software Rhinoceros.*

The main advantage of the NURBS models regards the possibility to be later approximated with different mesh sizes as desired or required by the application. For example in visualization we can use a distorted mesh with non uniform size depending on the details, while for simulations it is usually better to have a limited or gradual variation in the dimensions to avoid deformed elements (large skewness) and high gradients. In particular, the finite elements for simulations can be easily applied by the numerical

simulation software when the input model is a NURBS model, being able to vary more freely the mesh dimensions and the mesh type. In case the input is an already meshed model, for example the STL derived from 3D scanning, the software cannot change the position of the vertices and will be able only to add new nodes. Moreover, an important parameter that is always controlled by the mesh generator is the aspect ratio of the elements, which defines the quality of the mesh.

The step of conversion from the previous tessellated models were attempted with the following software packages: SpaceClaim in ANSYS 19.2, Dassault Catia v5 and Geomagic Studio 2012. The first offers the manual approximation with the command "Skin Surface", where the patches are created one after the other, by manually drawing the edges of the patches and by connecting the new edges to the already created patches. Catia v5 offers the command "Quick Surface" that created automatically the patches on the tessellated model with a special algorithm that analyzed the shape of the model. Geomagic has both an automatic reconstruction and a manual sequence of steps. With the manual approach, the whole layout of the patches has to be created in order to then generate the surface, thus allowing more control on the type of approximation.

After a first test of the different software, the conversion of all the parts was performed with the last software, due to its ease of use and quality of results in terms of stability when passing to other software. The models were initially converted by using the auto-patch layout mode and then manually applying a reduced number of patches based on the details. Figure 3.23 depicts a first comparison of the results on a single vertebra showing the limits of both approaches. On the left side, there are the polygonal models, which present the flat triangles, in the common format OBJ. On the right side of the figure it is possible to compare the automatic reconstruction of the patch layout with a fast manual definition of a limited number of patches. The first approach results in a better level of detail, but becomes too heavy for being applied to all the bones. The second approach uses a limited number of patches (about $1/10$ of the first) but reduces the quality in sharp regions, as highlighted with the red circles.

The picture reports also the file size for a direct comparison of the different models, and in particular it has to be noticed that the NURBS automatic and manual models are respectively about 25 and 5 time larger than the input symmetric OBJ model.

Subsequently, the initial tessellated models were remeshed with a finer mesh size and slightly smoothed in Autodesk Meshmixer. This step was added to limit the presence of spikes in the reconstructed NURBS model, in correspondence of the flat triangles edges.

The manual patch layout was then applied, part by part, considering the details of the model and the final approximation level. This was evaluated by analyzing the deviation of the NURBS model in respect to the input OBJ model, as shown in Figure 3.24, similarly to what was performed for comparing the 3D scanners and described in Chapter 2. The procedure was iterative and the maximum acceptable deviation was set to 1.5 mm, considering that this appears in the spiky regions while the average deviation was at least one order of magnitude smaller.

The final model of the lumbar vertebra number 5, depicted in Figure 3.24, had 68 patches with a file size equal to 1690 kB. This means that manually taking care of the spiky regions, with additional smaller patches, can produce a very good approximation without reaching the weight of the auto-surfaced models.
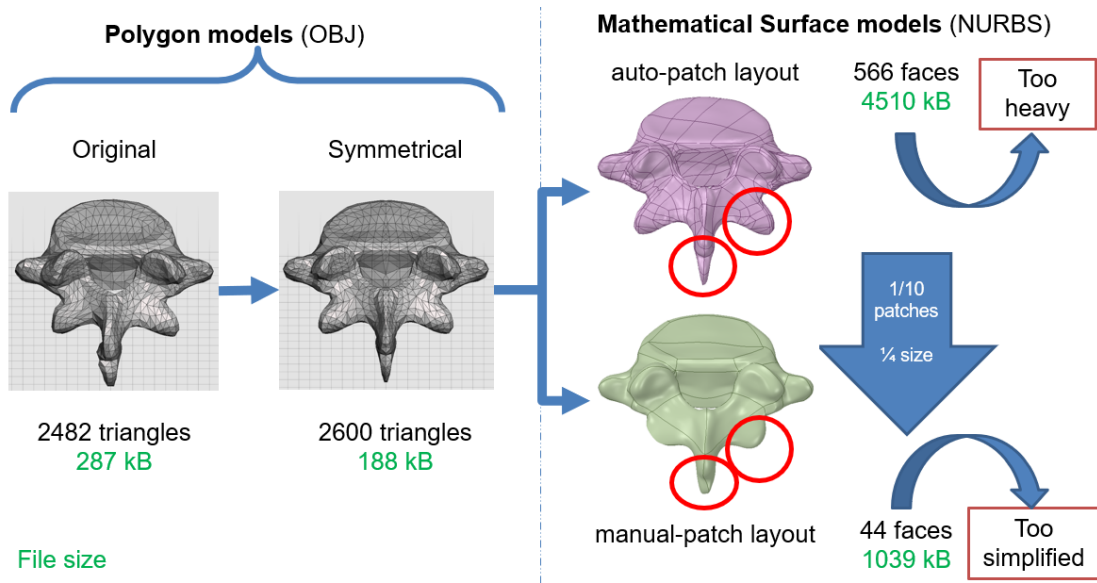
Figure 3.23: *First test of NURBS reconstruction for proper settings decision.*
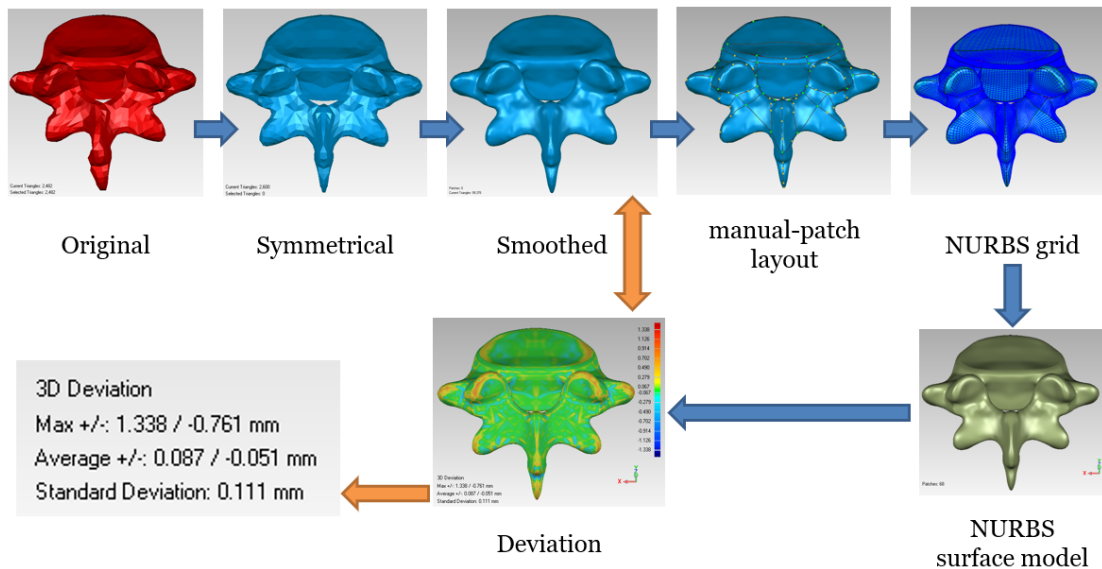
Figure 3.24: *Example of the sequence of steps executed for passing from the initial patient-specific model to the symmetrical NURBS approximation.*

Model definition

In spite of the bones being usually considered to be rigid due to the comparison with the surrounding softer tissues, our goal is to approximate the patient's anatomy. Therefore, we need to be able to deform also the shape of the single parts. For this reason, after the initial solution that allowed scaling the whole parts in the 3 directions (local x, y and z of each joint), the pelvis and the ribs were rigged and skinned with more than one joint per part. This enabled having more freedom in terms of modeling and personalization of the model.

The smooth skin weights were firstly set to be automatically applied by Maya, with

the *Bind Skin Option* set to *Distance*. Afterwards, little manual adjustment was assigned to the transition zones for smoothing the influence of near joints and for removing the influence of those joints related only to other ribs. The NURBS models were added in this version, as a different layer but with equal connections to the same kinematic chain and with the similar skin weights of the tessellated models. This meant that acting on the kinematic chain in order to modify the translations, the rotations and the scales, both the NURBS and the tessellated skeleton models were behaving in a comparable way.

3.4.5   Final version of the rigged model

When using the second version of the model, some problems appeared on the NURBS models due to the fact that the skin weights were manually smoothed to provide a better deformation. The automatic painting did not show a gradual variation of the weights, so that the obtainable deformation was "stepped". Moreover, the manual change created a non-continuity problem when passing from one patch to the other of the same model, with a consequent detachment of the edges in the moment of morphing.

Thus, the skin weights were set back to uniform (flat / flooded) for all the vertebrae and ribs in relation to a single joint, simplifying the second version and the relative test on the deformations. The same skin weights were applied again to both the tessellated model and to the NURBS one, in the same way. Hence, the user can act on the chain visualizing the tessellated model, which is lighter, and in parallel the exact same deformations are applied to the NURBS model, which can be left hidden in computers with limited graphic processing power.

Moreover, in this final version, the main change regarded the structure of the kinematic chain for the rib cage. The ribs were connected to the sternum that in turn was associated to the first thoracic vertebra. This meant that the ribs were not connected the respective vertebrae, but allowed to maintain a better connection between ribs and sternum, which appeared to be more critical in the other versions.

Figure 3.25 shows and example of the manual control that can be quickly performed acting on the joints. The user can select the joint that controls a single vertebra to translate, rotate and scale it. The operation can be performed quickly by moving directly the manipulators in the three directions X, Y and Z. A finer control can be obtained by inserting precise values on the side menu. As depicted by the figure, the children joints will move with the parent in order to maintain the relative position, without being directly affected by the scaling. The same applies to the models that are bound to the joints.

3.4.6   Test with bi-planar X-ray images

The different versions of the model were tested during the development phases with a low resolution set of bi-planar X-ray images, which were taken from a previous work that presented the EOS system [31]. These tests were crucial for deciding the best approach and guided the changes applied to the presented versions.

The final version of the model was then tested on a high resolution digital set of X-ray images, reported in Figure 3.26. Because of the use of a traditional machine for the acquisition, the operator required the patient to change the position of the arms
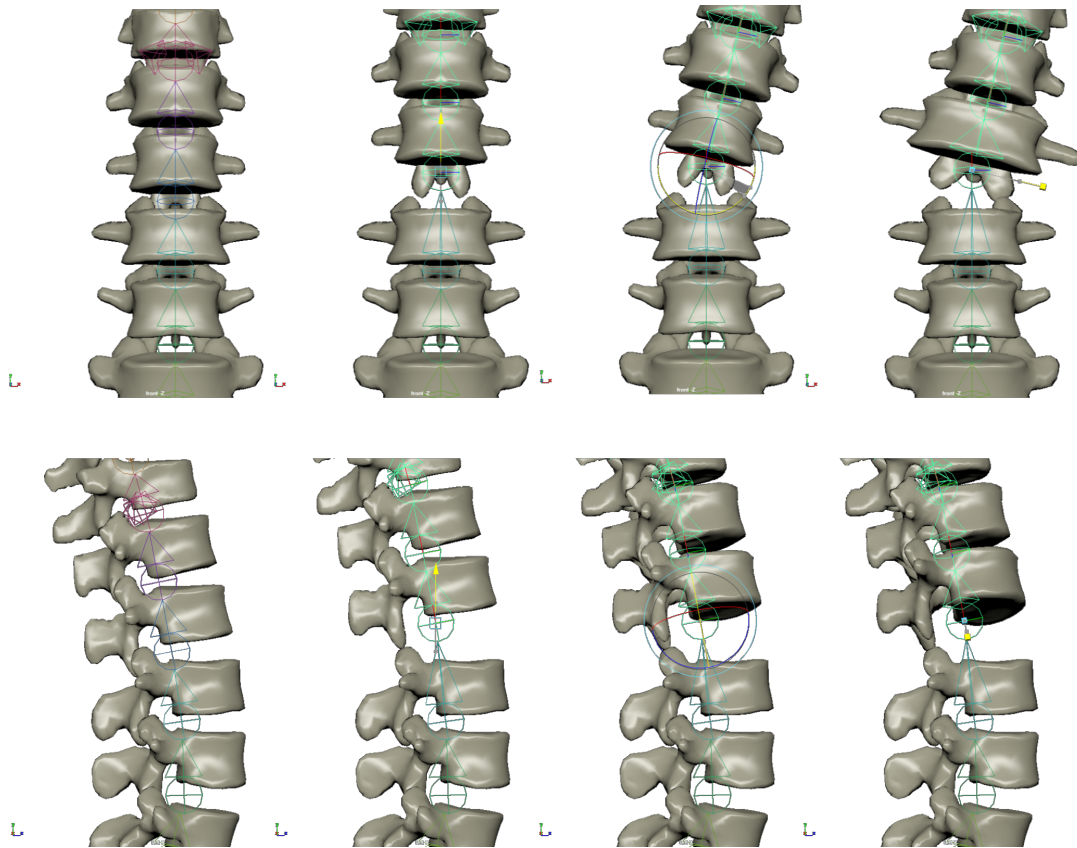
Figure 3.25: *Basic commands to control the skeleton model acting on the selected joint: translation, rotation and scaling, respectively in the second, third and forth columns. The first column represents the undeformed model, the top row shows the front view while the bottom row reports the right view.*

when acquiring the frontal and the lateral images. This could have brought to another approximation in the morphing phase, but in the future, the ideal machine could be similar to the EOS system, allowing to acquire both images in the same moment, without introducing posture changes.

In any case, the X-ray images were added to the scene keeping the correct relative alignment in height and with the same scale. The frontal X-ray is then locked parallel to the frontal plane and can translate in the perpendicular direction only, *i.e.* front and back. Similarly, the lateral X-ray is positioned on the lateral view and can translate right and left only. The user can thus act on the model by selecting the joints one after the other, preferably following the parent to children order, and adjusting the position, rotation and scale of each.

3.4.7 Python script

An additional feature of the skeleton model developed in Maya was created with a script in Python language. This script enables importing and exporting the numerical values associated to the different joints. In particular, it extracts the 3 translations, rotations and scaling values associated to the morphing of the skeleton for the particular brace.

Thus, exporting this data in a text file permits us to store the information of that patient for further analyses. For example, it is possible to compare the results along
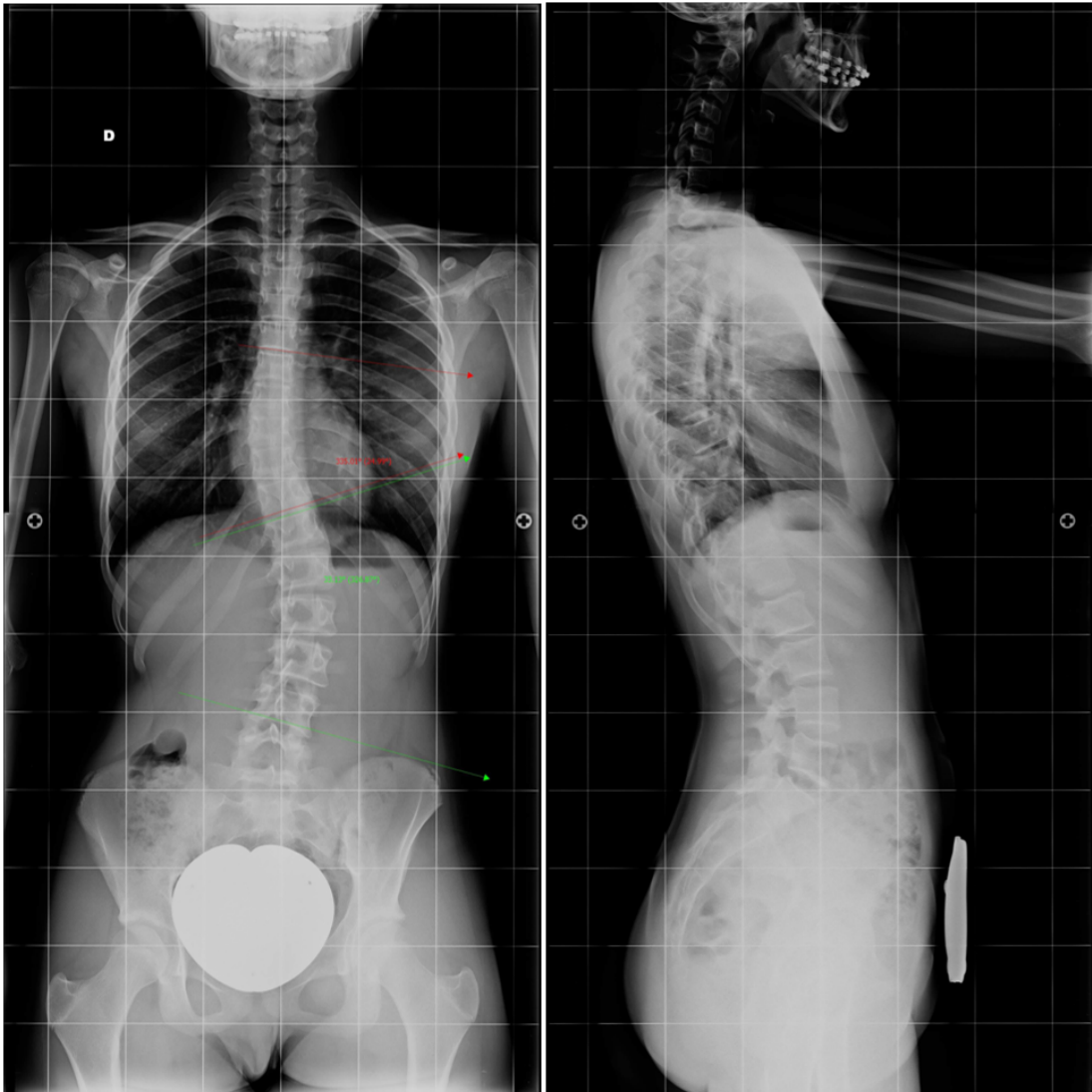
Figure 3.26: *High resolution X-ray images captured with a traditional machine. Evaluation of the scoliotic spine on the left side, reporting the 33° of Cobb angle.*

time to evaluate the bracing treatment or also to compare the same treatment across multiple patients.

Moreover, the import function enables applying the stored set of data to the standard model and re-obtain the patient-specif model. This function was also created with the idea of limiting the amount of storage required for each patient to the size of a short text file.

3.5 Results and discussion

It is possible to notice in Figure 3.27 how the model became completely symmetric with a perfectly vertical spine. Even if any person presents a natural asymmetry, it is important that the connected kinematic chain is correctly aligned to the vertical axis in the initial configuration to perform correctly the comparison of the absolute rotational

deviations to the standard values.
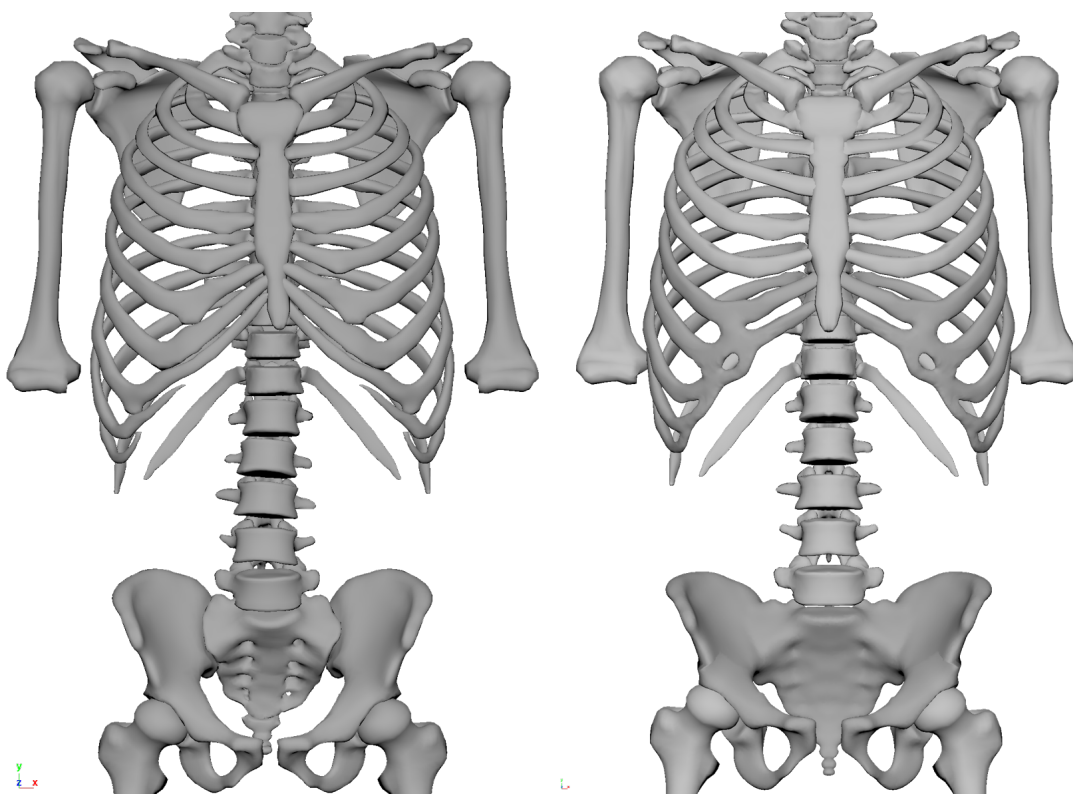
Figure 3.27: *Original model from previous segmentation on the left and final model on the right. The models are both meshed with flat faces but the smooth view is obtained with the rendering settings.*

As shown in Section 3.4.1, the model that is derived from a quick segmentation of the DICOM files usually presents fused vertebrae and ribs. The model that was created in Stanford instead was finely segmented, isolating bone by bone. Using such a model helps understanding better how the single vertebrae are located in the space and open the possibility of adding elastic inter-vertebral discs for the simulations.

3.5.1 File size comparison

Considering the bone models that were preserved in the original model, as reported in Figure 3.27, the final version of the whole model became heavier in terms of file size (30 MB for the polygonal model and 42 MB for the NURBS version, against 22 MB of the original polygonal model), because of the different changes described before. The most relevant factor for the polygonal models regards the finer mesh of some parts, such as the pelvis model depicted in Figure 3.20. Considering the NURBS models, they are heavier because their different type of information contained in the model.

3.5.2 Skin weight comparison

The smooth skin weight enabled to better approximate the patient's anatomy in respect to the flat skin weights, because of the higher flexibility given by the degrees of freedom of the additional joints. Nevertheless, the approximation took much more time

to control the various joints, mainly for the ribs deformation, and it can also bring to topological or geometrical errors, such as self intersecting faces.

With the intent of modeling a virtual brace around the patients body and keep the skeleton model only as a visual reference, the result obtained with the flat skin weights of the final version, reported in Figure 3.28, can be considered sufficient. Analyzing this picture, the reader can notice how the arms were set considering only the frontal view, while, due to the traditional X-ray machine, the patient had to change posture for the lateral projection. A long sequence of the steps necessary to obtain the skeleton model deformed with the use of the X-rays is reported in Appendix A, with the Figures A.4–A.8.

To avoid possible reconstruction errors deriving from this input, the ideal X-ray machine should be similar to the EOS system, which can acquire both images at the same time. Moreover, it could be interesting to embed a 3D scanner in the same acquisition to improve also the skin model alignment to the images, and consequently to the reconstructed internal organs.
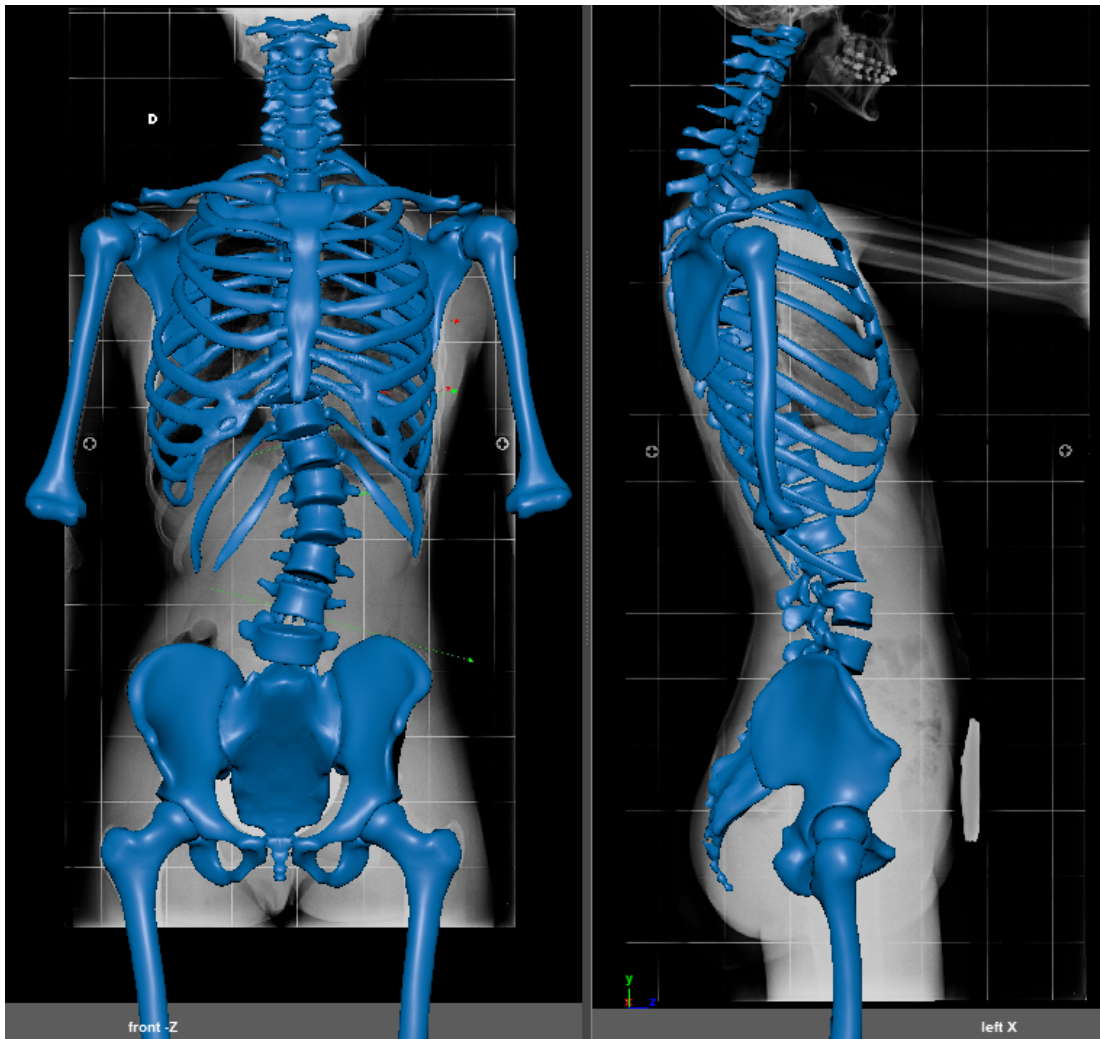
Figure 3.28: *Frontal (left) and lateral (right) views of skeleton model morphed according to patient's X-ray.*

The above mentioned topological errors, derived from the use of smooth skin weights, are even more important when considering the NURBS models for numerical simulations. For the ribs, in particular, the ideal solution could be to have a continuous spline representing the center-line instead of using the presented kinematic chain with a discrete number of joints. The spline curve, thanks to its mathematical formulation, provides a very high continuity even with few points, as depicted in Figure 3.22.

The issues with manually smoothed skin weights should be improved either imposing a clear continuity of the influence values on the corresponding edges of adjacent patches, or improving the automatic skin weight algorithms. These should avoid the detachment of NURBS patches, as happened when working on the second version of the model.

3.5.3 CT segmentation vs proposed model

A comparison test was produced using CT scan of the chest of a patient. At first, the reference 3D model for the skeleton was produced with the fast segmentation approach, presented in Section 3.4.1. Then, the stack of CT scan images was elaborated to obtain the two X-ray views (frontal and lateral) that we usually have with the traditional bi-planar X-ray imaging examination, as shown in Figure 3.29.

Figure 3.29: *Frontal (left) and lateral (right) views obtained from CT scan images.*

These two images and the reference model were imported in Maya. The images

had to be manually aligned to the reference model which was then fixed in position while the planar translations of the images were blocked leaving free the perpendicular direction to the images themselves. In other words the frontal image can shift forward and backward, while the lateral projection can shift right and left. With this, the user is able to translate the pictures and properly use them as a reference across the 3D model.

Figures 3.30 and 3.31 present the comparison of the results obtained using the final version of the model in respect to the reference model. We can notice how the spine and most of the other bones approximate well the patient's anatomy. The largest differences belong to the ribcage. The overall volume is respected, but the shape appears to be different. The problem of using the flat skin weight becomes very visible in the fused ribs 6-10. The shape in the frontal view becomes rounder for ribs 9-10 of the proposed model while the reference model shows a more triangular shape of the ribcage. In the lateral view, it is instead clear how the direction of the ribs varies between the models.
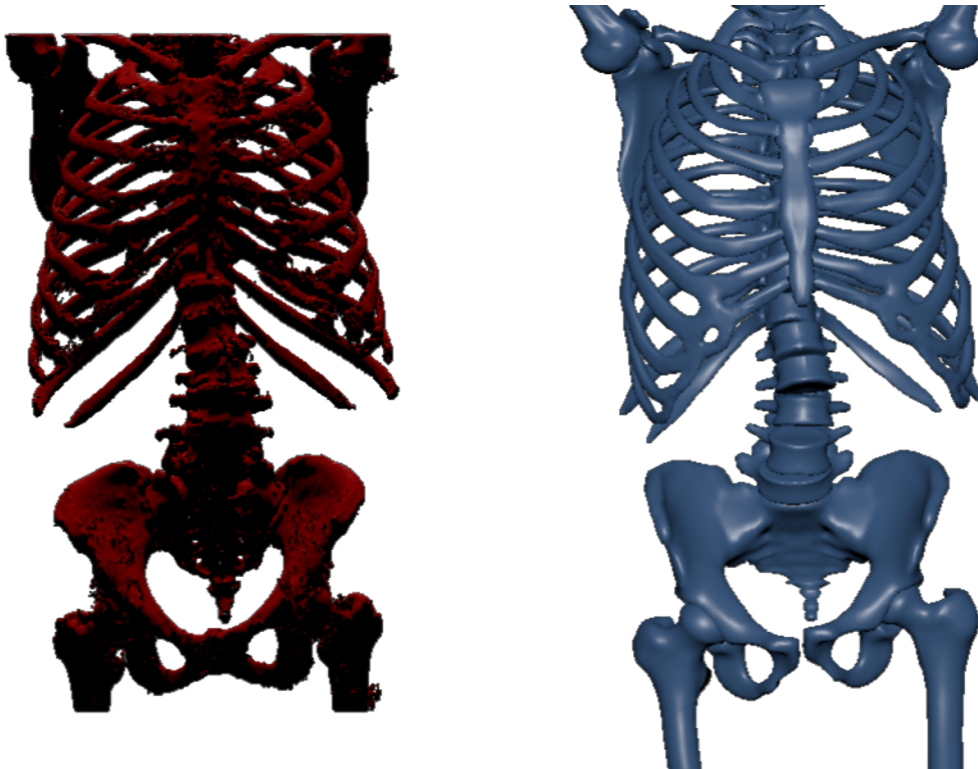
Figure 3.30: *Frontal view of the reference (left) and the final (right) model generated.*

Finally, it is important to highlight that the model reconstructed from CT scan segmentation presents many topological errors that have to be fixed in order to properly run a simulation. Moreover, the file size in STL binary format is equal to 185 MB, while the Maya model, containing both the polygonal model and the NURBS model with the relative kinematic chain, has a file size of 99 MB.

In the case of reconstructing the skeleton model from CT scan segmentation, the database of patients should then provide almost 300 MB of data per patient, considering that the CT scan files would be about 100 MB (if not double for the type of quality). On the contrary, the proposed standard model would take about 100 MB per se, and then each patient would need less than 5 MB for the two images and about 50 kB for
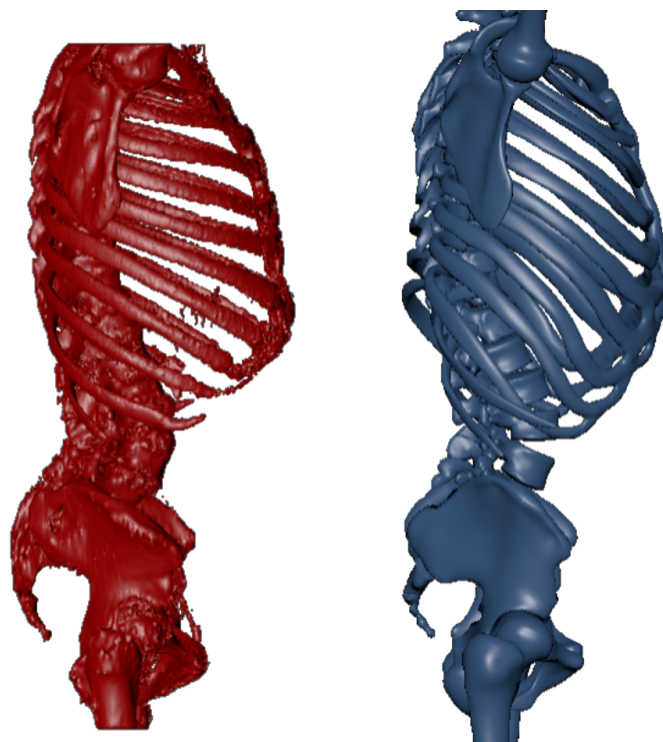
Figure 3.31: *Lateral view of the reference (left) and the final (right) model generated.*

the text file containing all the information of the joints for recreating at any time the patient-specific model.

3.5.4 Final remarks

In general, the final results obtained for the spine approximation can be considered to be appropriate both for the purpose of geometry reconstruction and for the analysis of the spine curvature.

In particular, the proposed model presents the following advantages.

- No need for invasive and expensive exams, such as CT scans or MRI.

- Fast manual reconstruction and easiness of use.

- Very light database of text files, even for having the patient specific model.

Of course, further investigation for improving the adaptability of the model with smooth skin weights and additional joints is required. Moreover, the future work should contemplate the possibility of adding also other deformable tissues, such as lungs, muscles, inter-vertebral discs and relative ligaments.

Static structural analyses

This chapter describes the use of the static structural analyses as a tool for analyzing the interaction between the patient's body and the back brace. Moreover, the simpler case of a wrist orthosis is used for testing the possible use of the Topology Optimization as a future improvement also for the scoliosis braces. The different steps for running properly the simulations are presented highlighting the important settings for this type of non-linear contact analysis.

Two types of simplified static structural simulations are presented with the goal of verifying the quality of the 3D parametric skeleton model presented in Chapter 3. It was indeed developed to be deformed according to the X-ray images of a patient and then used for running a simplified simulation that could give information about the interaction of the designed brace with the patient's body.

The simulations were simplified using linear elastic materials and fixing the skeleton surface in order also to test the feasibility of a fast simulation. The main reason was the pursuit of a simple setting that could allow looping in the modeling phase of the scoliosis brace on the computer. This enables testing the quality of the designed brace shape and verifying the correct position of the loading regions, before 3D printing it.

A set of simulations were developed for the simpler case of a wrist orthosis, as a preliminary study for the integration of the Topology Optimization step.

The choice is justified by the fact that the wrist orthosis can be constrained as a cantilever beam with a roller support, avoiding the interaction with the arm-hand anatomy. Instead, for the scoliosis braces, it would not have be correct to apply ideal loads without considering the patient's particular anatomy.

The simulations on the wrist orthosis were developed as an improvement of the thesis work of Maria Prieto Casado. Part of the work is also based on the previous personal experience of the author during the Master's Degree final work, described in

the thesis [84]. That previous project regarded the analysis of the interaction between the lower limb prosthesis socket and the amputee's residual limb.

The whole work on both back brace and wrist orthosis is considered for two papers currently in preparation: the first for validating the skeleton model presented in the previous chapter, while the second for a case study that contains the whole process from the modeling phase to the 3D printing of an optimized orthosis.

4.1 Background - FEM analysis

The Finite Element Method (FEM) is a numerical technique widely used in different engineering fields for solving complex problem, obtaining a good approximate solution. As the name reveals, the main characteristic of the method is to divide the model in discrete elements, both for space and time. The amount of elements is associated to the accuracy of the solution, in other terms, considering a 3D object, the smaller the elements we use, the closer we are to the real continuous object. Thus, the method applied to complex problems generates equation systems large enough to be unsolvable by hand and require the computational power of good computers. For this reason, in the past years the researchers developed different software for solving these large equation systems.

4.1.1 Types of simulations

Oftentimes, we can find the acronym FEA to categorize the FEM analyses, briefly Finite Element Analysis, and distinguish them from other types of analyses, such as the multi-body dynamics simulations. In the mechanical engineering field, we typically refer to the first type for the analysis of the deformations of the objects when loaded under static conditions, while the multi-body dynamic systems instead analyze the rigid (or flexible) bodies displacement.

The latest versions of FEM software embedded also a particular type of analysis that helps optimizing the material distribution during the design phase, called Topology Optimization (TO). This method is usually connected to a structural analysis in which the loads and the constraints are applied to a large design volume. After solving the first analysis, the software suggests the portion of volume to be kept for structural resistance and the part of volume that can be removed, according to the stress distribution in the material. This allows to obtain a possible optimized solution for a specific product.

4.1.2 Ansys workbench

The software Ansys Workbench is a platform for performing different types of virtual simulations, both in independent and in connected way. From the window named *Toolbox* we can select the different types of analyses, as depicted in Figure 4.1, for example static structural, rigid or explicit dynamics, thermal-electric, fluid-dynamics, etc.

The software is developed for being used both by expert users of simulation tools and by users without a wide background. Indeed, compared to other software (*e.g.* Abaqus), the user interface is simple and the presence of default values or the highlighted missing values allows to run simple simulations without many pre-processing errors. At the same time, it allows to insert also custom command in form of script
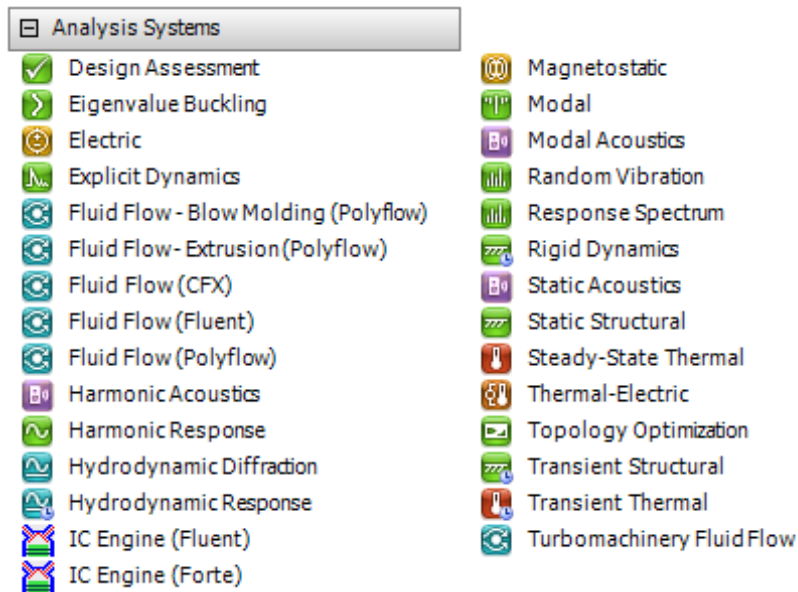
Figure 4.1: *Example of the different numerical simulations available in the software Ansys Workbench, version 19.2.*

in different parts for the generation of the input for the solver, for the setting of the solution and for the visualization of the results.

Available contact types

Before starting with a complex and heavy simulation, it is always useful to test the settings with a simple model. For verifying the available contact options, the case of the Hertz contact of a cylinder acting on a flat surface was considered. The simple example, depicted in Figure 4.2, can be compared to a 2D simplification of the wheel contact on the groud.

   In Ansys Mechanical, which is the module that is activated for performing the Static Structural analysis performed for this thesis, there exist the following five types of contact. The explanation is based on the software that was adopted, but equivalent formulations are usually available in the other software packages, even if different names could be used.

- *Bonded*: it does not allow to have penetration between the model and it does not allow the sliding of faces and edges, once they get in contact they cannot detach anymore.

- *No Separation*: similar to *Bonded*, with the exception that frictionless sliding is allowed between contact faces.

- *Frictionless*: it still does not allow penetration but the surfaces are free to detach and slide without resistance.

- *Rough*: similar to *Frictionless* but no sliding is allowed.

- *Frictional*: it is the most realistic option, allowing the sliding with a resistance
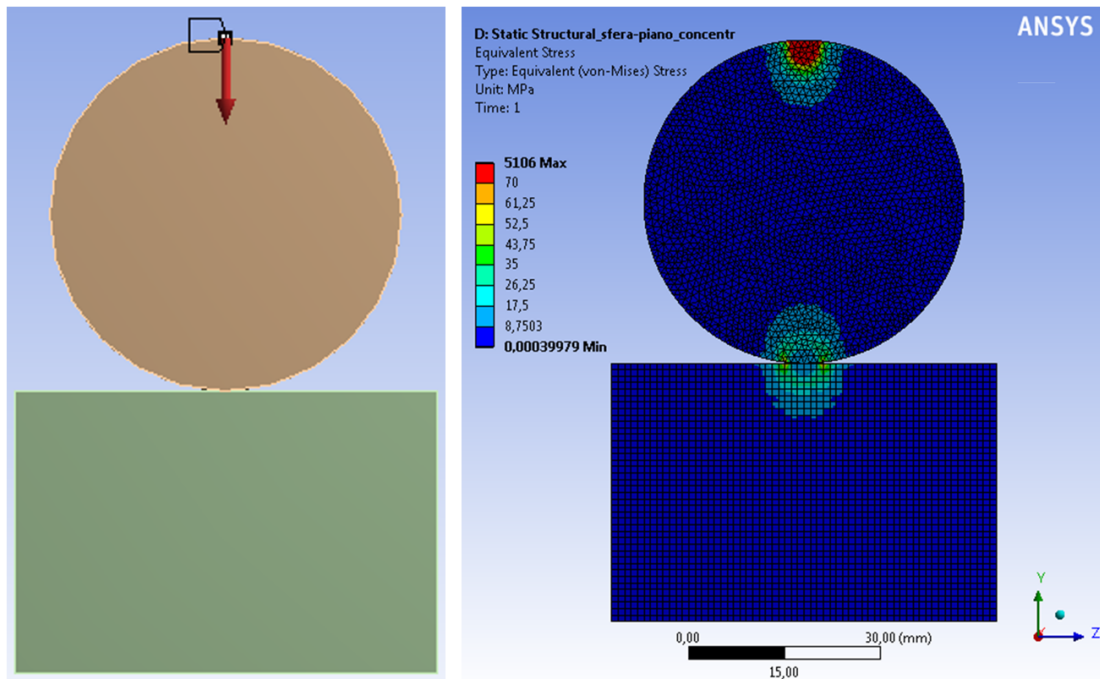
Figure 4.2: *Simulation example of the Hertz contact between a cylinder and the flat ground.*

proportional to the friction coefficient defined by the user, with the possibility of separation without resistance.

A particularity of the first two typologies regards the fact of having a linear formulation, thus requiring a single iteration to reach the solution. These have been probably developed to simulate the various mechanical junctions present in complex assemblies, for which a non linear formulation could be useless if the focus of the analysis is far. Indeed, the *Bonded* type is the setting that the software automatically creates for all the couples of surfaces that identified to be close to each other.

This type of contact can be used for the interaction between the bones and the soft tissues, where also in practice the coupling is fixed. Regarding the brace interaction with the patient's body, it could instead be important to set a *Frictional* contact for allowing a more realistic sliding adjustment of the brace in respect to the skin. Also the *Frictionless* type could be used to represent the interposition of the cotton layer between the skin and the brace that reduces the friction. Nevertheless, from the numerical point of view, it is often better to help the convergence of the solution applying a small friction coefficient, in order to avoid infinite or uncontrolled sliding of the components.

Contact formulations

Proceeding with another step into the software settings, we can find that the previous contact types offer some different formulations. Ansys always propose a *default* option, that for the formulation is called *"Program controlled"*. This can be changed by selecting a particular type among the available ones.

With the aid of the *help* guide of Ansys and other tutorials, I report here briefly the available formulations to let the reader understand better the choice in the simulations.
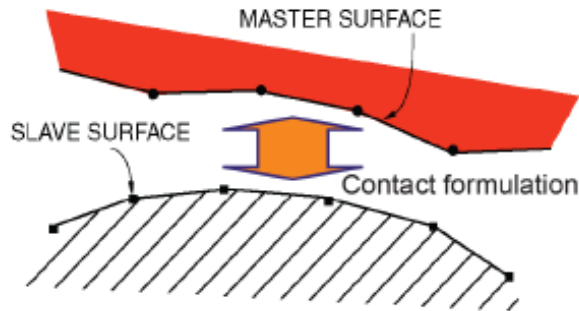
Figure 4.3: *Model of contact between meshed surfaces, the points represent the nodes of the mesh.*

- *Multi Point Constraint (MPC)*: it is the simplest formulation that consists in blocking the relative displacements of the surfaces that are recognized to be in contact, typically by setting a distance threshold. It is a direct type of formulation, non-iterative, that is used for the *Bonded* and *No Separation* types of contact.

- *Pure Penalty*: this is an iterative method that evaluates the depth of the penetration between the surfaces in contact and applies a proportional force $F = k \times x$, where F is the applied force, x represents the penetration and k is the stiffness constant. This last parameter can be left as *"Program controlled"* or can assume a custom value. The final step of the iteration is the evaluation of the new position of the surfaces once the force F is applied; once the solution converges, the force F represents the final contact force.

- *Normal Lagrange*: in this method, the procedure is opposed to the *Pure Penalty* approach, because instead of evaluating the force in respect to the penetration, the software tries to apply a displacement equal to the penetration to obtain the ideal contact. The force is thus defined as a consequence of the applied deformation.

- *Augmented Lagrange*: it is similar to *Pure Penalty* but it considers an additional term in the force $F = k \times x + p$, where p is a parameter similar to the force generated by the displacement in *Normal Lagrange*, that helps the convergence.

The *Pure Penalty* ideally works as a spring system and the solution will converge, instead of oscillating forever, only if a good damping is applied. Moreover, a penetration tolerance, that is the residual penetration gap, has always to be accepted with this formulation. The *Normal Lagrange* theoretically tends to the perfect solution by deleting any penetration, but the force to be applied could tend to infinity. For these reasons, the last method is proposed as a trade-off solution of the previous two formulations in order to combine the advantages of each, for example improving the convergence and reducing the penetration tolerance. Indeed, it is usually selected as *default* by the software.

4.1.3 Meshing models for numerical simulations, difference from faceted surface

Similarly to the polygonal surface models presented in Chapters 2 and 3, also for the numerical simulations there is a discretization of the geometric models. Depending on

the type of object we want to analyze, the 3D surface models can represent either a solid or an ideal surface object.

In the first case, the surface represents the boundary of the volume contained inside and it can be meshed with solid elements: tetrahedrons, prisms and hexahedrons. In the second case, the surface can be discretized using shell elements, both triangular and quadrilateral.

In both cases, the elements can be linear, when the nodes are located only in the intersection of the edges, or have a quadratic formulation, meaning that there are additional nodes along the edges or inside the elements. The linear case is similar to the polygonal surface models *.stl and *.obj, having edges that are polylines. The quadratic formulation allows to have also curved edges that are splines passing from the additional nodes; in this case the visualization appears smooth and comparable to the use of render filters for the tessellated models.
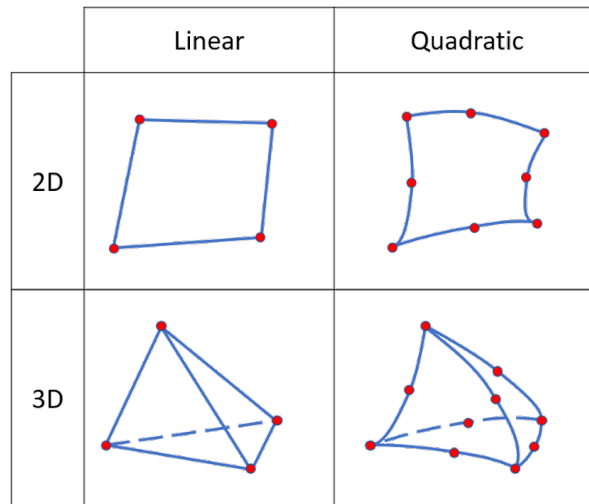
Figure 4.4: *Example of elements for numerical simulations, 2D quadrilaterals and 3D tetrahedrons in both linear and quadratic formulation.*

As visible from Figure 4.4, the additional nodes of the quadratic elements allow a smoother reconstruction in curved models. It has to be noticed that their geometrical flexibility corresponds also to an increased mechanical compliance in respect to the linear formulation.

The polygonal models derived from 3D scanning or used in the Virtual Reality applications are composed only of 2D linear elements, typically triangles but in some cases also quadrilaterals can be used. If the surface is closed and no holes are present, the surface contains a volume that can be identified by the 3D printing software, but no elements are created inside.

The corresponding 2D elements, used for 3D simulations, are instead used for representing surfaces with defined thicknesses. The software (in my case ANSYS) uses the ideal surfaces for the simulations but at the same time can show the corresponding thickened elements. There exists also the case of 2D simulations, where we can work on ideal slices. Using the 3D solid elements, the software fill the volume of the object with tetrahedrons, prisms or hexahedrons, by setting the nodes with the parameters decided by the user.

These mesh elements for simulations can be easily applied by the software when the input model is a NURBS model, with freely variable mesh dimensions. In case the input is an already meshed model, for example the STL derived from 3D scanning, the software cannot change the position of those vertices and will be able only to add new nodes. Moreover, an important parameter that is always controlled by the mesh generator is the aspect ratio of the elements, which defines the quality of the mesh. For this reason, it was preferred to convert the tessellated model into NURBS, as presented in the previous chapter. This allowed to have a high quality mesh even when the skeleton geometry was deformed to comply with the patient's anatomy.

4.2 Related works

In the field of Orthotics and Prosthetics (O&P), the FEM simulations have been used mainly to analyze the prosthesis design for amputees and for comparing different solutions of implants. A typical example is the study of the optimal shape and orientation of femoral stems for hip replacement surgery [12]. Another implant that is widely studied with the goal of improving the interacting surfaces both for material resistance and for better is the knee implant [38]. Passing to prosthetic legs for amputees, many studies regarded the feet shape and the materials, mainly for sport applications (*e.g.* running prosthesis). Another case involved the socket shape design, which is the main component to determine the comfort of a prosthesis due to its direct interaction with the amputee's limb [22, 84].

Some authors used this kind of simulations also to verify the surgical treatment of spine fusion, with the goal of defining the best configuration of the connecting rods in respect to the vertebral positions. This type of research has been performed on highly defined models restricted to the zone of interest, for example only in the lumbar or thoracic spine regions [116]. This could be considered as a micro-scale approach, where the vertebrae and the cartilages are defined in all the different regions (*e.g.* cortical and cancellous bone, cartilage and ligaments), as opposed to macro-scale approaches where the bone has a single mechanical property and the elasticity of the ligaments is embedded in the discs properties.

Regarding the study of scoliotic spines, some researchers proposed the development of even more sophisticated models and simulations. An examples is a 3D parametric model of the whole spine used for teaching and scoliosis screening [44], considering a high quality of the reconstruction requiring about 10 minutes but neglecting the pelvis, the ribcage and other bones. Another example concerns the use a multi-body approaches for the numerical analysis of the musculo-skeletal interaction [80], adopting simplified CAD models of the vertebrae and beam elements for the ribs.

Only few tests were performed on the interaction of the back brace with the patient's body. The first attempts found in the literature were made by the group of Prof. Aubin at Ecole Polytechnique de Montreal. In the beginning [21], the simulations were quite rough in terms of mesh dimensions, also due to the limited computational power of those years (*i.e.* 2011-2012). Only recently, Courvoisier et al. [26] presented a new brace simulator with 3D smooth models instead of the previous simplified 3D elastic beams. Even in his recent work the approximations regarded the connection of the ribs to the vertebrae and the sternum (applying 3 constraints for translations and 3 for rota-

tions) and the brace has been considered as a rigid body. This last approximation is correct for rigid types of braces, such as the sforzesco brace, but not for the thin semi-rigid type analyzed in the present thesis. Moreover, the moderate-to-good the simulation results demonstrated that the approach can give an initial idea of the possible interaction, but the variability in respect to the experimental data showed that further work is required to identify patient-specific characteristics also for the simulation settings.

Finally, Zhang and Kwok [118] developed a new tool for performing Topology Optimization of surface models, as opposed to the traditional solid volume, which could reduce the computational time for brace simulations. As briefly presented in the background, the Topology Optimization simulations usually require to define a "design volume", which corresponds to the space in which the software will have to define the mesh element to be kept and the ones to be deleted, maintaining good performance in terms of mechanical resistance. Typically, the material can be removed from the regions without any constraint, while the surfaces where there are the loads or the boundary conditions have to be maintained, to properly loop the simulations while removing the material. The novelty of the work presented by Zhang and Kwok resides in the use of surfaces instead of volumes and shows the feasibility of removing the material even on a surface loaded with a distributed pressure. The real case of the brace instead requires the pressure to be continuously adjusted inrespect to the contact interaction with the patient's body, so that when removing the material in low pressure regions the contact would be redistributed over the remaining surface. Due to the previous observation and to the fact that no commercial solution is currently available, the approach was discarded for the development of the present thesis.

4.3   Requirements

The numerical simulations for the brace modeling validation should consider the following requirements.

- *Simple pre-processing*: the setup should be already prepared to run the simulation without requiring excessive operations to the user, such as applying the boundary conditions or setting the material properties.

- *Fast solution for iterative modeling*: the analysis should provide a solution in short time to let the operator to iterate with the modeling phase to improve the brace shape before the production.

- *Qualitative indication*: the most important output should be a color map that gives the idea of where to modify the shape of the brace; obtaining the precise values of the stresses acting in each point would be interesting but, due to the different approximations that are introduced and due to the results of other studies, a deeper analysis with an experimental validation of the settings would be required.

4.4   Methods and tools

4.4.1   Engineering data

The first step commonly performed when dealing with simulations is the definition of the material properties. Conceptually, it could be required after the definition of the

geometry in order to assign the material to each model part, as happens in other software packages. The workflow in ANSYS Workbench, for the static structural simulation, requires instead to first define the properties in the first block called "Engineering Data", allowing to assign the material to the parts only later when the simulations setup is prepared in the Mechanical environment. The software always pre-selects the structural steel, but it is possible to insert custom material choosing the properties from a long list (*e.g.* regarding physical, mechanical and thermal characteristics) or also import materials available from the Engineering Data Sources.

For linear static structural simulations, which is the case presented here, the only two parameters that we have to insert are the Young's (or Elastic) Modulus and the Poisson's Ratio. In this work, the setting was initially based on the different layers of tissues of the models: bones, generic soft tissues, cartilages and ligaments. For the orthoses, the plastic materials were PETG (Polyethylene Terephthalate-Glycol) and the more common 3D filament PLA (Polylactic Acid).

The characteristics of the human tissues were chosen based on the literature review. The bones and the generic soft tissues were also chosen after the Master's thesis experience of simulations for lower limb prosthetic sockets [84]. The properties of the plastic materials were selected comparing both the databases, literature review and datasheets provided by the filament producers.

The Table 4.1 summarizes the material properties that were chosen for the analyses.

Table 4.1: *Material properties set in ANSYS software.*

Material	E [MPa]	ν
Structural Steel (default)	200000	0.3
Bone	10000	0.3
Soft Tissue	0.2	0.49
Polyethylene Terephtalate (PET)	2200	0.4
Polylactic Acid (PLA)	3050	0.39

4.4.2 Models preparation

Scoliosis brace simulation

The skin and the brace models were aligned to the skeleton model developed in Maya, based on the same visual information obtainable from the bi-planar X-rays. Due to the fact that they were polygonal models obtained starting from the scan of the patient, both the skin and the brace were then imported in ANSYS SpaceClaim and approximated with NURBS patches. Thanks to their simple shape, the operation was performed using the manual *Skin Surface* tool available in SpaceClaim, avoiding the steps presented in the previous chapter for the case of a single vertebra (Figure 3.24). The right side of Figure 4.5 shows the result of the skin surface operation on the external model of the patient, while the left side shows the skeleton model reconstructed with the producer explained in the previous chapter.

A preliminary test of the simulation resulted in convergence errors for the sharp edge of the brace. Thus, the brace was modified adding a rounded extension to the edges.

The 3D skeleton model described in Chapter 3 is composed only of bones (pelvis, vertebrae, ribs, etc.), without any cartilage or ligament to connect one each other. More-
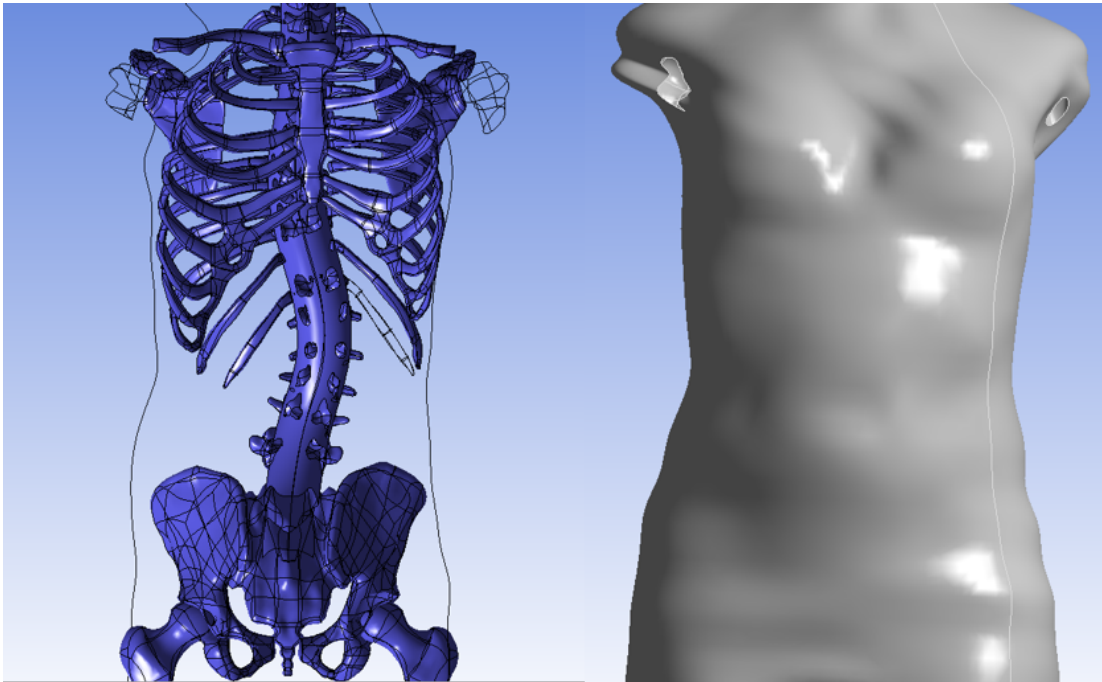
Figure 4.5: *Skeleton model with approximated sweep spine and skin model.*

over, the connecting kinematic chain available in Maya could not be imported in AN-SYS to define the bone connections. If the bone models were embedded in the skin volume, which represents the soft tissues envelope, there would have been the problem of a too flexible connection, with the vertebrae able to move freely with the large deformation of the soft tissue, due to its low stiffness. So, in order to connect the vertebrae and the ribs and have a better interaction with the brace, I created an additional 3D model, by sweeping a circle along a curve using Autodesk Inventor 2019. The sweep passes through the vertebrae and encapsulates also the head of the ribs. Ideally, this model should define a simplified connection, similar to the action of discs, cartilages and ligaments. Once all the models were defined, they were imported into the same geometry assembly, using ANSYS SpaceClaim. Finally, the bones were merged with the additional connecting sweep model and then they were all subtracted from the skin volume model.

Therefore, the model is composed only of a single soft tissue, which volume is represented by the skin surface on the outside and by the bones surfaces on the inside.

Wrist orthosis

The model for the wrist brace simulation was obtained starting the 3D scanned geometry of an healthy male volunteer. The polygonal model was cleaned and smoothed using Autodesk Mehsmixer and then imported in SolidWorks. Here, the shape was firstly intersected with a set of parallel planes, orthogonal to the long bone direction as depicted in Figure 4.6.

The small sections of the thumb that were disconnected from the main curves were discarded and the remaining sections, one per plane, were connected with a loft in to create a NURBS approximating surface (see Figure 4.7). This operation works well
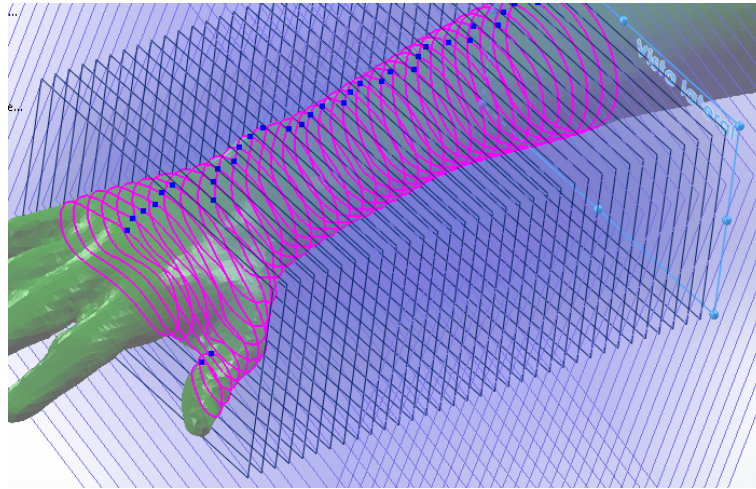
Figure 4.6: *Plane sections for wrist reconstruction.*

only when the user aligns the reference points of each section, otherwise wrinkles could appear.
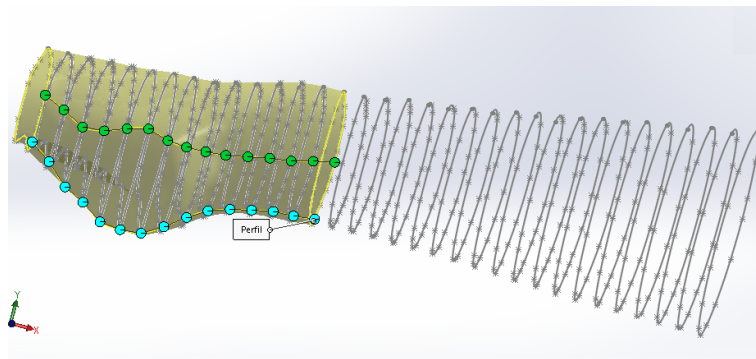
Figure 4.7: *Loft creation for orthosis surface starting from the sections.*

The inner surface of the orthosis was saved as a shell model that was used in a preliminary round of simulations, for deciding the proper thickness value. The surface was then thickened uniformly to create the volume and the opening for the thumb was created as we can see from Figure 4.8. On the side opposite to the thumb, a long opening was created in order to finish the orthosis and preserve the borders needed for wearing it. For the goal of simulations, then three rings were added in correspondence of the ideal closure straps and two planes were used to create a face slit, obtaining auxiliary edges for applying the boundary conditions.

4.4.3 Analyses setup

Scoliosis brace simulation

Once the geometry has been defined, the model can be passed from the CAD module to the one concerning the settings, which is the core of the simulation. Even with a series of simplifications, the complexity of such simulation is related to the large penetration that appears when the brace is worn. In Figure 4.9, we can see the values of
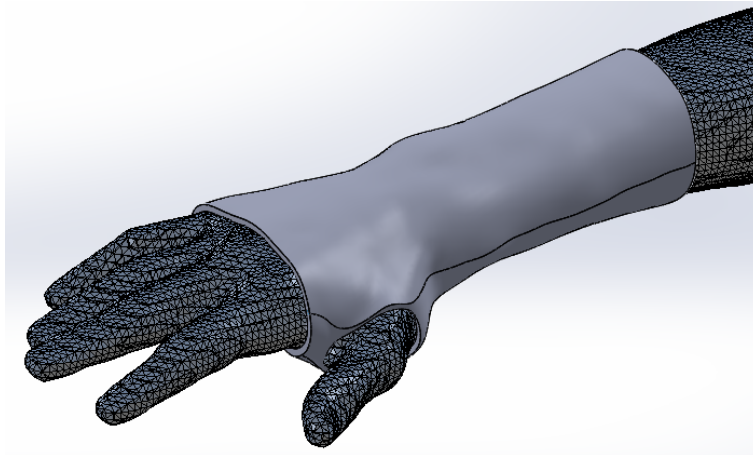
Figure 4.8: *Final wrist orthosis model overlapped on the skin scanned surface*

initial penetration, almost 20 mm, evaluated in the analyzed model. This penetration is not casual, the orthopedic technician starts from the skin model and sculpts the brace shrinking some regions in order to press the body of the patient, thus applying the corrective forces. This is coupled with the only non-linearity preserved for the simulation, connected to the Pure Penalty formulation.
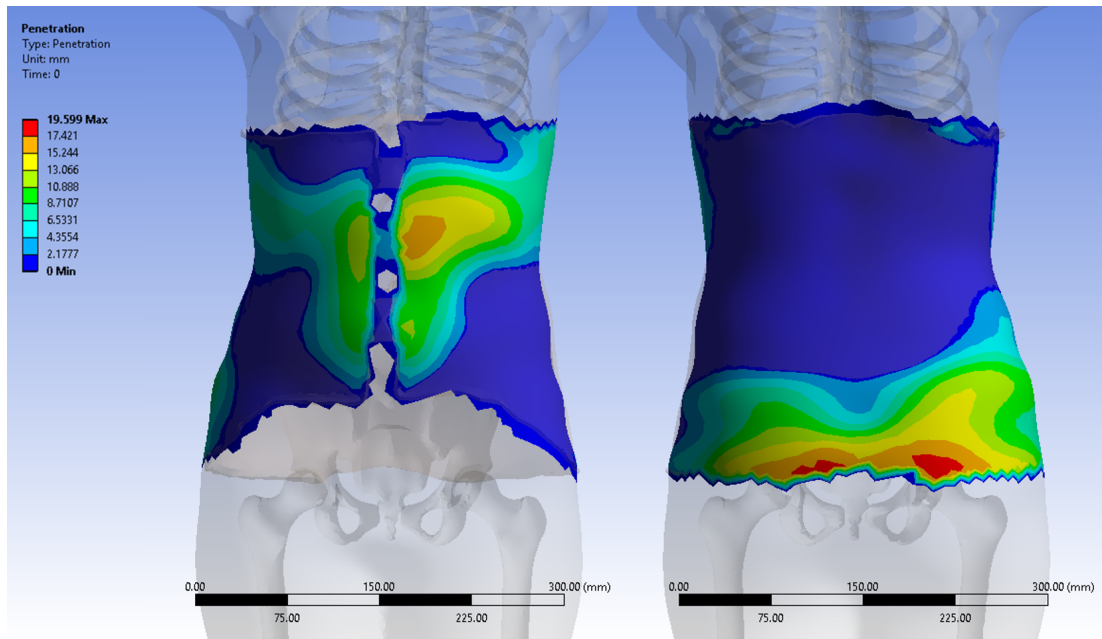
Figure 4.9: *Initial penetration of the brace over the skin, front and back view.*

The simulation was simplified to the extreme of removing the bones and the sweep model, constraining their surfaces as completely fixed to the ground. This is equivalent to assigning a rigid behavior to the bones and to the sweep model, avoiding the creation of mesh elements in these regions. Thus, no bones, discs or cartilage material properties were currently assigned. The skin model is completely defined with the general soft tissue property, which was set as a linear elastic isotropic material.

Regarding the constraints for the brace, two approaches were tested in order to solve the penetration.

Fixed brace with automatic penetration solution

In the first case, three small surface bridges were added in the front region of the model, to represent the real closure straps located in this region, and then a fixed constraint was applied onto these new surfaces in order to obtain an automatic solution of the penetration. The choice of constraining only these regions, instead of the whole border is related to the higher deformability of the brace for solving the interaction problem with the patient's body. In this case the contact was always active since the beginning and the option "add ramped offset" was used to solve the penetration.

Opening and closing brace around patient

The second test is ideally equivalent to a donning simulation thanks to the displacement applied in opposite directions to the front vertical edges, thus simulating the opening and closing movement. The steps of this test are illustrated in Figure 4.10. In this case the contact was initially deactivated to let the brace open without any interaction. Once the maximum required opening is reached avoiding any residual penetration, the contact is activated and the brace is closed around the patient's body. Due to the possibility to open the front edges, the strap surfaces were removed and the displacement in the two opposite directions was applied directly to the two end vertical edges of the frontal opening.
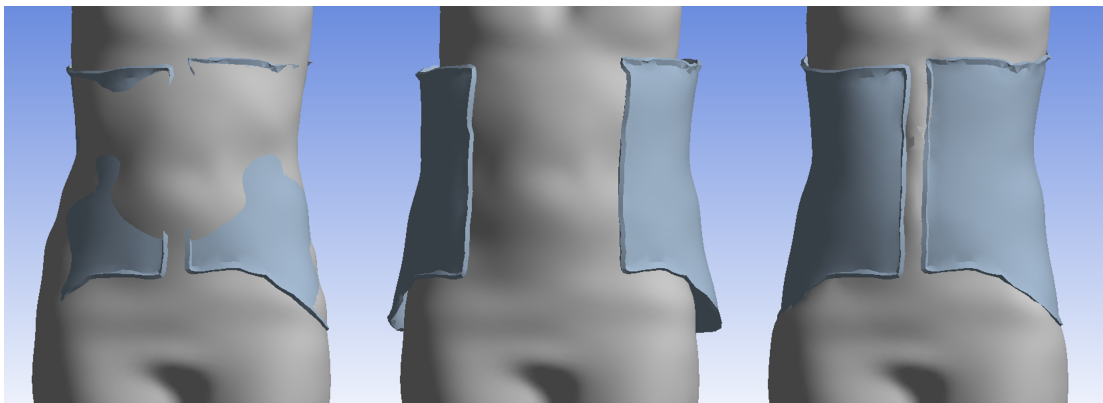
Figure 4.10: *Opening movement applied to the brace front edges.*

In both cases, the *Frictional* contact (with a low coefficient equal to 0.2) was applied to the whole skin surface of the body model, defined as "Contact", and to the inner surface of the brace, defined as "Target". This choice is in accordance with the general ANSYS guidelines available from the training manuals, briefly reported in the list below. The setting is very important when the contact is set with Asymmetric Behavior, while it should be irrelevant in case of Symmetric Behavior.

- Between convex and concave (or flat) surface, the last should be the Target.

- Between the coarser and the finer meshed surface, the first should be the Target.

- The stiffer surface should be the Target.

- The lower order surface (in case one has a linear formulation and the other is quadratic) should be the Target.

- The larger surface should be the Target.

Also, the mesh settings was the same for both constraints cases. The soft tissues were meshed using linear tetrahedral elements with a global maximum dimension of 10 mm, but allowing the software to reduce the mesh size in the regions automatically identified to be critical (e.g. near the bones or where the curvature was higher). The shell brace model was meshed with linear triangular elements, uniformly distributed, with a mesh size equal to 10 mm too. The mesh produced for the first case is shown in Figure 4.11,
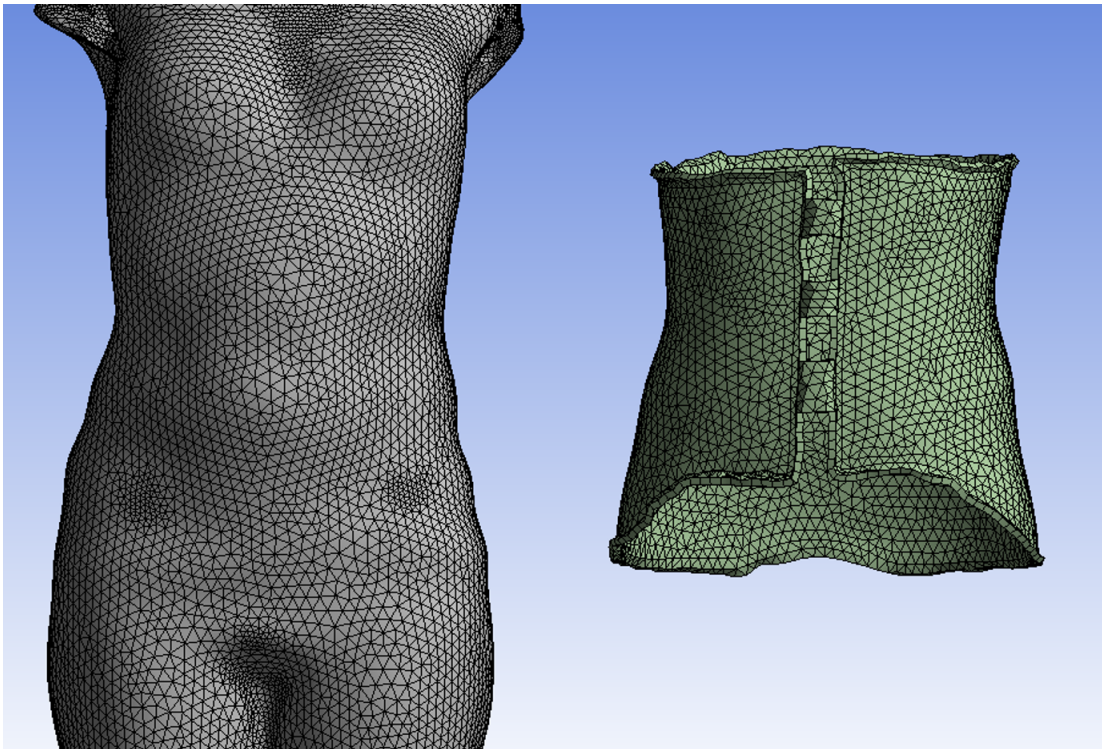
Figure 4.11: *Mesh applied to the models in the different simulations, front view.*

Wrist orthosis

For the wrist orthosis, even though the shape was defined from the skin model, no arm-hand model was considered. The focus was only the test of the best approach to optimize the material distribution considering a set of load cases. Considering again the possible final application in orthopedic centers, the idea is to simplify the simulation and have a fast solution to loop in the modeling phase. With the goal of producing the orthosis by 3D printing, the material for the orthosis was chosen to be the most common filament for 3D printing, the PLA, which is considered to be valid for its higher stiffness and for the lower elongation required. Regarding the solid rings that were added for

keeping the lateral opening closed, the static structural steel was assigned because of their ideal rigid behavior, while using the rigid setting for these models did not allow the deformation of the orthosis.

The constraints to the orthosis were always applied as a cantilever beam, fixed on the end closest to the elbow, supported in the region of the wrist with a roller support and loaded next to the palm of the hand with a force applied to a surface partition as depicted in Figure 4.12. The choice of the roller support was taken after a test without it, which resulted in a deformation distribute also in the forearm. This was considered to be non-realistic due to the presence of the forearm bones (radio and ulna).
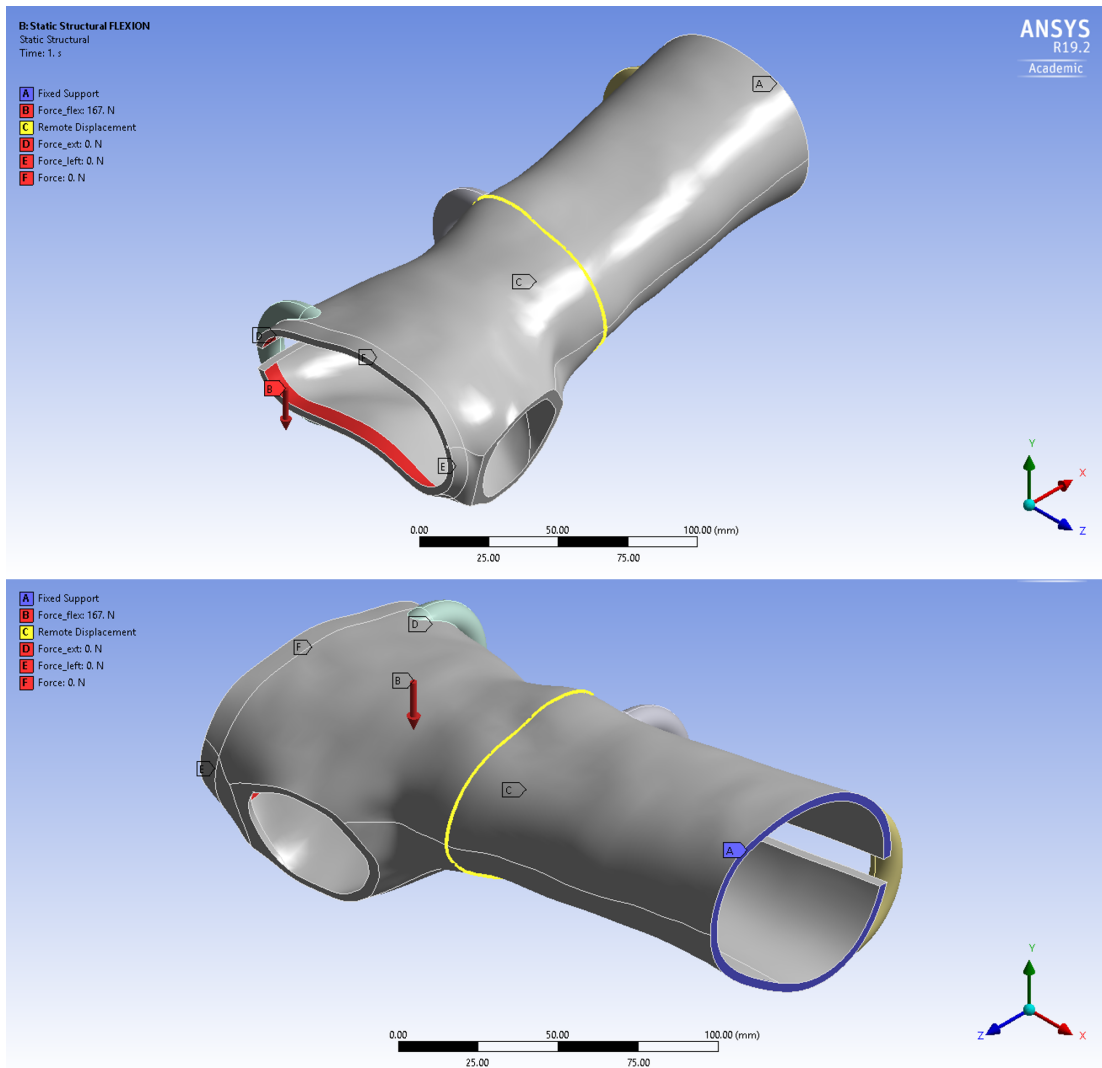
Figure 4.12: *Boundary conditions applied to the wrist orthosis as a cantilever beam supported with a roller.*

The value of the force was computed considering that the maximum moment evaluated in the wrist by Vanswearingen *et al.* in [104] was equal to 15 Nm. The distance between the roller support and the force loading zone was equal to 90 mm, thus the flexion force was set as follows, $F = 15000$ Nmm / 90 mm = 167 N.

Thickness evaluation

A first set of preliminary simulations adopted the shell model for verifying the thickness to be applied to the final solid model used for the topology optimization. The thickness can be simply applied to the shell model in the simulations by changing a parameter to the finite elements, without affecting the geometry and avoiding any expensive intervention of the operator. The mesh was composed of linear triangular shell elements with a size equal to 3 mm, which was considered to be appropriate for the detail level.

Mesh convergence

In the second round of preliminary simulations, the solid model of the orthosis was analyzed, with the thickness equal to 3 mm on the basis of the previous results, which is also consistent with the range for traditional wrist braces, that goes from 2 mm to 3.5 mm. This allowed to establish the proper mesh size by analyzing only the case of flexion, which is the most critical one in terms of force values. For evaluating the convergence of the mesh, it was varied between 20 and 0.5 mm, verifying the maximum total displacement, which was composed almost completely by the component in the direction of the force.

Topology optimization

In the final simulations, in order to obtain a good result considering the different loading conditions, flexion-extension and lateral rotation, a series of steps in the Static Structural simulation was set, varying for each the direction of the loading force. Each step contained only one force at a time with the following sequence: flexion, extension, inward rotation and outward rotation. The values for the forces were computed similarly to the one presented before for the flexion, but considering the different moment values.

For the Topology Optimization, a maximum number of 500 iteration was set, but in practice the maximum number reached only 50 iterations, and a convergence accuracy of 0.1%, which is larger than the usual 10^{-4} but has to be considered in relation to the number or iterations required for the solution. The whole orthosis was set as design region, not considering the closure rings, with the exception of the edges of the border, in order to preserve the smoothness, and the ones of the rings connections, because the rivets could be located there. The response constraint worked on the reduction of the mass with the objective of minimizing the compliance, which means maximizing the stiffness, based on the results of the Static Structural simulation. Finally, a constraint related to the Additive Manufacturing was set, with the limit of 45°for the overhangs when printing the orthosis with the forearm axis in the vertical direction.

The mesh elements were 3D solid tetrahedrons and the characteristics were chosen thanks to the preliminary tests, which corresponded to have a single layer of elements in the thickness. In this way, the solution proposed by the software after the optimization step could be removing completely the material across the thickness itself, avoiding further evaluations for interpolating the material variation in the layers. The ideal situation would be to have an optimization tool that works directly on shell models, so that the material removal would be applied to the surface before thickening and that the simulation could be lighter and faster. Unfortunately, this option is not yet available for

the commercial but still under research, as shown by Zhang and Kwok in [118].

As depicted by Figure 4.13, the solution of the static structural was assigned for the setup of the optimization step. The choice of such setup is related to the major control in the different solution steps, assigning the values for each direction (+/- Y and +/- Z) in distinct solution steps.
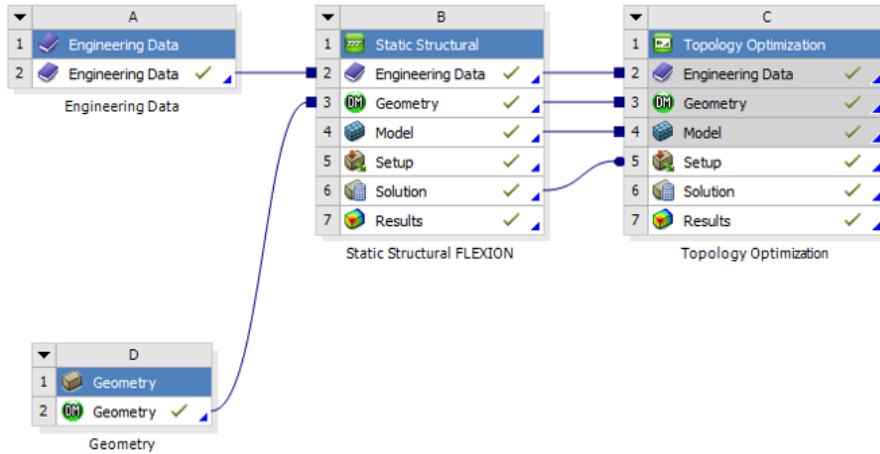
Figure 4.13: *Project scheme in ANSYS workbench for a topology optimization.*

4.5 Results and Discussion

The simulations described were computed using ANSYS Workbench 19.2 on a Windows 10 notebook with i7-6700HQ CPU, 16GB of RAM memory and NVIDIA GeForce GTX 960M (2GB GDDR5 video memory). In ANSYS, the *Solve Processing Settings* were modified to use 3 cores but the graphic board did not allow the GPU acceleration option.

4.5.1 Scoliosis brace simulation

As mentioned above, the main goal of the tested simulations was to verify the quality of the skeleton model developed in this project and presented in the previous chapter. The analyses were focused on understanding the eventual issues that could arise from the deformation of such model in order to approximate the patient's anatomy. With both approaches, the simulations converged properly, solving the initial penetration. A residual penetration, which is reported in Figure 4.14 was left and the maximum values after the solution converged were of about 1 mm. This can be neglected for the purpose of the final application on the patient's chest, considering all the approximations used in the simulations. Moreover, most of the penetration appeared near the borders, but we have to consider that, on a side, the skeleton and spine model was constrained to the ground as if it was completely rigid and on the other side the type of elements, linear triangles/tetrahedrons that allow a faster solution but are also characterized by a stiffer behavior.

The time required to solve the penetration with the automatic approach in the fixed position took was about 1 hour and 10 minutes. Even if the solution depends on a
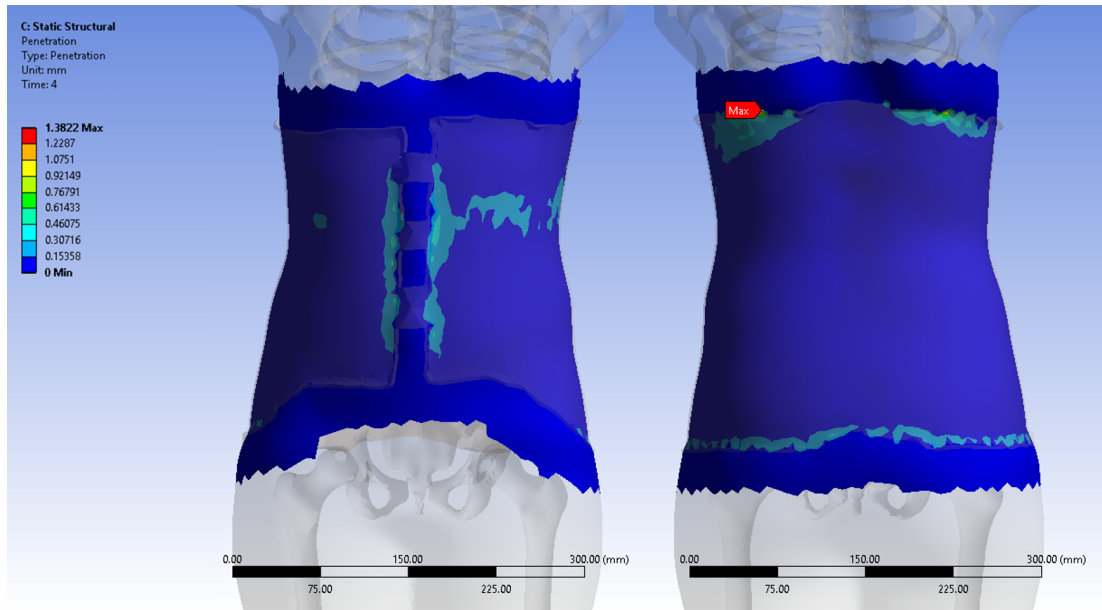
Figure 4.14: *Residual penetration remaining at the end of the simulation, front and back view.*

single step, passing from no-contact to contact-enabled, the solution was reached with an automatic subdivision in 3 sub-steps (0.35, 0.7 and 1.0), due to the large initial penetration. Moreover, a total of 54 iterations were computed to reach the solution of the single step.

The solution permits to visualize the interaction properties, particularly interesting are the contact pressure on the skin and the stresses acting on the brace. The first could be related both to the comfort for the patient, evaluating the maximum pressure values, and to the regions of corrective forces, evaluating the pressure distribution. The seconds could be instead interesting for verifying the resistance of the printed brace and for improving the material distribution.

Fixed brace with automatic penetration solution

The pressure distribution, shown in Figure 4.15 is related both to the initial penetration and to the thickness of the soft tissues, *i.e.* the distance between the skin surface and the underlying bones. As the purpose of the simulation was just to have an idea of the distribution and due to the use of all the approximations, the absolute values are not to be considered as representative of real pressure values.

However, comparing the the values with other studies about the pain threshold, we can notice that they could be considered as an indication of the comfort of the brace. The different threshold limits found in literature are around 200 kPa and, with the exception of the border effects, the pressures on pelvis and ribcage are below this limit [51].

Another interesting result regarded the stresses acting on the brace in order to verify the resistance to the loading conditions, which can be seen in Figure 4.16. As the bones were set to be fixed to the ground, we expected that the resulting forces acting on the brace were actually over-constrained, so the real stress during normal conditions should be even lower. As expected, the constraints on the additional strap surfaces created a
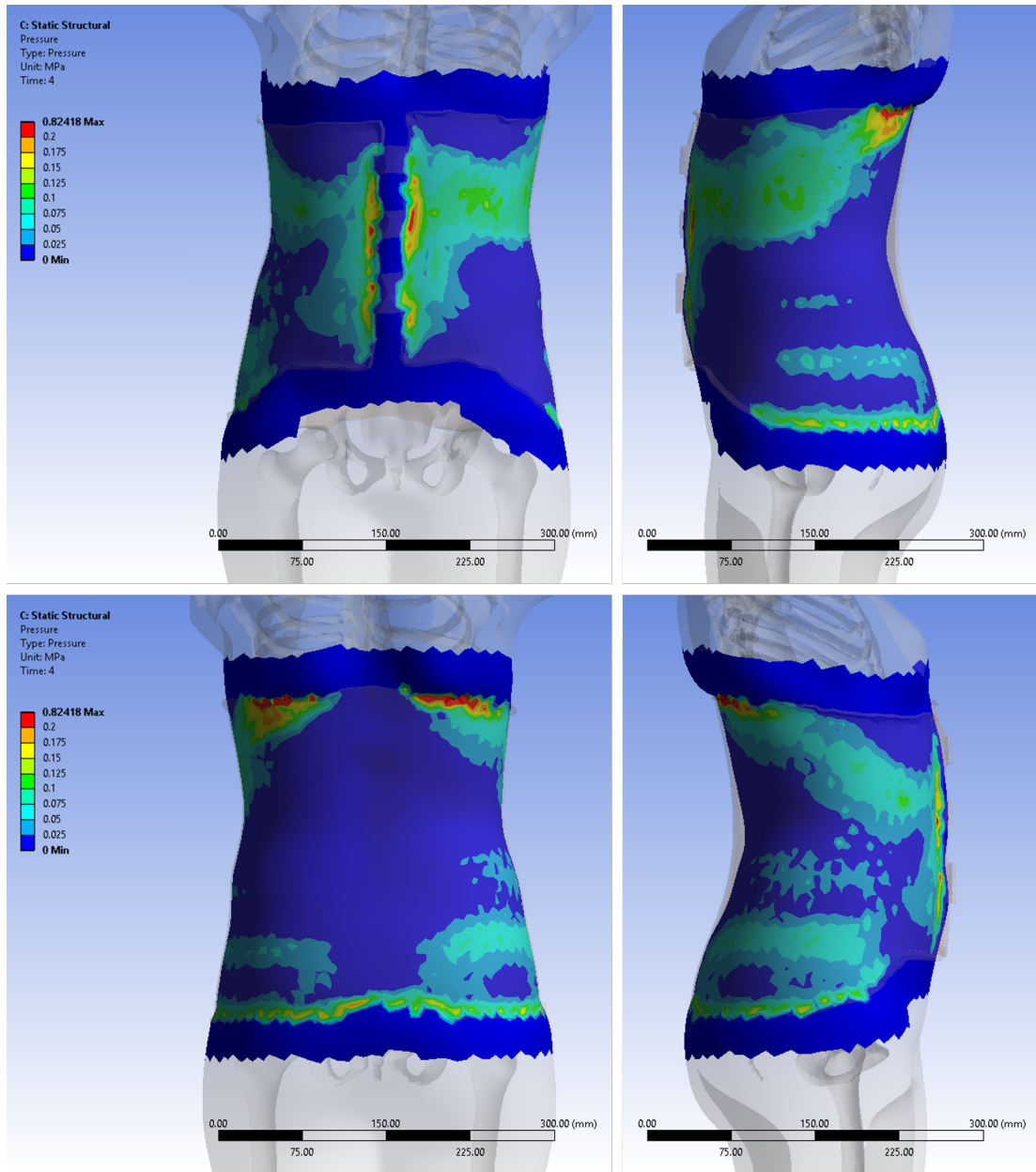
Figure 4.15: *Results of the contact pressure for the fixed brace. Respectively front and left view in the top row, back and right view in the bottom row.*

stress concentration is present but should be neglected. The maximum values, equal to 51,74 MPa on the straps and 42,05 MPa on the front of the brace, are anyway below the material limits (*i.e.* the *Flexure Strength* reported by FiloAlfa datasheet is 73 MPa).

Opening and closing brace around patient

The opening and closing motion presented issues in terms of convergence with the frictional contact settings due to the applied motion, stretching and pressing the skin in the front opening with a strong pinch effect, even with a low friction coefficient equal to 0.2.
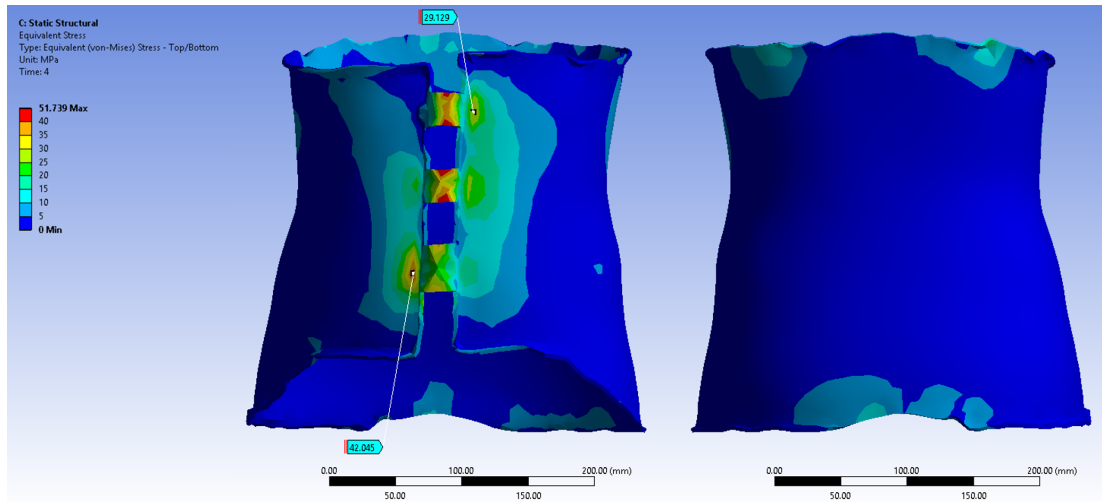
Figure 4.16: *Von Mises stresses on the brace in the fixed configuration, front and back view.*

The contact was thus tested also in frictionless mode which allowed to obtain a good convergence, due to the possibility for skin to slide under the brace surface when closing it. The maximum stresses acting on the brace were concentrated on the edge that was constrained, while the maximum pressure on the skin was found on the back side, in correspondence of the top and bottom border of the brace.

The results are graphically more interesting for the possibility to evaluate eventual criticalities, in respect to the fixed brace. Indeed, the orthopedic technicians always perform a manual evaluation of the resulting stiffness of the brace by opening it beyond the normal use for wearing it, in order to establish if the brace can resist to eventual overstressing.

Bringing back the front edges in the initial configuration, the results appeared to be comparable to the previous simulation with the fixed brace. As we can see in Figure 4.17, the brace is pressing correctly more on the left side of the patient in order to apply the supporting and corrective load.

As observed in Figure 4.18, opening the brace the stresses reach higher values on the back side due to the bending effect. This is indeed the region where the fracture or the delamination of 3D printed brace could happen more easily, while the double curvature present on the sides makes the regions stiffer.

4.5.2 Wrist orthosis

Thickness evaluation

Regarding the preliminary test on the thickness, the results on the shell model presented the expected decrease of the maximum deflection of the orthosis with the increasing dimension, as shown in Figure 4.19. Even if the values are smaller than the maximum strength of the PLA ($\sim$55 MPa), the choice of 3 mm was taken as best compromise between the bulky thicker layers and the thinner but also more fragile ones. The choice of avoiding thinner layers considered also the further operation of material removal, which could increase the values of deformation and stresses, also due to stress intensification in correspondence of removed material areas.
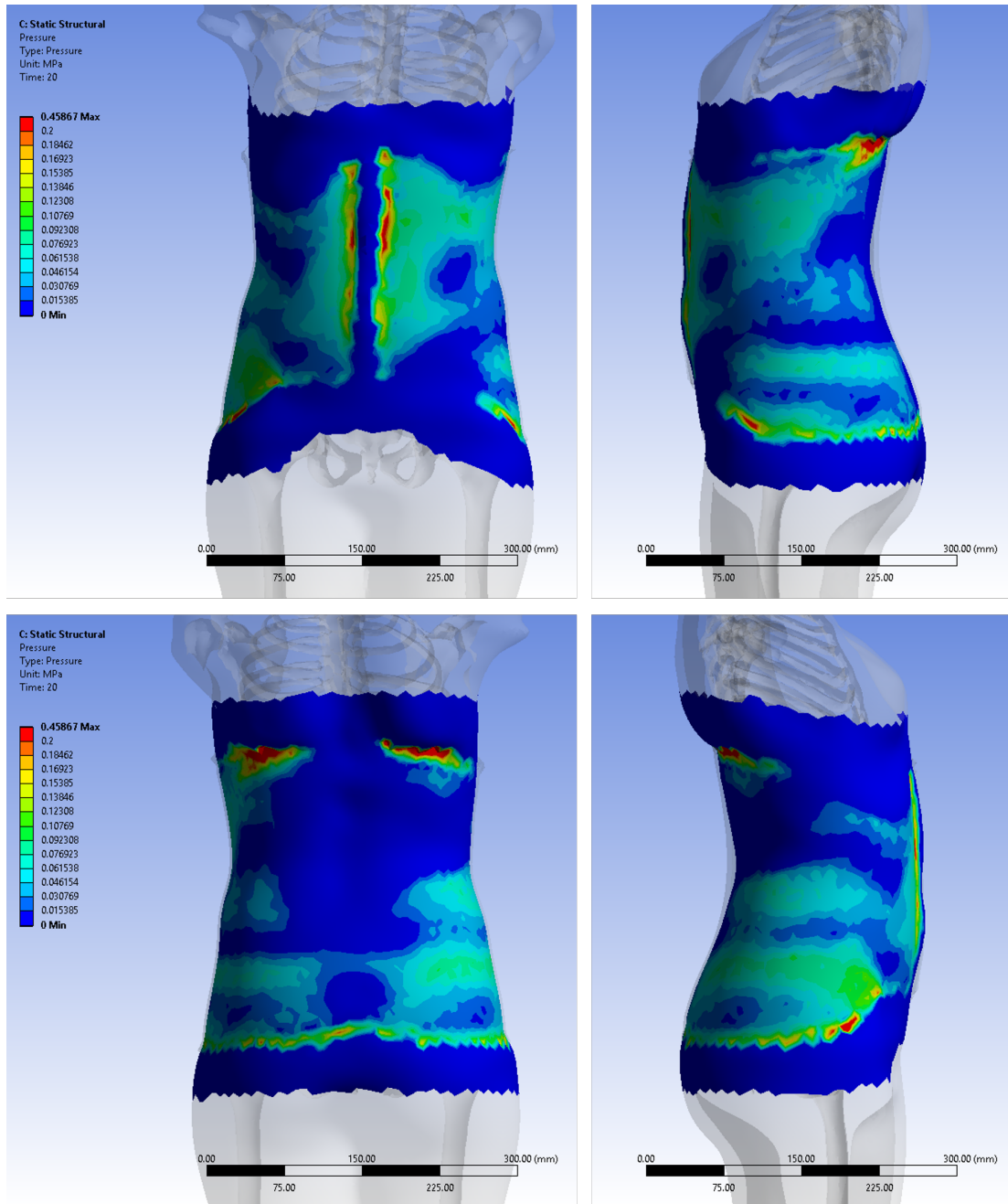
Figure 4.17: *Results of the contact pressure for the opening and closing brace. Respectively front and left view in the top row, back and right view in the bottom row.*

Mesh size convergence

The mesh size reduction observed in Figure 4.20 implied that the results started converging in correspondence of 4 mm. This means that a further reduction of the mesh size did not imply a significant variation of the result (in our case, the maximum total displacement), but only an increase in the time required for solving the numerical problem. Since the value was close to the selected thickness, I chose a mesh dimension exactly equal to the thickness, with the idea of avoiding possible consequences on the

97
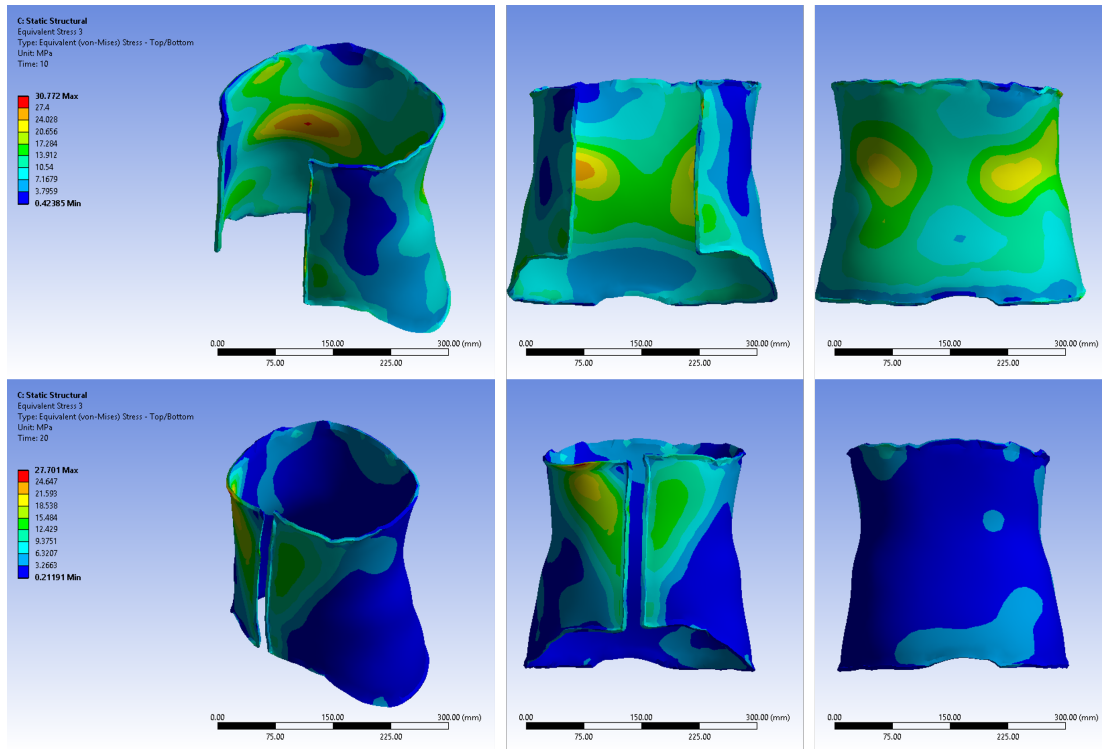
Figure 4.18: *Vom Mises stresses on the brace in the opening and closing configuration.*
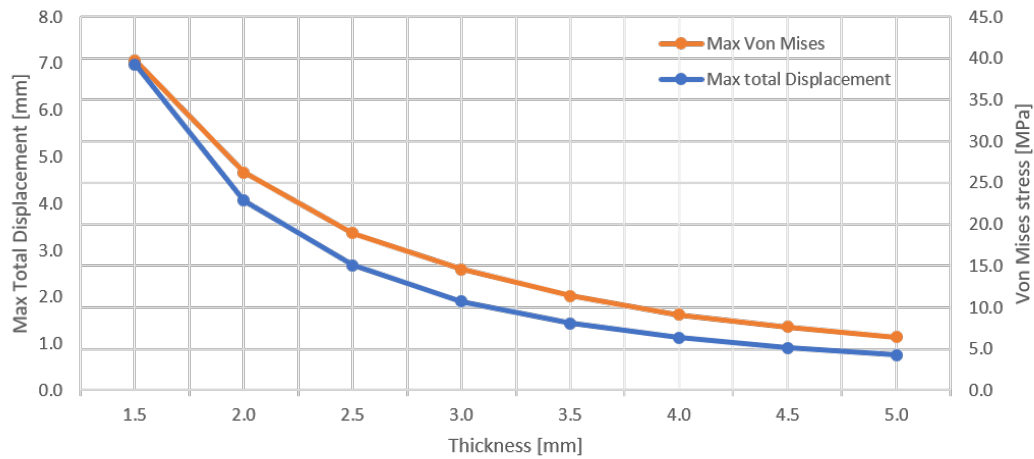
Figure 4.19: *Variation of the stresses and deformation as a function of the shell model thickness.*

aspect ratio. This also allowed to run the following simulations of topology optimization obtaining a direct removal of the material across the whole thickness, avoiding further evaluations for interpolating the material variation in the layers.

Topology optimization

Even though the settings was requiring the 70% of mass reduction, the final solution reached 76% of mass, equivalent to 76% of volume due to the uniform density. The
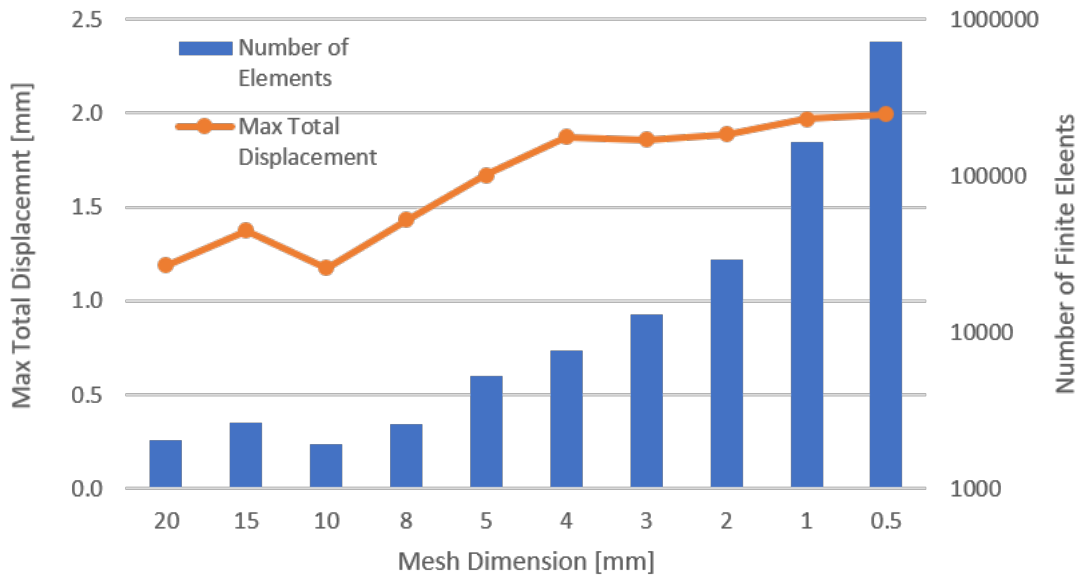
Figure 4.20: *Convergence of the total maximum displacement and amount of elements when reducing the mesh dimension.*

resulting geometry is depicted in Figure 4.21, where it is possible to notice that the constraints on the border and on the overhangs angles were respected, but apparently the constraint on preserving the interface with the rings was not considered.

The most important result regards the time for the solutions: the Static Structural simulation took only 40 seconds for the software to both pre-process and solve the problem, while the Topology Optimization lasted about 6 minutes. The speed to reach a final model can be considered to be very interesting for the case of the final application, where the technicians cannot wait for many hours just to have an idea of the possible geometry. Instead, with the simplified simulations, that did not consider the realistic interaction with the patient anatomy, the final shape was reached in few minutes. The further steps, before 3D printing, could regard the possible smoothing of the borders in the removed material regions, for the resultant sharp edges due to the coarse mesh.

We have to remember that the Topology Optimization aims at providing a possible solution for the mass reduction. It does not mean that the solution is the best, as for any other type of numerical simulations. The results have to be considered more as a possible guideline in order to improve the product we are testing. Thus, also for the orthosis, some final adaptations could be necessary, for example in order to add the closure to the opening.

4.6 Final remarks

The main goal of the simulations on the scoliosis brace was on testing the 3D skeleton model developed as a standard adult male and then deformed to approximate a young female subject. The secondary purpose was to evaluate the possibility of having a fast solution for the interaction between the designed brace and the patient chest, in order to loop in the design phase. The simplified simulations enabled having a fast result for
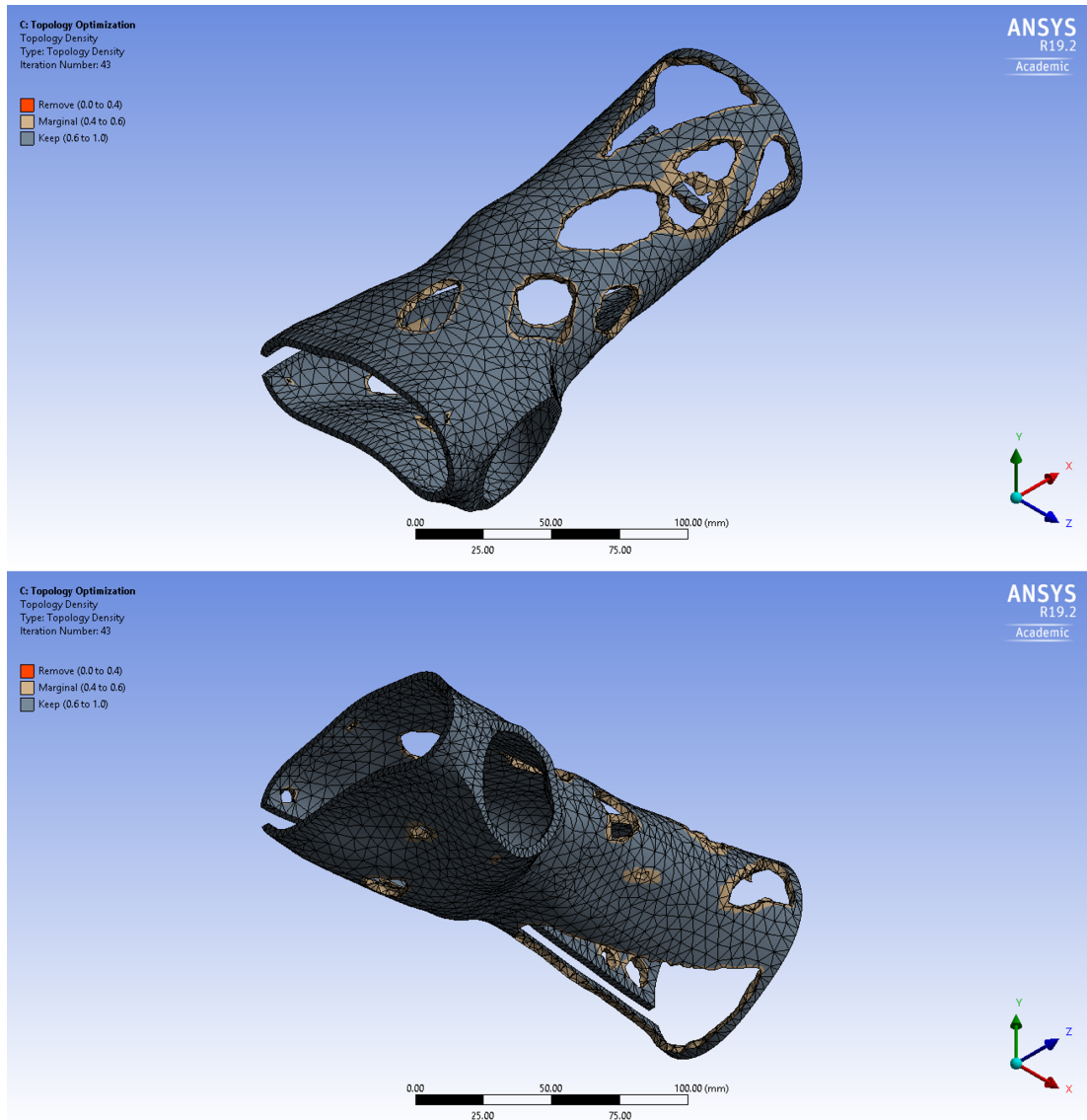
Figure 4.21: *Resulting wrist orthosis from the topology optimization simulation.*

evaluating the quality of the designed brace and for verifying the location of the loading in correspondence to the spine deformity.

The geometry did not show any issue neither in the import step nor in the meshing phase. The two contact solutions, with fixed brace and with the opening-closing motion, converged and the software properly solved the initial penetration due to the shape of the brace. The results confirmed the possible use of the skeleton model for running a simulation of the brace-patient interaction before producing the brace.

The simplification of fixing the whole spine allowed to obtain a relatively fast solution, but not to reach a real correction of the patient's spine itself. Further improvement should try to solve the problem with a flexible connection between the bones, enabling a more realist representation of the brace effects. Nevertheless, the solution time would be increased exponentially for each solution step, thus moving away from the idea of using the simulation in the loop of the design process.

The simulations on the wrist brace presented instead a first attempt to understand if the topology optimization could well apply to the production process of the orthoses. The results are interesting but the use of just one layer of mesh elements in the thickness is usually not advised. It would be better to use the shell elements, developed properly for the thin objects. Unfortunately, there are no software available for applying the topology optimization method to the shell models.

The use of the topology optimization allows to obtain a fast solution, in about 6 minutes, for the wrist orthosis without considering the real interaction with the anatomy of forearm and hand. The time difference with the static structural, taking less than a minute, means that solving the topology optimization required to solve more steps. If we think of adding such a tool also for the scoliosis brace, the simulation would become again too long to be used in the design loop.

Additive Manufacturing

This chapter presents the study of additive manufacturing of polymers for the production of custom scoliosis braces. After an introduction to the topic and a brief literature review, the text continues with the definition of the requirements for the final application. The methods and the tools are then defined for different steps: choice of the printing machines, choice of the materials with a focus on their characterization and finally the full brace production.

The purposes of this chapter are: 1) to investigate and evaluate suitable materials for the fabrication of back braces by means of Fused Deposition Modeling (FDM) 3D printer, 2) to describe the reverse engineering and the production process of an orthopedic back brace by 3DP, and 3) to present a case study involving a 16-year-old patient affected by Adolescent Idiopatic Scoliosis (AIS).

The work is part of the project EMPATIA@Lecco, with the collaboration of the Scientific Institute *E. Medea*, of the *Institute of Polymers, Composites and Biomaterials* (IPCB) of the Italian Research Council (CNR), and also of the orthopedic centers *Labsan* of Lecco and *Biomedica su Misura* of Brescia, all located in Italy. A journal publication is currently in preparation about the content of the chapter, in particular for the material characterization focused on the final orthopedic application.

5.1 Background

As the name itself can unveil, the Additive Manufacturing (AM) differs from the conventional manufacturing techniques because the production of an object is based on adding the material instead of removing it. There exists a variety of technologies that are part of the AM category, mostly depending on the adopted materials. All the techniques work by creating the final product adding material layer by layer to the build

platform. AM is often called 3D printing, with the idea that the extruder deposits the material on each layer similarly to 2D inkjet printers. Nevertheless, there exist also techniques that do not have a printhead, but work with lasers or other light sources that can either melt powder or solidify liquid. The technology itself is not new, but the expiration of some patents allowed it to be widespread on the market with a massive reduction of cost [37].

Starting from the geometry generated with the Computer Aided Design (CAD) software, the model is passed to a slicing package, that can be external or included in the same modeling software, which performs the decomposition of the object in sections parallel to the build plate, the so-called layers, and converts the information in commands for the machines. In the slicing tool, the user can set and customize the printing properties, both acting on the movement parameters and on the temperature (or laser/-light intensity) to be used for the selected material.

The focus of this thesis is the additive production of braces that are composed of polymeric materials. For this reason, a brief presentation of the most common techniques available for this type of materials is presented, excluding the other technologies for metals and ceramics.

Stereolithography (SLA)

This technology is probably the oldest Additive Manufacturing technique with research dated back to the 1970s. The object is produced by the effect of some liquid polymers to solidify when exposed to a light. Depending on the materials and on the printers, the light-source can vary from laser to digital light projector.

The object can be produced by keeping it immersed in a tank full of liquid polymer. The build platform is moved downward and the light placed over the tank solidifies the layer of liquid on top. Recently, other machines were developed to work by pulling the model out of the liquid so that the new layers are added below.
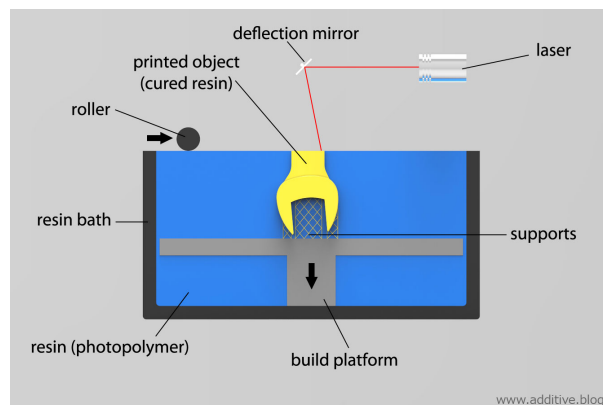
Figure 5.1: *Simplified scheme of classic SLA technology [3]*

Selective Laser Sintering (SLS)

Instead of solidifying a liquid, the SLS works by placing a layer of polymeric powder over the build platform and melting it thanks to the light-source moving in the selected slice in correspondence of the object cross-section, which then solidifies. The build
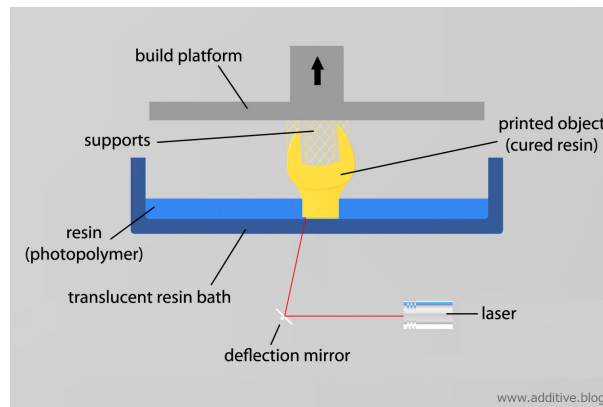
Figure 5.2: *Simplified scheme of reverse SLA technology [3]*

platform moves downward and a new layer of power is placed on top. The new cross-section is then melted and connected to the other layers in order to create the full object.

In this case, the light source has to be usually more powerful and thus the lasers seem to be the most appropriate. Thanks to the powder of the lower layers, in many cases it possible to avoid the creation of additional support structures.
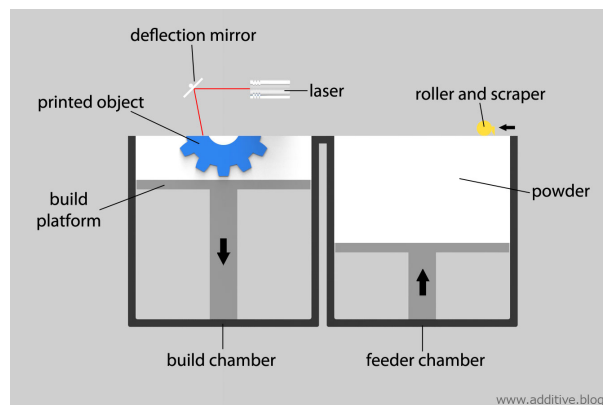
Figure 5.3: *Simplified scheme of SLS technology [3]*

Fused Deposition Modeling (FDM)

As the name unveils, this technique creates a model by depositing layers of fused polymer over the build plate. The input material can be in the form of filament or pellet, which is passed in a hot chamber and extruded through a nozzle, the combination of which is then called extruder. In case the machine works by using the filament, the technology is called Fused Filament Fabrication (FFF).

This is the most diffused technique thanks to the cheaper prices of the machines, available also in Do It Yourself (DIY) kits, and of the wide variety of materials. Moreover, they do not require any intensive training, as required to safely handle the powders or to discharge the liquids.
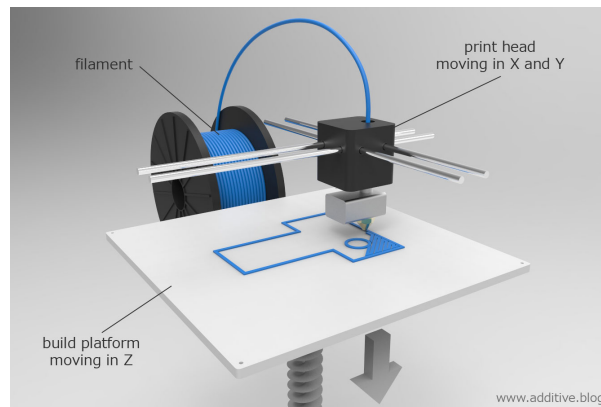
Figure 5.4: *Simplified scheme of FFF technology [3]*

5.2   Related works

In the medical sector, the use of scanning technologies combined with Computer Aided Design (CAD) and 3D printing have shown great advantages over conventional techniques for the fabrication of customized medical aids, devices, implants and accessories [70, 89]. 3D printing is an AM technique involving overlapping of layers to create an object based on a previously generated design using specific modeling software [36]. Because of technological advances, 3D printing has recently gained recognition in medicine due to its potential benefits. 3D printers are becoming necessary in various medical applications, including surgical planning, implants and prostheses production, and medical education [71]. The greatest advantage that 3D printers provide is the freedom to produce custom-made medical products and equipment. The use of 3D printing to customize prosthetic and implants can provide great value for both patients and physicians due to its ability to produce items more quickly and cheaply than traditional manufacturing methods [9]. Traditional manufacturing methods remain less expensive for large-scale production; however, the cost of 3D printing is becoming more and more competitive for small-customized productions [68]. Moreover, 3D printing can be inexpensive, less time consuming and more controllable than traditional manufacturing techniques for custom-made orthopedic devices: costs for molds and waste produced in machining by chip removal are reduced; milling, forging and finishing phases are not necessary; less manual handwork is needed, reducing the risks of human errors [9, 68]. The three most commonly used 3D printing technologies in medical applications are: Selective Laser Sintering (SLS), and Fused Deposition Modeling (FDM) [27, 43]. Among these techniques, FDM is the most common and inexpensive method and is available for a wide range of materials such as thermoplastic polymers, elastomers and investment casting wax. In this technique, a computer controlled heated nozzle deposits the filament on the build platform in X, Y and Z orientation in order to create 3D objects.

This thesis presents a rapid manufacturing approach for the fabrication and mechanical testing of customized orthopedic back braces for scoliosis treatment. Different models are available and they can be divided in off-the-shelf and custom made. Depending on the type and severity of scoliosis and on the number and locations of the contact regions, the effects of orthopedic braces can be limited to stabilization or also

spine curvature correction.

The current production of the back braces is based on the thermoforming of a plastic plate around a sculpted positive mold. However, to allow the production of back braces using AM, the process has to rely completely on virtual modeling software [85]. Others have described a similar virtual modeling process for wrist orthoses, where the body surface is acquired with reverse engineering techniques [11, 58]. However, in these cases, no major correction is applied to the model: the surface is only cleaned, trimmed and thickened. In contrast, as presented in Chapter 3, the creation of a back brace requires a further step of sculpting the acquired shape in order to apply the correction, with loading and unloading areas. This is a very critical phase of the design process for the orthopedic technicians, and is currently performed by manual sculpting of the physical positive mold. It is indeed the main reason why a completely virtual modeling process is not yet common practice.

Another major limitation to the use of 3D printing in orthopedics is related to the choice of the optimal material for each application. Despite the number of available filaments on the market, information regarding material properties are often limited and essential, leading to difficulties in the comparison of specification sheets. Indeed, producers often use different testing standards (*e.g.* ASTM D638, ASTM D790, ASTM D882, ISO 527) and provide incomplete characterization of the filaments. Moreover, the numerical values that are provided, often refer only to the material before being 3D printed, while mechanical characterization of printed samples of the filaments is very scarce.

In this project, samples of Polylactic Acid (PLA) and Polyethylene Terephthalate Glycol (PETG) were obtained by 3D printing and they were characterized in terms of mechanical, thermal and morphological properties. In addition, a pre-existing brace, created with the traditional thermoforming process, was scanned and then the model was 3D-printed. The preliminary feedback was obtained from the patient, who was already using the thermoformed back brace due to AIS, and from both the physician and the orthopedic technicians.

5.3 Requirements

Considering the final application in the orthopedic centers for the manufacturing of scoliosis braces, the following requirements should be satisfied.

- *Build volume of at least 0.3 x 0.3 x 0.6 m^3*: the printer dimensions should be large enough to print a brace in a single piece.

- *Comparable materials properties*: the starting point is to find materials that are similar to the currently thermoformed ones, both for mechanical properties and for possible use in contact with the skin of the patient.

- *Time to print within a working day*: the printing time should be limited in order to be comparable to the production of a brace with the modern process.

- *Low-cost machine*: the printer should have a price limited to about 10000 €, in order to be comparable with the current thermoforming equipment, *e.g.* infrared heating oven [45].

- *Equivalent material cost*: the cost of the printed material should be similar to the costs of the positive mold and the plastic plate in the modern process, *i.e.* about 50 € per brace.

- *Post-processability*: the printed brace should resist to further manual operations of the technician for finishing the brace, *e.g.* applying the closure straps.

5.4 Methods and tools

5.4.1 Technology and machine selection

The choice of the best technology to be used for printing the scoliosis brace fell on the Fused Filament Fabrication, as a balance of different aspects.

It is well known that both SLA and SLS machines can reach higher quality in terms of resolution, both in the printing plane and in the height, in respect to the FDM technology. Nevertheless, the first big limitation was the build volume. The currently available SLA printers can reach only a volume of 200 mm ∗ 335 mm ∗ 300 mm, with the latest FormLabs 3L [34]), which could be good for printing some valves of the sforzesco brace but not for a whole mono-valve brace. The SLS printers can go a bit beyond with a build volume that reaches 381 mm ∗ 330 mm ∗ 460 mm, with the 3D Systems ProX SLS 6100 [1]. However, there exist many FDM machine with larger build volumes, some of which go even beyond 1 m^3.

The second main parameter was the analysis of the costs, not only for purchasing the machine but also for the materials to be used. In both cases, the best choice seemed to be the FFF technology that, thanks to the large variety of low-cost machines, has the widest choice of available materials for reasonable prices. In any case, we can find the super engineered materials, like carbon fiber-reinforced filaments or other modified polymers. Moreover, the most common filaments have prices of about 40 €/kg, which are cheaper than the SLA resins or the SLS powders.

Finally, but not less important, also the FFF machines reaches higher print speeds in respect to the other technologies, fact that confirmed the choice. The compromise on the surface finishing, as presented later, did not result in a limit for the final application. Moreover, the FFF is the easiest technology to be used.

In the category of FDM technology, the FFF is just a possible technology, but there exist also the pellet extruding printers. Due to the common use in large volume machines, the initial price for the printer is also higher but it could be balance by the pellet material price (about $1/10$ of the filaments). The main disadvantages are the unstable printing quality, *e.g.* it is common to have bubbles due to air entering with the pellets in the melting chamber, and to the more difficult procedure to clean the extruder and change material type.

Table 5.1: *Comparison of 3D printing technologies in terms of build volume, resolution, speed and cost.*

Technology	Build volume	Resolution	Speed	Costs
Stereo Lithography Apparatus (SLA)	-	+	-	-
Selective Laser Sintering (SLS)	-	+	-	-
Fused Filament Fabrication (FFF)	+	-	+	+

Among the available printers, the Delta WASP 4070 was selected as best balance in terms of all the above-mentioned factors. It is a printer built on the "delta" system, which differs from the simpler cartesian ones for the vertical motion of the rails that move the three arms connected to the extruder block (see Figure 5.5). Moreover, even when the nozzle moves on a straight line in the horizontal plane, the motors of the delta printer have to use non linear motion, causing the control to be more complicated. However, the advantages of delta printers are usually the higher speed and the better quality when printing circular shapes, which are both characteristics that well apply to our case.
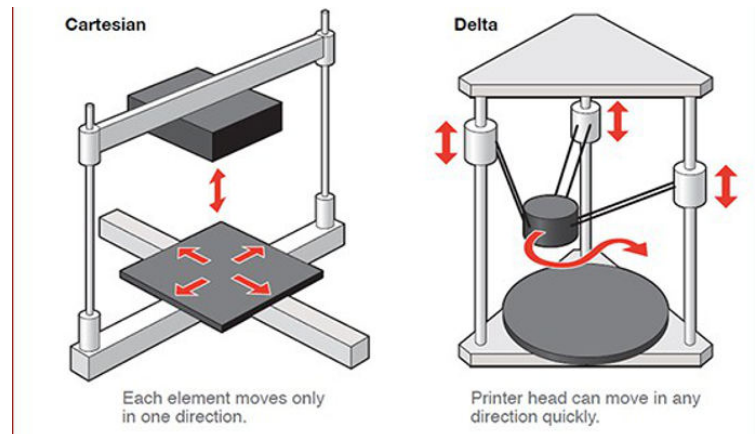
Figure 5.5: *Scheme of a cartesian (left side) and of a delta 3D printer [92].*

The Delta WASP 4070 has a cylindrical build volume with a diameter of 400 mm and a height of 670 mm. The minimum layer height is equal to 100 microns and the speed can reach a maximum value of 200 mm/s both for printing and for traveling. It has a heated printer bed that can reach up to 110°C to ensure the adhesion of most materials. The extruder has two configurations: the Low Temperature (LT) nozzle-cartridge for temperature up to 230°C, or the High Temperature (HT) one for reaching about 300°C. Each type of cartridge works with the filament with a diameter of 1.75 mm, but can have different nozzle diameters, equal to 0.4, 0.7 or 1.2 mm.

5.4.2 Preliminary material screening

Common materials currently used in the thermoformed and off-the-shelf braces include Polyethylene (PE), Polypropylene (PP) and Podialene (a PE dense foam). Their mechanical properties, *i.e.* Elastic Modulus, Yield Stress and Elongation, were compared to those of the available commercial filaments, using the CES Edupack software database. When selecting potential filaments, the materials already used broadly for biomedical applications were preferred. However, scoliosis braces are typically used over a t-shirt and not directly in contact with the patient's body, so biocompatibility is not a strict concern. The problem could be anyway related to the possible formation of mold due to sweating and the request of having a washable material. In both cases, it is well known that the water absorption is higher in PLA with a reduction of the mechanical strength, while the PET is commonly used for water bottles.

Among the materials listed in 5.2, Acrilon Butadiene Styrene (ABS) and PolyCar-

Figure 5.6: *The selected Delta WASP 4070 printer [66].*

Table 5.2: *Basic mechanical properties of typical materials available for FDM 3D printers.*

Manufacturing type	Material	Young Modulus [GPa]	Elongation to Rupture [%]	Melting Temperature [°C]
Thermoforming	Polycarbonate (PC)	2 – 2.44	70 – 150	250 – 343 *
	Polyethylene (PE)	0.621 – 0.896	200 – 800	125 – 132
	Polypropylene (PP)	0.896 – 1.55	100 – 600	150 – 175
3D printing	Polylactic-acid (PLA)	3.3 – 3.6	3 – 6	145 – 177
	Acrylonitrile Butadiene Styrene (ABS)	1.1 – 2.9	1.5 – 100	180 – 274 *
	Polyethylene Terephthalate (PET)	2.76 – 4.14	30 – 300	212 – 265

bonate (PC) were excluded a priori because of the high printing temperature and the possible toxic smokes that are produced when printing. In addition, the higher printing temperatures, respectively 250-290°C and 260-280°C, would have required the change of the extruder on our 3D printers, which could have affected the reproducibility and the comparability of the tests.

5.4.3 3D printed hemicylindrical samples

After a first screening of the potential filaments, hemicylindrical samples were chosen as simple models, representative of a brace section. This allowed to perform a mechanical characterization of materials in conditions that are as close as possible to the final

application, without the need of printing a full brace for each material. The main advantages of using such geometry are: i) the possibility to test the real printing settings for the final back brace, as opposed to printing flat specimens; ii) the higher stability of hemicylinders rather than the flat samples printed vertically; and iii) the correct evaluation of the deposition accuracy and of the adhesion in higher layers with such curved path.

Figure 5.7: *Real back brace and hemicylinder, representative of its section.*

The hemicylinders were created with the CAD software Autodesk Inventor and exported as .stl file with the preset high level of accuracy, thus obtaining 1190 triangles. The dimensions of 150 mm diameter, 50 mm in height and 2 mm of thickness 5.7 were decided after measuring the sections of a real brace on the reverse engineered 3D model. A short straight part of 30 mm was added on an end of the hemicylinder as it is representative of the regions on the back of the brace, where the curvature decreases and tends to zero. The file was then imported in Ultimaker Cura 3.6, where it is possible to perform the slicing and to apply the printing settings, thus creating the *.gcode file that controls the machine. In order to improve the adhesion with the printing bed, a

small brim composed of 5 lines at the first layer was added 5.8.
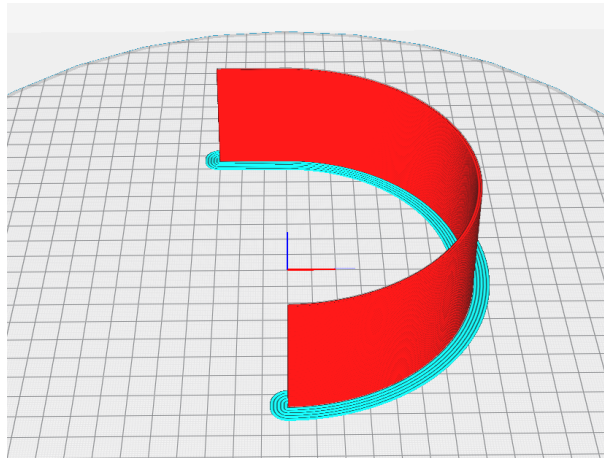
Figure 5.8: *Model of hemicylinder (red) with brim setting in the bottom layer (light blue) to improve the adhesion to the build plate and the stability during the printing.*

The hemicylinder was used as a standard object to compare the different materials and the printing settings in substitution to the traditionally proposed flat printed specimens [57] or to the ideal possibility to 3D print a whole orthosis for each material and printing setting parameter.

The hemicylindrical samples were manufactured using both the WASP 4070 and the smaller WASP 2040 printers (WASP, Italy) [66]. The two devices have different printing volumes but have the same inter-changeable nozzle, motion control, bowden extruder and type of heated bed and closed volume.

Preliminary tests were performed to identify the most appropriate printing settings for each selected material, including printing speeds, the optimal temperature within the range provided by the filament producers, the layer height, and the flow rate. The latter is a critical parameter for materials that are prone to thermal shrinkage and can be increased if necessary to fill gaps between printing lines. Figure 5.9 shows an example of the initial experienced issues related to either too fast movements or improper flow rate (amount of filament extruded) or even wrong temperature.

Figure 5.9: *Setting tests of hemicylinder shape with defects in the higher layers.*

5.4.4   3D printing settings CURA

The initial values for the selection of the nozzle temperature was always the mean value of the range provided by the producers. This was then adjusted by decreasing it, in case of excessive plastic oozing out of the nozzle, or increasing it, in case the low fluidity of the extruded filament or when higher speeds were tested.

The layer heights were varied considering the reasonable maximum limit of 75% of the nozzle diameter. This has to be considered as a general guideline that can be hacked by increasing the flow rate (which is the amount of extruded filament) but reducing the final surface quality. As an example, with the nozzle diameter equal to 1.2 mm we tested a maximum layer height of 0.8 mm. Similarly, some materials were tested with the nozzle of 0.4 mm and the layer height equal to 0.3 mm.

Also for the printing speed, I started with the recommended values and then tested higher speeds when the quality was already good, in order to find the minimum time achievable, and reducing them when the prints were showing some defects, for example with the hemicylinders of Figure 5.9.

The following Figure (5.10) shows another test object that I developed for verifying the quality of the results when adjusting the settings on the go. It is indeed possible to act on the printer modifying the overall speed (all the speed will be increased or reduced of the same percentage), on the temperatures of nozzle and build platform, and also on the flow rate percentage. The left image represents the ideal CAD model, while the right image depicts the real printed object, with an additional brim on the base. The different temperature-speed-flow variations were manually written on the left side, useful to control the resultant printing quality on the other side, where it is possible to notice the presence and the different position of small heaps of material.
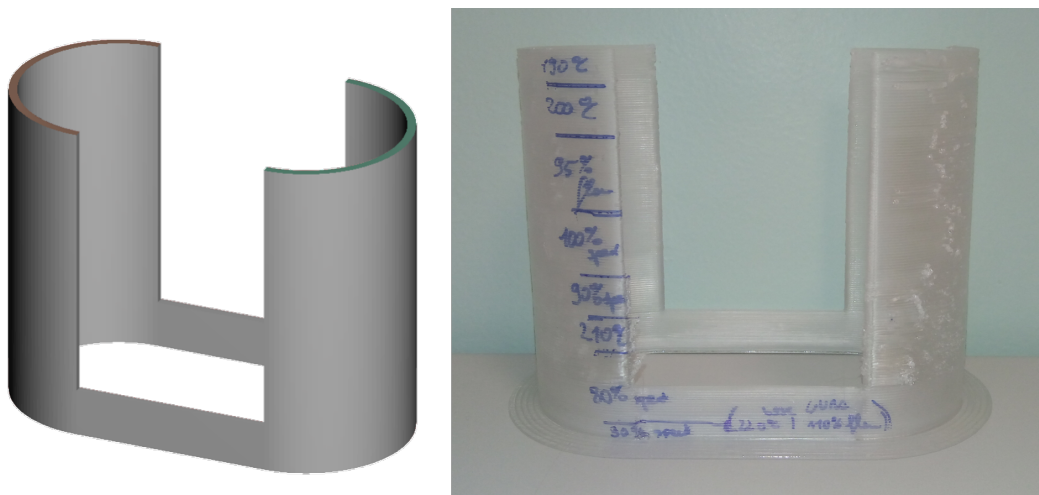
Figure 5.10: *Small test object used for assessment of quality and stringing effects varying the temperature in height.*

After printing the samples, we excluded the elastomers and the High Impact Poly-Styrene (HIPS) due to very low stiffness, even with different shore values, and to print-

ing issues, such as strong delamination or improper loading of the filament through the bowden and the extruder. Two commercial filaments were selected for the realization of the 3D printed back brace: a PLA and a PolyEthylene Terephthalate-glycol (PETG).

Figure 5.11 demonstrates part of soft materials that were excluded from the present study because they clearly would not support the patient. The printed shape is the one of the transparent and white hemicylinders on the left (respectively, PETG and HIPS), while the different soft filament on the right are a set of Thermoplastic-urethane (TPU) with different shore values. The orange one is the softest material tested and simply loses the initial shape under the effect of solely the gravity. The respective shore values are unfortunately given with two different scales D and A: 55 D for the hardest white sample, 95 A for the blue one, 90 A and 43 D for the two black materials, and finally 80 A for the softest orange one.

Both the delta printers had issues in printing the soft elastomers both for the presence of the bowden (tube in which the filament is pushed from the driver to the nozzle) and for the shape of the driver itself. The samples presented below were thus printed with a prusa i3 printer that mounted a direct drive extruder (without the bowden). A possible improvement for the use of such materials could be the use of a remote direct drive, such as the one developed by Zesty [117].
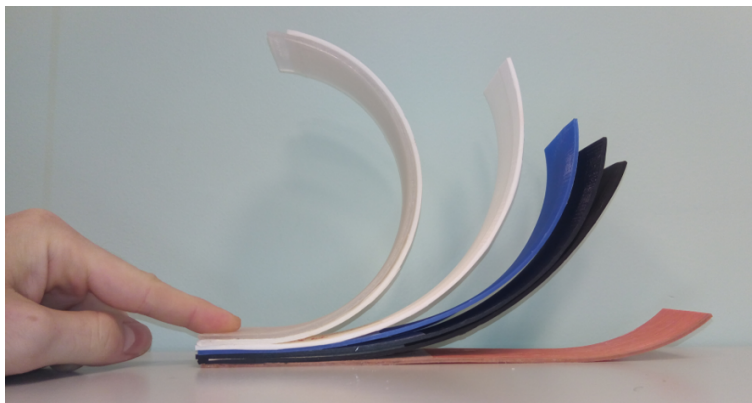
Figure 5.11: *Hemicylindrical samples of softer materials that were excluded.*

5.4.5 Mechanical and thermal characterization of 3D printed samples

The specimens for material and morphological characterization were obtained from the 3D printed hemicylinders, in collaboration with the IPCB of the Italian Research Council. In particular, the 3D printed samples were characterized by their mechanical properties. Moreover, a surface analysis by Scanning Electron Microscopy (SEM) was conducted to understand the effect of printing parameters on the surface finishing of the 3D printed parts. Two different fiber orientations have been chosen for the mechanical test, parallel to the fiber direction (*i.e.* parallel to the printing bed) to test the material elastic modulus and perpendicular to the fibers (*i.e.* perpendicular to the printing bed) to test the fiber-fiber interface. In addition, three different layer thicknesses were assessed for the 3D printed specimens: 0.4, 0.6 and 0.8 mm.

Tensile test

Tensile properties were evaluated at room temperature by an Instron machine using a load cell of 1kN and a crosshead speed of 1 mm/min. Dumbbell shape samples were cut from the 3D printed hemicylinder according to the ASTM D1708 standard. The study was carried out through analysis of five samples for each type of scaffold. The elastic modulus E' was calculated by the slope of the stress-strain curve in the strain range of 0-0.1 mm/mm.
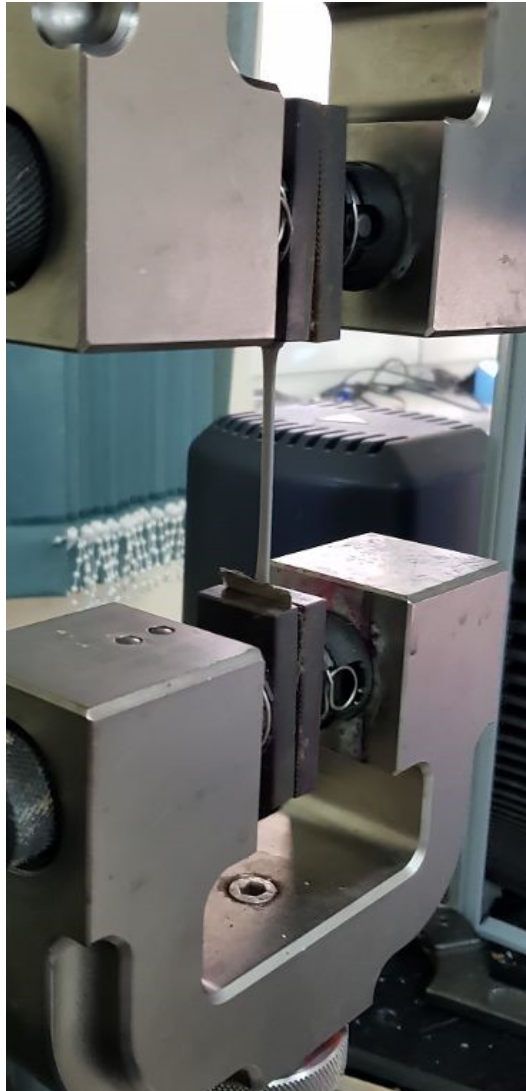
Figure 5.12: *Inston machine used for tensile test.*

Charpy impact test

Charpy impact properties were assessed on V-notched rectangular specimens (60 mm x 13 mm), loaded along the length and were provided with a 3 mm deep notch. At least six determinations for each material were performed by using an instrumented apparatus (CEAST Mod. 6545) equipped with a Charpy pendulum hammer (mass:

3.65 Kg) positioned at a starting angle of 30°. The tests were carried out at a speed of 1 m/s and room temperature. In all cases, linear load-deflection trends witnessed the occurrence of a brittle crack growth and, consequently, the validity of the Linear Elastic Fracture Mechanics (LEFM) principles. Thus, result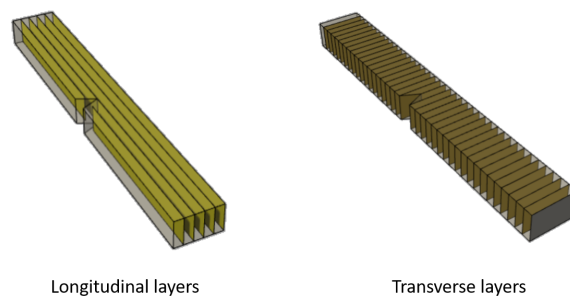s are reported and discussed in terms of the so-called critical stress intensity factor (Kc) and critical energy release (Gc). In particular, the former was calculated according to the equation: $K_c = Y_\sigma * \sqrt{a}$, where Kc is the stress intensity factor, Y is the compliance calibration factor and a is the actual notch length.

Longitudinal layers   Transverse layers

Figure 5.13: *Specimens for Impact test.*

Surface morphological analysis

SEM was performed to obtain qualitative information related to the surface morphology of the 3D printed parts as a function of printing parameters, analyzing in particular the quality of inter-layer adhesion. The specimens were gold sputtered and observed with a FEI QUANTA 200 FEG scanning electron microscope.

5.4.6 3D printed brace and patient test

A 16-year-old female subject affected by AIS volunteered to test a 3D printed scoliosis brace. The patient was already using the traditional back brace for the treatment of AIS for about 1 year.

Reverse engineering of the thermoformed back brace

A virtual replica of her latest thermoformed back brace was created by reverse engineering. The infrared triangulation scanner Structure Sensor was used connected to a computer via USB and controlled with the software Skanect. This sensor was already evaluated and considered adequate for this orthopedic application, as reported in [86].

After the initial scan, the model was imported in a free mesh sculpting software, Autodesk Meshmixer [6]. The mesh was repaired and the model was cleaned by removing the straps from the external front surface. In this region, the inner surface of the brace was used as a reference to recreate the external geometry. Finally, the model was completed by deleting the whole internal surface, cropping the border and applying a uniform thickness of 2.2 mm to produce the final solid model to be imported in the slicing software, Ultimaker Cura.
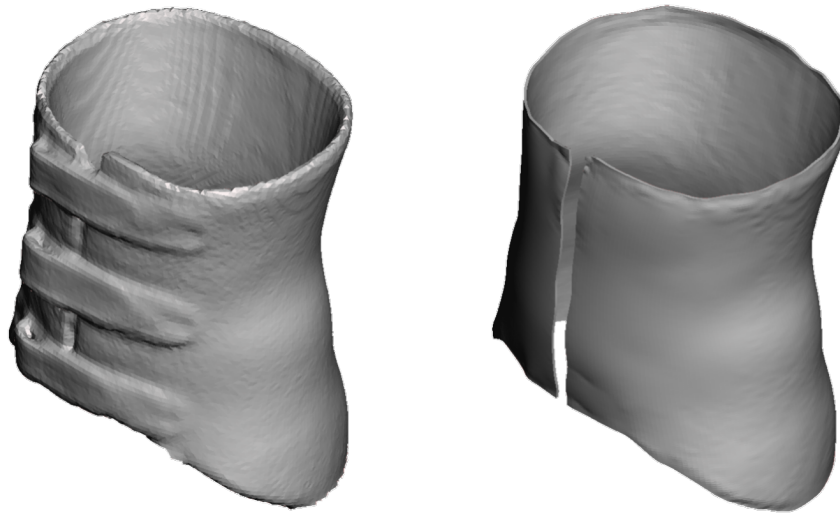
Figure 5.14: *Scanned model of the brace on the left and printed model after stripe removal and proper thickening.*

Full brace 3D printing

The back brace was printed in PETG (by FiloAlfa). The nozzle temperature and the printing speed were the same used for PETG hemicylindrical samples. The layer height was set to 0.6 mm, as a compromise between printing time and surface finishing.

We decided to print the brace upside-down instead of the normal vertical direction in order to minimize the amount of the supports required by the lower border, not equivalent to a flat plane cut. A small support was produced with a single line deposition but setting the path to "zig-zag" as a compromise between a good stability and the ease to remove the supports from the brace.
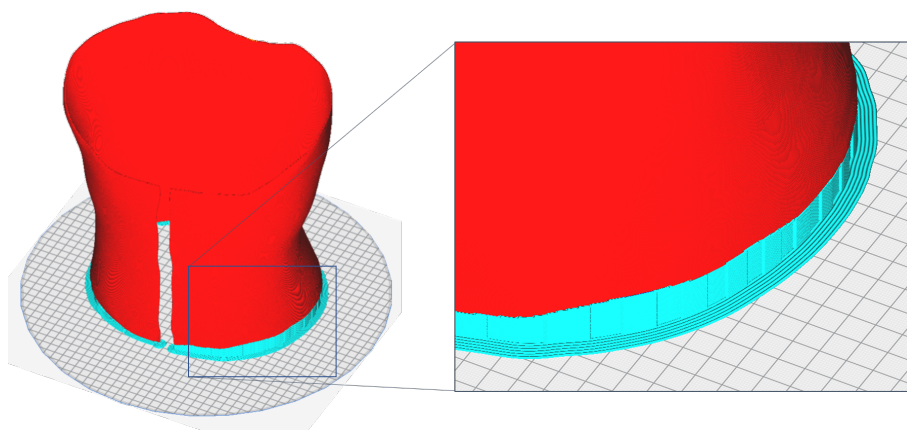
Figure 5.15: *Printing setup of the brace in Ultimaker CURA, where the model is depicted in red and the supports in blue.*

5.4.7 Qualitative analysis of the back brace on a patient

An expert technician finished the brace with laces and straps. The printed brace was tested by the patient. In order to evaluate this pilot case study, a direct feedback was requested to the patient regarding the comfort and the general comparison, in respect to the traditional brace produced by thermoforming, asking to complete an *ad-hoc* questionnaire. Thermal images were obtained using the FLIR ONE thermal camera to compare loading and unloading areas of both the 3D printed and the thermoformed braces. These pressure points define the correction of the scoliosis, but also influence the comfort of the brace itself.
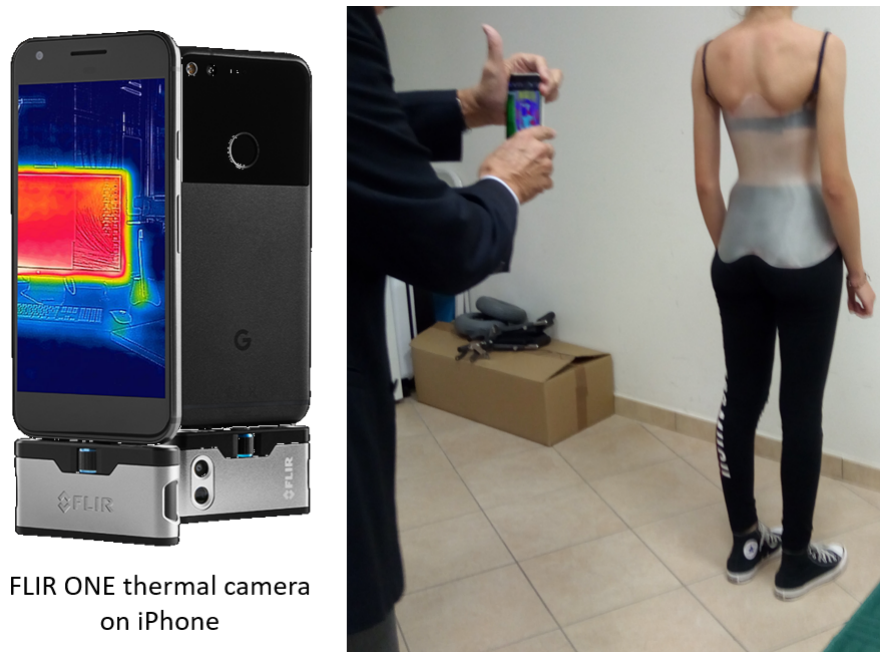
FLIR ONE thermal camera
on iPhone

Figure 5.16: *Termal camera used for qualitative assessment by the physician.*

5.5 Materials analysis

All the printed hemicylinders were initially observed with the naked eye and manually tested also by the physician and the orthopedic technicians. Figure 5.17 shows part of these samples, considering also the materials that were excluded for the declared properties or because unable to be printed on the selected printer. This could seem a trivial test but the idea was to obtain an initial response based on their life-long experience in the orthopedic field. Without telling them the declared characteristics of the materials, they could classify the samples properly, all agreeing on selecting the possible ones: normal PLA, flexible PLA and PETG. As a result of the material selection, the characterization was then performed only on the standard PLA and the PETG.

5.5.1 Mechanical characterization

FDM printed parts presented different mechanical behaviour depending on the building orientation. In terms of elastic modulus, PETG and PLA showed similar behaviour
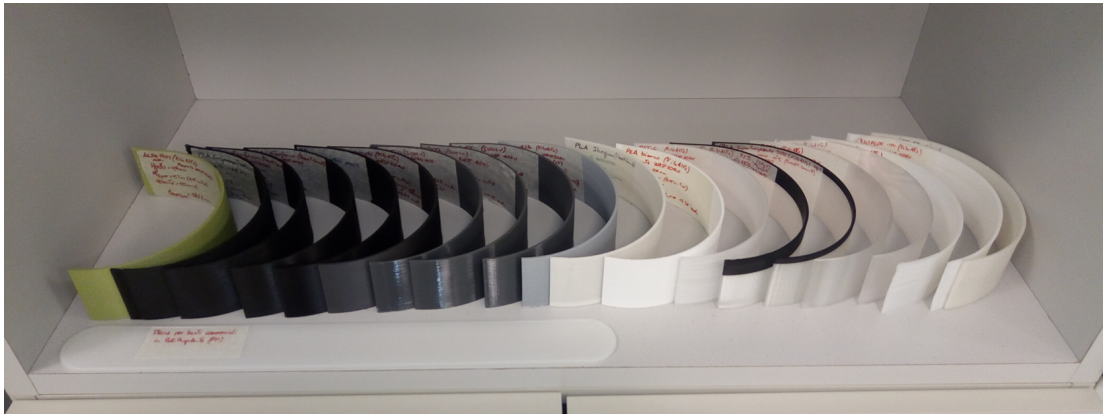
Figure 5.17: *Hemicylindrical samples for mechanical tests.*

if tested along fibres direction. Printing speed and layer thickness do not have great influence on mechanical performance, both for PLA and PETG. The elastic modulus (E') for PETG and PLA printed part are $1489, 93 \pm 39, 05$ MPa and $1358, 17 \pm 54, 21$ MPa respectively. However, the two polymers exhibit different behaviour in term of elongation at break (ϵ_r) that are $211, 00 \pm 11, 00$ for PETG and $17, 77 \pm 4, 90$ for PLA.
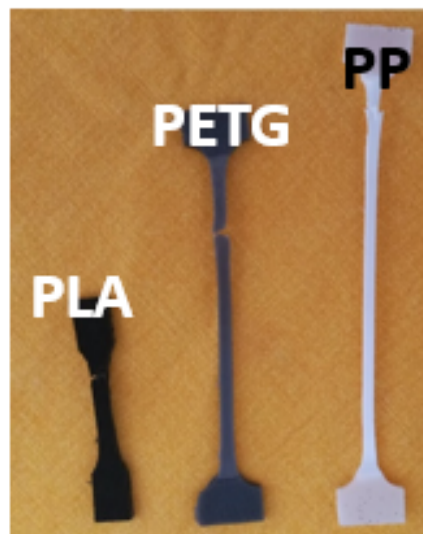
Figure 5.18: *Mechanical Tests Sample Rupture.*

Results showed that FDM parts presented different mechanical response depending on how the layers were placed regarding the direction, of the load. Mechanical characterization and Morphological analysis reveal that PETG parts showed better elongation at break and really good interface between layers. So, it is possible to conclude that is the best materials better than PLA for the realization of back brace in medical applications.

The PP presented a very high elongation to rupture, with values of about 300 %. PETG reached about 200 % in the direction of the fibers (parallel to the printing plate), while in the transverse direction the material behaved as fragile, comparably to the

behavior of PLA in both directions. The comparison of the rupture values is not reported here, preferring the elongation to yielding. In the final application, the material should not overcome the irreversible deformation, otherwise the designed shape would be permanently altered. The elongation to rupture could be representative only of a safety factor for the case of impacts and energy absorption, but if the deformation goes beyond the elastic limits, the brace should be changed.

Figures 5.19, 5.20 and 5.21 report the comparison of the PLA and PETG in respect to the PP, depicted with an horizontal green line due to the fact that was not printed but taken from a commercial sample plate. The test on each layer dimension was repeated 3 times, for this reason the histograms represent the average values while the black error bar are representative of the measurement variation.
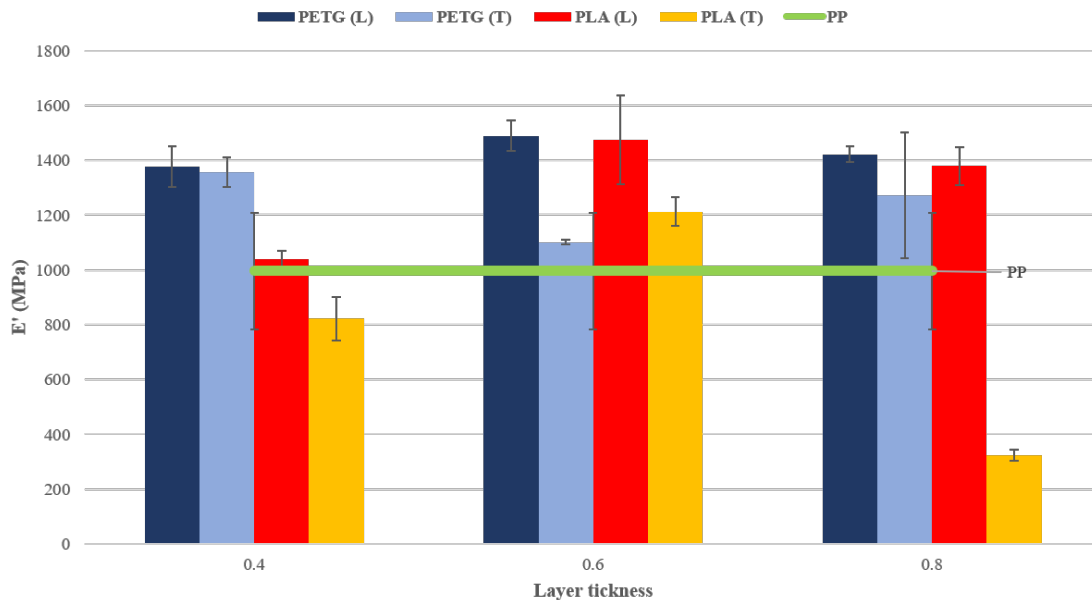
Figure 5.19: *Results of the Elastic Modulus from the experimental mechanical tests.*

5.5.2 Morphological analysis

The specimens printed with PLA presented an evident irregularity of the surface, as shown in Figure 5.22 due to the printing process. Moreover, it was possible to analyze the quality of the inter-layer adhesion, which resulted discontinuous with cavities and defects. This low quality of the connection is coherent with the results of the mechanical characterization. Instead, the morphological analysis revealed good surface finish for the PETG samples and optimal cohesion between fibers with different layer heights (see Figure 5.23), even if the tensile stresses showed the brittleness of such connection. This could be due to the different temperature when the new layer is deposited on the previous one that already solidified.

Figure 5.20: *Results of the elongation to yield from the experimental mechanical tests. In case of brittle behavior, the elongation displayed refers to the rupture.*
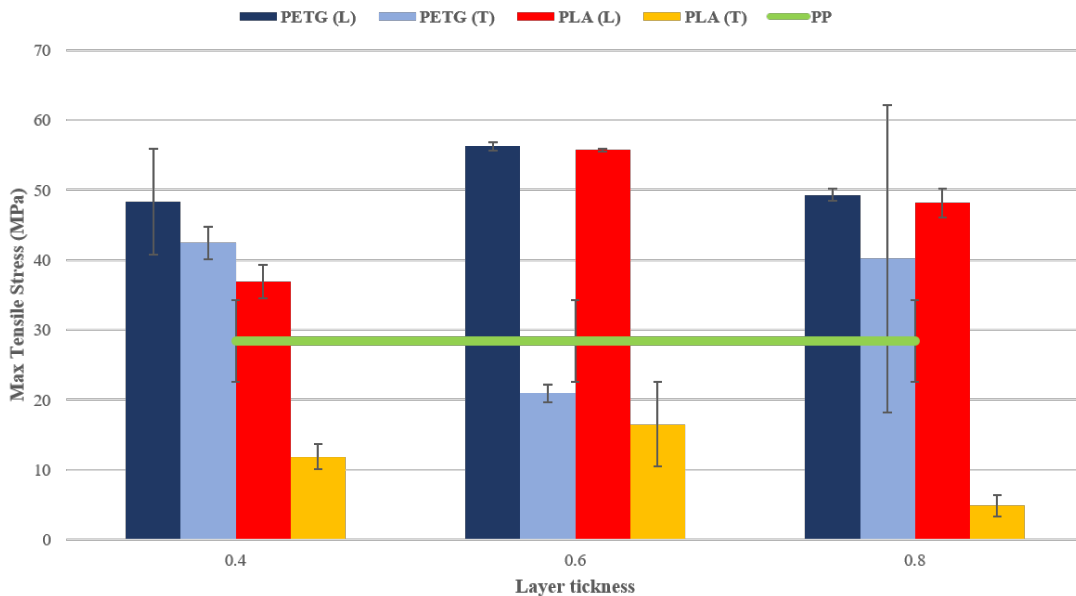
Figure 5.21: *Results of the maximum tensile stresses from the experimental mechanical tests.*

5.6 3D printed back brace and preliminary patient test

The time for acquiring the model of the patient's old brace was of about one minute. The brace was carefully acquired for both the outside and the inside surfaces. When scanning the patient wearing the brace, the time was reduced to about 20 seconds because the only surface acquired was the external one. In addition, the rest of the patient's body helped the alignment of the frames, allowing a faster movement of the
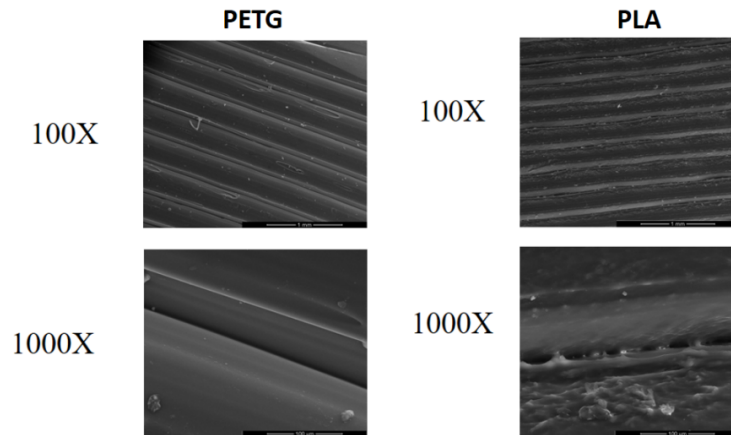
Figure 5.22: *Comparison of the interlayer adhesion between PLA and PETG using SEM.*
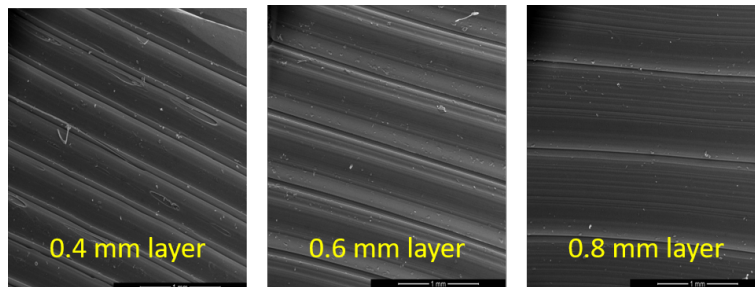
Figure 5.23: *Morphological analysis on PETG with different layer heights.*

scanner.

The model had to be manually cleaned to perform the extraction of the single surface to be then thickened. This part of the process took about 1 hour to be completed. The final brace was printed in the vertical direction with limited supports. The time require to complete the print was of 4 hours 30 minutes. A certified technicians completed the finishing for the border and applied the closure straps, using the traditional tools available in the orthopedic center, for an additional half an hour of time.

The overall time for completing the entire production would be comparable to a full working day, as required by the modern thermoforming process. Moreover, it has to be considered that in the printing time, the technician does not have to stay controlling the printer, but can work on other products in parallel. Finally, once the production reaches stable settings, the printers could also run during the night without any supervision, thus reducing the total man-hours.

The 3D printed orthosis resulted slightly shorter than the original existing orthosis for two possible effects. The first could be related to the possible error in the cleaning phase, when cropping the surface according to the border. The second could be due to the post processing operations performed by the orthotist, when removing the supports and smoothing the borders for the comfort of the patient.

The PETG did not present any visible defect and the inter-layer adhesion seemed to be corresponding to the one of the samples. In particular, during the opening of the brace for being worn, the material did not show any delamination and the patient

managed to wear it without any difference in respect to the traditional one.

Figure 5.24: *Test of printed brace with patient.*

5.6.1 Patient test and response

The patient wore the brace as prescribed by the physician for a period of about 4 months. The main differences in respect to the thermoformed one were the stiffness, the apparent brittleness and the height of the brace.

According to the patient, the 3D printed brace was stiffer than the thermoformed one, improving the supporting action. She also reported a possible increased brittleness that caused a bit of anxiety during different activities, with the fear of breaking the brace. However, she was also conscious that the orthosis would have not been harmful.

The different height of the 3D printed brace, that can be related to an approximation error on the top border of the brace when 3D scanning it, actually improved the wearability and the overall comfort, while reducing the pain of the old brace. Finally, the patient stated to find the semi-transparent aesthetics of the 3D printed brace to be better than the traditional white one.

5.6.2 Physician/technician response and comparison

The orthopedic physician controlled the interaction of the brace with the patient by means of the FLIR ONE thermal camera, mounted on his smartphone. Figure 5.25 shows the visual comparison the doctor performed and the temperature measurements in few relevant points. The final response of the physician after this comparison resulted in an equivalent loading condition and a negligible temperature difference between the two braces.

Another comment of the physician regarded the material properties. He confirmed the idea of the patient, the brace is effectively stiffer. The important annotation regards the good function of a stiffer material for applying a stronger correction, also in those cases of older patients with AIS where the spine becomes less flexible. Moreover, he noticed how this solution could be comparable to the stiff braces with metal rods (*e.g.* Milwaukee and Sforzesco braces) but with the advantage of a reduced mass and an increased acceptability. According to him, indeed, the patients usually do not like the old-style braces with metal rods.
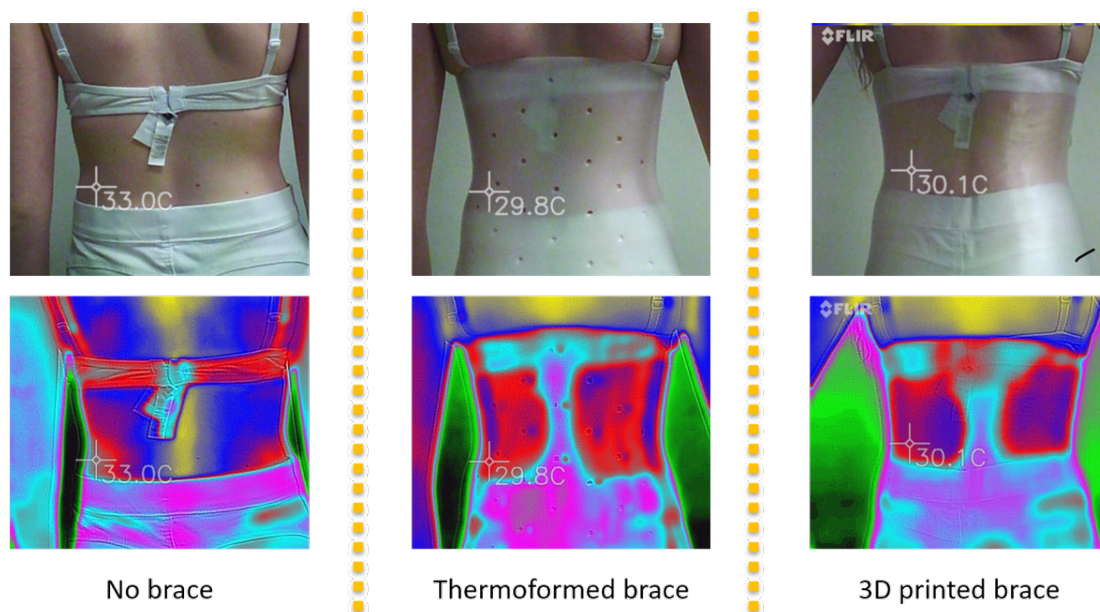
Figure 5.25: *Thermographic pictures of the brace.*

The orthopedic technicians who post-processed the brace found some differences in term of machinability. The use of the jig saw had to be avoided, because of possible delamination of the printed layers. Also the creation of the holes for the rivets that hold the closure straps had to be performed more carefully and with a lower drilling speed. Nevertheless, they found no limitation in using the grinder, both with rough and fine sandpaper wheels for removing material and with a felt grinder wheel for smoothing the border.

They also performed a typical manual test for the stiffness by moving the front edges alternatively up and down and by forcing the opening gap. The first resulted to be comparable to the thermoformed braces, while for the second they noticed a stiffer behavior.

As a conclusion, all the involved people (patient, physician and technicians) noticed the stiffer behavior of the brace, but did not define it to be bad. One of the relevant aspects is the brittleness that arises from the manufacturing process, with the delamination effect of limited interlayer connection, in the transverse direction. The material itself has an elasto-plastic behavior with a reduced elongation to rupture in respect to the thermoformed PE. Nevertheless, the brace should not work beyond the yield stress otherwise the shape would be modified.

Figure 5.26: *Manual post-processing of the 3D printed brace with rough and smooth grinders for the border.*

Clinical protocol

A clinical protocol was thus presented for the experiment with more patients, as part of the project EMPATIA@Lecco, which was approved in June 2019. The trial has started and the first patients were recruited. The protocol includes children and adolescents with scoliosis and consists of 3 visits at a time distance of about two weeks.

In the first visit, which takes place in a lab of the IRCCS E.Medea, the patient performs some basic tests for walking and standing straight both with and without the thermoformed brace. Then the patient's body is scanned and also the orthosis is acquired. Finally, the patient has to fill in a survey about the use of the scoliosis brace.

During about two weeks, the patient wears the thermoformed brace. In the meanwhile, we have to design the brace either from the thermoformed brace (if very recent and without issues) or from the patient's skin model. Then the brace can be 3D printed and delivered.

The second visit takes place in a orthopedic centers, where the technicians test the brace with the patient and can complete the finishing operations, such as cutting more border in certain regions (typically close to the legs for sitting), smoothing the border,

drilling the holes and apply the strap closure system. The physician can then compare the braces by using the FLIR ONE thermal camera.

The patient has to wear the 3D printed brace for other two weeks, after which the third visit can take place in the same lab of the first visit. Here, the same walking and standing tests are performed with the new brace and without any. Finally, a new survey is filled in order to obtain a feedback about the new brace in comparison to the thermoformed one.

In addition, some of the patients will be tested also by acquiring the temperature variation of the brace along the day, in order to verify the compliance to the prescribed therapy and to compare the auto evaluation achieved by compiling a usage agenda.

5.7 Final remarks

Among the available polymer Additive Manufacturing technologies, the FFF resulted to have the best compromise in terms of costs, speed and resolution. Moreover, the selected delta printer (WASP 4070) well behaved considering the final application.

In order to evaluate the different materials and choose the most appropriate for the final application, an initial selection was performed with the comparison of both databases and datasheet of the filament producers. A hemicylindrical sample was adopted both for optimizing the printing settings and for testing the performances of the materials in conditions similar to the final application, as opposed to the typical flat specimens that are printed with predefined orientations.

Two filaments were chosen, PLA and PETG, and printed samples were characterized with mechanical test. Moreover, a morphological analysis was performed using the electronic microscope to have a qualitative result about the layer adhesion. Results showed that FDM parts presented different mechanical response depending on how the layers were placed regarding the direction, of the load. Mechanical characterization and Morphological analysis reveal that PETG parts showed better elongation at break and really good interface between layers. So, it is possible to conclude that it is better than PLA for the realization of back brace for in medical applications.

Moreover, having a physical sample to be handled represented a great opportunity to discuss about the material choice with orthopedic technicians. In fact, they usually rely their choices on the experience, more than considering the numerical values of the mechanical properties. For instance, touching and deforming a cylinder-shaped sample has been considered more comparable to their experience with a back brace. On the other hand, it has to be noticed that the brace is not completely comparable to a cylinder jwith the single curvature. This can be typically found only in limited regions close to the upper (ribcage) and lower (pelvis sides) borders, while the central zone around the belly button has a double curvature, thus resulting stiffer.

Finally, a 3D printed brace was produced based on the existing thermoformed brace of a volunteer patient. The results were positive, both according to the patient and according to the orthopedic physician and technicians. The test was considered successful and showed both the feasibility of the process and the possible competitiveness of the 3D printing manufacturing in respect to both traditional and modern production processes. In particular, the overall time is expected to satisfy the single full-working day requirement, with the clear reduction of the man-hours related to the manual operations

of the other processes. For these reasons, a clinical protocol for an extended experiment with 10 patients was submitted and approved in the Scientific Institute E. Medea.

Discussion and Conclusions

In the single chapters a precise discussion of the separate topic is proposed, here instead a general evaluation of the whole process composed of the different steps is described.

6.1 Main Contribution and Overall Considerations

As presented in **Chapter 1**, the current manufacturing is still strongly handcrafted and manual. Therefore, the thesis proposed improvements under different aspects: low-cost 3D scanning for acquiring the patient's external anatomy, virtual modeling with CAD software and design support with a 3D pseudo-parametric skeleton model, use of numerical simulation for verifying the quality of the designed shape, and directly 3D printing the brace without the use of a positive mold.

In **Chapter 2**, a set of 3D scanners were compared using the standard test objects, as required by the VDI/VDE 2634 guidelines (flat plane and spheres). Beyond this common practice in the field, I also used three mannequin parts that are representative of different anatomical regions, typical of the orthopedic applications. The hand, the thigh and the chest enabled to investigate the behavior of the scanners with organic shapes, as the human body, with different levels of detail and different acquired volumes.

The results demonstrated the higher accuracy of the fixed devices in respect to the hand-held ones. However, the total time and the setup required to complete the acquisitions with the mannequin parts did not meet the requirements for a possible final application with a real patient. The hand-held devices instead enabled performing a fast reconstruction of the chest model in about 20-30 seconds. This limit is acceptable for a person that has to stand as still as possible in the straight position in order to be reconstructed.

In the comparison between Artec Leo, Structure Sensor, the two Kinect (V1 and V2) and the Rodin4D O&Pscan, the results clearly showed the higher quality of the Artec Leo, which is not a low-cost device due to the price beyond 25k€. The old but expensive manual laser scanner, developed for orthopedic applications by Rodin4D, has proved to have issues for the alignment of the acquired strips, probably related to the magnetic tracking system. Among the low-cost devices, the Structure Sensor demonstrated better accuracy than the Kinects.

The accuracy of the Structure Sensor on the plane was limited to about 1.6 mm and the deviation in the acquisitions with the mannequin parts was below 0.6 mm. These values satisfy the requirements of the orthopedic application for the back braces design. Another advantage of this a device is the possibility to be used both connected to a computer, using the software Skanect, for obtaining models with high resolution and mounted on a tablet to work in free hand-held mode in any location. This last configuration is important for the end-users of orthopedic workshops that would acquire the patient's chest in the available room. For all these reason we can state that this scanner is the most appropriate among the tested ones for the introduction of a low-cost 3D scanning technique in the orthopedic field.

Finally, the Structure Sensor used as a handheld scanner was also tested with different user's motions around the chest to evaluate the stability of the approaches, due to the fact that the acquisition is the input to model the brace with CAD tools. Performing two full laps around the chest instead of a single lap, keeping a constant speed, did not show significant improvements. The analysis on the smaller region of the hip demonstrated that moving the scanner up and down, or tilting it, while moving around the patient improves the acquisition. The technician should acquire the patient's chest as fast as possible, but paying articular attention to the movement speeds because of the limited frame rate (resulting in eventual blurring) and for possible issues in the alignment of the frames.

Chapter 3 describes an initial analysis of the current sculpting and modeling tools to deal with the tessellated models. This showed that all the commands necessary for shaping the brace are already currently available in different software packages. However, there are still some issues related to finding a single software that provides all of them. For example, the free Autodesk Meshmixer has many tools for sculpting, but not for deforming the model according to predefined axes, such as the bending option available in the orthopedic-oriented software. The tests with Rodin4D Neo showed it is one of the most complete, but it still lacks the possibility to thicken the surface for creating the solid model needed for 3D printing, thus requiring to pass from a software to another.

However, in all software packages, the modeling is performed without any 3D reference of the internal organs of the patient. The technicians can import the bi-planar X-ray images, but they have to imagine the three-dimensional spatial position of the bones in respect to the acquired 3D skin model. Other studies presented either fine models for visualization (*e.g.* for medical education purposes) or complex models but limited to the spine or portions of it (*e.g.* for structural comparison of vertebral rod fixations). For this reason, I developed a pseudo-parametric 3D skeleton model in Autodesk Maya, starting from a patient-specific reconstruction of medical images, containing the

whole chest bones.

The model presented in this thesis was developed both for visualization purposes during the brace modeling phase and for the possible in-silico validation of the designed brace. For the first goal, I used the low polygonal tessellated format. For the validation step, I created another version composed of NURBS models in order to use more easily the numerical simulations. The skeleton can be quickly morphed by controlling the joints of a kinematic chain to which each bone is connected. The deformation and customization of the skeleton, by translating, rotating and scaling the bones, was tested with a real patient based on the bi-planar X-ray projections. It was then compared also to the reconstruction obtainable with the segmentation of CTscan images.

The results showed that the models can be used efficiently for the purpose of visualization and brace modeling. The time required to morph the skeleton model based on the frontal and lateral projections of the X-rays images reaches values below 20 minutes for a trained user. This would be important to avoid the invasive radiations of CT scans, allowing to have a patient-specific skeleton model for the standing posture, to be embedded in the skin model acquired with external 3D scanning.

In **Chapter 4**, I described the use of FEM simulations to test the above-mentioned skeleton model, analyzing the interaction between the patient and the scoliosis brace. The final goal is to use such approach in the design loop before 3D printing the final brace. In addition to the scoliosis brace, I tested the possibility of using the latest Topology Optimization tools by considering the simpler case of a wrist orthosis constrained as a cantilever beam, thus avoiding the interaction with the anatomical model of the arm.

The first set of simulations on the scoliosis brace successfully proved the feasibility of using the simplified patient-specific skeleton model I developed, with the goal of obtaining a qualitative indication of where the loading is applied in respect to the scoliotic curve. The verification of the interaction between the designed brace and the patient's body is relatively quick, requiring about 1 hour 10 minutes for the fixed brace approach, on a medium quality notebook. Nevertheless, the approximation of fixing the skeleton to the ground prevents the patient model from bending under the brace action. However, the goal of these simulations was to obtain an indication for the brace design and not to verify the corrective effects on the patient, which would depend on many different aspects, such as the personal flexibility and the compliance to treatment (bracing and physical therapy). For this reason, further research is required for improving the model adding a flexible connection, at least between the vertebrae.

Also the Topology Optimization tests performed well with the smaller case of a wrist orthosis. The absence of the anatomical model of the arm and the substitution with a roller supported cantilever beam scheme enabled obtaining fast solutions. The Static Structural simulations took less than a minute, while the iterations required by the TO increased the time to about 6 minutes. This can be considered to be acceptable for such a simple case, but could bring to an exponential increase in the time to solve the more complex case of the scoliosis brace with the patient's body interaction problem.

In order to select the proper AM technology, a comparison based on printing volume, speed, cost and resolution of the machines was performed and described in **Chapter**

5. The FFF delta printer WASP 4070 was accordingly chosen, as it satisfies the requirements for the final application: build volume able to contain a full brace, high speed for printing in a working day, cost under 10k€, material costs comparable to the thermoformed ones (*i.e.* about 40€per brace).

With the goal of identifying the printable material that could best substitute the thermoformed PolyPropylene, a set of filament spools available on the market was analyzed. A hemicylindrical test object was used to assess the printing settings and compare the results. The shape is in contrast with the traditional flat samples printed with predefined orientations, but it is more representative of the printing settings for the final application with the back braces. A mechanical characterization was performed only for PLA and PETG, based on expert screening. For these two materials, the properties were analyzed with tensile stress tests, impact tests and SEM examination. The results proved that the PETG was better than PLA in terms of elastic modulus and interlayer adhesion, having as a reference the thermoformed material PP.

Finally, a test was performed with a volunteer patient with scoliosis, by 3D scanning her current thermoformed brace, reconstructing its shape and printing it with the chosen PETG and the selected settings. The printing time was limited to 4 hours 30 minutes, thus satisfying the requirement of maximum 8 hours. The patient wore the brace without finding any big difference in comparison to the thermoformed one. The physician and the orthopedic technicians stated that the brace was slightly stiffer even with a reduced weight. This means providing a better support action for the spine alignment, without the disadvantages of the current braces. Indeed, Milwaukee and Sforzesco types present metal bars that increase the weight and reduce the possibility to be hidden under the clothes.

Since the test was successful, a clinical protocol was submitted and approved in the Scientific Institute E. Medea. This pilot study aims to test the 3D printed braces with 10 patients, with the main goal of comparing the differences in comfort and usability of the new braces with respect to the thermoformed ones.

As a general conclusion, the thesis demonstrated the feasibility of the proposed process step by step in the different chapters. The integration of the multiple components and of the various software packages would allow to better design the brace and obtain a more reliable 3D printed product.

6.2 Future Works

For the different production phases analyzed during the project, some possible improvements are still available and are reported in the following section.

Full body scanners and integration with X-ray system

Future analysis of the 3D scanners should consider also the full body scanners. These have been excluded for the present study for incompatibility of available space and budget for the use in orthopedic centers; however, it could be useful to integrate them in the bi-planar x-ray imaging systems. This combined acquisition would enable a precise and automatic alignment of the 3D skeleton model inside the skin surface, considering

the limited time of acquisition (some scanners take only one second) and the same posture of the patient.

PCA for 3D skeleton morphing

An evolution of the 3D skeleton morphing, considering the X-ray images of the patient, should integrate the use of the Principal Component Analysis (PCA). This would enable obtaining a semi-automatic scaling and deformation of the bones, thanks to the use of a set of markers on the images. This approach could based on the work on the mandible morphing presented by Pascoletti [79], which was presented in the ADM 2019 International Conference I attended.

Personalized spine flexibility

The skeleton model should be improved by adding flexible components connecting the bones (disc, cartilages and ligaments). This should not only consider the anatomically correct information about the 3D models, but also enable running more realistic numerical simulations with the adaptation of the spine curve under the action of the brace. Particular attention should be provided for the definition of the connections properties, which can vary significantly between different subjects, mainly when considering pathological cases where the spine flexibility is decreased. Thus, new research should consider testing experimentally the values of the stiffness in the different regions of the spine.

Other 3D printers

The future test of different 3D printer for the final application could consider the use of FDM machines with pellet extruders, maybe optimized for avoiding air bubbles, instead of the only filament. This would allow both the reduction of the material costs, since the pellet cost is usually about 1/10 of the equivalent filament, and also the use of a customized mix of polymers, which could help obtaining a variable material property along the brace. Moreover, new material mix could be created in order to improve the characteristics in terms of Elastic Modulus and Tensile Yield Elongation, without losing in terms of stress resistance.

Use multi-material printers

In addition, we could also think of using the simple FFF machines, but with a dual extruder in order to produce a brace composed of two different shells: a stiff frame with the optimized topology, on the outer side, and a soft layer for the interaction with the patient's body, in the inside, as suggested already in [87].

Clinical study and HTA

In order to properly establish the quality of the results obtainable with AM, deeper analyses involving larger populations should be performed. These could regard the use of all the tools described in the thesis and include the use of other printers and materials. The main goal should be to define the difference in terms of correction of the spine during a long period of time. For this, it should also consider in parallel the

effects on production costs and time, and the possible change of the business model of the orthopedic workshops.

Bibliography

[1] 3D Systems. Prox sls 6100. `https://www.3dsystems.com/3d-printers/prox-sls-6100`. Accessed: 2019-12-1.

[2] 3Dsystems.

[3] Additive Blog. 3d printing and design. `https://www.additive.blog/`. Accessed: 2019-12-1.

[4] AlignClinic. Formetric 4d system. `http://www.align-clinic.com/advancedtechnology.html`. Accessed: 2019-12-1.

[5] M. G. Antonelli, P. Beomonte Zobel, F. Durante, and T. Raparelli. Additive manufacturing applications on flexible actuators for active orthoses and medical devices. *Journal of healthcare engineering*, 2019.

[6] Autodesk. Autodesk meshmixer: Free software for maxing awesome stuff. `http://www.meshmixer.com/`. Accessed: 2019-12-1.

[7] BA-HEM ortopedi. Rodin4d cnc skolyoz kalibi isleme ve kesme islemi. `https://www.youtube.com/watch?v=KM5SNabbtW4`, 2012. Accessed: 2019-12-1.

[8] C. S. Bamji, P. O'Connor, T. Elkhatib, S. Mehta, B. Thompson, L. A. Prather, D. Snow, O. C. Akkaya, A. Daniel, A. D. Payne, et al. A 0.13 μm cmos system-on-chip for a 512$\times$ 424 time-of-flight image sensor with multi-frequency photo-demodulation up to 130 mhz and 2 gs/s adc. *IEEE Journal of Solid-State Circuits*, 50(1):303–319, 2014.

[9] J. Banks. Adding value in additive manufacturing : Researchers in the united kingdom and europe look to 3d printing for customization. *IEEE Pulse*, 4(6):22–26, 2013.

[10] G. Baronio, S. Harran, and A. Signoroni. A critical analysis of a hand orthosis reverse engineering and 3d printing process. *Applied bionics and biomechanics*, 2016.

[11] G. Baronio, P. Volonghi, and A. Signoroni. Concept and design of a 3d printed support to assist hand scanning for the realization of customized orthosis. *Applied Bionics and Biomechanics*, 2017.

[12] S. L. Bevill, G. R. Bevill, J. R. Penmetsa, A. J. Petrella, and P. J. Rullkoetter. Finite element simulation of early creep and wear in total hip arthroplasty. *Journal of Biomechanics*, 38(12):2365–2374, 2005.

[13] BioSculptor. Biosculptor innovative solutions. `http://biosculptor.com/`. Accessed: 2019-10-11.

[14] M. Carfagni, R. Furferi, L. Governi, M. Servi, F. Uccheddu, and Y. Volpe. On the performance of the intel sr300 depth camera: metrological and critical characterization. *IEEE Sensors Journal*, 17(14):4508–4519, 2017.

[15] M. Ceran. *Parametric human spine modelling*. PhD thesis, Loughborogh University, 11 2006.

[16] P. Cerny and I. Marik. Idiopathic and congenital spinal bracing of the czech children. In *The 8th Prague-Sydney-Lublin Symposium*, 04 2007.

[17] S. L. Chan, K. MC. Cheung, K. D. K. Luk, K. W. H Wong, and M. S. Wong. A correlation study between in-brace correction, compliance to spinal orthosis and health-related quality of life of patients with adolescent idiopathic scoliosis. *Scoliosis*, 9(1), 2014.

Bibliography

[18] J. C. Cheng, R. M. Castelein, W. C. Chu, A. J. Danielsson, M. B. Dobbs, T. B. Grivas, C. A. Gurnett, K. D. Luk, A. Moreau, P. O. Newton, et al. Adolescent idiopathic scoliosis. *Nature Reviews Disease Primers*, 1:15030, 2015.

[19] N. Chitresh, A. Singh, and C. Himanshu. Customised prosthetic socket fabrication using 3d scanning and printing. In *Additive Manufacturing Society of India*, 2014.

[20] J. Clin, C. E. Aubin, S. Parent, and H. Labelle. A biomechanical study of the Charleston brace for the treatment of scoliosis. *Spine*, 35(19):E940–7, 2010.

[21] J. Clin, C. E. Aubin, S. Parent, and H. Labelle. Biomechanical modeling of brace treatment of scoliosis: effects of gravitational loads. *Medical & Biological Engineering & Computing*, 49(7):743–753, 2011.

[22] G. Colombo, C. Comotti, D. F. Redaelli, D. Regazzoni, C. Rizzi, and A. Vitali. A method to improve prosthesis leg design based on pressure analysis at the socket-residual limb interface. In *ASME 2016 International Design Engineering Technical Conferences and Computers and Information in Engineering Conference*. American Society of Mechanical Engineers Digital Collection, 2016.

[23] G. Colombo, G. Facoetti, and C. Rizzi. A digital patient for computer-aided prosthesis design. *Interface focus*, 3(2), 2013.

[24] Comite Europeen de Normalisation. Ergonomics - 3-d scanning methodologies for internationally compatible anthropometric databases - part 2: Evaluation protocol of surface shape and repeatability of relative landmark positions. Standard, Comite Europeen de Normalisation, Brussels, Belgium, May 2017.

[25] C. Comotti, D. Regazzoni, C. Rizzi, and A. Vitali. Additive Manufacturing to Advance Functional Design: An Application in the Medical Field. *Journal of Computing and Information Science in Engineering*, 17(3):31006–31009, feb 2017.

[26] A. Courvoisier, M. Nesme, J. Gerbelot, A. Moreau-Gaudry, and F. Edgard Faure. Prediction of brace effect in scoliotic patients: blinded evaluation of a novel brace simulator - an observational cross-sectional study. *European Spine Journal*, 28:1277–1285, 2019.

[27] X. Cui, T. Boland, D. D. D. Lima, and M. K. Lotz. Thermal inkjet printing in tissue engineering and regenerative medicine. *Recent Patents on Drug Delivery & Formulation*, 6(2), 2012.

[28] G. Devedzic, B. Ristic, M. Stefanovic, S. Cukovic, and T. Lukovic. Development of 3d parametric model of human spine and simulator for biomedical engineering education and scoliosis screening. *Computer Applications in Engineering Education*, 20(3):434–444, 2012.

[29] N. M. DiFilippo and M. K. Jouaneh. Characterization of different microsoft kinect sensor models. *IEEE Sensors Journal*, 15(8):4554–4564, 2015.

[30] C. E. Dombroski, M. E. R. Balsdon, and A. Froats. The use of a low cost 3d scanning and printing tool in the manufacture of custom-made foot orthoses: a preliminary study. *BMC research notes*, 7(1):443, 2014.

[31] EOS. Eos imaging. `https://www.eos-imaging.us/us/professionals/eos/eos`. Accessed: 2019-11-10.

[32] S. Negrini et. al. 2016 sosort guidelines: orthopaedic and rehabilitation treatment of idiopathic scoliosis during growth. *Scoliosis and Spinal Disorders*, 13(3), 2018.

[33] A. Fedorov, R. Beichel, J. Kalpathy-cramer, J. Finet, J. C. Fillion-robin, S. Pujol, C. Bauer, D. Jennings, F. Fennessy, M. Sonka, J. Buatti, S. Aylward, J. V. Miller, S. Pieper, and R. Kikinis. 3D Slicer as an image computing platform for the Quantitative Imaging Network. *Magnetic Resonance Imaging*, 30(9):1323–1341, 2012.

[34] FormLabs. Form3l. `https://formlabs.com/it/3d-printers/form-3l/`. Accessed: 2019-12-1.

[35] D. Fortin, F. Cheriet, M. Beauséjour, P. Debanné, J. Joncas, and H. Labelle. A 3D visualization tool for the design and customization of spinal braces. *Computerized Medical Imaging and Graphics*, 31(8):614–624, 2007.

[36] M. Galvez, T. Asahi, A. Baar, G. Carcuro, CuchacovichN., J. A. Fuentes, R. Mardones, C. E. Montoya, R. Negrin, F. Otayza, G. M. Rojas, and A. Chahin. Use of three-dimensional printing in orthopaedic surgical planning. *Journal of the American Academy of Orthopaedic Surgeons. Global Research & Reviews*, 2(5), 2018.

[37] I. Gibson, D. W. Rosen, and B. Stucker. *Additive manufacturing technologies*, volume 17. Springer, 2014.

[38] A. C. Godest, M. Beaugonin, E. Haug, M. Taylor, and P. J. Gregson. Simulation of a knee joint replacement during a gait cycle using explicit finite element analysis. *Journal of Biomechanics*, 35(2):267–275, 2002.

[39] D. Grauer, L. S. H. Cevidanes, and W. R. Proffit. Working with dicom craniofacial images. *American Journal of Orthodontics and Dentofacial Orthopedics*, 136(3):460 – 470, 2009.

[40] G. Guidi, S. Gonizzi Barsanti, and L. Micoli. 3d capturing performances of low-cost range sensors for mass-market applications. *International Archives of the Photogrammetry, Remote Sensing and Spatial Information Sciences*, XLI-B5:33–40, 06 2016.

[41] S. Guidotti. Use of 3d printing in the orthopedic prosthetics industry: evidences on scoliosis chest brace production. Master's thesis, Politecnico di Milano, 12 2019.

[42] J. Harrington, E. Sochett, and A. Howard. Update on the Evaluation and Treatment of Osteogenesis Imperfecta. *Pediatric Clinics of North America*, 61(6):1243–1257, 2014.

[43] M. B. Hoy. 3d printing: Making things at the library. *Medical Reference Services Quarterly*, 32(1):93–99, 2013.

[44] L. Humbert, J. A. De Guise, B. Aubert, B. Godbout, and W. Skalli. 3d reconstruction of the spine from biplanar x-rays using parametric models based on transversal and longitudinal inferences. *Medical Engineering & Physics*, 31(6):681–687, 2009.

[45] Landis International inc. Infrared and convection ovens. `http://landisusa.com/us-en/orthopedic/infrared-and-convection-ovens.html`. Accessed: 2019-10-20.

[46] Y. Jin, J. Plott, R. Chen, J. Wensman, and A. Shih. Additive Manufacturing of Custom Orthoses and Prostheses – A Review. *Procedia CIRP*, 36:199–204, 2015.

[47] J. D. John, G. Saravana Kumar, and N. Yoganandan. Rear-impact neck whiplash: Role of head inertial properties and spine morphological variations on segmental rotations. *Journal of Biomechanical Engineering*, 141(11), 2019.

[48] Bateman C. K. Design, validation, and clinical testing of a novel fastening device for a scoliosis brace. Master's thesis, University of Tennessee Health Science Center, 5 2017.

[49] T. P. Kersten, M. Lindstaedt, and D. Starosta. Comparative geometrical accuracy investigations of hand-held 3d scanning systems-an update. *International Archives of the Photogrammetry, Remote Sensing & Spatial Information Sciences*, 42(2), 2018.

[50] K. Khoshelham and S. O. Elberink. Accuracy and resolution of kinect depth data for indoor mapping applications. *Sensors*, 12(2):1437–1454, 2012.

[51] E. Kosek, J. Ekholm, and P. T. Hansson. Pressure pain thresholds in different tissues in one body region. the influence of skin sensitivity in pressure algometry. *Scandinavian journal of rehabilitation medicine*, 31(2):89–93, 1999.

[52] E. Lachat, H. Macher, T. Landes, and P. Grussenmeyer. Assessment and calibration of a rgb-d camera (kinect v2 sensor) towards a potential use for close-range 3d modeling. *Remote Sensing*, 7(10):13070–13097, 2015.

[53] E. Lachat, H. Macher, M. A. Mittet, T. Landes, and P. Grussenmeyer. First experiences with kinect v2 sensor for close range 3d modelling. *The International Archives of Photogrammetry, Remote Sensing and Spatial Information Sciences*, 40(5):93, 2015.

[54] B. Lange, C. Y. Chang, E. Suma, B. Newman, A. S. Rizzo, and M. Bolas. Development and evaluation of low cost game-based balance rehabilitation tool using the microsoft kinect sensor. In *2011 Annual International Conference of the IEEE Engineering in Medicine and Biology Society*, pages 1831–1834. IEEE, 2011.

[55] D. Law, M. C. Cheung, J. Yip, K. L. Yick, and C. Wong. Scoliosis brace design: influence of visual aesthetics on user acceptance and compliance. *Ergonomics*, 60(6):876–886, 2017.

[56] D. Lee. Spine modeler - g (global and structural deformity). `http://www.dgp.toronto.edu/~dwlee/spinemodelerg/index.html`. Accessed: 2019-11-9.

[57] J. Lee and A. Huang. Fatigue analysis of fdm materials. *Rapid Prototyping Journal*, 19(4):291–299, 2013.

[58] J. Li and H. Tanaka. Feasibility study applying a parametric model as the design generator for 3d-printed orthosis for fracture immobilization. *3D Printing in Medicine*, 4(1), 2018.

[59] J. E. Lloyd, I. Stavness, and S. Fels. Artisynth: A fast interactive biomechanical modeling toolkit combining multibody and finite element simulation. In Yohan Payan, editor, *Soft Tissue Biomechanical Modeling for Computer Assisted Surgery*, pages 355–394. Springer, New York, 2012.

[60] J. E. Lonstein. Milwaukee brace treatment of scoliosis. *Scoliosis Research Society Bracing Manual*, 2003.

[61] E. Lou, D. Hill, D. Hedden, J. Mahood, M. Moreau, and J. Raso. An objective measurement of brace usage for the treatment of adolescent idiopathic scoliosis. *Medical Engineering and Physics*, 33(3):290–294, 2011.

Bibliography

[62] Aniwaa Pte. Ltd. The 16 best 3d body scanners in 2019. `https://www.aniwaa.com/best-3d-body-scanners/`. Accessed: 2019-10-20.

[63] T. Mallick, P. P. Das, and A. K. Majumdar. Characterizations of noise in kinect depth images: A review. *IEEE Sensors journal*, 14(6):1731–1740, 2014.

[64] Discovery District MaRS and University of Copenhagen. Parametric human project. `https://parametrichuman.org/`. Accessed: 2019-11-9.

[65] P. McAfee. Types of scoliosis braces. `http://www.spine-health.com/conditions/scoliosis/types-scoliosis-braces`. Accessed: 2019-11-10.

[66] WASP Med. 3d printing in medicine. `https://www.3dwasp.com/en/3d-printing-in-medicine-waspmed/`. Accessed: 2019-11-10.

[67] Medtronic. Types of braces for scoliosis. `https://www.iscoliosis.com/articles-brace_types.html`, 2007. Accessed: 2019-12-1.

[68] L. Mertz. Dream it, design it, print it in 3-d: What can 3-d printing do for you? *IEEE Pulse*, 4(6):15–21, 2013.

[69] S. Mishra. Application of 3D printing in medicine. *Indian Heart Journal*, 68(1):108–109, 2016.

[70] I. Molnár and L. Morovič. Design and manufacture of orthopedic corset using 3d digitization and additive manufacturing. *IOP Conference Series: Materials Science and Engineering*, 448:012058, 2018.

[71] T. P. Mpofu, C. Mawere, and M. Mukosera. The impact and application of 3d printing technology. *International Journal of Science and Research*, pages 2148–2152, 2014.

[72] R. Munhoz, C. A. C. Moraes, H. Tanaka, and M. E. Kunkel. A digital approach for design and fabrication by rapid prototyping of orthosis for developmental dysplasia of the hip. *Research on Biomedical Engineering*, 32:63–73, 2016.

[73] L. E. Murr, S. M. Gaytan, E. Martinez, F. Medina, and R. B. Wicker. Next generation orthopaedic implants by additive manufacturing using electron beam melting. *International Journal of Biomaterials*, 2012.

[74] R. A. Newcombe, S. Izadi, O. Hilliges, D. Molyneaux, D. Kim, A. J. Davison, P. Kohli, J. Shotton, S. Hodges, and A. W. Fitzgibbon. Kinectfusion: Real-time dense surface mapping and tracking. In *ISMAR*, pages 127–136, 2011.

[75] K. J. L. Ng. A novel 3d printed brace manufacturing process for the treatment of adolescent idiopathic scoliosis. Master's thesis, University of Alberta, 2019.

[76] University of British Columbia. A 3d mechanical modeling system combining multibody and finite element simulation. `https://www.artisynth.org/Main/HomePage`. Accessed: 2019-11-9.

[77] A. Oliver, S. Kang, B. C. Wünsche, and B. MacDonald. Using the kinect as a navigation sensor for mobile robotics. In *Proceedings of the 27th conference on image and vision computing New Zealand*, pages 509–514. ACM, 2012.

[78] D. Pagliari, F. Menna, R. Roncella, F. Remondino, and L. Pinto. Kinect fusion improvement using depth camera calibration. *The International Archives of Photogrammetry, Remote Sensing and Spatial Information Sciences*, 40(5):479, 2014.

[79] G. Pascoletti, M. Cali, C. Bignardi, P. Conti, and E. M. Zanetti. Mandible morphing through principal components analysis. In *Design Tools and Methods in Industrial Engineering*, pages 15–23. Springer International Publishing, 2020.

[80] S. Pasha. *Biomechanical modeling and characterization of the postural parameters in adolescent idiopathic scoliosis*. PhD thesis, Ecole Polytechnique de Montreal, 2012.

[81] A. Payne, A. Daniel, A. Mehta, B. Thompson, C. S Bamji, D. Snow, H. Oshima, L. Prather, M. Fenton, L. Kordus, et al. 7.6 a 512× 424 cmos 3d time-of-flight image sensor with multi-frequency photo-demodulation up to 130mhz and 2gs/s adc. In *2014 IEEE International Solid-State Circuits Conference Digest of Technical Papers (ISSCC)*, pages 134–135. IEEE, 2014.

[82] Y. Petit, J. Dansereau, and H. Labelle. Biomechanical Evaluation of the Boston Brace System for the Treatment of Adolescent Idiopathic Scoliosis Relationship between Strap Tension and Brace Interface Forces. *Spine (Phila Pa 1976)*, 29(1):26–32, 2003.

[83] K. Rathnayaka, T. Sahama, M. A. Schuetz, and B. Schmutz. Effects of ct image segmentation methods on the accuracy of long bone 3d reconstructions. *Medical engineering & physics*, 33(2):226–233, 2011.

[84] D. F. Redaelli. Analisi sperimentale e modellazione numerica dell'interazione tra l'invaso di una protesi di arto inferiore e l'arto residuo. Master's thesis, Politecnico di Milano, 12 2015.

[85] D. F. Redaelli, E. Biffi, G. Colombo, P. Fraschini, and G. Reni. Current and future manufacturing of chest orthoses, considering the case of osteogenesis imperfecta. In *ASME 2018 International Design Engineering Technical Conferences and Computers and Information in Engineering Conference*. American Society of Mechanical Engineers Digital Collection, 2018.

[86] D. F. Redaelli, S. Gonizzi Barsanti, P. Fraschini, E. Biffi, and G. Colombo. Low-cost 3d devices and laser scanners comparison for the application in orthopedic centres. *ISPRS - International Archives of the Photogrammetry, Remote Sensing and Spatial Information Sciences*, XLII-2:953–960, may 2018.

[87] D. F. Redaelli, F. A. Storm, E. Biffi, G. Reni, and G. Colombo. A virtual design process to produce scoliosis braces by additive manufacturing. In C. Rizzi, A. O. Andrisano, F. Leali, F. Gherardini, F. Pini, and A. Vergnano, editors, *Design Tools and Methods in Industrial Engineering*, pages 860–870, Cham, 2020. Springer International Publishing.

[88] Rodin4D. Rodin4D Global CAD/CAM solution for CPO. `http://rodin4d.com/en`. Accessed: 2019-10-11.

[89] J. M. Saleh and K. W. Dalgarno. Cost and benefit analysis of fused deposition modelling (fdm) technique and selective laser sintering (sls) for fabrication of customised foot orthoses. In *Innovative Developments in Design and Manufacturing*, pages 723–728. CRC Press, 2009.

[90] A. Sato, J. Ouellet, T. Muneta, F. H. Glorieux, and F. Rauch. Scoliosis in osteogenesis imperfecta caused by COL1A1/COL1A2 mutations - genotype-phenotype correlations and effect of bisphosphonate treatment. *Bone*, 86:53–57, 2016.

[91] C. G. Saunders, M. Bannon, R. M. Sabiston, L. Panych, S. L. Jenks, I. R. Wood, and S. Raschke. The canfit system: shape management technology for prosthetic and orthotic applications. *JPO: Journal of Prosthetics and Orthotics*, 1(3):122–130, 1989.

[92] B. M. Schmitt, C. F. Zirbes, C. Bonin, D. Lohmann, D. C. Lencina, and A. C. S. Netto. A comparative study of cartesian and delta 3d printers on producing pla parts. *Materials Research*, 20:883–886, 2017.

[93] J. Sell and P. O'Connor. The xbox one system on a chip and kinect sensor. *IEEE Micro*, 34(2):44–53, 2014.

[94] Siemens. Human-centered design, simulation and ergonomics. `https://www.plm.automation.siemens.com/global/it/products/tecnomatix/human-modeling-and-simulation.html`. Accessed: 2019-11-9.

[95] J. J. Sinikumpu, M. Ojaniemi, P. Lehenkari, and W. Serlo. Severe osteogenesis imperfecta Type-III and its challenging treatment in newborn and preschool children. A systematic review. *Injury*, 46(8):1440–1446, 2015.

[96] Scoliosis Research Society. Adolescent idiopathic scoliosis. `https://www.srs.org/patients-and-families/conditions-and-treatments/parents/scoliosis/adolescent-idiopathic-scoliosis`. Accessed: 2019-11-10.

[97] Clinique Spinecor. Screening for scolliosis - signs and symptoms. `https://www.cliniquespinecor.ca/en/scoliosis_screening.php`. Accessed: 2019-11-10.

[98] Sportinjuryclinic. Kyphosis. `https://www.sportsinjuryclinic.net/sport-injuries/back/upper-back-neck/kyphosis`, 2016. Accessed: 2019-11-10.

[99] Sunshine Prosthetics & Orthotics. Pediatric spinal orthoses. `https://sunshinepando.com/spinal-orthotics-pediatric/`. Accessed: 2019-12-1.

[100] M. D. Tam, S. D. Laycock, D. Bell, and A. Chojnowski. 3-d printout of a dicom file to aid surgical planning in a 6 year old patient with a large scapular osteochondroma complicating congenital diaphyseal aclasia. *Journal of radiology case reports*, 6(1):31–37, 2012.

[101] S. Telfer and J. Woodburn. The use of 3d surface scanning for the measurement and assessment of the human foot. *Journal of foot and ankle research*, 3(1):19, 2010.

[102] J. Tong, J. Zhou, L. Liu, Z. Pan, and H. Yan. Scanning 3d full human bodies using kinects. *IEEE transactions on visualization and computer graphics*, 18(4):643–650, 2012.

[103] I. Valverde, G. Gomez, A. Gonzalez, C. Suarez-Mejias, A. Adsuar, J. F. Coserria, S. Uribe, T. Gomez-Cia, and A. R. Hosseinpour. Three-dimensional patient-specific cardiac model for surgical planning in nikaidoh procedure. *Cardiology in the Young*, 25(4):698–704, 2015.

Bibliography

[104] J. M. Vanswearingen. Measuring wrist muscle strength. *Journal of Orthopaedic & Sports Physical Therapy*, 4(4):217–228, 1983.

[105] VDI. Optical 3d-measuring systems. Standard, VDI, Dusseldorf, Germany, December 2008.

[106] C. L. Ventola. Medical Applications for 3D Printing: Current and Projected Uses. *P & T : a Peer-Reviewed Journal for Formulary Management*, 39(10):704–711, 2014.

[107] P. Volonghi, G. Baronio, and A. Signoroni. 3d scanning and geometry processing techniques for customised hand orthotics: an experimental assessment. *Virtual and Physical Prototyping*, 13(2):105–116, 2018.

[108] Vorum. The inventor of prosthetics and orthotics cad/cam. `https://vorum.com`. Accessed: 2019-10-11.

[109] X. L. Wang, P. J. Stolka, E. Boctor, G. Hager, and M. Choti. The kinect as an interventional tracking system. In *Medical Imaging 2012: Image-Guided Procedures, Robotic Interventions, and Modeling*. International Society for Optics and Photonics, 2012.

[110] Warren Chiropractic Center. Scoliosis braces: navigating the differing types. `https://www.warrenchiro.com/scoliosis-braces-navigating-the-differing-types/`, 2015. Accessed: 2019-12-1.

[111] S. L. Weinstein. The natural history of adolescent idiopathic scoliosis. *Journal of Pediatric Orthopaedics*, 39(6, Supplement 1):S44–S46, 2019.

[112] S. L. Weinstein, L. A. Dolan, J. G. Wright, and M. B. Dobbs. Effects of bracing in adolescents with idiopathic scoliosis. *New England Journal of Medicine*, 369(16):1512–1521, 2013.

[113] H. R. Weiss, N. Tournavitis, X. Nan, M. Borysov, and L. Paul. Workflow of CAD / CAM Scoliosis Brace Adjustment in Preparation Using 3D Printing. *The Open Medical Informatics Journal*, 11(1):44–51, 2017.

[114] K. Wenzel, M. Abdel-Wahab, A. Cefalu, and D. Fritsch. High-resolution surface reconstruction from imagery for close range cultural heritage applications. *International Archives of the Photogrammetry, Remote Sensing and Spatial Information Sciences*, 39:B5, 2012.

[115] M. S. Wong and J. H. Evans. Biomechanical evaluation of the Milwaukee brace. *Prosthetics and orthotics international*, 22(1):54–67, 1998.

[116] M. Xu, T. Scholl, P. Berjano, J. Cruz, and J. Yang. Rod stress prediction in spinal alignment surgery with different supplementary rod constructing techniques: A finite element study. In *International Design Engineering Technical Conferences and Computers and Information in Engineering Conference*, volume 1B, 08 2018.

[117] Zesty Technology. The numble v2. `https://zesty.tech/products/the-nimble-v2`. Accessed: 2019-12-1.

[118] Y. Zhang and T. H. Kwok. Customization and topology optimization of compression casts/braces on two-manifold surfaces. *Computer-Aided Design*, 111:113–122, 2019.

APPENDIX $\mathcal{A}$
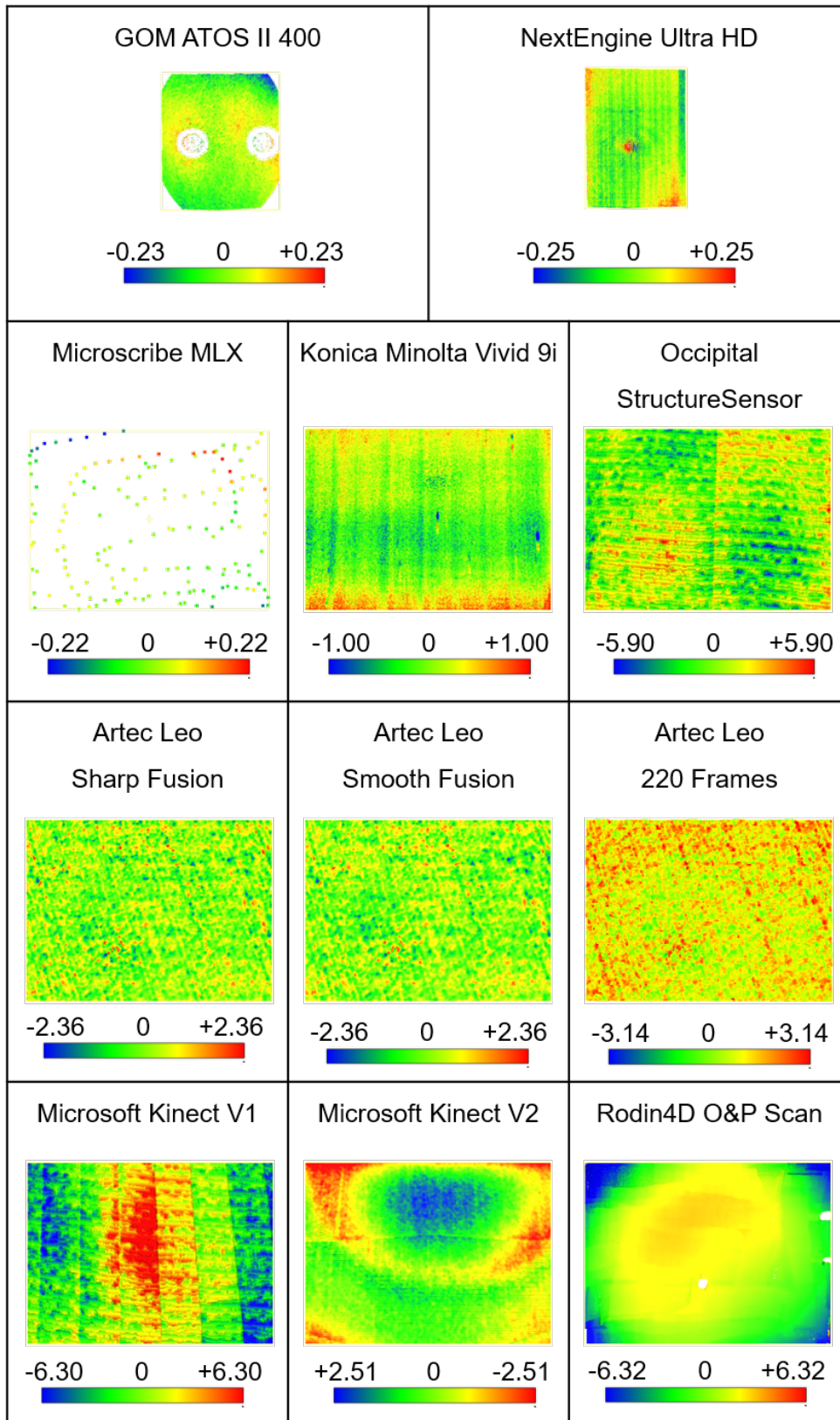
Detailed images

A.1 Scanner Comparisons
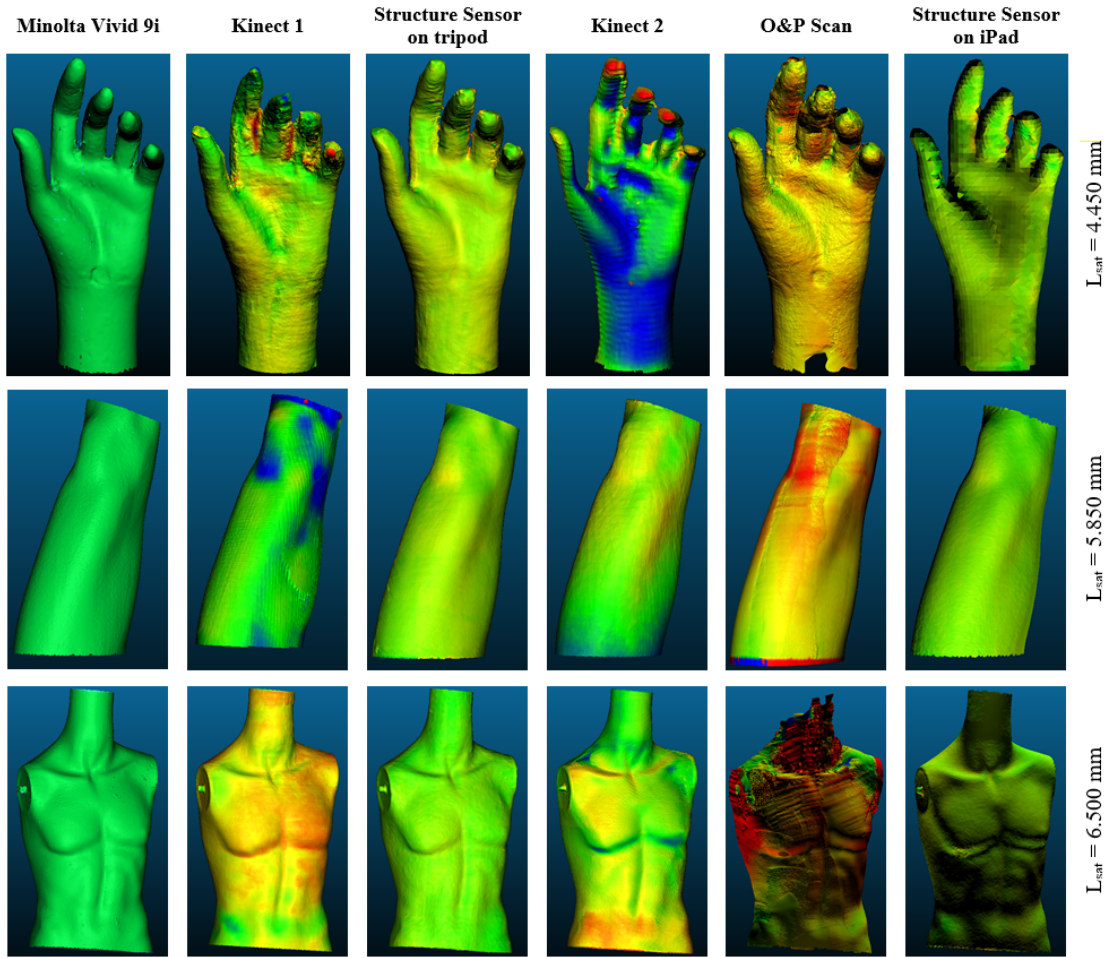
Figure A.1: *Results of the comparison on the flat plane scanned with each tested device, with color maps representing the distance from the ideal plane.*

| Minolta Vivid 9i | Kinect 1 | Structure Sensor on tripod | Kinect 2 | O&P Scan | Structure Sensor on iPad |

Figure A.2: *Results obtained by the different devices as published in [86], organized by column, acquiring the three anatomical objects, organized by row. The models acquired with Minolta, first column, were used as reference in the comparison of all the other devices. The colour scale is the same gradual one depicted in the first column of Figure 2 and it has been set to be the same in the row with the limits for saturation indicated by the value Lsat on the right side, different for each object.*

A.2 Virtual Modeling of the Brace
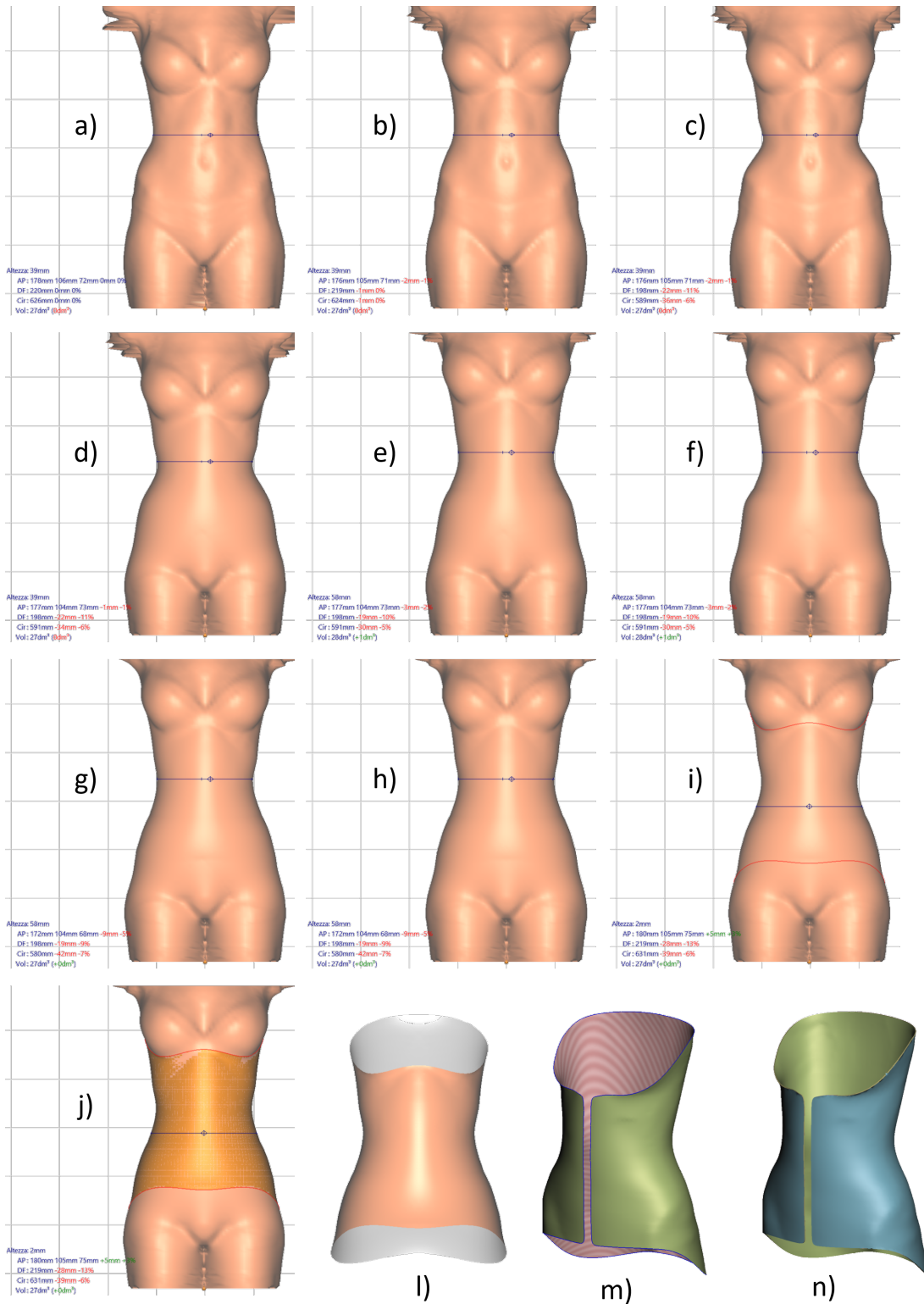
Figure A.3: *Long modeling sequence using the orthopedic-oriented software, Rodin4D Neo and finalizing it in the general-purpose one, Autodesk Meshmixer. a) Starting point with reconstruction from 3D scanner. b) Symmetrization of the model. c) Waist diameter reduction. d) General smoothing. e) Vertical stretching. f) Pelvis enlargement for anchorage. g) Hips smoothing. h) Final balancing. i) Brace borders cut. l) Surface extraction. l) and m) Surface model from Rodin4D Neo to Autodesk Meshmixer with from opening. n) Thickening.*

145

A.3 Morphing of Parametric Skeleton Model

For the sake of a better visualization, in the following figures the kinematic chain is presented only for the pelvis, the whole spine and the sternum. The morphing sequence stars by deforming the pelvis, then the vertebrae, finally the ribcage, the shoulder girdle and the humeri.
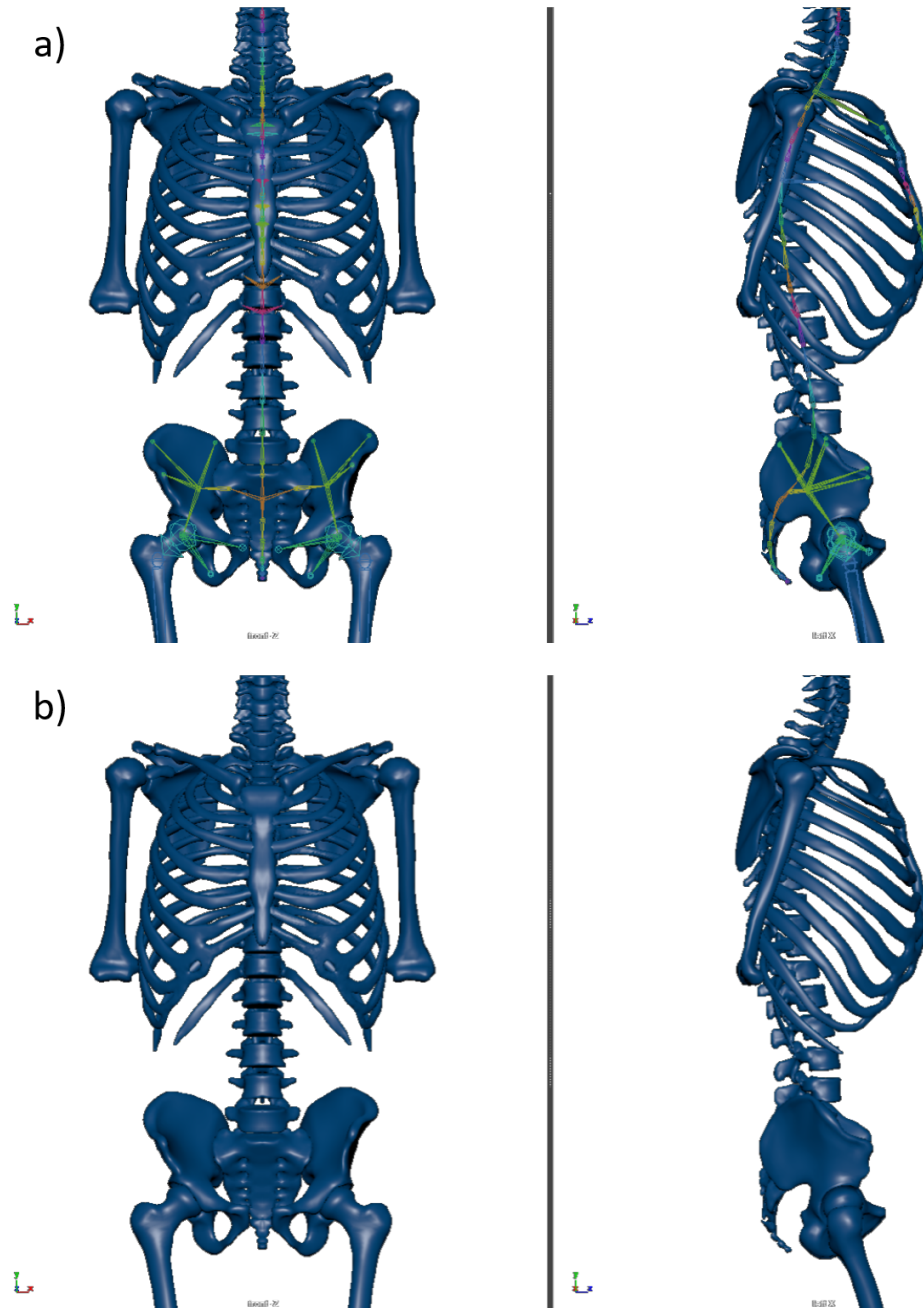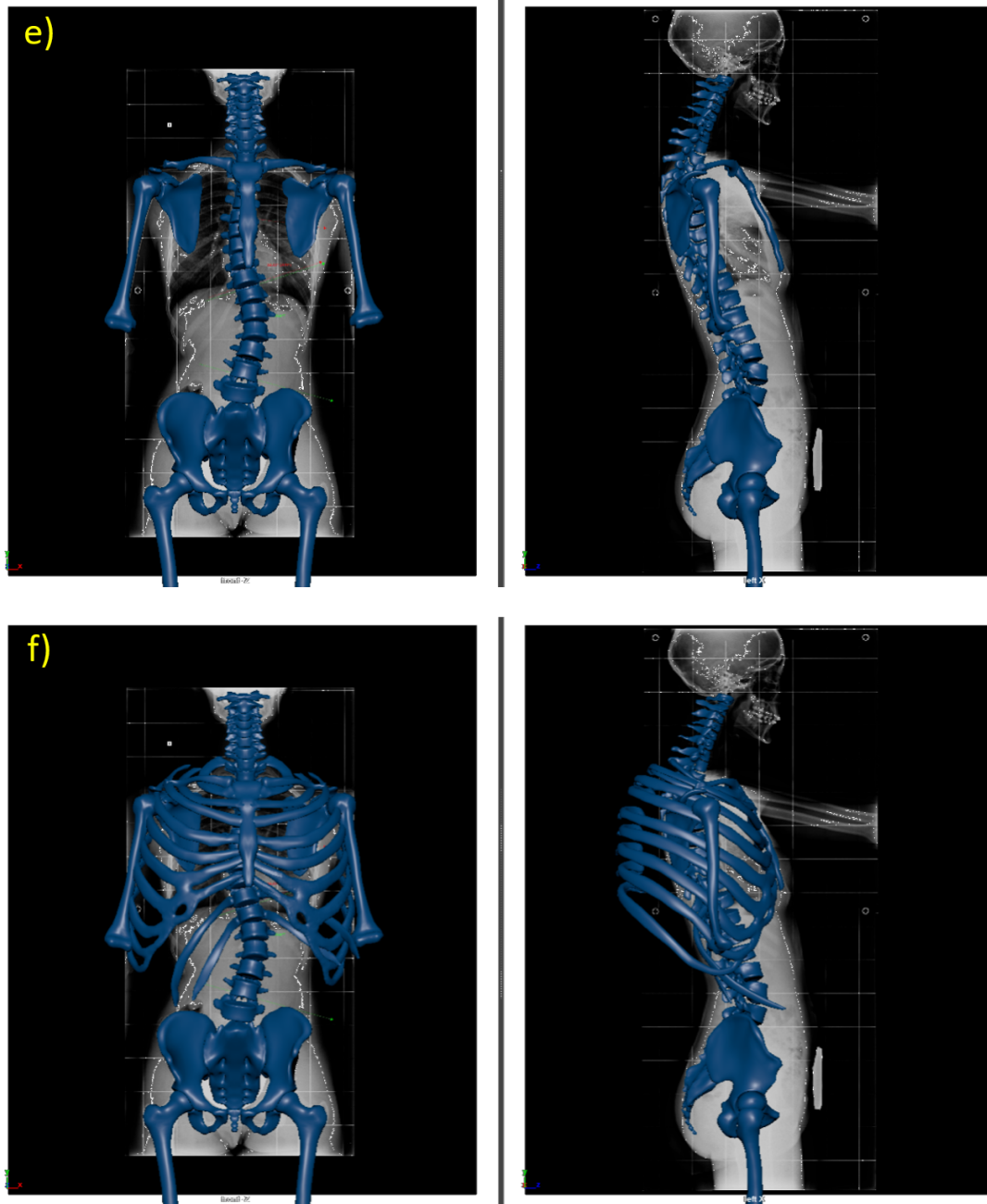

Figure A.4: *Frontal and right views of the undeformed model with (a) and without (b) partial kinematic chain.*
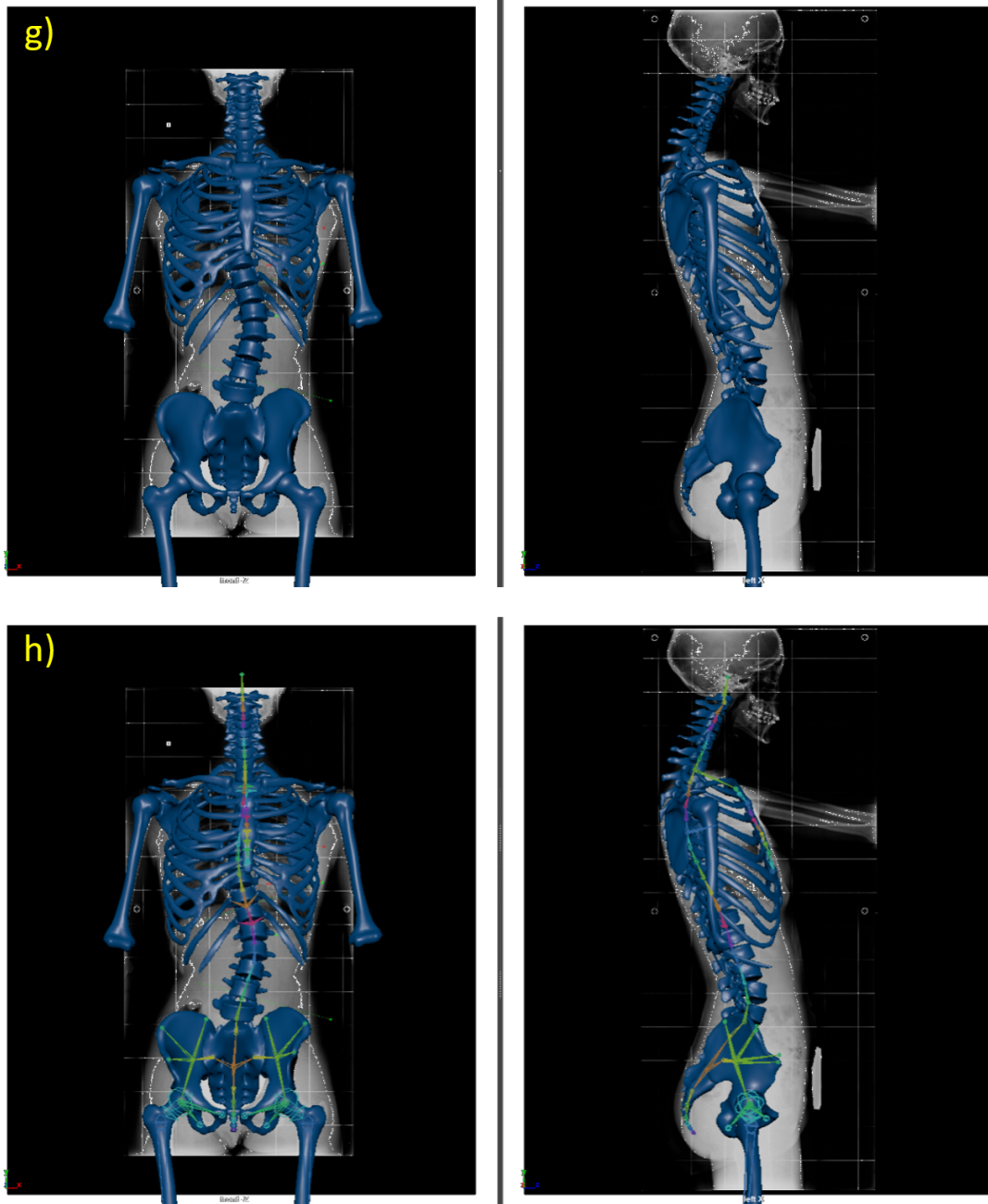
Figure A.5: *Frontal and right views with active X-ray images of the undeformed model (c) and without the ribcage (d).*
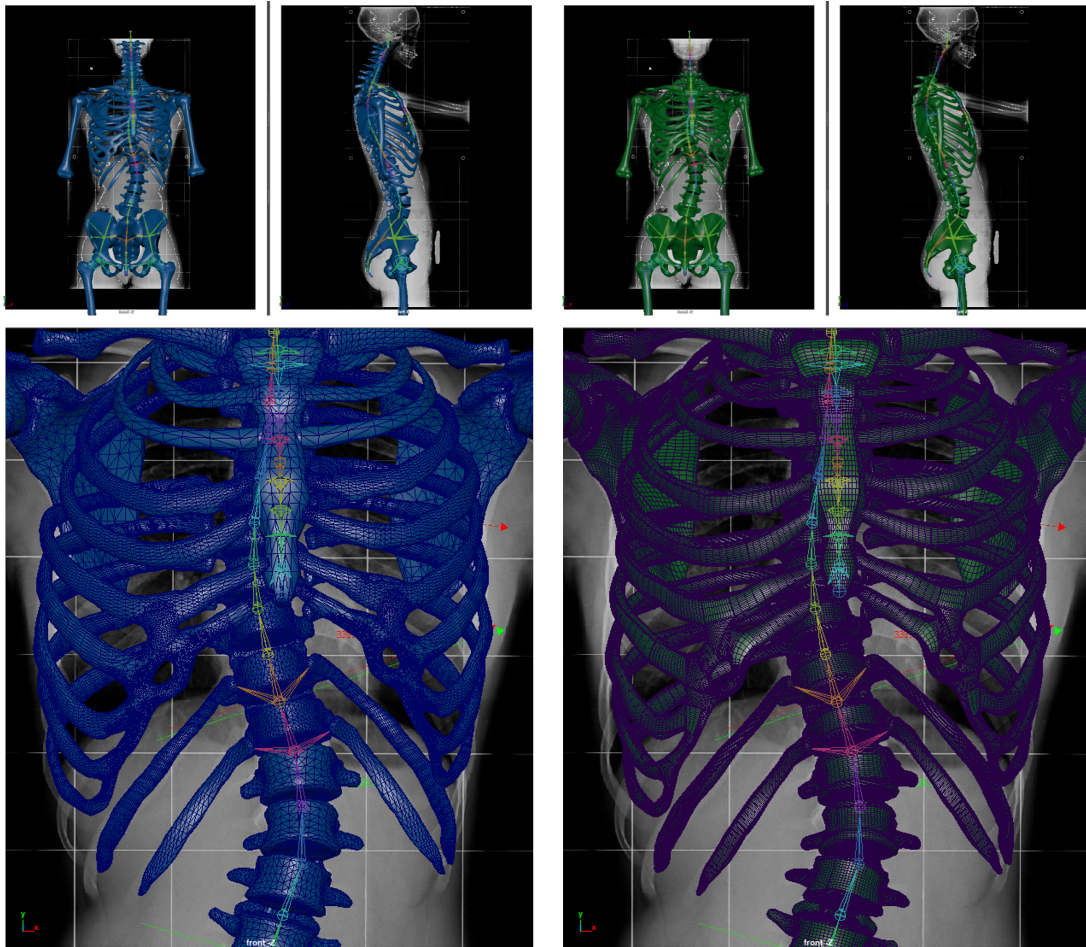
Figure A.6: *Frontal and right views with active X-ray images of the spine deformation (e) and with undeformed ribcage (f).*

Figure A.7: *Frontal and right views with active X-ray images of the complete deformation of the skeleton model without (g) and with (h) partial kinematic chain.*

Figure A.8: *Final model deformed for the specific patient, both for the polygonal version (left side, in blue) and for the NURBS one (right side, in green). The bottom images show an enlargement of the chest region with the wireframe over the surfaces, showing the edges of the triangles (polygonal model on the left) and of the rectangular patches (NURBS on the right).*